Aircraft-based in situ measurements of CH_4 and CO_2 downstream of European and Asian urban centres at local to synoptic scales

Theresa Maria Klausner

SIGILL. UNIVERSITAT. LUDOVIC. MAXIM.

München 2020

Aircraft-based in situ measurements of CH_4 and CO_2 downstream of European and Asian urban centres at local to synoptic scales

Theresa Maria Klausner

Dissertation
an der Fakultät für Physik
der Ludwig-Maximilians-Universität
München

vorgelegt von
Theresa Maria Klausner
aus München

München, den 24.07.2020

Erstgutachter:	Prof. Dr. Markus Rapp
Zweitgutachter:	Prof. Dr. Mark Wenig
Tag der mündlichen Prüfung:	24.09.2020

Zusammenfassung

Die zwei wichtigsten anthropogenen Treibhausgase (THG) sind Kohlenstoffdioxid (CO_2) und Methan (CH_4), mit globalen Konzentrationen von zurzeit ~414,5 ppm bzw. ~1897 ppb. Zur Begrenzung der globalen Erwärmung ist ein genaues Verständnis ihrer Quellen und Senken erforderlich. Städtische Gebiete sind relevante THG Emittenten, aber aufgrund ihrer vielen individuellen kleinen Quellen sind die gesamten städtischen CO_2 und CH_4 Emissionen, deren Aufteilung in einzelne Quellsektoren und deren räumliche Verteilung unzureichend bekannt.

In dieser Arbeit wird die Hypothese evaluiert, dass flugzeuggestützte in-situ Messungen geeignet sind, um die Auswirkungen urbaner CO_2 und CH_4 Emissionen auf die lokale bis synoptische THG Verteilung zu identifizieren und zu quantifizieren. Eine hoch empfindliche laser-gestützten Absorptionstechnik (*Cavity Ring-Down Spektroskopie*) wurde bei drei wissenschaftlichen Messkampagnen eingesetzt: $[UC]^2$ (Urban Climate Under Change), EMeRGe-Europa und EMeRGe-Asien (Effect of Megacities on the transport and transformation of pollutants on the Regional to Global scales). Aufgrund der umfangreichen Charakterisierung des Instruments sowie der Verwendung von Kalibrationsstandards, welche auf die WMO Skala rückführbar sind, beläuft sich die Gesamtunsicherheit der CO_2 und CH_4 Messungen auf 0,2 ppm bzw. 1,1 ppb (~1 % der atmosphärischen Mischungsverhältnisse).

Anhand einer lokalen Fallstudie am 20. Juli während $[UC]^2$ wurde die Berliner THG Fahne vom atmosphärischen Hintergrund abgegrenzt und Emissionsraten für CH_4 ($5{,}20 \pm 1{,}70\,\mathrm{kg\,s^{-1}}$) und CO_2 ($1{,}39 \pm 0{,}76\ \mathrm{t\ s^{-1}}$) mit Hilfe einer Massenbilanz-Methode abgeleitet. Während die extrapolierten jährlichen CO_2 Emissionsraten innerhalb der Fehlergrenzen mit aktuellen Emissionskatastern übereinstimmen, liegen sie für CH_4 zwei bis siebenmal höher. Der Grund für die Diskrepanz wurde mithilfe von Ergebnissen eines hochauflösenden regionalen Chemie-Klimamodells auf eine Unterschätzung der CH_4 Emissionen innerhalb der Stadt, sowie auf fehlende Inventarquellen im Umland zurückgeführt. Für letzteres könnten zahlreiche Mülldeponien und/oder Kläranlagen verantwortlich sein. Diese Arbeit zeigt erfolgreich, dass unabhängige *top-down* Schätzungen wichtig sind um *bottom-up* Emissionsraten zu überprüfen.

Signaturen von europäischen und asiatischen urbanen CO_2 und CH_4 Emissionen konnten während EMeRGe im Abwind von London (UK), Barcelona (Spanien) und Manila (Philippinen) detektiert werden. Da die Messentfernung zu den jeweiligen Städten bis zu 250 km betrug, und sich somit die Abluftfahnen bereits mit der Umgebungsluft vermischten, wurde ihre Herkunft mit numerischen Modellsimulationen und zeitgleichen Messungen von kurzlebigen Spurengasen verifiziert. Die Beobachtung von großräumigen CH_4 und CO_2 Erhöhungen in der freien Troposphäre deuten darauf hin, dass das regionale THG Budget im Frühjahr stark durch den Einfluss vermischter Emissionen von Clustern von Megastädten des chinesischen Festlandes bestimmt wird. Frühere Messkampagnen in Asien (TRACE-P und KORUS-AQ der NASA) weisen ähnliche Muster in der regionalen THG Verteilung auf. Wie erwartet wurden jedoch höhere mittlere Mischungsverhältnisse während EMeRGe-Asien aufgrund der globalen Zunahme atmosphärischer CO_2 und CH_4 Konzentrationen detektiert. Diese Arbeiten bestätigen, dass in-situ Messungen ebenso erfolgreich eingesetzt werden können, um städtische THG Emissionen auf der meso- bis synoptischen Skala zu untersuchen.

Abstract

The two most important anthropogenic greenhouse gases (GHG) are carbon dioxide (CO_2) and methane (CH_4) with current global mole fractions of ~414.5 ppm CO_2 and ~1897 ppb CH_4. In order to develop efficient mitigation strategies limiting global warming, an accurate understanding of their sources and sinks is necessary. Urban areas are recognised as significant GHG emitters but constitute of a large variety of individual smaller sources. Hence, there is a lack of information on the magnitude of total urban CO_2 and CH_4 emissions, on their division into different source sectors and on their spatial distribution.

This thesis evaluates the hypothesis that aircraft-borne in situ measurements are a useful tool to identify and quantify the impact of urban CH_4 and CO_2 emissions on the local to synoptic scale GHG distribution. A sensitive laser-based absorption technique, cavity ring-down spectroscopy, was deployed within three scientific field campaigns: $[UC]^2$ (Urban Climate Under Change), EMeRGe-Europe and EMeRGe-Asia (Effect of Megacities on the transport and transformation of pollutants on the Regional to Global scales). The extensive characterisation and calibration with gas standards traceable to the WMO scales allows for measuring CO_2 and CH_4 mole fractions with an overall uncertainty of 0.2 ppm and 1.1 ppb, respectively, representing less than 1 % of the current atmospheric background.

Based on a local case study on July 20th during $[UC]^2$ it was possible to clearly distinguish Berlin's urban GHG plume from the atmospheric background and to derive emission rates for CH_4 (5.20 ± 1.70 kg s^{-1}) and CO_2 (1.39 ± 0.76 t s^{-1}) using a mass balance method. While extrapolated annual CO_2 emission rates agree within error bars with current inventories, they are two to seven times higher for CH_4. Combining aircraft measurements with results from a high-resolution regional chemistry climate model, it was shown that the discrepancy is due to an underestimation of urban CH_4 emissions within the city, as well as due to missing inventorial sources in the surroundings, which may include numerous waste dumps and/or wastewater treatment plants. This study successfully demonstrates that such independent airborne top-down estimates are important to evaluate bottom-up emission inventories.

Signatures of European and Asian urban CO_2 and CH_4 emissions were detected in the regional GHG budget during EMeRGe for London (United Kingdom), Barcelona (Spain) and Manila (the Philippines) even at downwind distances up to 250 km. Due to the large distances from the respective sources, emissions were already mixed with cleaner background air or other pollution plumes. Their identification therefore was verified by numerical model simulations and co-measured short-lived species. The frequent observation of large-scale GHG plumes in the free troposphere downstream of China, indicate that the regional GHG budget during springtime is heavily impacted by the outflow from mixed emissions from megacity clusters from mainland China. A comparison with previous aircraft campaigns conducted in Asia (TRACE-P and KORUS-AQ of NASA) shows that similar patterns were observed in the regional GHG distributions. However, as expected, larger mean mole fractions were detected during EMeRGe-Asia due to the increase in global atmospheric CO_2 and CH_4 concentrations. These studies show that in situ instruments can also be successfully used to study the impact of urban emissions on the meso- to synoptic scale GHG budget.

Parts of the methods and results presented in this thesis have been published in the following article:

Klausner, T., Mertens, M., Huntrieser, H., Galkowski, M., Kuhlmann, G., Baumann, R., Fiehn, A., Jöckel, P., Pühl, M., and Roiger, A.: Urban greenhouse gas emissions from the Berlin area: A case study using airborne CO_2 and CH_4 in situ observations in summer 2018, Elem. Sci. Anth. 2020a, 8. DOI:10.1525/elementa.411.

T. Klausner performed the measurements, analysed all data and wrote the manuscript. M. Mertens and P. Jöckel performed the MECO(n) simulations. A. Roiger developed the research idea and supported together with H. Huntrieser the interpretation and the ongoing analyses. M. Galkowski performed and analysed the VPRM simulations. G. Kuhlmann pre-processed the emission data for BERLIN. R. Baumann provided the HYSPLIT simulation tool. A. Fiehn and M. Pühl supported the measurements.

Parts of the thesis are literal excerpts of the paper and include paragraphs from Sect. 2.1.3, 2.2.1, 2.2.2, 3.2, 3.3 and 4.1; from Chapter 5; as well as from Appendix A.5 to A.10.

Content

1 Introduction

1.1 Motivation

The global climate has been changing throughout the last century. In 2019 a rise of approximately 1.1 °C (±0.1 °C) in global mean surface temperature above pre-industrial levels (1850 to 1900) was recorded (WMO, 2020). With the beginning of the 1980s, each decade has become warmer than the previous one. Hence, the recent decade (2010 to 2019) is the warmest on record, and especially the past five years (2015 to 2019) are the hottest ones.

This human-induced global warming is already impacting the climate system itself, as well as civilisation, ecosystems and organisms. This was summarised by the World Meteorological Organization (WMO, 2020) for the year 2019: Rising sea levels, especially enhanced by the melting of ice sheets in Greenland and Antarctica, reached record high values of +90 mm compared to 1993. The growth and reproduction of some organisms, like mussels and corals, declined because the higher acidity of sea water lowers their ability to calcify. Extreme heat waves, recorded in Europe with maximum temperatures of 41 to 46 °C, increased heat-related illnesses and deaths. Conversely, cold waves in the Midwestern United States reached a temperature minimum of -39 °C. Significant flooding persisted in the Mississippi basin for nearly seven months, which led to economic losses. In contrast, droughts in the Mekong basin resulted in water shortages and agricultural losses. Australia experienced an exceptionally long and severe fire season of two months and more, killing people, destroying property and wildlife habitats. This is only a selected number of examples regarding the consequences of climate change. However, it must be expected that such events will occur more frequently and will intensify with a sustained greenhouse effect.

The increasing atmospheric levels of well-mixed greenhouse gases (GHGs) are a major driver of this human-induced global warming. Water vapour (H_2O), methane (CH_4) and carbon dioxide (CO_2) hereby contribute the most to the greenhouse effect of the Earth (Myhre et al., 2013). While H_2O is a natural GHG and less affected by anthropogenic activities, the atmospheric abundances of the two latter ones are strongly influenced by humans (e.g. Le Quéré et al., 2018; Saunois et al., 2019). Global averaged surface CO_2 mole fractions increased to levels of ~408 ppm in 2018, which is ~150 % higher compared to levels before 1750 (WMO, 2020). Mole fractions of CH_4 reached ~1869 ppb, which even corresponds to an increase of ~260 %. If anthropogenic GHG emissions and the current rate of the observed temperature increase persist, global warming will likely reach +1.5 °C somewhere between 2030 and 2052 (IPCC, 2018). To achieve a lower temperature rise, especially on short-terms, CH_4 is an excellent target to reduce its emissions since it has a shorter atmospheric lifetime (9.1 ± 0.9 years; Prather et al., 2012) compared to CO_2 (tens to thousands of years; Archer et al., 2009), in combination with a stronger Global Warming Potential (GWP_{100} of 26).

However, for the prediction of future global warming and the trend of the atmospheric GHG budget, an accurate understanding of its sources and sinks is essential. On the one hand, the

GHG emissions serve as input for carbon coupled climate models, which are used as a baseline to develop efficient mitigation strategies. On the other hand, observational datasets of atmospheric GHG mole fractions are implemented to strengthen and validate the model capabilities to better understand the past, present and future climate. Currently, total CO_2 emissions of developed countries can be estimated with high accuracy due to the precise knowledge of national fossil fuel consumption. For example, the widely used gridded emission inventory EDGAR (Emission Database for Global Atmospheric Research), retrieved standard deviations (2σ) of European CO_2 emissions of only 5 % (Janssens-Maenhout et al., 2019; with respect to EU15 countries). However, their spatial and temporal distribution is less well known (Bréon et al., 2015) and emissions from different source sectors are typically spatially distributed using proxies related to e.g. population density or road networks. The global net CH_4 budget is also relatively well constrained (Kirschke et al., 2013; Saunois et al., 2016 and 2019), but the individual contribution of single source sectors, especially broken down on the national, regional or even city scale, is not sufficiently understood (e.g. Dlugokencky et al., 2011; Kirschke et al., 2013; Saunois et al., 2017). Thus, it is necessary to expand and improve the quantification of local and regional CO_2 and CH_4 emissions to better understand the global GHG budget.

More than half of the world population lives in urban areas (UN, 2018b), which in turn occupy less than 3 % of the earth's terrestrial surface (Liu et al., 2014). This spatial concentration of high population density, and hence, established economy and intense energy usage, inevitably leads to the release of large amounts of GHGs into the atmosphere (Kennedy et al., 2012; Marcotullio et al., 2013; Zhu et al., 2013). Almost two-thirds of the total global CH_4 emissions are released from human activities and are mainly linked to agriculture and waste, as well as to fossil fuel production and use (Saunois et al., 2019). With respect to anthropogenic CO_2, emissions are closely coupled to the consumption of fossil fuels for energy production and transport (Helfter et al., 2011) which represent roughly 53 to 87 % of global emissions (Seto et al., 2014).

In order to develop efficient mitigation strategies, GHG emissions must be well known. The so-called top-down approach uses measurements of atmospheric GHG mole fractions to derive emission rates for individual point sources or larger areas like cities. The challenge hereby is to detect only small GHG enhancements above a relatively high atmospheric background concentration. Top-down results can then be used to independently validate total bottom-up emissions. These are based on known or assumed statistical activity data and specific emission factors, which are often subject to large uncertainties (Nisbet and Weiss, 2010; Brandt et al., 2014). While the focus of airborne GHG studies has so far been especially on American cities (e.g. Mays et al., 2009; Cambaliza et al., 2015; Ren et al., 2018; Plant et al., 2019; Ryoo et al., 2019; Turnbull et al., 2019), they are relatively sparse for Europe (Gioli et al., 2014; O'Shea et al., 2014; Pitt et al., 2019) and to my knowledge not apparent for Asia.

It is important to note that cities are not only recognised as a large source of GHGs, but they are also more vulnerable to climate risks and weather events being linked to climate change. For example, dense urban agglomerations in Asia are located in the plains of large rivers (e.g. the Yangtze River Delta) and are thus immediately affected by more frequent and intense heavy rain and flooding events (Huq et al., 2016). China, having the largest urban population living in coastal zones, needs to adapt to the sea level rise (McGranahan et al., 2016). The higher frequency of heat-waves, as well as increasing mean temperatures, forces cities to deal with additional electricity demand to run an increasing number of air condition systems (LCCP, 2002). In return, cities also have a huge potential for emission reductions by composing and adapting mitigation policies at the local scale. Policy expertise is already shared e.g. among the C40 Cities Climate Leadership Group (*www.c40.org*). To name only two case studies (*www.c40.org/case_studies*), Copenhagen (Denmark) recycles half of their waste to produce heat and less than 2 % is stored in landfills. The city of London (United Kingdom) reduced CO_2 emissions in the central business district by 16 % due to introducing a fee for freight and other heavy good vehicles, hence minimising the total number of vehicles.

1.2 Research objectives

In order to contribute to the limited knowledge of European and Asian urban GHG emissions and to study their impact on the GHG budget from the local to the meso- and synoptic scale, the present thesis investigates an aircraft-based in situ data set of lower tropospheric CO_2 and CH_4 mole fractions, which was gathered within the framework of this thesis.

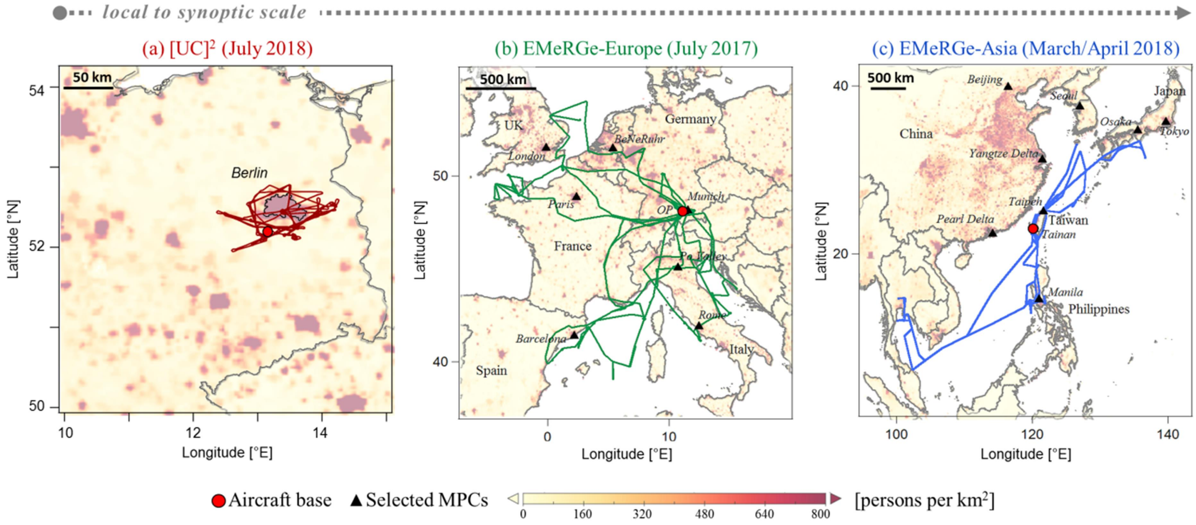

Figure 1.1: (a) DLR Cessna flight routes of the $[UC]^2$ mission in July 2018. (b and c) HALO flight routes of the EMeRGe-Europe and Asia mission in July 2017 and March/April 2018, respectively. Red dots mark the aircraft bases during these campaigns; black triangles the selected major population centres of interest; the colour-coded map underneath reflects the population density in persons per km^2 for the combined years 2000, 2005, 2015 and 2020 (CIESIN, 2018).

To this end, high-accuracy CO_2 and CH_4 measurements were conducted downwind of selected urban agglomerations within three airborne scientific missions: $[UC]^2$ (Urban Climate Under Change), EMeRGe-Europe and EMeRGe-Asia (Effect of Megacities on the transport and transformation of pollutants on the Regional to Global scales). An overview of the target regions and the respective flight tracks are given in Fig. 1.1. The investigation on the local scale (panel a) focuses on the area of few kilometres to tens of kilometres downwind of the German capital Berlin and was subject of the $[UC]^2$ campaign in summer 2018. Research flights were carried out within the boundary layer using the DLR research aircraft

Cessna Grand Caravan. Observations on the meso- to synoptic scale (100s to few 1000s of km) are covered by the EMeRGe missions and were conducted with the German research aircraft HALO in summer 2017 in Europe (panel b) and spring 2018 in Asia (panel c).

The following hypothesis is formulated:

“Aircraft-borne in situ measurements are a useful tool for both identifying urban CH_4 and CO_2 emissions and quantifying their source strength. The signatures of urban GHG emissions can also be detected in the regional GHG distribution.”

To verify this hypothesis, the following scientific questions need to be answered:

Investigations on the local scale ─ the city of Berlin

RQ 1) To what extent do annual GHG emission rates from different bottom-up inventories agree for a major European capital like Berlin?

RQ 2) Can emission rates of GHG be estimated for the city of Berlin from airborne in situ instruments using a mass balance approach?

RQ 3) How do top-down emission rates derived with the mass balance method compare to bottom-up inventories?

RQ 4) Can simulations of regional models in combination with airborne measurements be used to identify GHG sources which are missing in the bottom-up inventories?

Investigations on the meso- to synoptic scale ─ European and Asian urban agglomerations

RQ 5) Can signatures of urban and other emission sources be detected by airborne measurements in the regional scale distribution of CH_4 in Europe and Asia?

RQ 6) How do the regional CH_4 emission distributions in Europe and in Asia compare with each other and with previous observations?

To answer these research questions, the thesis includes the following parts: Chapter 2 presents background information needed to understand the necessity for accurate and independent atmospheric CO_2 and CH_4 measurements, especially with respect to urban agglomerations. In Chapter 3 the applied measurement instrument and two numerical models, used to complement the analysis of the airborne observations, are described. Chapter 4 assesses the performance of the used GHG measurement instrument. Chapter 5 and 6 present selected case studies on the local and larger spatial scales and discuss the data in the context of previously published measurements. In Chapter 7 the main findings are summarised and recommendations for future studies are given.

2 Theoretical background

In this chapter background information relevant for this thesis is presented. The goal is to provide an understanding of the need for precise and independent airborne measurements of CO_2 and CH_4 in urban areas. Section 2.1 focuses on the two anthropogenic GHGs methane and carbon dioxide. Their contribution to global warming is discussed, as well as trends in atmospheric GHG mole fractions since the industrial revolution, the concomitant global budgets and their emission sources in urban areas. The second section, 2.2, describes the principle methods used for estimating GHG emissions. Two different approaches are introduced: the bottom-up and the top-down method. This work uses the airborne mass balance approach, which is one example of a top-down method to infer city-wide GHG emission rates. The corresponding in situ CO_2 and CH_4 measurements rely on cavity ring-down spectroscopy. Section 2.3 addresses the vertical structure of the atmosphere. The focus is on the boundary layer, connected to the earth's surface, where most of the anthropogenic emissions are released.

2.1 Methane and carbon dioxide

The chemical composition of the earth's atmosphere (with respect to dry air and up to ~105 km) is almost constant with ~78 % nitrogen (N_2) and ~21 % oxygen (O_2). Apart from these two main components, GHG such as H_2O, CO_2 and CH_4 only account for less than 1 % (Wallace and Hobbs, 2006). The amount of these GHGs varies largely in time and space, and due to their high climatological significance, they are interesting from a scientific point of view. H_2O is the main driver for the natural greenhouse effect (Myhre et al., 2013). Its maximum amount in the atmosphere depends mostly on air temperature and not on anthropogenic emissions. In contrast, CO_2 and CH_4 mole fractions in the atmosphere are strongly altered by humans (e.g. Le Quéré et al., 2018; Saunois et al., 2019) and are thus considered as anthropogenic GHG, being the largest contributors to the anthropogenic greenhouse effect (Myhre et al., 2013).

2.1.1 Contribution to global warming

There is a consensus among the scientific community that anthropogenic GHGs contribute substantially to the recent global warming (e.g. Oreskes, 2004; Anderegg et al., 2010; Verheggen et al., 2014) as GHGs absorb and re-emit infrared (IR) radiation emitted from the earth's surface. IR-active species, such as CO_2 and CH_4, are molecules whose dipole moment changes during molecular vibration and who exhibit characteristic IR spectra, unlike the diatomic gases N_2 and O_2 (e.g. Günzler and Gremlich, 2003).

The radiation transmitted by the atmosphere depends on the wavelength (see Fig. 2.1a). Incoming solar radiation (with its emission maxima roughly at 0.5 µm) is absorbed by the earth's surface. From the earth's surface upward thermal radiation is emitted with a maximum of ~9 µm. Parts of this radiation is transmitted into space within a narrow spectral range (~8 to

~14 µm), the so-called atmospheric window. CO_2 and CH_4 (highlighted in orange) restrict the size of the atmospheric window because they absorb upward thermal radiation at characteristic wavelengths. Hence, less energy is transmitted into space and more is trapped within the system.

This change in the earth's energy budget, which is driven by well mixed GHGs and other external factors (e.g. aerosols, solar irradiance or surface albedo), is described by the term radiative forcing (RF). The RF quantifies the change between downward solar and outgoing thermal radiation occurring at the top of the atmosphere or at the climatological tropopause. A positive RF indicates a net gain of energy, which results in surface warming. The total anthropogenic effective RF for the year 2011 (relative to 1750) was estimated to be positive with +2.3 W m^{-2} (range from 1.1 to 3.3 W m^{-2}) and is with more than 90 % determined by the contribution of CO_2 and CH_4 (Myhre et al., 2013). From 1880 to 2018 the average global surface temperature increased by 1 °C (see Fig. 2.1b). If no action is taken, and the current rate of warming persists, global warming will likely reach 1.5 °C between 2030 and 2052 (Allen et al., 2018).

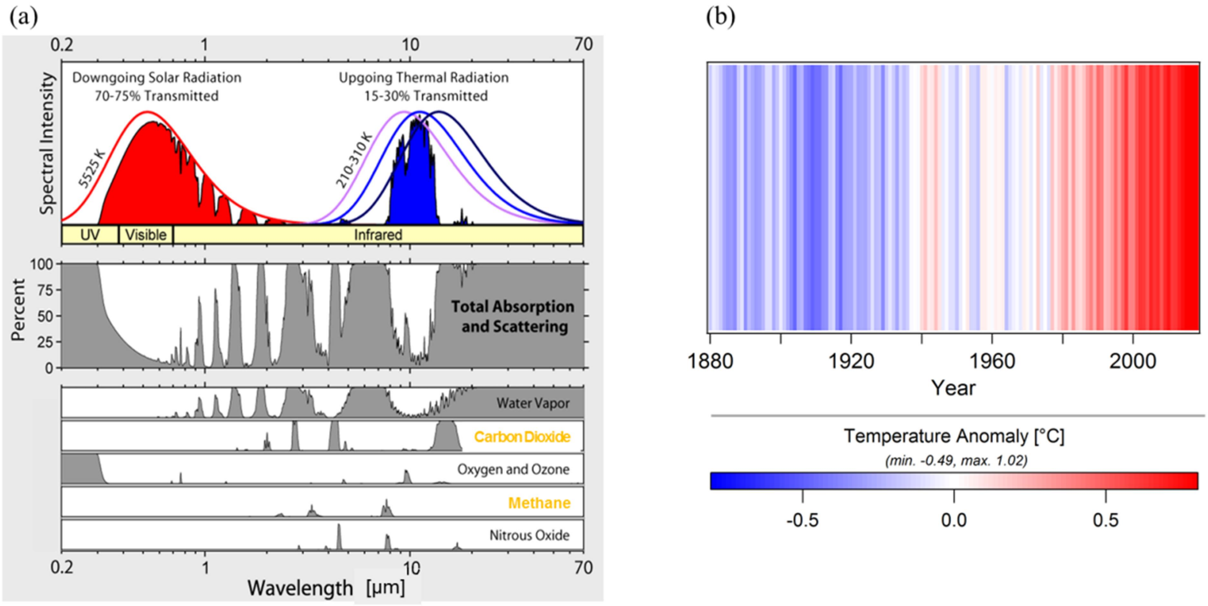

Figure 2.1: (a) Spectra of incoming solar (red) and outgoing thermal (blue) radiation, together with absorption bands (grey) of the major atmospheric constituents and the total absorption and scattering; adapted from Alimonti et al. (2018). (b) Change in global surface temperature relative to the 1951 to 1980 average (NASA Goddard Institute for Space Studies, data retrieved from *https://climate.nasa.gov/vital-signs/global-temperature*; last access 04.11.2019).

2.1.2 Decadal trends and global atmospheric budget

The mole fraction of a particular trace gas in dry air is usually expressed in mol mol^{-1} and relates the number of moles of the targeted gas to the number of moles in dry air. Within the thesis the term µmol mol^{-1} is referred to as ppm (parts per million) and nmol mol^{-1} as ppb (parts per billion).

Atmospheric mole fractions of CH_4 and CO_2 are primarily affected by anthropogenic activities within recent decades (e.g. Le Quéré et al., 2018; Saunois et al., 2019). The Mauna Loa Observatory in Hawaii records CH_4 and CO_2 mole fractions since the mid-80s and mid-70s, respectively (see Fig. 2.2). This long-term monitoring station, run by NOAA (National Oceanic and Atmospheric Administration), is suitable to determine global GHG mole fractions and trends because of its remote oceanic location. The influence of short term GHG emissions by local vegetation and anthropogenic activities at this station is negligible. Blue dots represent the monthly average of in situ measurements, indicating that in March 2020 CH_4 mole fractions reached 1897 ppb and 414.5 ppm CO_2 is detected. In comparison to pre-industrial times, CH_4 and CO_2 have increased by a factor of ~2.7 and ~1.5 respectively. Pre-industrial reference values (i.e. the average mole fraction between 1000 and 1800) are taken for CH_4 from Etheridge et al. (1998) with 695 ± 40 ppb and for CO_2 from Etheridge et al. (1996) with 275 to 284 ppm.

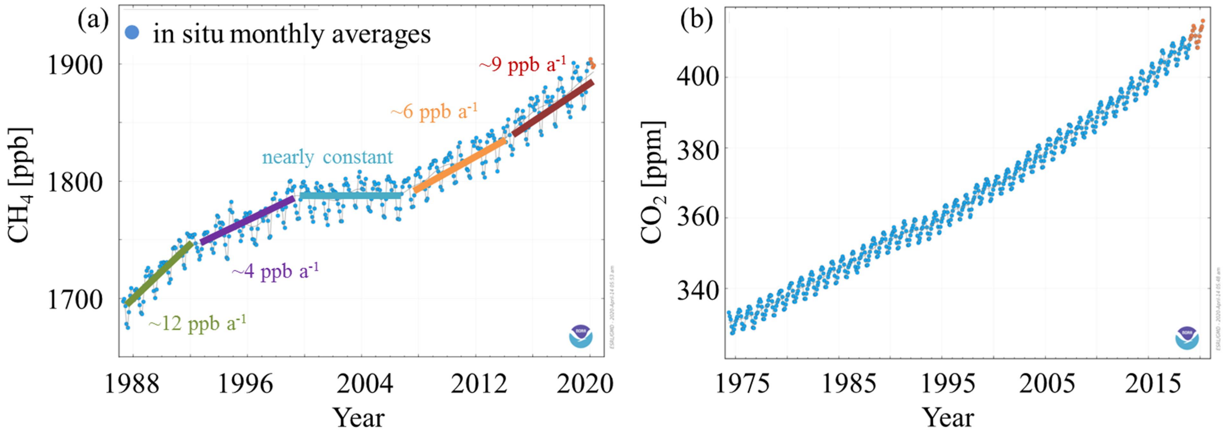

Figure 2.2: Monthly in situ observations of (a) CH_4 and (b) CO_2 at Mauna Loa (Hawaii). Orange markers are preliminary data. Panel (a) also shows the mean growth rate of CH_4 in ppb a^{-1} calculated for the indicated time periods. Both panels are adapted from NOAA's Earth System Research Laboratory, Global Monitoring Division Carbon Cycle Interactive Atmospheric Data Visualization Website *https:/.esrl.noaa.gov/gmd/dv/iadv/graph.php?code=MLO&program=ccgg&type=ts*; last access 14.04.2020.

Methane budget

The atmospheric methane budget is determined by its various sources and sinks. Saunois et al. (2019) have estimated the CH_4 budget for the decade 2008 to 2017, as illustrated in Fig. 2.3. The emission sources are of anthropogenic and natural origin and they predominate the sinks, hence, global CH_4 mole fractions are increasing.

According to Saunois et al. (2019) roughly 60 % of global CH_4 emissions are released by anthropogenic activities. They are linked to agriculture and waste treatment (219 Tg a^{-1}), production and use of coal, oil and gas (109 Tg a^{-1}), as well as to biomass and biofuel burning (30 Tg a^{-1}). The remaining ~40 % of total emissions originate from natural sources, where the largest contribution is associated with wetlands (178 Tg a^{-1}). Other natural sources like inland waters, oceans, termites and wild ruminant animals are responsible for 37 Tg a^{-1}, but they are much more uncertain. All sources sum up to 572 Tg a^{-1} (range 538-593). Emission estimates by Saunois et al. (2019) for the previous decade (2000-2009) result in 545 Tg a^{-1} (range 522-

559), which is consistent within ~1 % to values reported by Saunois et al. (2016) and Kirschke et al. (2013). Hence, total global emissions of methane are relatively well known. But the quantitative contribution of these single source sectors broken down on the national, regional or even city scale, is not sufficiently understood (e.g. Dlugokencky et al., 2011; Kirschke et al., 2013; Saunois et al., 2017).

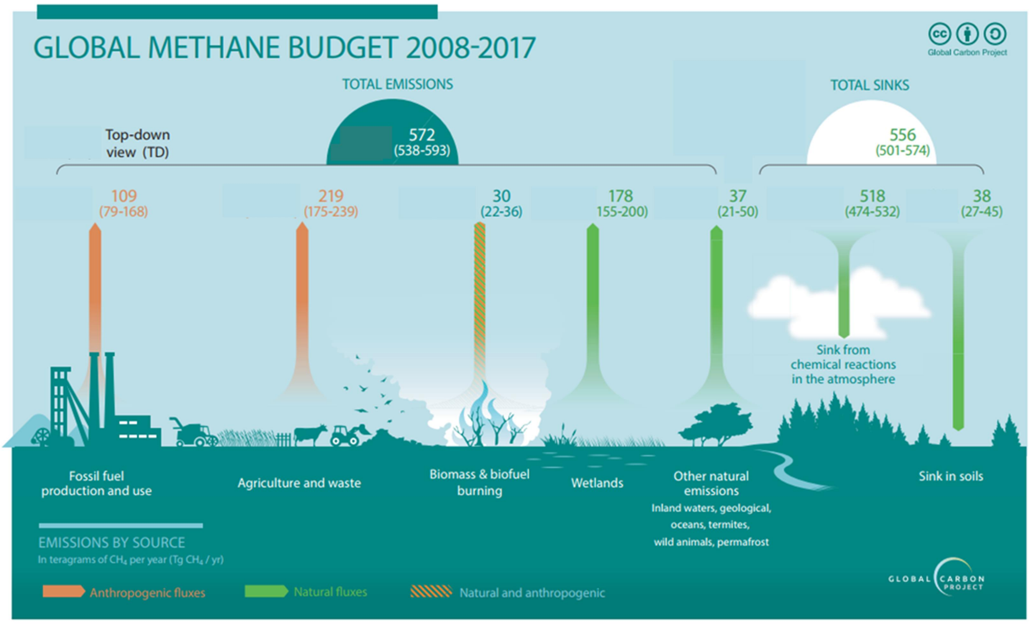

Figure 2.3: Global methane budget for the decade 2008 to 2017, given in Tg CH_4 a^{-1}. Only the top-down estimates (see Sect. 2.2.1) are shown for emission sources and sinks (adapted from Saunois et al., 2019).

Methane emissions are countered by sinks, which are responsible for the removal of 556 Tg a^{-1} (range 501-574). The depletion is dominated by chemical reactions in the atmosphere (518 Tg a^{-1}). The largest part thereby is the oxidation of CH_4 by the tropospheric hydroxyl (OH) radical (~90 %; Kirschke et al., 2013). The resulting reaction products are H_2O and methyl radicals (CH_3), which in turn are successively oxidised (via multiple steps) to CO and ultimately to CO_2 (Jacob, 1999). To a minor extent CH_4 is oxidised in the stratosphere by atomic oxygen, chlorine and fluorine, and also in the marine boundary layer by atomic chlorine from sea salt (Kirschke et al., 2013; Saunois et al., 2019). Once in the ground, CH_4 is lost in soils (38 Tg a^{-1}) by methanotrophs (archaea), which use CH_4 as only carbon source for their metabolism, and by diffusive transport of air into the soil. The resulting atmospheric lifetime of CH_4 amount to $9.1 \pm 0.9\,a^{-1}$ (Prather et al., 2012). Therefore, after only a decade a CH_4 molecule is removed from the atmosphere. On the timescales of only few hours to days, as covered in the analysis of this thesis, the sinks of CH_4 can however be neglected.

The CH_4 growth rate, i.e. the imbalance between sources and sinks, is also depicted in Fig. 2.2a and is still subject of debate in many contradictory studies. Especially the renewed increase since 2007 (highlighted in orange and red) and the long stagnation period (indicated in blue) are difficult to explain. In addition, the growth rate was exceptionally strong in 2014 and 2015 with ~13 and ~10 ppb a^{-1}, respectively (Nisbet et al., 2019). Potential explanatory attempts include:

(a) increasing emissions from biogenic sources linked to agriculture (Schaefer et al., 2016) or expanded natural wetlands (Bousquet et al., 2011; Nisbet et al., 2016);
(b) a larger dominance of fossil fuel emissions (Schneising et al., 2014; Hausmann et al., 2016; Schwietzke et al., 2016; Turner et al., 2016);
(c) a decrease in OH concentration (Rigby et al., 2008; Voosen, 2016); or
(d) a combination of (a) to (c).

Methane emission sources are not only classified by their origin (natural vs. anthropogenic), but also by their underlying emitting process into biogenic, thermogenic and pyrogenic CH_4. A strong tool to distinguish them is the isotopic signature of CH_4, which is reported in the delta notation, see Eq. (2.1):

$$\delta^{13}C = \left(\frac{R_{sample}}{R_{standard}} - 1\right)1000 \tag{2.1}$$

where R is the stable isotope ratio of ^{13}C:^{12}C and the $\delta^{13}C(CH_4)$ value relates the ratio R of a sample to the ratio R of a standard called (Vienna) Pee Dee Belemnite, expressed in per mil [‰]. Biogenic CH_4 is produced by archaea, which decompose organic matter under anaerobic conditions (e.g. in wetlands, ruminants, rice paddies or landfills). Hence, methane is enriched in ^{12}C and is characterised by a more negative isotopic signature compared to thermogenic or pyrogenic CH_4 (Quay et al., 1999; see also Fig. 2.4). Thermogenic CH_4, released during the exploitation and distribution of fossil fuels (which was earlier formed by the destruction of organic matter due to high pressure and temperature in the earth's crust) and pyrogenic CH_4, released by the incomplete combustion of organic matter, are both enriched in ^{13}C.

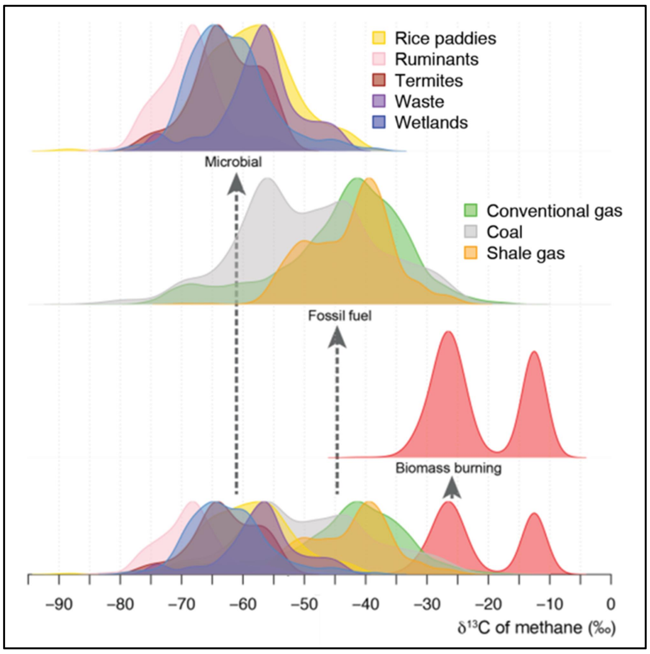

Figure 2.4: Normalised probability density distribution of $\delta^{13}C(CH_4)$ for microbial, fossil fuel and biomass burning sources based on a global database (Sherwood et al., 2017).

During the stagnation period (Fig. 2.2a, indicated in blue) the isotopic signature of CH_4 shifted towards more positive values, i.e. indications of thermogenic sources. However, since the growth rate is on the rise again (indicated in orange and red), $\delta^{13}C(CH_4)$ values have become more negative by ~0.3 ‰ (Nisbet et al., 2019). Therefore, if CH_4 emissions rose due to the increased use of natural gas and oil (as proposed earlier), it has to be accompanied by one (or a combination) of the following features in order to agree with the observed isotopic CH_4 trend: The fossil fuel emissions must have a more negative isotopic value than before and/or a simultaneous decrease of a $^{13}C(CH_4)$-rich source must occur (Nisbet et al., 2019).

Carbon dioxide budget

The natural carbon cycle redistributes carbon between the atmosphere, ocean, biosphere and geological reservoirs and seems to be in balance over the long term. However, in recent decades the cycle is perturbed by adding constantly CO_2 released from anthropogenic activities. This additional CO_2 originates mainly from the combustion of fossil fuels (~9.4 ± 0.5 Gt C a^{-1}) used for transport, heating, cooling and industrial activities, but also from the change in land-use (~1.5 ± 0.7 Gt C a^{-1}), e.g. by deforestation and land clearing for harvest yield. CO_2 is removed by land (~3.2 ± 0.7 Gt C a^{-1}) and ocean (~2.4 ± 0.5 Gt C a^{-1}) uptake, resulting in an atmospheric increase of ~4.7 ± 0.02 Gt C a^{-1}. All numbers represent the average from 2008 to 2017 and are taken from Le Quéré et al. (2018), a report on the global carbon budget, which is corrected and updated every year.

Total CO_2 emissions of developed countries can be estimated with high accuracy due to the precise knowledge of national fossil fuel consumption amounts. However, the spatial and temporal distribution of emissions is less well known because of lack of appropriate data (Bréon et al., 2015). The atmospheric lifetime of CO_2 is difficult to estimate since CO_2 is redistributed among different reservoirs but not entirely removed. A broad agreement is achieved with timescales between tens and thousands of years (Archer et al., 2009). The constantly increasing trend of CO_2 in the atmosphere is unambiguous (see Fig. 2.2b), and neither the Kyoto Protocol of 2005, nor the Paris Agreement of 2015 seemed to cause any changes to it.

2.1.3 Emissions from urban areas

Currently urban areas cover less than 3 % of the terrestrial earth surface (Liu et al., 2014), but accommodate more than half of the world population, with a persistent increasing trend (UN, 2018b), see also Fig. 2.5. In Europe the level of urbanization (i.e. the percentage of urban population in total population) is already at 74 %. Asia, with roughly 50 % urban residents, is expected to urbanise much faster until the mid of the century (+16 %) compared to Europe (+10 %). This spatial concentration of high population density, growing economy, increasing energy usage and rapid industrialization in such small areas leads to reduced air quality, which is often measured by short lived air pollutants, such as sulfur dioxide (SO_2), nitrogen oxides (NO_x), carbon monoxide (CO), volatile organic compounds (VOCs), particulate matter (PM) and ozone (O_3). Only in recent years, the attention was also drawn towards cities being a hotspot for GHG emissions (Kennedy et al., 2012; Marcotullio et al., 2013; Zhu et al., 2013).

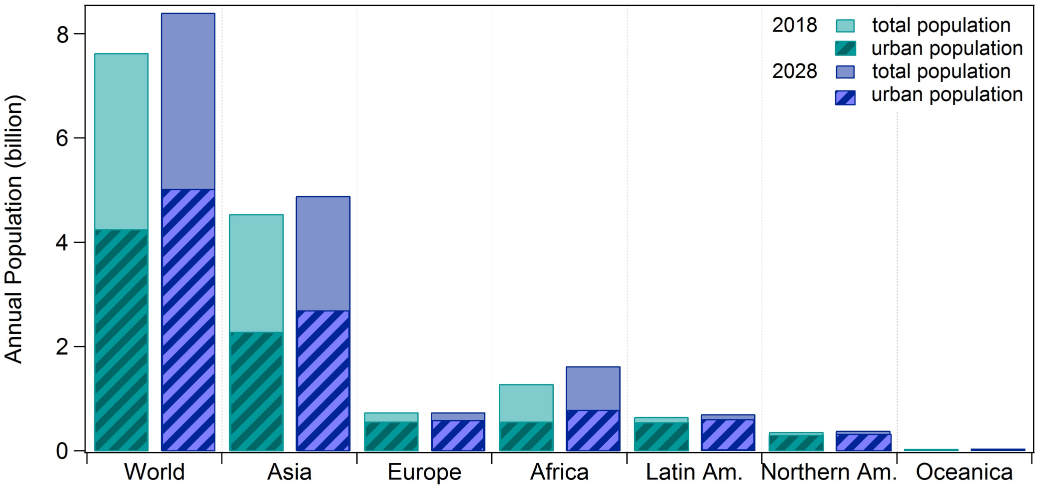

Figure 2.5: Annual total (solid bars) and urban (striped bars) population in 2018 and projected to 2028 for different regions of the world (UN, 2018b). America is abbreviated with Am.

Cities are highly diverse, not only between different continents but also between and among different countries. Therefore, only few studies exist which attempt to scale up their emissions to global values. Wunch et al. (2009) estimated correlation coefficients between measured column abundances of CH_4 and CO_2 in the greater Los Angeles area in spring 2008. Under the assumption that such correlations are representative for other major cities, 21 to 34 % of global anthropogenic CH_4 is estimated to be of urban origin. This number is 7 to 15 % larger than currently assumed. According to the "megacities project" by NASA (Nautical Aeronautics and Space Administration) Jet Propulsion Laboratory, cities and power plants emit 70 % of fossil fuel CO_2 to the atmosphere. Seto et al. (2014) states, that energy related CO_2 emissions contribute with 53 to 87 % to the global budget.

Several studies have been performed with focus on individual metropolis to estimate individual CH_4 and CO_2 emissions. Recent studies are more often found for cities in the United States, e.g. Indianapolis (Mays et al., 2009; Cambaliza et al., 2015), Los Angeles (Hopkins et al., 2016), the Baltimore-Washington area (Ren et al., 2018), Boston (Phillips et al., 2013) and urban centres along the east coast (Plant et al., 2019). GHG studies on European cities have been conducted e.g. in London (O'Shea et al., 2014; Helfter et al., 2016; Pitt et al., 2019), Paris (Bréon et al., 2015; Lian et al., 2019), Cracow (Kuc et al., 2003; Zimnoch et al., 2019), Florence (Gioli et al., 2012) and Rome (Gioli et al., 2014).

The studies mentioned above use a variety of observations: airborne and ground-based (mobile, long-term stations), in situ and remote sensing, simultaneous measurements of methane and ethane (C_2H_6; a tracer for fugitive fossil emissions) or isotopic $\delta^{13}C(CH_4)$ signatures. Based on airborne measurements a major source of elevated CH_4 from cities in the United States was attributed to natural gas and landfill emissions (e.g. Cambaliza et al., 2015; Ren et al., 2018; Plant et al., 2019). While airborne derived CO_2 emissions from Rome were found to agree with inventorial data (Gioli et al., 2014), CO_2 and CH_4 emissions from London need to be scaled by a factor of 1.57 and 0.7, respectively, in order to agree with airborne derived fluxes (Pitt et al., 2019). While this estimate accounts for peri-urban emissions from the greater London area, their previous estimate (given in the same study) was based on the conventional mass balance approach, where correction factors yielded to a much higher value of 3.08 for CO_2 and 1.22 for CH_4. Ground-based observations in London (Helfter et al., 2016), Paris (Bréon et al., 2015), Cracow (Kuc et al., 2003; Zimnoch et al., 2019) and Florence (Gioli et al., 2012) provide additional information on urban GHG emissions, e.g. long-term CO_2 observations in Florence indicate 19 % higher emissions than reported by inventories (Gioli et al., 2012). Atmospheric monitoring sites in Paris, together with an atmospheric inversion approach, point towards an overestimation of urban emissions by the local inventory (Bréon et al., 2015).

Comprehensive studies on the role of Asian megacities on air pollution and climate change are summarised in a report of the World Meteorological Organization and the Global Atmosphere Watch (Zhu et al., 2013). One key aspect for Asia is that megacities are highly diverse regarding their level of economic development. Thus emission sources are different, e.g. traffic emissions dominate in developed cities and biomass burning is particularly important in developing cities. In Beijing, Hong Kong, Manila, Osaka, Pearl River Delta, Shanghai and Tokyo (selected cities for the EMeRGe-Asia mission) air quality is regularly monitored by automatic measurement stations and specific research programmes, which also lead to reduction strategies of local emissions. However, mainly SO_2, NO_x, PM_{10}, CO and O_3 are monitored and only sparse measurements on CO_2 and CH_4 exist in three of the cities. Although GHG trends were studied for 10 years in Beijing (Liu et al., 2005) and CO_2 measurements were analysed in Shanghai (Li et al., 2008), the reports of these studies are only available in Chinese. Based on the consumption of fuels and average emission factors, Leung and Lee (2000) estimate that CO_2 accounts for ~90 % of the calculated local Hong Kong GHG emissions, resulting mainly from the usage of coal. CH_4 contributes with ~5 %, especially due to waste decomposition. No mass balance or mass balance like study for an Asian city is reported in the current literature.

2.2 Estimating greenhouse gas emissions

In order to keep the global temperature rise well below 2 °C compared to pre-industrial levels (Paris Agreement; UNFCCC, 2015), a reduction of GHG emissions must take place. As presented in Sect. 2.1 large uncertainties exist in sources and sinks of GHGs, especially at smaller spatial scales. To develop efficient mitigation strategies and to predict future climate impacts, an accurate knowledge of the GHG budget is crucial. To improve the understanding and quantification of the budgets, different methods and measurement strategies are used. In the following sections a common division in the bottom-up and top-down approach is introduced with a focus on the airborne mass balance approach, as one example of the top-down method applied within this thesis. Furthermore, the measurement technique of cavity ring-down spectroscopy is presented to obtain GHG mole fractions.

2.2.1 Top-down vs. bottom-up approach

Typically, two different approaches are used to quantify emissions. With the bottom-up (B-U) approach emission factors for specific source categories are multiplied with statistical activity and technology mix data. Hence, emissions can be calculated for a large size of emitters, ranging from single factories to a larger set of industries, or from national to global scales. The top-down (T-D) approach instead uses dedicated atmospheric measurements, which allow for an independent quantification of emissions.

The B-U approach has the advantage that emissions can be calculated globally and sector-wise, e.g. as provided in gridded emission inventories. Furthermore, it provides detailed information about the different emission processes. However, it is well known that emission factors and activity data are subject to large spatial and temporal heterogeneity, as well as to simplified assumptions with large uncertainties (Nisbet and Weiss, 2010; Brandt et al., 2014). E.g., inventories often distribute emission totals for countries with a proxy for population density and/or apply same emission factors for larger areas (Janssens-Maenhout et al., 2012), hence, disregarding local and regional differences. The T-D approach is independent of activity data or emission reports and is therefore commonly used to validate total bottom-up emissions. The atmospheric observations can be performed on different scales and from different measurement platforms (see Sect. 2.2.3) and are combined with, e.g., a mass-balance approach (see Sect. 2.2.2) or inverse modelling techniques to quantify emissions. However, a source attribution to different emission processes usually is much more challenging.

On the one hand, combining the B-U and T-D approach can provide insight into large discrepancies as shown, e.g., by an ensemble of seven different inverse models estimating ~30 % higher European CH_4 emissions (2006 to 2012) than B-U reported values in 2012 (Bergamaschi et al., 2018). On the other hand, reported emissions can be confirmed as shown, e.g., for the city of Indianapolis (Turnbull et al., 2019). A study of Kirschke et al. (2013) examines regional CH_4 budgets for Europe, China and SE-Asia separated by source sectors, see Fig. 2.6. Dark-coloured bars (to the right) present B-U estimates and light-coloured bars (to the left) are inferred from independent T-D estimates. T-D fossil fuel emissions (brown) in Europe and China were found to be ~6 % and ~20 % higher than estimated by B-U inventories (equal in SE-Asia). Emissions from agriculture and waste (blue) tend to be overestimated by ~20 % in Europa and ~14 % in SE-Asia, but slightly underestimated by ~3 % in China.

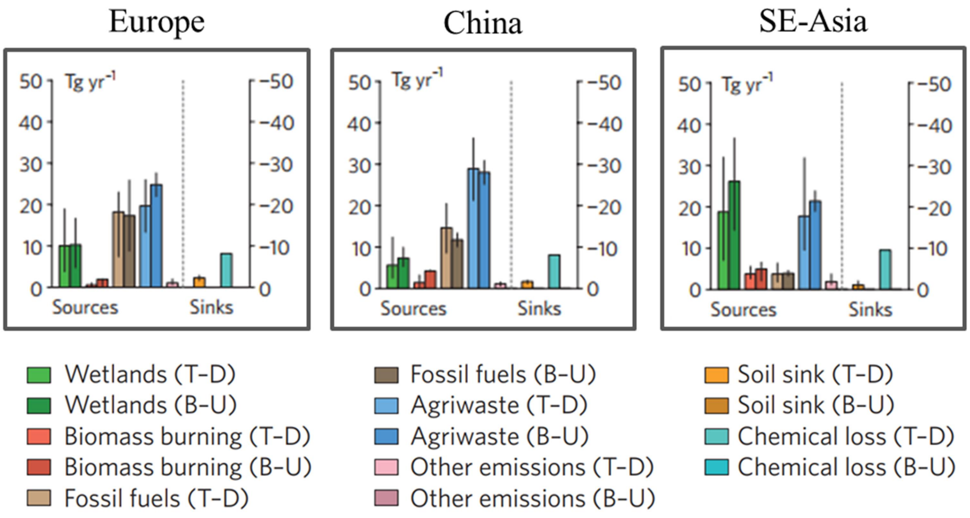

Figure 2.6: CH_4 budgets from Kirschke et al. (2013) for selected regions: Europe, China and SE-Asia (2000-2009). T-D estimates are shown in light-coloured bars, B-U estimates in dark-coloured bars.

2.2.2 The airborne mass balance approach

The aircraft-based mass balance approach is a well-established T-D method to infer CH_4 and CO_2 emission rates. Measurements can focus on individual point sources like landfills, oil and gas facilities or power plants (e.g. Lavoie et al., 2015; Krautwurst et al., 2017; Krings et al., 2018) or on area sources, like cities or larger oil and gas fields (e.g. Mays et al., 2009; O'Shea et al., 2014; Cambaliza et al., 2015; Karion et al., 2015; Heimburger et al., 2017; Ren et al., 2018). This section describes the theoretical background of this method, which is applied within this thesis to derive emissions of Berlin (see Sect. 5.3).

In an idealised mass balance experiment (see Fig. 2.7), the pollution plume from various collocated emission sources within a city is advected and dispersed within the boundary layer (BL, see Sect. 2.3) according to the prevalent wind direction. The flight pattern includes one upwind transect as well as multiple transects at an appropriate downwind distance from the source. They are aligned perpendicular to the wind direction and flown at constant altitudes. The upwind transect is centred at the middle of the BL and is used both, to identify possible emission inflows already being transported into the target region from a distant source, and to identify the natural atmospheric variability. The downwind transects, stacked at several altitudes within the BL, capture the urban outflow downstream of the source. Vertical profiles, extending into the free troposphere, are used to determine the BL depth. Other attempts may include one single downwind flight transect in the centre of the BL (Karion et al., 2013a) or several transects at the same altitude but at different horizontal distances from the source (Turnbull et al., 2011). For single point sources a circular flight route at different heights has also been established (Ryoo et al., 2019).

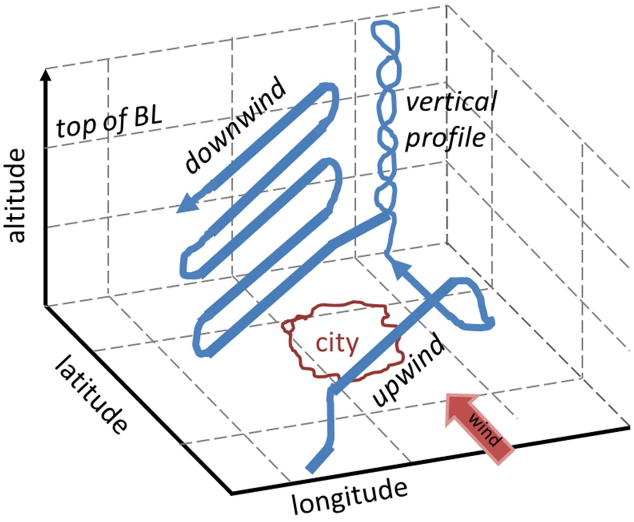

Figure 2.7: Idealised mass balance experiment with the aircraft track in blue and the city boundary in red (adapted from Mays et al., 2009). The aircraft track consists of one upwind leg and several downwind legs at stacked altitudes, as well as of a vertical profile characterising the BL. The wind is perpendicular to the flight track and disperses the urban GHG plume according to the prevalent wind direction within the BL.

All mass balance flights are usually conducted in the afternoon when the BL is fully developed and its height is less variable during the time of the research experiment (see Sect. 2.3). The assumption of constant emission fluxes has to be applied. Steady wind speed and wind direction several hours before and during the flight experiment itself have to be fulfilled. The flux or mass flow rate f [g s^{-1}] through a normal plane downwind of a source is derived using Eq. (2.2):

$$flux = \int_0^{BL} \int_{-k}^{+k} \left([X]_{ij} - \left[X_{bgr}\right]_{ij} \right) \frac{p_{ij}}{T_{ij}*R} \; M \; u_{ij} \; dxdz \qquad (2.2)$$

The background mole fraction X_{bgr} is subtracted from the observed mole fraction X at location x_{ij} and z_{ij} and is converted to molar density using the ideal gas law with observed pressure p and temperature T, and the ideal gas constant R. Combined with the molar mass M and the perpendicular component u of the horizontal wind, a mass flow per unit area is obtained. By integrating along the horizontal boundaries of the plume ($-k$ to k) and in the vertical from ground to the top of the BL, the mass flux through the plane is calculated. Uncertainties in the mass flux arise mainly from varying wind speed, the choice of background determination, varying BL depth, and limited observational data between the lowest altitude transect and the surface (Cambaliza et al., 2014). For the background the mean or the lowest detected mole fractions from an upwind transect or from edges of the downwind transects can be used (Cambaliza et al., 2014; Peischl et al., 2015).

2.2.3 Atmospheric greenhouse gas observations

On the basis of atmospheric measurements the top-down approach can be applied on different spatial scales with observations from various platforms. Greenhouse gas observations can be grouped according to their sampling location into ground-based (surface and tall towers), airborne (aircraft, unmanned aerial vehicles and balloons), and space-based (satellite) measurements. With respect to the measurement technique itself, in situ instruments sample the ambient air at the point of interest, while active and passive remote sensing instruments are located at some distance and rely on propagated signals. In active remote sensing the instrument has its own source of light and actively emits e.g. radio or microwave pulses in radar systems (radio detection and ranging) or laser pulses in LIDAR systems (LIght Detection And Ranging) and measures the reflected energy. Passive remote sensing relies on direct or indirect sunlight.

Ground-based in situ networks are used extensively in studies to estimate global, regional and local GHG budgets and trends. For example, the Mauna Loa Observatory (see Sect. 2.1.2) provides global mole fractions because of its remote location. In combination with inverse modelling, regional networks can be used to estimate the European GHG budget (Kadygrov et al., 2015). Or a single station downwind of China can characterise temporal changes in Chinese CH_4 and CO emissions (Tohjima et al., 2014). A drawback of ground-based in situ stations is the dependence on local emissions and meteorological processes, which are often not representative for larger regions. In addition, the distribution of permanent measurement stations is relatively sparse. Regional networks such as ICOS (Integrated Carbon Observation System; *https://icos-atc.lsce.ipsl.fr*) maintains 29 measurement stations in Europe, but mainly covers Central and Northern Europe. The Global Greenhouse Gas Reference Network (*https://www.esrl.noaa.gov/gmd/ccgg*), on the other hand, lists 73 active measurement sites in

36 countries to monitor CO_2 and CH_4 (status December 2019), but most of the stations are concentrated in the United States and only nine stations are operating in Asia.

Space-based remote sensing instruments on board satellites have the advantage to cover the full globe and recent improvements were made towards a higher spatial resolution and improved retrieval algorithms. SCIAMACHY (SCanning Imaging Absorption SpectroMeter for Atmospheric CHartographY), measuring until 2012, had a footprint of ~30 km × 60 km, while the recently launched Sentinel5Precursor with TROPOMI (TROPOspheric Monitoring Instrument) can resolve gradients already on a 7 km × 7 km scale. A recent study by Miller and Michalak (2020) summarises the changes in the OCO-2 (Orbiting Carbon Observatory) CO_2 retrievals, indicating that with the newest version even magnitudes of comparatively small biospheric CO_2 enhancements can be studied. However, satellite observations provide only column averaged mole fractions and thus the information on the vertical distribution of GHG is missing.

Therefore, aircraft are often used as a spatial and temporal flexible platform to provide snapshots of a current situation covering the horizontal and vertical domain. They may carry a large suite of instruments to simultaneously measure atmospheric gases and particles together with meteorological parameters. In situ instruments aboard research aircraft are able to resolve GHG gradients with high spatial resolution. Dependent on the aircraft speed and the measurement frequency, a few tens of meters can be achieved. Despite the fact that aircraft campaigns are expensive and complex, the challenge in measuring GHG is also precisely detecting small enhancements above a high atmospheric background mole fraction. Therefore, very sensitive instruments are required. One example of such an instrument is the well-established Picarro GHG analyser based on cavity ring-down spectrometry (CRDS).

2.2.4 In situ measurements using cavity ring-down spectroscopy

In conventional spectroscopy, the radiant intensity of the incident (I_0 [W m^{-2}]) and transmitted (I_t [W m^{-2}]) signal is used to determine the concentration of a specific species in a gas sample based on Lambert-Beers Law, see Eq. (2.3):

$$I_t = I_0 \exp(-\sigma L N) \tag{2.3}$$

The cross section of the absorbing species is given with σ [cm^2 molec^{-1}], L [cm] is the path length, and N [molec cm^{-3}] the number density. However, if the absorption is very weak, the small difference between I_0 and I_t is difficult to quantify. Especially when tiny fluctuations in the intensity of pulsed lasers introduce noise (Busch and Busch, 1999). One possibility to obtain the needed sensitivity is to increase the effective absorption path length, e.g. by using multi pass absorption cells, or by reducing the noise in the signal, e.g. by applying modulation techniques.

The measurement technique of CRDS is a highly sensitive in situ technique relying on molecular absorption that can be adapted to a wide range of trace gases. An introduction to CRDS, its history and various applications can be found in Busch and Busch (1999). Hereby the so-called ring-down time is monitored, which is the exponential decay of radiation within a stable optical cavity. The simplest setup consists of a cavity with two highly reflective mirrors, as depicted in Fig. 2.8a. If a short pulse from a laser with narrow spectral width is introduced into the cavity through a partially reflective mirror, light intensity first builds up due to constructive interference. After the laser is shut off, the light gradually decays with every reflection between the mirrors as a small fraction of energy is leaking out of the cavity. The exponential decay is depicted as grey solid line in Fig. 2.8b and is monitored with a photodetector located outside the cavity. The leaking is proportional to the intensity of radiation trapped. In case, the cavity is filled with a gas containing an absorbing species with an absorption feature in the spectral range of the used laser light, the losses within the cavity are enhanced and the exponential decay is more pronounced, depicted by the shorter ring-down time (grey dashed line).

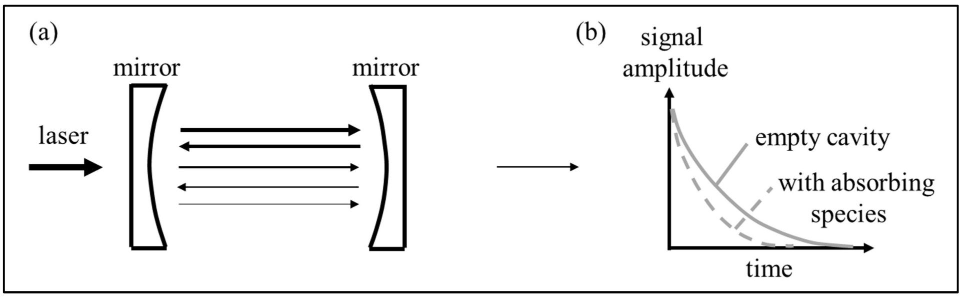

Figure 2.8: Schematic setup of (a) a simple optical cavity with two mirrors and (b) signal of the ring-down time as observed on the detector of an empty and filled cavity (both adapted from Berden and Engeln, 2009).

If both ring-down times are monitored, one can obtain the absorption coefficient α [cm^{-1}] following Eq. (2.4) where c [cm s^{-1}] is the speed of light, τ_1 [s] the ring-down time for the cavity containing the absorbing species and τ_2 [s] the ring-down time for the empty cavity (for a detailed derivation of Eq. (2.4) see Appendix A.3). The number density N is related to the absorption cross section σ and the absorption coefficient α as given in Eq. (2.5). The mole fraction X [mol mol^{-1}] of the absorbing gas is derived by dividing its number density N by the number density of air N_{air} (Eq. (2.6)).

$$\alpha = \frac{1}{c}\left(\frac{1}{\tau_1} - \frac{1}{\tau_2}\right) \tag{2.4}$$

$$N = \frac{\alpha}{\sigma} \tag{2.5}$$

$$X = \frac{N}{N_{air}} \tag{2.6}$$

Hence, the CRDS measurement depends only on the ring-down times and is thus insensitive to fluctuations of the laser source. Together with the ultra-long absorption path lengths of several tens of kilometres these are the major advantages allowing for ultra-sensitive absorption measurements (Paldus and Zare, 1999).

2.3 The atmospheric boundary layer

In this section relevant aspects with respect to the atmosphere and its boundary layer (BL) are summarised. For in-depth details the reader is referred to general meteorology textbooks like Wallace and Hobbs (2006) or Seinfeld and Pandis (2016), from where the following information was taken if not otherwise indicated. The earth's atmosphere can be divided into four distinct layers based on the atmospheric temperature profile, see Fig. 2.9a. From space inward they are named thermosphere, mesosphere, stratosphere and troposphere. In the troposphere an increase in altitude leads to a decrease in temperature at a rate of ~0.65 Kelvin (K) per 100 m up to the tropopause. The tropopause is an important interface at an altitude of roughly 7 km at the poles and 17 km at the equator. The tropopause represents a local temperature minimum in the atmosphere. By this layer the vertical transport of air masses is inhibited and thus weather processes within the troposphere are separated from the stratosphere.

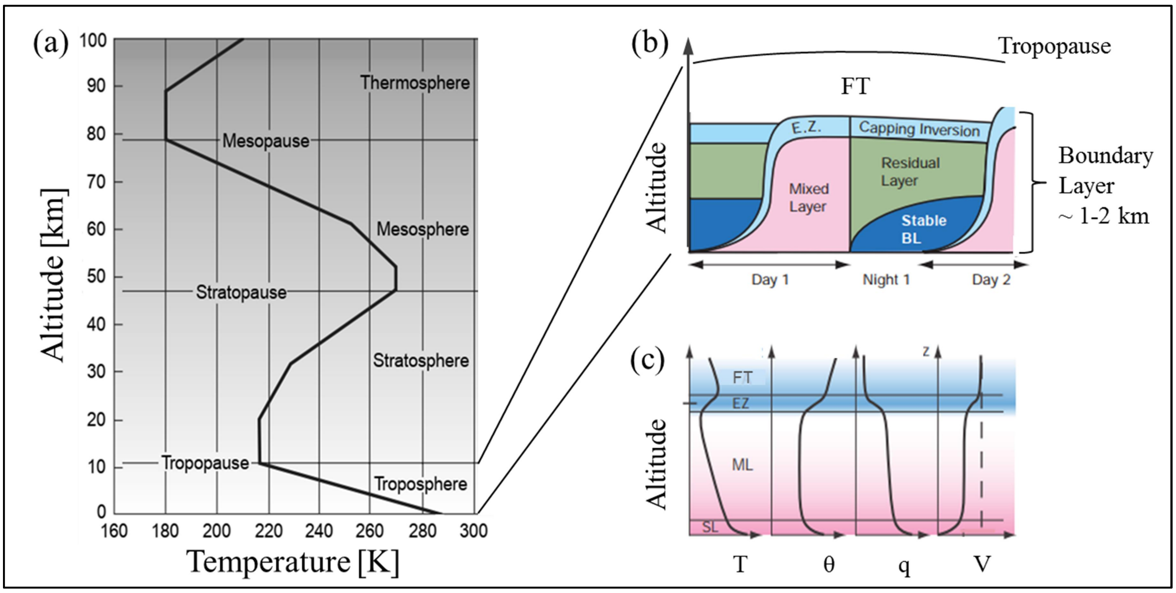

Figure 2.9: (a) Temperature profile of the atmosphere; (b) zoom on the troposphere including the diurnal cycle of the boundary layer; (c) typical daytime profiles of temperature (T), potential temperature (θ), specific humidity (q) and wind speed (V). SL is the surface layer, ML the mixed layer, EZ the entrainment zone, FT the free troposphere. All figures adapted from Wallace and Hobbs (2006).

The BL is the lowermost part of the troposphere and is in direct interaction with the earth's surface. At the earth's surface almost all anthropogenic activities take place, hence, pollutants, GHGs, and particles are released into the surrounding air. In case the release height is within the BL, anthropogenic emissions are transported and can either be enriched or diluted by atmospheric processes. A crucial role hereby plays the temperature profile and the volume of air, which is in turn determined by the top edge of the BL, hereafter referred to as BLH (Boundary Layer Height). Severe air pollution is often connected with a low BLH, stable stratification and strong inversions, as observed e.g. during strong haze events in Shanghai (Leng et al., 2016), Beijing (Zheng et al., 2015) or London (Wilkins, 1954).

Typically, the BL above land extends over the lowermost 1 to 2 km of the troposphere but its height is strongly dependent on the daytime as well as the geographical location and meteorological conditions. The BL reacts to external changes of daytime solar heating and nighttime radiative cooling within only few hours as land has a relatively small specific heat capacity (<1 J g^{-1} K^{-1}). This fact leads to a characteristic diurnal cycle during fair weather conditions, as depicted in Fig. 2.9b. At sunrise a shallow mixed layer (ML, depicted in pink) is formed. It reaches its maximum thickness in the afternoon, mainly driven by convective turbulence, which in turn is caused by thermals of warm air rising or cold air sinking. Around sunset, decaying convective turbulence, and hence, weaker vertical mixing, leads to a breakdown of the ML, which is called residual layer (depicted in green). Due to the subsequent radiative cooling at the surface a shallow stable layer forms and gradually increases in height during the night (depicted in blue), superseded by the rising sun on the next day when the cycle evolves from the beginning. At the top of the BL, inmixing of air from the free troposphere (FT) can occur in the so-called entrainment zone (EZ) through an increase in the BLH or by subsiding air masses, dependent on the strength of the inversion as discussed in the following.

Associated with the BL evolution, characteristic vertical daytime profiles of temperature (T), potential temperature (θ), specific humidity (q) and wind speed (V) evolve, see Fig. 2.9c (for a description of the meteorological terms see Appendix A.2). Air temperature and humidity are highest in the surface layer (SL) due to heat exchange and evaporation at the surface, while the frictional drag force reduces the winds speed and forces the flow across isobars towards lower pressures. Throughout the ML temperature steadily decreases with altitude. At its height, the inversion (reversed temperature gradient) represents a layer of high stability and thus efficiently inhibits turbulence from penetrating from the ML into the FT. This effective vertical mixing causes nearly uniform and constant profiles of θ, q and V within the ML. Across the inversion humidity decreases rapidly towards the relatively dry FT and the wind speed increases and reaches almost geostrophic values and a flow nearly parallel to isobars.

Unlike the boundary layer over land, the Marine Boundary Layer (MBL) is distinguished from it due to several reasons: Since the MBL is in direct contact with the ocean, large amounts of heat and moisture are exchanged. The relative humidity is higher, promoting the formation of clouds. Hence, the radiation budget is much more complex, but due to the presence of clouds the inversion is usually more intense, which in turn minimises the entrainment of dry air from above. Due to the large heat capacity of water (~4 $J\ g^{-1}\ K^{-1}$) the diurnal cycle of the MBL is suppressed. Further, the MBL is usually much shallower with only few hundreds of metres in its depth.

In the context of this thesis, the height and characteristics of the BL, especially over Berlin with respect to the mass balance study (see Sect. 5.3), are of great importance. For the city-wide emission rate calculation, research flights were carried out predominantly within the BL, which needs to be well-determined, homogenously mixed and relatively stable throughout the measurement period (see Sect. 2.2.2). While the research flights of the EMeRGe-Europe and Asia campaign were mainly planned above the sea (see Sect. 6.2), the transport of emissions from the BL over land towards the sea and above the MBL plays an especially crucial part.

3 Instrument and numerical models

In the previous chapter the advantages of airborne in situ measurements were outlined and an introduction to the measurement technique of cavity ring-down spectroscopy (CRDS) was given. In the context of the thesis observational CO_2 and CH_4 data were collected using a commercial GHG analyser from Picarro Inc, which is introduced in Sect. 3.1. The scientific data analysis is supported by two different numerical models, complementing each other: the regional atmospheric chemistry climate model MECO(n) (Sect. 3.2) and the Lagrangian atmospheric transport and dispersion model HYSPLIT (Sect. 3.3).

3.1 Cavity ring-down greenhouse gas analyser (Picarro G1301-m)

The Picarro G1301-m analyser is a flight ready measurement instrument providing mole fractions of CO_2, CH_4 and H_2O based on wavelength-scanned cavity ring-down spectroscopy. Detailed information on the analyser can be found on their website (*www.picarro.com*) or in Crosson (2008), important aspects are summarised below.

A block diagram of the basic components is depicted in Fig. 3.1a. Two continuous wave (CW) lasers are operated at wavelengths in the near infrared: for CO_2 at 1603 nm, for CH_4 and H_2O at 1651 nm. With an optical switch the light from each laser is selected and ~20 % of their power is transported to the wavelength monitor (*zero order beam*). The wavelength monitor assures within microseconds that only the spectral feature of interest is targeted, and thus the sensitivity to interfering gas species is limited. As absorption spectra at sub-atmospheric pressure are well resolved with a series of narrow sharp lines, the cavity pressure is kept constant at 140 ± 0.05 torr (~187 hPa). Since the size and shape of the spectral lines is also dependent on the temperature, the cavity is thermally stabilised at 45 °C (± 10 mK).

The remaining ~80 % of the power enters the cavity (*first order beam*), which is composed of three mirrors having a reflectivity of 99.999 %. Due to the large amount of reflections very long absorption path lengths of more than 20 km are achieved, while maintaining a small cell volume of 35 cm^3. The latter one allows for fast gas exchange and thus high measurement speed (~2 s). The pressure within the cavity is controlled by the inlet and outlet proportional valves. The outlet proportional valve is kept at a fixed opening position, while the inlet valve adjusts to the input pressure change, monitored by a pressure transducer. As the inlet valve has a limited operating range, the pressure at the inlet should be around ± 400 hPa of ambient conditions. The flow through the cavity is, in general, triggered by the pressure differential between the outlet (negative pressure due to vacuum pump) and the inlet (ambient atmospheric pressure).

After the light content reaches a predefined threshold in the cavity, the CW laser is turned "off" (100 % of the power goes to the *zero order beam* and is not provided to the cavity in the *first order beam*) and the exponential ring-down can occur. The photodetector outside the cavity monitors the small amount of light leaking through the mirror. By tuning the laser to wavelengths where the gases of interest absorb, and to wavelengths where they do not absorb, both ring-down times (τ_1 and τ_2, see Eq. (2.4)) are obtained. Further, the laser tunes to multiple known points of the absorption and base line (increments the wavelength) and thus accurately fits the absorption line shape, and hence determines GHG mole fractions with high sensitivity.

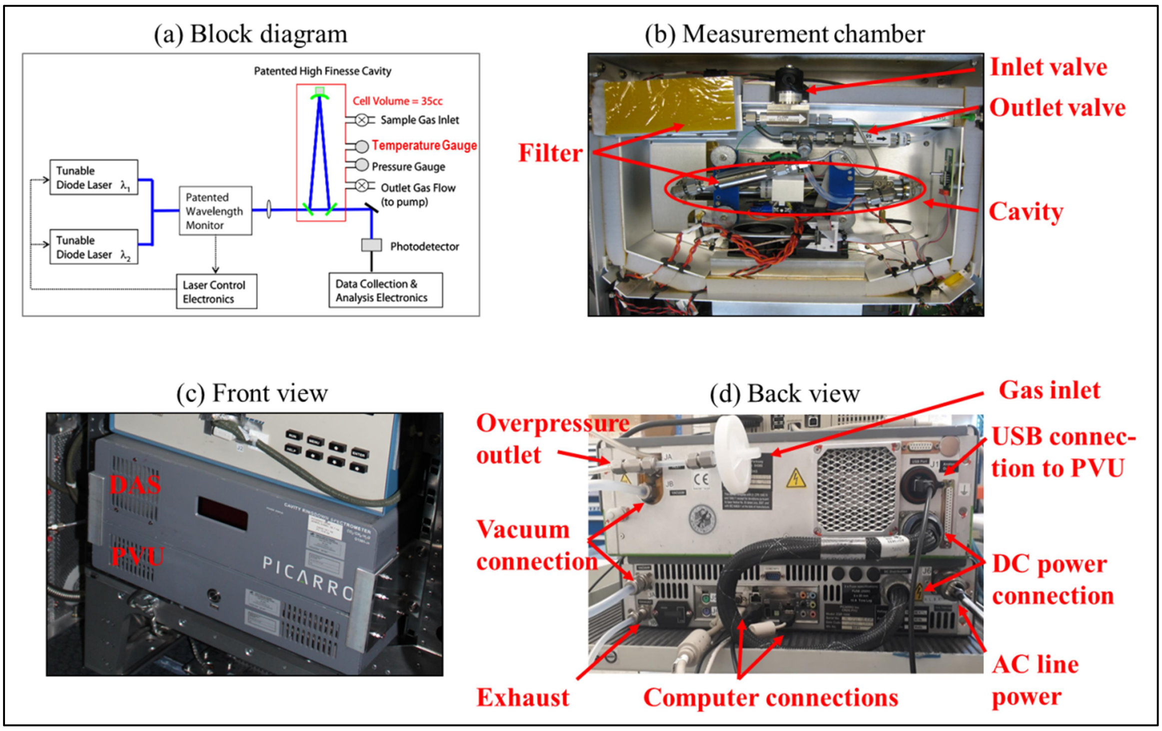

Figure 3.1: (a) Schematic block diagram, adapted from Crosson (2008); (b) (c) and (d) show photographs of the measurement chamber, the front view of the Picarro modules mounted in the aircraft rack, and the back view of the connected modules. Photo (b) courtesy of M. Scheibe (DLR-IPA).

The photographs in Fig. 3.1b, c and d are taken from the instrument used within this thesis and serve as illustration. The optical cavity is embedded in the measurement chamber of the instrument, see panel (b). Two upstream filters ensure that the sensitive cavity will not get polluted. The measurement chamber itself is part of the Data Acquisition System (DAS), which further consists of hard- and firmware for acquisition, controlling and communication. The second module is the Power Vacuum Unit (PVU). The PVU incorporates controlling parts like the computer, an AC (Alternating Current) to DC (Direct Current) converter to supply the analyser, and a vacuum pump to maintain the pressure difference needed for the sample flow. The front view of both modules is shown in panel (c). Panel (d) presents their back view with electric and wiring connections. A filter membrane (Pall Life Sciences, 0.2 µm, made of polytetrafluoroethylene (PTFE)) is added upstream of the Picarro inlet to avoid liquid water infiltration.

3.2 Regional atmospheric chemistry climate model MECO(n)

In global models the resolution to resolve meteorological and chemical processes is often not sufficient especially when it comes to e.g. emissions of point sources. Hence, smaller scale models are needed which down-scale such processes from the global scale to the meso scale.

The MECO(n) model couples on-line the global chemistry-climate model EMAC[3.1] with the regional chemistry-climate model COSMO-CLM[3.2]/MESSy[3.3] in order to achieve this regional refinement. Hence, MECO(n) stands for MESSy-field ECHAM[3.4] and COSMO models nested n times. Details can be found in Hofmann et al. (2012), Kerkweg and Jöckel (2012a, 2012b) and Mertens et al. (2016). COSMO-CLM (Rockel et al., 2008) is based on the COSMO model and jointly further developed by the CLM-Community. At DLR-IPA (Institut für Physik der Atmosphäre), the model is maintained by the group of P. Jöckel and especially for the [UC]^2 and EMeRGe campaigns by M. Mertens. Within the scope of the thesis, MECO(n) was used to simulate emissions of anthropogenic CO_2 and CH_4 sources and their dispersion in the atmosphere. The simulation results are compared in space and time with the airborne observational data to better understand the source contribution to the detected emission plumes. The general setup for the different airborne campaigns is presented in the following, while the various simulated chemical tracers are introduced in the campaign specific sections (Sect. 5.1.2 and Sect. 6.1.2).

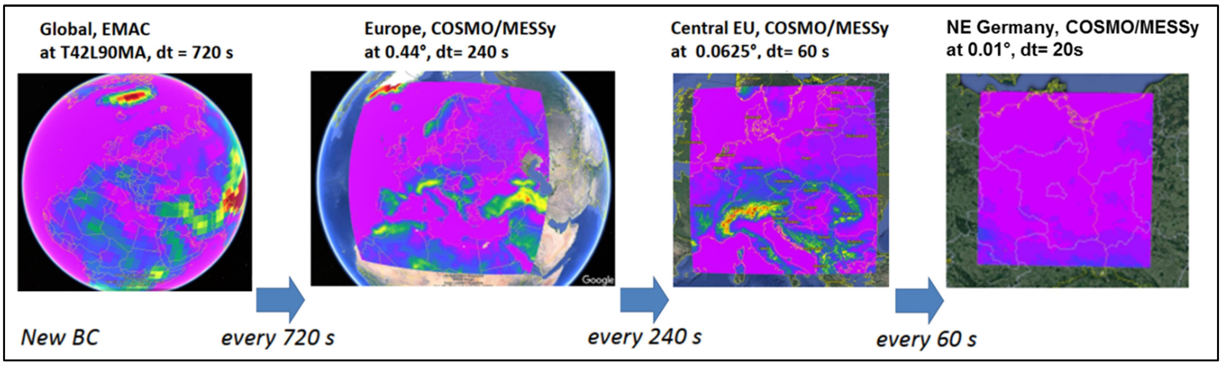

Figure 3.2: Schematic MECO(n) setup during the [UC]^2 campaign with three COSMO-CLM/MESSy instances within the global EMAC model. Adapted from a poster of Mertens et al. (2019). T42L90MA stands for the resolution with a spherical truncation of T42 (~quadratic Gaussian grid ox approx. 2.8 by 2.8 degrees) and 90 vertical hybrid pressure levels.

For the [UC]^2 campaign a setup of three simultaneously running COSMO-CLM/MESSy instances nested into each other are used within the global EMAC model, see Fig. 3.2. The finest instance (right panel) covers NE Germany at a horizontal resolution of 0.01° (~1 km × 1 km), a time step length (*dt*) of 20 s and a vertical resolution of 50 model levels. The coarser resolved nesting instances (middle panels) are centred over central Europe (at 0.0625°, *d*t = 60 s) and over Europe (at 0.44°, *dt* = 240 s). In the global EMAC model (left panel, at 2.8°, *dt* = 720 s, 90 vertical levels) the prognostic variables temperature, divergence, vorticity and the logarithm of the surface pressure are nudged by Newtonian relaxation towards ECMWF (European Centre for Medium-Range Weather Forecasts) operational analysis data. The COSMO-CLM/MESSy nests are directly driven by lateral and top boundary conditions from EMAC or from the corresponding coarser resolved nesting instance at each of the model time steps. The height of the midpoint of the uppermost grid box is approx. 80 km for EMAC and

---

[3.1] ECHAM/MESSy Atmospheric Chemistry; [3.2] COSMO model in CLimate Mode (with COSMO = COnsortium for Small-scale Modeling; [3.3] Modular Earth Submodel SYstem; [3.4] European Centre for Medium Range Weather Forecasts Hamburg General Circulation Model;

22 km for COSMO-CLM/MESSy, respectively. A direct nudging of the COSMO-CLM nests is not performed. Hence, the instances can develop their own dynamics to a certain degree. During the model simulation the vertical profiles of the tracers (and several meteorological quantities) are on-line sampled along the flight tracks (submodel S4D, Sampling in 4 Dimensions, described by Jöckel et al., 2010). This high-frequency output (at each model time step) is primarily used for comparison with the airborne observations.

For EMeRGe-Europe a similar setup of three COSMO-CLM/MESSy instances is used, as described above, but at different resolutions: 50 km (*dt* = 240 s), 12 km (*dt* = 120 s) and 7 km (*dt* = 60 s), where the finest nest extends roughly from Portugal to the Ukraine (W-E) and from Ireland to the northern coast of Africa (N-S). Each instance is resolved over 40 terrain following vertical levels from the surface to ~20 km altitude. EMAC is nudged towards ERA-Interim data and the COSMO-CLM nests are driven by the coarser resolved nesting instances.

3.3 Atmospheric transport and dispersion model HYSPLIT

Among the scientific community HYSPLIT (HYbrid Single Particle Lagrangian Integrated Trajectory) is one of the most common atmospheric transport and dispersion models (Stein et al., 2015). It can be used to compute back trajectories of air parcels or to simulate more complex dispersion processes including chemical transformation and deposition of various species. It has been widely applied in the context of e.g. synthetic tracer releases (Ren et al., 2015; Ngan et al., 2018), wildfires (Cottle et al., 2014), transport of dust (Escudero et al., 2011; Wang et al., 2011; Ashrafi et al., 2014) or volcanic ash (Crawford et al., 2016). HYSPLIT is based, as indicated in its name, on a hybrid method between the Lagrangian approach (following an air parcel as it is moving with time) and the Eulerian approach (observing air parcels at a fixed location moving by). A general description of the model can be found in Draxler and Hess (1998) or in Stein et al. (2015). In this thesis, the in-house adapted interface for both trajectory (V1.25.0) and dispersion (V1.26.0) calculations, developed by R. Baumann (DLR-IPA), were deployed.

For the $[UC]^2$ campaign backward trajectories from the encountered air masses were calculated and a so-called footprint was derived to examine the origin and to reconstruct the pathway of the encountered air masses. HYSPLIT is driven in this setup by meteorological forecast data from ECWMF because of their high spatial and temporal resolution. Gridded fields are provided hourly with a horizontal resolution of 0.08° in latitude and 0.125° in longitude (~9 km × 9 km). The 137 model levels allow a vertical resolution of ~20 m near the ground, increasing to about 200 m at 3 km altitude. Backward trajectories were started every 10 s from the flight track. Every 15 min along the trajectories information about latitude, longitude, height of the trajectory and depth of the model BL were provided. This information was used to define a so-called back trajectory footprint, which refers here to a more general definition of an area covered by the air mass within its residence time in the BL. Hence, the data points of the back trajectories, which were inside the BL, were extracted first. Then, their percentage residing in a defined grid box area between the downwind and upwind transects was defined.

For both EMeRGe campaigns backward trajectories were calculated as well, and so-called tagged plume plots were made available to the mission community by R. Baumann. Meteorological input data is also provided by operational ECMWF forecasts data with a time step of one hour. Due to the larger geographical extent of the EMeRGe campaigns, and to limit computational resources and time, data are horizontally interpolated at a resolution of roughly 0.1° × 0.1°. The intention of the tagged plume plots is to simulate individual enhancements of carbon monoxide (CO) from selected geographical regions, while omitting CO emissions from the surroundings. Figure 3.3 shows the extent of the specified Major Population Centres (MPCs; or their agglomerations) and the mean CO flux rate in Mg hr^{-1} based on the EDGAR HTAP v2 inventory for 2010 (*http://edgar.jrc.ec.europa.eu/htap_v2*). CO is a commonly used tracer for combustion processes and due to its long atmospheric lifetime of few months it is suitable to investigate pollution transport processes (Streets et al., 2006). Since the EMeRGe campaign deals with fresh emissions not being older than a few days, chemical and physical sinks of CO are disregarded. However, emissions are able to accumulate over 6 days (older particles are removed continuously to limit memory and computational time). This allows for an identification of local and regional enhancements near the source and also to distinguish between eight different age-classes of encountered air masses: 0 to 3 h, 3 to 6 h, 6 to 12 h, 12 to 24 h, 1 to 2 days, 2 to 3 days, 3 to 4 days and 4 to 6 days.

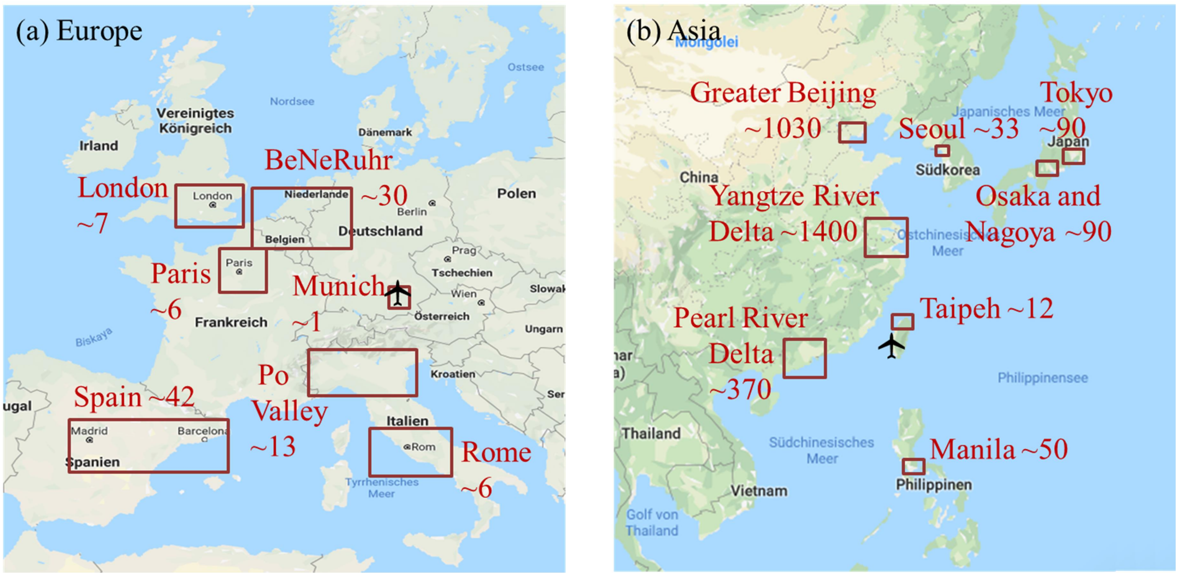

Figure 3.3: HYSPLIT target regions of selected MPCs with emission rates of CO in Mg hr^{-1} for (a) Europe and (b) Asia. Aircraft icon denotes the operation base. Map data is from Google.

4 Assessing the performance of the cavity ring-down analyser

Within the Paris Agreement (UNFCCC, 2015) all signed nations have to assess their GHG emissions. Therefore, accurate and well-calibrated observations are needed. Frameworks for quality assurance and quality control of in situ measurements are established by the Global Atmosphere Watch (GAW) programme. It aims for a consistent network, compatible with each other (WMO, 2016). This chapter describes the calibration (Sect. 4.1) and characterisation (Sect. 4.2) of the commercially available Picarro GHG analyser. Section 4.3 introduces the setup of the instrument deployed aboard the Cessna Grand Caravan 208B (Cessna) and the High Altitude LOng Range (HALO) aircraft during the three scientific airborne missions. An in-flight measurement intercomparison verifies the accurate performance of the analyser for operating conditions aboard aircraft (Sect. 4.4).

4.1 Calibration routine and measurement uncertainty

In general, the Picarro analysers' response is extremely linear to an increase in atmospheric GHG mole fractions. Therefore the calibration fitting line can be assessed with only three calibration standards. In addition, its high stability over time reduces the frequency of needed calibrations and complicated post processing (e.g. Rella, 2010). In the following the calibration routine (a), which consists of four different steps, and the uncertainty analysis (b) is introduced using exemplary data from the [UC]^2 campaign, however values for both EMeRGe missions are retrieved in a similar manner.

Table 4.1: The label of the calibration gas bottle is listed together with their stated mole fractions. The corrected mole fractions of the Air Liquide bottles are obtained by cross-calibration with NOAA standards.

Calibration gas bottle	**Stated CO_2 [ppm]**	**Stated CH_4 [ppm]**	**Corrected CO_2 [ppm]**	**Corrected CH_4 [ppm]**
D1GHLAL (AL)	369.2 ± 7.4	1.607 ± 0.032	373.9 ± 0.5	1.603 ± 0.007
D3C8UYN (AL)	411.8 ± 8.2	1.824 ± 0.036	415.9 ± 0.5	1.818 ± 0.007
D05170N (AL)	428.28 ± 8.6	2.010 ± 0.04	434.8 ± 0.5	2.008 ± 0.008
D0G76CN (AL)	(777 ± 16)	1.795 ± 0.036	(783 ± 1)	1.803 ± 0.007
CB11542 (NOAA)	349.23 ± 0.19	1.6310 ± 0.0031	*taken as truth*	*taken as truth*
CB11361 (NOAA)	417.24 ± 0.22	1.9739 ± 0.0038	*taken as truth*	*taken as truth*

The laboratory at DLR-IPA is equipped with two different types of calibration standards. So-called secondary standards, provided by Air Liquide (AL), contain compressed synthetic air with a given mole fraction of CO_2 and CH_4. The drawback of these standards is their large uncertainty on the order of ±2 %. So-called primary standards are provided by NOAA and are tied to the WMO-X2007 and WMO-X2004A scale (Dlugokencky, 2005; Zhao and Tans, 2006) as defined in the GAW framework. These standards consist of dried and compressed natural air with highly accurate concentrated calibration gases (CO_2 ±0.05 %, CH_4 ±0.2 %). Due to the high value of these NOAA standards, both as calibration gas and connection to the WMO scales, they are carefully managed, howeverare are relatively expensive. The calibration gases used for the measurement campaigns in this work are listed in the first column of Table 4.1 ("stated" CO_2 and CH_4). The second column ("corrected" CO_2 and CH_4) results from the intermediate step where the AL bottles are cross-calibrated against the NOAA standards to reduce the large error bars of ± 2 %.

a) Four-step calibration routine

Each calibration gas bottle is surveyed in the same way during ground operation (one exception of the setup was prepared for and used during EMeRGe-Europe, see Appendix A.4). The gas flow to the Picarro instrument is provided through a ¼" PFA tube (with an overflow) and is stabilised by a Mass Flow Controller (MFC) from Bronkhorst. The calibration gas is supplied for 10 minutes in order to avoid contamination of the previously sampled gas and to assure measuring dry gas i.e. that sensed H_2O mole fractions are close to zero. The last three minutes (180 data points) are averaged and taken with the 1σ standard deviation for the further four-step analysis. The highest CO_2 mole fraction from AL (777 ppm) is excluded, as the certificate of compliance (which comes with the purchase of the instrument) states a typical CO_2 operating range of 300 to 500 ppm.

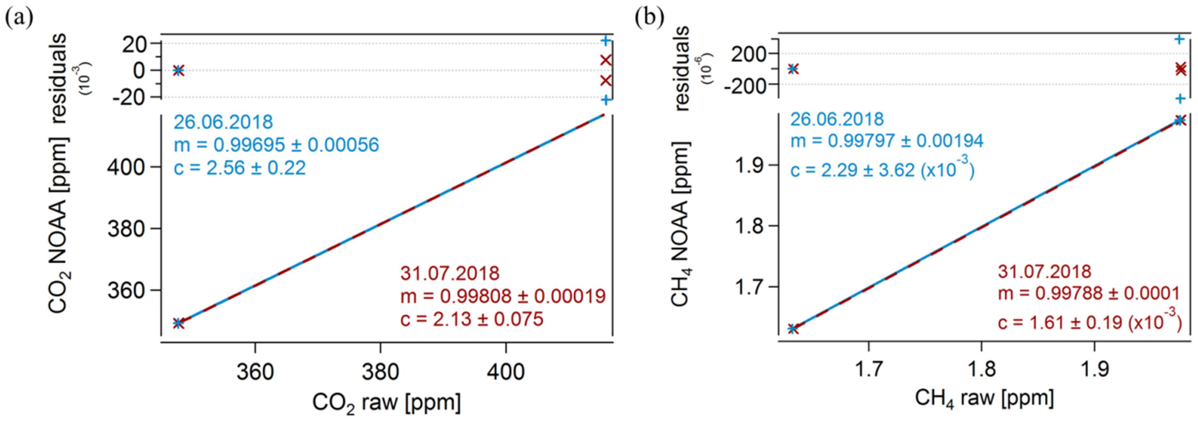

Figure 4.1: Regression line for (a) CO_2 and (b) CH_4 as obtained from surveying the NOAA calibration gases. The slope is given with *m*, the y-intercept with *c*. The residual plot shows a random pattern. During each experiment one of the two NOAA bottles was measured twice with ~3 hours in between.

The first step in the calibration procedure takes the stated NOAA mole fractions as the truth. From a linear fit applied to the NOAA mole fractions against the measured raw data, a regression slope is obtained, see Fig. 4.1. The blue and brown colours refer to two calibration days (June 26th and July 31st, 2018) prior to and after the main $[UC]^2$ mission phase. In the second step the mole fraction of the AL bottles, which are measured in the same experiment, are corrected with the just retrieved regression slope factors (*m*, *c*) according to Eq. (4.1):

$$AL_{corrected} = AL_{measured}\, m + c \tag{4.1.}$$

Hence, a mean corrected value for each AL bottle is derived from the two days with the total uncertainty being the square root of the quadratic sum of each standard deviation. These corrected mean values are summarised in Table 4.1 (second column). The step in procedure provides uncertainties of only 0.2 % for CO_2 and 0.5 % for CH_4. The third step involves the frequent calibration of the instrument with AL standards during the mission phase itself (performed on June 6th and July 6th, 10th, 18th, 23rd, 31st, 2018). Again, a linear best-fit equation is obtained, but by plotting all corrected AL mole fractions against the raw data a campaign-average slope (m_{avg}) and y-intercept (c_{avg}) is determined. Consequently, in the fourth and last step, the raw signals detected within the research flights are calibrated and the final GHG mole fraction (MF) is obtained following Eq. (4.2):

$$MF_{final} = MF_{raw}\, m_{avg} + c_{avg} \tag{4.2}$$

For accurate calibration, it is necessary to flush the pressure reducer, which is mounted at the gas bottle valve, at least three times with the desired gas prior to taking actual measurements. This is evaluated in a laboratory experiment performed on January 10th, 2018, see Fig. 4.2. In the beginning the chosen calibration gas is probed five times (with roughly one hour in between). Then three other calibration gases with variable (and different) mole fractions are measured (not shown), and the first calibration gas is resampled twice in succession. The first resampling is performed directly after the change of the calibration gas (without flushing, depicted in red) and the second one after purging the pressure reducer. For CH_4 no impact is detected, however, it is found to be important for CO_2, otherwise mole fractions tend to be overestimated by ~0.1 ppm.

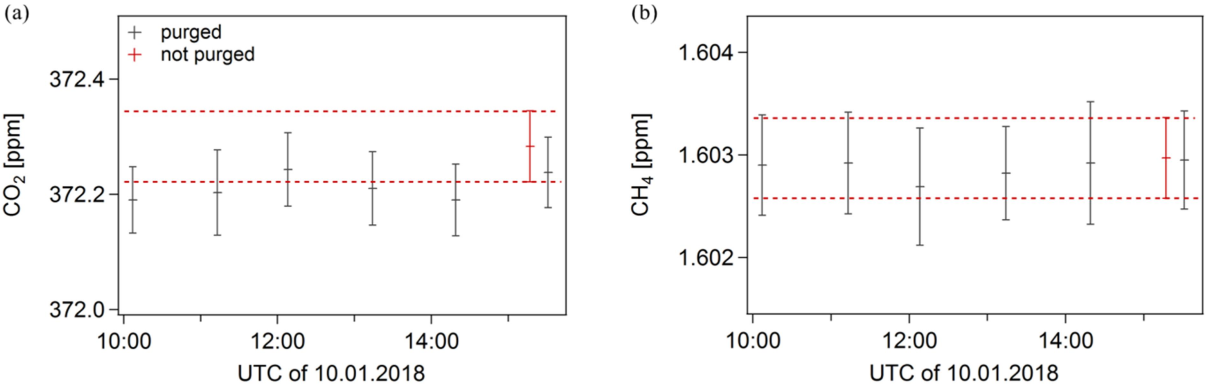

Figure 4.2: Mole fractions of (a) CO_2 and (b) CH_4 obtained from measuring a calibration gas bottle with (grey) and without (red) flushing the pressure reducer.

b) Uncertainty analysis

The total measurement uncertainty (*u_total*) of the Picarro analyser for the [UC]^2 campaign is determined to better than 0.2 ppm for CO_2 and 1.1 ppb for CH_4 based on the summation of the known sources of uncertainty in quadrature as given in Eq. (4.3). This equation is adapted from Peischl et al. (2012), Andrews et al. (2014), Verhulst et al. (2017) and the Picarro flight analyser data sheet (Picarro, 2009).

$$u_{total} = \sqrt{precision^2 + u_{water\ vapor}{}^2 + drift_T{}^2 + drift_t{}^2 + + reprod._{primary}{}^2 + reprod._{secondary}{}^2} \tag{4.3}$$

The measurement precision is equal to the 1σ standard deviation of a 180 s mean taken from the end of a 10 min calibration sequence. The uncertainty associated with the water vapour correction is taken from Rella (2010) with a maximum measured water vapour mole fraction of 2.2 %. Drift of the instrument with ambient temperature (T) is taken from Picarro (2009) with a maximum measured difference of T=15 °C. Drift of the instrument with time (t) is taken from the Picarro Certificate of Compliance with a maximum flight time of 2.5 hours. The scale reproducibility of the primary (and secondary) standards is given with the 68th percentile of the absolute values of the differences among all the pairs divided by the square root of two. The single terms and their values are summarised in Table 4.2. Compared to the overall uncertainty given in Peischl et al. (2012), Andrews et al. (2014) and Verhulst et al. (2017) with <0.15 ppm CO_2 and <1.4 ppb CH_4 the estimated values seem reasonable.

Table 4.2: Estimated uncertainties for CO_2 and CH_4 according to Eq. (4.3).

	CO_2 [ppb]	**CH_4 [ppb]**
Precision	70	0.64
Water vapour	35.2	0.16
Drift with temperature	112.5	0.75
Drift with time	3.4	0.02
Reproducibility of primary standard	15.6	0.28
Reproducibility of secondary standard	44.8	0.33
Total uncertainty	**145.1**	**1.09**

4.2 Laboratory experiments

The above-stated error analysis is rather conservative and mostly based on literature values. Hence, experiments in the laboratory were performed to assess and adapt the water vapour correction value (a). The instrument was placed in an environmental chamber to simulate flight conditions in an unpressurised cabin, as prevalent aboard the Cessna aircraft (b).

a) Water vapour correction

Mole fractions of GHG are not dependent on pressure or temperature but they vary to a significant extent with the abundance of H_2O in the atmosphere, which is itself fluctuating due to evaporation and condensation processes. The dilution effect implies that for any air mass at constant temperature and pressure an increase in the quantity of one component (e.g. increasing H_2O) results in a (linear) decrease in the remaining components (LI-COR, Application Note #129). Hence, it is convenient to express measured GHG mole fractions relative to dry air, where X_{rep} is the measured GHG mole fraction, X_{dry} is the GHG mole fraction in dry air and H_2O is the measured water vapour mole fraction:

$$X_{dry} = \frac{X_{rep}}{1-H_2O} \tag{4.4}$$

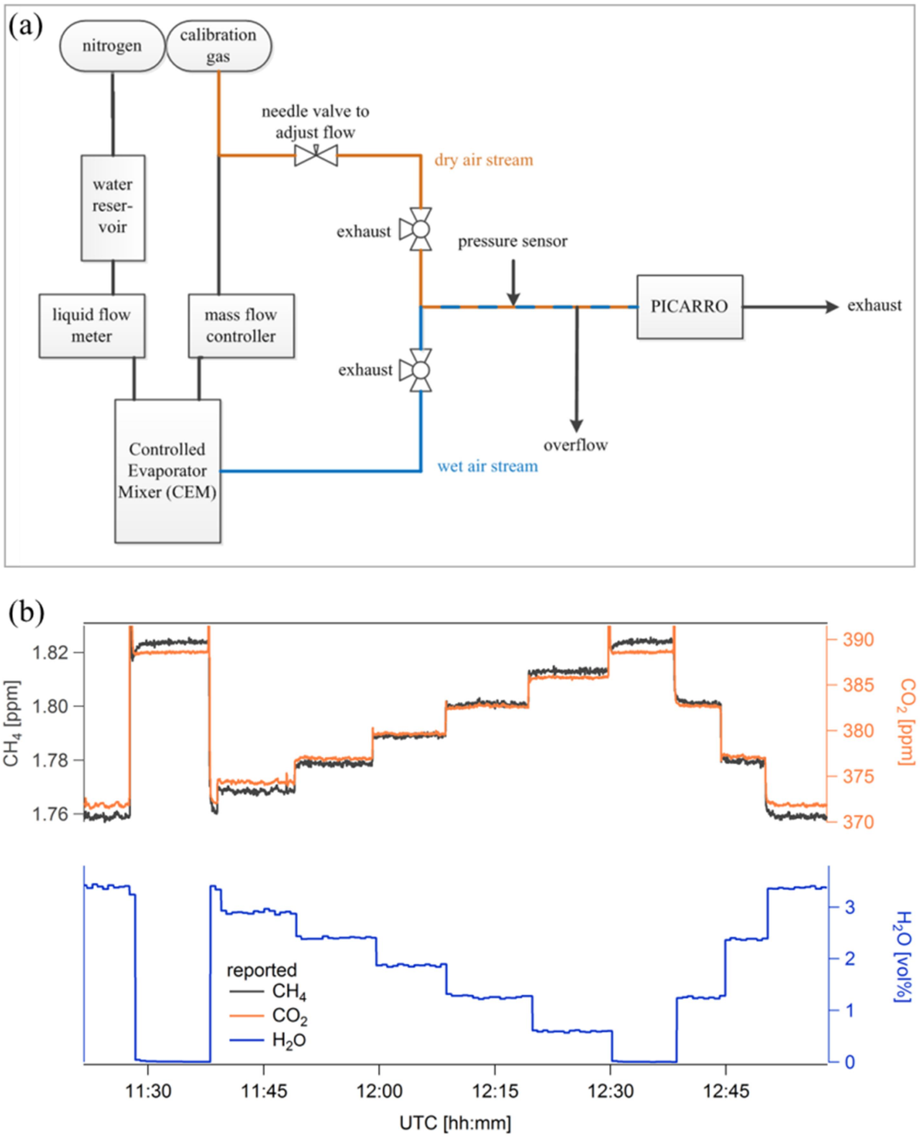

Figure 4.3: Setup (a) and measurement time series (b) of the laboratory experiment on April 10th, 2017 to determine the water vapour correction coefficients.

The Picarro analyser is providing these dry gas mole fractions with high precision and accuracy. In contrast to earlier methods, where the gas stream had to be dried, the analyser directly measures the H_2O content of the air stream (at the same time as CO_2 and CH_4) and quantifies the dry gas mole fractions with the help of H_2O correction factors denoted with a, b, c and d (Rella, 2010). In the offline data analysis the following equations Eq. (4.5) and (4.6) are applied to relate the actual dry gas mole fraction $(CO_2)_{dry}$ and $(CH_4)_{dry}$ to the measured H_2O mole fractions $(H_2O)_{rep}$.

$$(CO_2)_{dry} = \frac{(CO_2)_{rep}}{1+a\,(H_2O)_{rep}+b\,(H_2O)_{rep}^{\,2}} \tag{4.5}$$

$$(CH_4)_{dry} = \frac{(CH_4)_{rep}}{1+c\ (H_2O)_{rep}+d\ (H_2O)_{rep}{}^2} \tag{4.6}$$

In general, the H_2O correction factors obtained from an experiment performed by Chen et al. (2010) can be used for all G1301 instruments, however, it is more accurate to determine them for each instrument individually (Rella, 2010). It should be noted that the reported values $(CO_2)_{rep}$, $(CH_4)_{rep}$ and $(H_2O)_{rep}$ are only the output of the analyser, where no calibration prior to the determination is needed. The schematic setup in the DLR-IPA laboratory on April 10th, 2017 is shown in Fig. 4.3a with the goal to humidify a known dry gas stream and to determine the H_2O correction factors *a* to *d*. Two air streams were produced, one dry air stream (drawn in orange) and one wet air stream (drawn in blue), which could be chosen based on the position of the two 3-way valves. The dry gas stream was simply the gas from the calibration bottle. The wet air stream was produced by mixing the calibration gas with a humidified nitrogen stream (used as carrier gas) in the Controlled Evaporator Mixer (CEM, from Bronkhorst). The water reservoir upstream of the CEM was filled with distilled water to avoid the effects of dissolved CO_2. By adjusting the ratio between the wet air stream (using the LIQUI-FLOW, model M7204124B) and the dry air stream (using the MFC, model M14205574A) different levels of humidity were produced between zero and almost 4 vol%. The pressure sensor upstream of the Picarro instrument was used (together with the needle valve) to assure constant inlet pressure during the experiment. Figure 4.3b shows the corresponding measurements of CO_2, CH_4 and H_2O. Water vapour mole fractions were first reduced until zero and again increased to avoid hysteresis effects. For each H_2O mole fraction, a mean CO_2 and CH_4 mole fraction were derived.

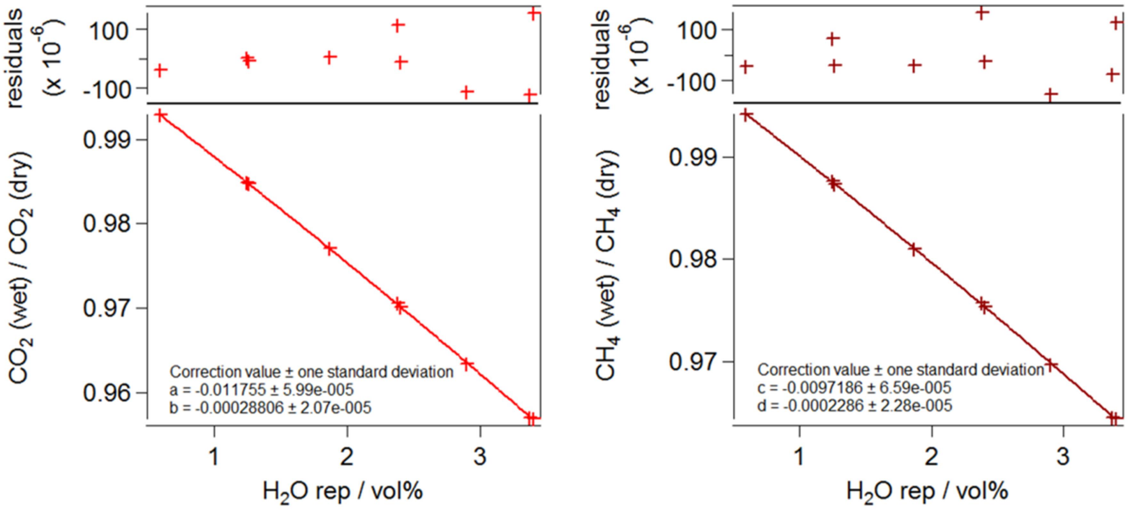

Figure 4.4: Quadratic fit of the CO_2 and CH_4 ratio in wet and dry gas streams. The residual plot shows a random pattern.

The ratio of the wet and dry mean mole fractions (X_{wet}/X_{dry}) is plotted as a function of the reported H_2O mole fraction, see Fig. 4.4. The following second order correction function (Eq. (4.7)) was applied to obtain the fitting parameters *a* and *b* (when X=CO_2) and *c* and *d* (when X=CH_4):

$$\frac{X_{wet}}{X_{dry}} = 1 + a\ (H_2O)_{rep} + b\ (H_2O)_{rep}{}^2 \tag{4.7}$$

The experimental results are listed in Table 4.3 together with the H_2O coefficients reported by Chen et al. (2010). When applying the experimentally obtained factors to Eq. (4.5) and (4.6), slightly lower mole fractions for CO_2 and CH_4 are obtained (~0.05 %) compared to using the literature values. Mean values derived with the reported coefficients lead to a mole fraction of 389.06 ± 0.05 ppm CO_2 and 1.8236 ± 0.0003 ppm CH_4, while values derived within the laboratory experiment give 388.87 ± 0.048 ppm CO_2 and 1.8228 ± 0.0003 ppm CH_4.

Table 4.3: Water vapour correction factors obtained in the laboratory (experiment) and by Chen et al. (2010).

	a	***b***	***c***	***d***
Experiment	-0.011755	-0.000288	-0.009719	-0.000229
Chen et al. (2010)	-0.012000	-0.000267	-0.009823	-0.000239

b) Performance in the environmental chamber

The Picarro instrument was placed in an Environmental Chamber (EC, Fig. 4.5) at the Karlsruhe Institute of Technology (KIT). To characterise its behavior under simulated flight conditions in an unpressurised aircraft cabin (as prevalent during the Cessna flights) different altitudes were realised from the ground up to ~5 km (545 hPa). It is analysed whether the changing ambient pressure has an impact on CO_2 and CH_4 detection.

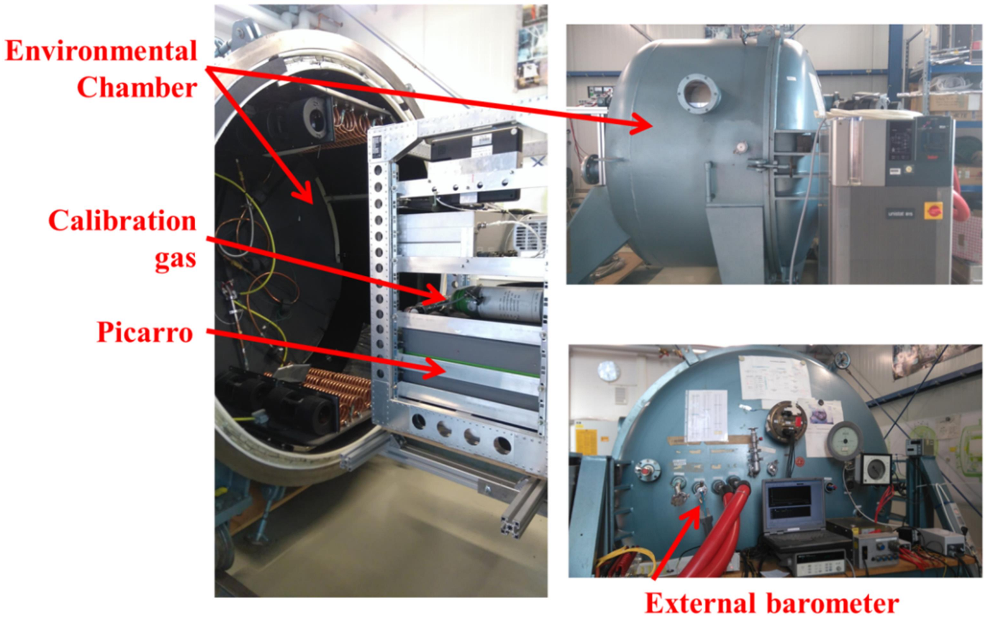

Figure 4.5: Environmental chamber at the KIT with the Picarro instrument mounted in the Cessna aircraft rack.

On April 19th, 2017, calibration gas with a known mole fraction of CH_4 and CO_2 was supplied to the instrument for roughly 3.5 hours, see Fig. 4.6. The EC pressure was regulated towards constant levels (grey shaded) and oscillations (blue shaded). The latter ones simulate gradients in the outside pressure as observed during aircraft climbs and descents. Different pressures were recorded at the inlet of the instrument (in green), within the EC by an external analog barometer (Vaisala PTB210C3C1M, in grey) and within the cavity by the instrument itself (in black). The inlet pressure was roughly 10 to 15 hPa lower than the ambient pressure as depressurization occurs at the tubes and filters. The cavity pressure was stably regulated to 139.97 ± 0.05 Torr (~187 hPa). With respect to the four constant pressure levels listed in Table 4.4, the mean value for CO_2 and CH_4 show slight deviations (ΔCO_2 = 60 ppb, ΔCH_4 = 0.65 ppb), however, they agree within the measurement precision (see Table 4.2). Shortly alternating oscillations were induced, corresponding to an aircraft climb and descend rate of 25 and 13 m s^{-1} (recorded at ~11:30 and ~12:45 UTC respectively). No significant variations or spikes were observed during the oscillations and in addition, the vertical speed of the Cessna is much smaller than simulated in this experiment (ascends with ~3 m s^{-1}, descends with 7 m s^{-1}). Chen et al. (2010) performed a similar study finding insignificant differences in their mean values, but a slightly larger noise compared to ambient conditions, which was not observed during this experiment.

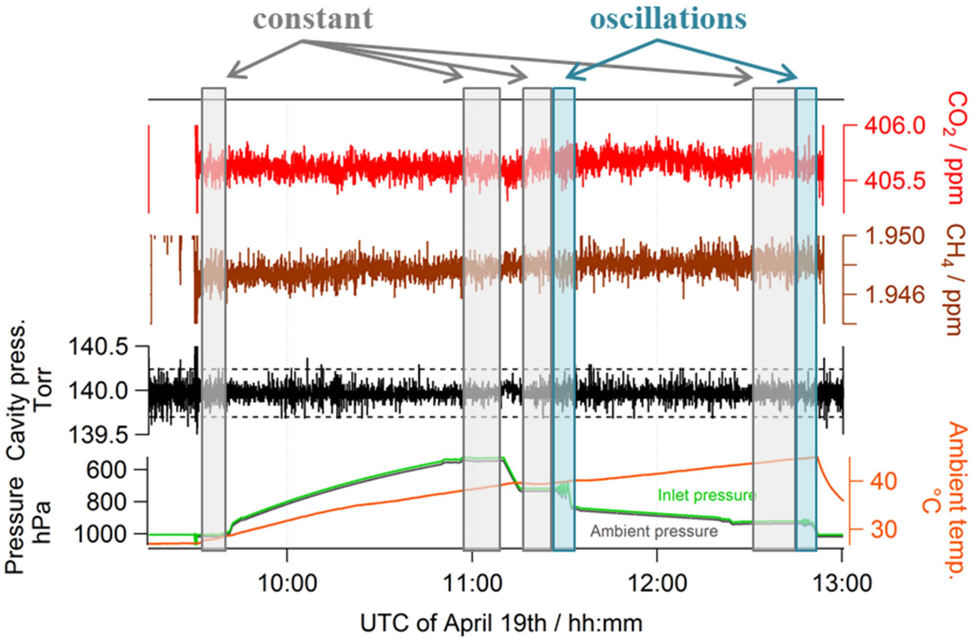

Figure 4.6: Measurement of calibration gas under simulated flight conditions from the surface up to ~545 hPa in an environmental chamber. Constant flight levels (grey) are induced as well as oscillations (blue) as observed during aircraft climbs and descents.

The temperature in the EC was recorded by the Picarro instrument (DAS_temp, orange line in Fig. 4.6) and strongly increased during the experiment from 27 °C to 45 °C. Although the temperature within the cavity and the laser temperature are held constant (see Sect. 3.1), the drift of the instrument itself with ambient temperature is given 7.5 ppb CO_2 and 0.05 ppb CH_4 per °C (Picarro, 2009). These values were taken for the uncertainty analysis. From a linear fit of the CO_2 mole fractions against the EC temperature, however, no obvious trend is detected (the correlation coefficient is below 0.5). Therefore, the above given value for CO_2 can be reduced towards 3.4 ppb CO_2 per °C, while CH_4 is the same as stated. During the $[UC]^2$ calibrations the temperature varied between 30 and 36 °C (avg. 32 °C), and during the flights between 32 and 45 °C (avg. 38 °C), thus similar to the temperatures observed in the EC.

Furthermore, the delay time of the instrument becomes important when comparing data from different measurement systems aboard the same aircraft. The delay time reflects the time difference of the sampling position at the inlet and the time when the same parcel of air reaches the measurement cell. This delay, caused by the length of the inlet line and by flow restrictions slowing down the gas flow, was experimentally determined within the EC. Alternately ambient air and synthetic air (or Zero Air, ZA) was provided to the instrument. The valve of a MFC was either completely open, letting ZA from the gas bottle to flow to the instrument, or fully closed, supplying ambient air from the overflow to the instrument. By switching between the air flows the difference between the valve signal and where the mole fraction reaches 90 % of the desired value (t_{90}) was calculated, hence, the delay time was determined to be 15 s. During the $[UC]^2$ research flights, the correlation between the Picarro H_2O measurements and the observations from the meteorological sensor package can be used to cross check the delay time. Correlations improve from $R = 0.96$ without any correction to $R = 0.98$ with the 15 s delay. For EMeRGe see Appendix A.4.

Table 4.4: Mean CO_2 and CH_4 mole fractions (180 s) and their standard deviation (1σ) as measured during constant pressure levels.

Pressure level [hPa]	**CO_2 [ppm]** mean	**1σ**	**CH_4 [ppb]** mean	**1σ**
545	405.62	0.06	1947.76	0.00044
734	405.64	0.07	1947.91	0.00037
939	405.66	0.06	1948.09	0.00042
1019	405.60	0.07	1947.44	0.00065

4.3 Aircraft deployment

When conducting an aircraft measurement campaign, a suitable set of instruments to collect atmospheric data needs to be deployed aboard the aircraft and certified to ensure airworthiness. The associated individual measurement components of the Picarro analyser were mounted at the bottom within so-called aircraft racks, see Fig. 4.7. The measurement system consisted also of an electrical switch panel and an external pump (Agilent IDP-3 Scroll Pump) in the upper part of the racks.

A schematic gas flow of the instrument setup is shown in Fig. 4.8a. The sample flow is provided through the inlet towards the analyser by a ¼ inch PFA (perfluoroalkoxy) tube, a chemically inert and flexible material. Downstream of the inlet two main flow paths can be chosen by a manual operated needle valve, indicating the usual set up during a flight (blue arrow), and during the warm up phase on the ground (red arrow). During the flight air is drawn through the external pump, where the majority of the air flow ventilates through the overflow into the aircraft cabin. This allows a higher flow rate in the sampling tubes and therefore a fast air exchange, while the instrument itself only draws the required flow of

~0.3 L min^{-1}. Note that due to the operation of the external pump in front of the Picarro inlet valve the sample flow in this setup is triggered by the pressure differential between cabin (inlet) and atmosphere (outlet) rather than between the ambient atmospheric pressure and negative pressure due to the vacuum pump as stated in Sect. 3.1. On the ground during the warmup phase, the pump is off (the needle valve upstream to the pump is closed), the overflow is closed and the Picarro instrument gets its air from outside the cabin through the bypass using only its internal pump. This setup allows a longer lifetime of the external pump (since the warmup of the instrument needs several hours) and reduces the noise level in the cabin prior to a flight. For a following setup, it would be more appropriate to replace the tee and the needle valve by a simple 3-way cock to eliminate the possibility that the bypass tube acts as a dead volume.

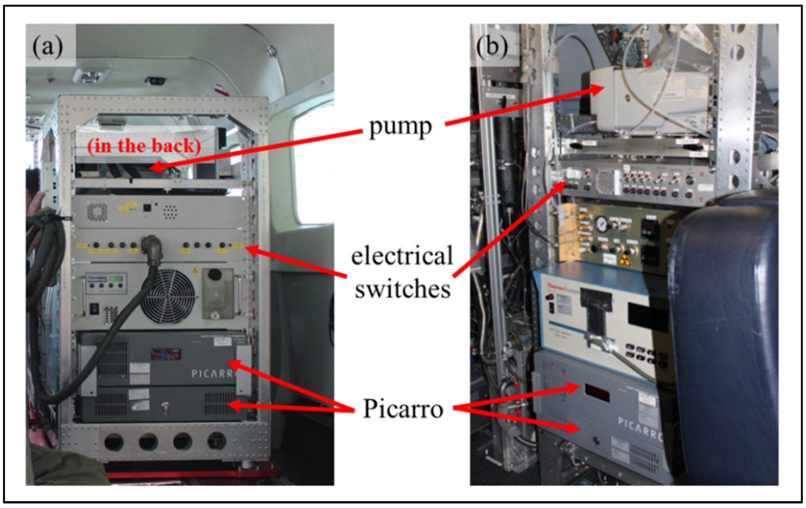

Figure 4.7: Photo of the aircraft racks deployed aboard (a) the Cessna and (b) HALO, with the two Picarro modules at the bottom and the external pump in the upper part.

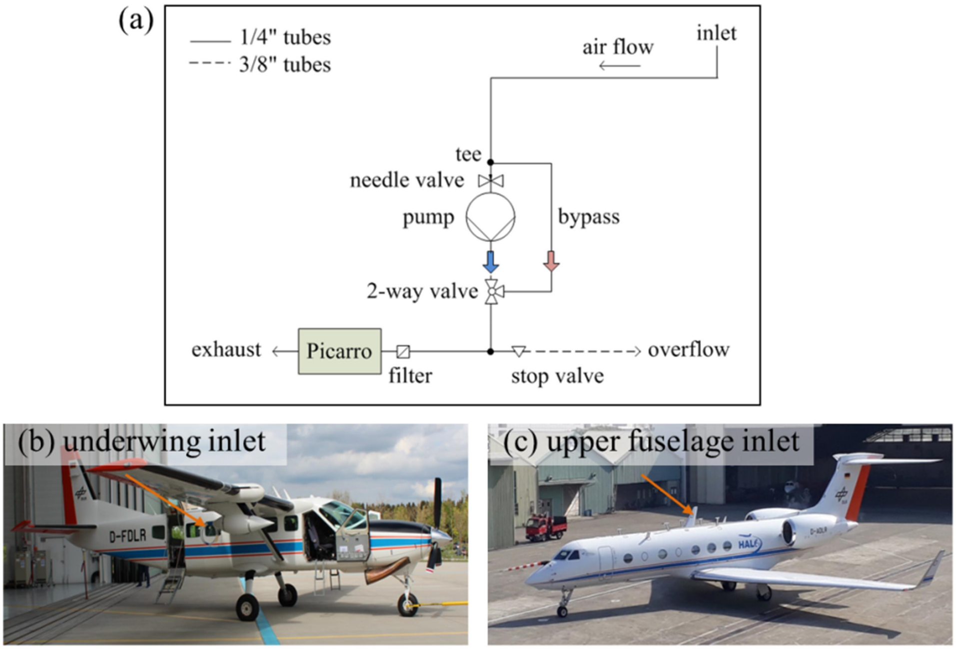

Figure 4.8: (a) Schematic gas flow of the instrument setup and backward facing inlets at (b) the underwing pod of the Cessna (photo courtesy of J. Kostinek) and (c) at the upper fuselage of HALO. The flow diagram is valid for both aircraft, however aboard the Cessna no stop valve was used.

4.4 In-flight measurement comparison

During EMeRGe-Europe a “blind” measurement intercomparison was performed during a formation flight of HALO and the UK research aircraft BAE146 - FAAM (Facility for Airborne Atmospheric Measurements) on July 13th (see the comprehensive report by U. Schumann, 2019). The CO_2 and CH_4 measurements obtained from both aircraft are used to assess the quality of the Picarro data.

A racetrack pattern was flown at three different altitudes (4.7, 3.2 and 1.2 km) ranging from the dry and clean free troposphere to the polluted boundary layer. Both aircraft were flying wing-by-wing (Fig. 4.9a) and were on average only 106 m (8 m) in the horizontal (vertical) apart. CO_2 and CH_4 were measured aboard both aircraft, but with different instruments. Aboard FAAM a modified Los Gatos Research Inc. Fast Greenhouse Gas Analyser (FGGA) Model RMT-200 (Palmer et al., 2018) was deployed, relying on cavity-enhanced absorption spectroscopy. The measurement data were provided under “blind” conditions, i.e. the exchange of information on the data between the research groups was restricted before the comparison. For the comparison flight segments with strong curves (roll angle up to 20°) and large separations between both aircraft (>180 m horizontal, >50 m vertical) were excluded. The results are shown in Fig. 4.9 for CH_4 (panel b) and CO_2 (panel c), indicating a very good correlation between the two instruments (R = 0.8 for CH_4 and 0.9 for CO_2).

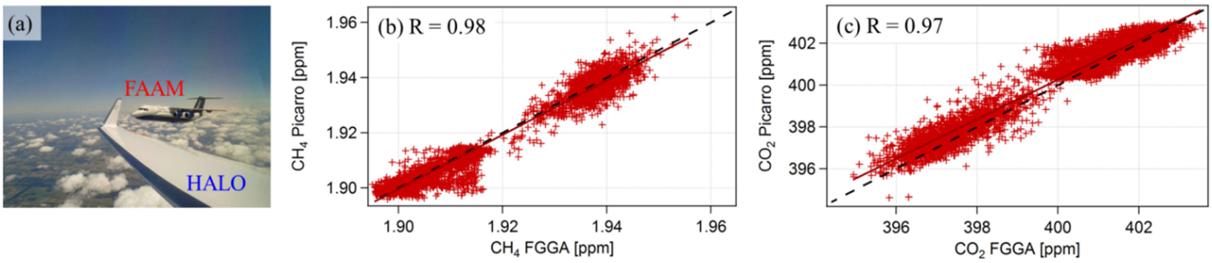

Figure 4.9: (a) Photo of HALO and FAAM research aircraft flying wing-by-wing (courtesy of K. Kaiser, MPI). Comparison of (b) CH_4 and (c) CO_2 measurement data between Picarro aboard HALO and the FGGA aboard FAAM shows good agreement between both instruments. R denotes the correlation coefficient. FAAM data are provided by J. Pitt, S. O’Shea and S. Bauguitte.

4.5 Concluding remarks

The total measurement uncertainty of the Picarro analyser for the $[UC]^2$ campaign is determined to be 0.2 ppm for CO_2 and 1.1 ppb for CH_4. The error estimate is based on calibrations performed with secondary standards from Air Liquide, which were cross-calibrated towards primary NOAA standards. To further improve the error estimation laboratory experiments with respect to the water vapour correction values and the drift with time were performed. An in-flight “blind” measurement intercomparison revealed excellent correlation and agreement within combined errors with an independent second GHG measurement system. However, to further improve airborne measurements with the CRDS instrument, three improvements are proposed.

Firstly, during the calibration of the Picarro instrument, dry synthetic air standards were used. In such standards, compared to humid ambient air standards, the ratio of O_2 and N_2 can vary and argon is often absent. Since the analysis of CO_2 and CH_4 by IR spectroscopy depends on the gas matrix composition, while temperature and pressure are held constant, additional uncertainties might be introduced. The CRDS instruments model the shape of the absorption line using the Galatry function which includes parametrizations for the line-broadening (Doppler and Lorentzian) and line-narrowing effects (Nara et al., 2012). In ambient air the variations in the main components N_2, O_2 and argon are usually small so that the function is a good approximation, however in synthetic air biases for CO_2 could be around 0.49 to 0.87 ppm and for CH_4 around 1 to 1.4 ppb (Nara et al., 2012). Therefore it should be considered to only use standards with compressed and dried natural air in the future.

Secondly, the Picarro instrument uses for the detection of $^{12}CO_2$ and $^{12}CH_4$ the wavelengths at 1603 nm and at 1651 nm, respectively. Although, the majority of carbon in CO_2 and CH_4 on Earth (98 to 99 %, HITRAN*online*) is found as ^{12}C, the next heavier isotope ^{13}C accounts for ~1 % and these isotopes might differ between the calibration gas and the air sample. If a synthetic CO_2 standard differs from the atmospheric background by an isotopic $\delta^{13}C(CO_2)$ value of ~30 ‰, the bias in the measured CO_2 mole fraction is in the order of 140 to 160 ppb (Chen et al., 2010). For CH_4, a divergent standard by ~8 ‰, leads to a bias of only 0.06 to 0.07 ppb, thus negligible (Chen et al., 2010; Peischl et al., 2012). However, it would be important for the CO_2 measurements to determine the isotopic abundances in the calibration gas standards to assess their uncertainty.

Third, during EMeRGe-Europe the cavity pressure was occasionally fluctuating especially when flying within the boundary layer (±3.3 hPa instead of ±0.4 hPa), which in turn reduces the precision of the CO_2 and CH_4 measurements during the flight in the range of 260 ppb for CO_2 and 3 ppb for CH_4. Although less than 1 % of the whole dataset is affected, pressure fluctuations for the subsequent campaigns might be reduced by changing the original inlet proportional valve, similar as described in Karion et al. (2013b). The original inlet valve (manufactured by Parker, EPCA55SSVXAA 3011) is very sensitive to aircraft vibration and motion due to a components large mass, whereas the newer inlet valve (manufactured by Clippard; EV-PM-10-4025-V) has lighter components and hence is less sensitive to aircraft motion. Therefore, the noise in the measurements should be reduced. The change of the valve is not a big effort, however communication and delivery problems since the first idea (12/2017) delayed the replacement until all campaigns for the present thesis were already finished. For an upcoming airborne deployment it should however be considered to test the Clippard valve.

5 Studying urban greenhouse gas emissions on the local scale: the German capital Berlin

With the mass balance approach (see Sect. 2.2.2) emission rates of point and area sources can be derived based on atmospheric observations. Such top-down estimates are used to independently validate total bottom-up emissions. With respect to Europe, airborne mass balance studies have been conducted in Rome (Gioli et al., 2014) and London (O'Shea et al., 2014; Pitt et al., 2019), as presented in Sect. 2.1.3. This thesis will expand these studies with a focus on the German capital Berlin using in situ CO_2 and CH_4 observations. The following specific research questions (see also Sect. 1.2) are of interest for the local scale analysis:

RQ 1) To what extent do annual GHG emissions from different bottom-up inventories agree for a major European capital like Berlin?

RQ 2) Can emission rates of GHG be estimated for the city of Berlin from airborne in situ instruments using a mass balance approach?

RQ 3) How do top-down emission rates derived with the mass balance method compare to bottom-up inventories?

RQ 4) Can simulations of regional models in combination with airborne measurements be used to identify GHG sources which are missing in the bottom-up inventories?

This chapter describes the current knowledge on Berlins GHG emissions and introduces the implementation of various emission sources in the MECO(n) model setup (Sect. 5.1). Further, an overview of the Urban Climate Under Change $[UC]^2$ mission, performed in summer 2018, is given in Sect. 5.2. On the basis of the research flight conducted on July 20th GHG emission rates are derived using the mass balance approach (Sect. 5.3). Section 5.4 presents additional results for the research flight performed on July 20th, and a conclusion is given in Sect. 5.5.

5.1 Berlin and its greenhouse gas emissions

The German capital Berlin is an interesting target for studying urban GHG emissions, as it is the largest German city in terms of area and second largest city in terms of population density (Statistisches Bundesamt, 2018). With respect to the aircraft-based mass balance approach Berlin appears to be an ideal testbed as three conditions are fulfilled: a) the topography is relatively flat to provide a steady and unperturbed air flow; b) the city of Berlin is relatively separated from the surrounding area in terms of population density (84 vs. 4055 inhabitants per km^2), which is depicted in Fig. 5.1. In addition, the metropolitan area does not extent very far into the surroundings; and c) GHG emissions should be strong enough to be detectable with in situ instruments. The greater Berlin area is expected to emit roughly the same amount of CO_2 as the well-studied London area. According to estimates from Pitt et al. (2019) and the CAMS GHG inventory for 2015 (Kuenen et al., 2014) both cities emit ~33 $Mt\,a^{-1}$. CH_4 emissions could be ~50 % lower for Berlin (~28 $kt\,a^{-1}$ vs. ~53 $kt\,a^{-1}$).

To the best of my knowledge, the only published study on experimentally determined GHG fluxes from Berlin is by Hase et al. (2015), who deployed five ground-based Fourier-Transform infrared spectrometers around Berlin in June and July 2014. They were able to distinguish urban emissions apparent in XCO_2 signals (column-averaged dry air mole fraction) and based on a simple dispersion model they retrieved a CO_2 source strength of $0.8\,t\,s^{-1}$. In contrast, the observed XCH_4 signal did not follow the XCO_2 pattern (due to different sources) and a distinct background could not be observed. The city of Berlin has also been in the focus in several studies on the potential use of satellite measurements for estimating CO_2 emissions using synthetic satellite observations (Pillai et al., 2016; Kuhlmann et al., 2019b). They showed that even for future and highly sophisticated satellite systems, the identification and quantification of the Berlin city plume is extremely challenging.

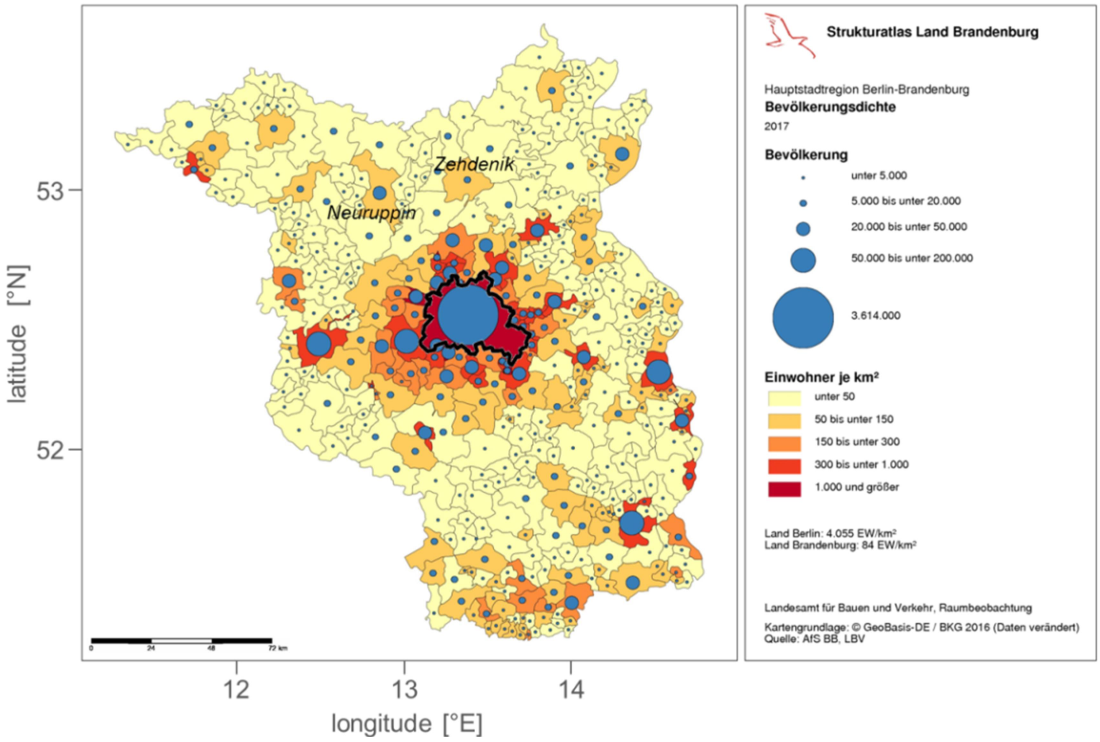

Figure 5.1: Population density for Berlin and the state Brandenburg (adapted from Strukturatlas Land Brandenburg, 2017). The yellow to red colours indicate the inhabitants per km^2, the blue dots show numbers for total population in each municipality. The Berlin city boundary (black) is added as well as latitude and longitude labels for better orientation.

5.1.1 Comparison of gridded inventories

In this section three available GHG emission inventories are compared for the city of Berlin and its surrounding area from a global, European, and local inventory.

(a) the global inventory EDGAR v5.0 for the year 2015 with a resolution of 0.1° × 0.1° (Crippa et al., 2019);

(b) the European inventory CAMS-REG (Copernicus Atmosphere Monitoring Service) v1.1 for 2015 with a resolution of 0.0625° × 0.125° (Kuenen et al., 2014); and

(c) a local inventory, referred to as BERLIN, for 2012 (Berliner Emissionskataster v1.0, AVISO GmbH and IE Leipzig, 2016). It originally consists of individual area, point and line sources provided by the Senatsverwaltung für Stadtentwicklung und Umwelt Berlin (A. Kerschbaumer) and includes different emission sectors for air pollutants and GHG. The species have been projected to a 0.01° × 0.01° lat-lon grid (~1 km resolution). Parts of this inventory are described by Brunner et al. (2019) and Kuhlmann et al. (2019a).

Figure 5.2 shows the CO_2 (upper row) and CH_4 (lower row) emission maps for the EDGAR, CAMS-REG and BERLIN inventories along with the city boundary of Berlin. Member states of the EU have to report emissions from single industrial facilities to the European Pollutant and Transfer Register (E-PRTR, *https://prtr.eea.europa.eu/#/home)* if their release to air exceeds a threshold of 0.1 Mt a^{-1} for CO_2 or 0.1 kt a^{-1} for CH_4. In Fig. 5.2b these point sources are superimposed on the CAMS-REG inventory. Table 5.1 lists the estimated CO_2 and CH_4 emission totals within the city boundary together with the main contributing sectors in detail. The first column presents for each inventory the emissions in Mt CO_2 and kt CH_4 per year, while the second column lists the relative share of the sectors in percent. CO_2 is split into contributions from fossil fuel (ff) and biofuel (bf) for the EDGAR and CAMS-REG inventory, while for the BERLIN inventory this information is not available.

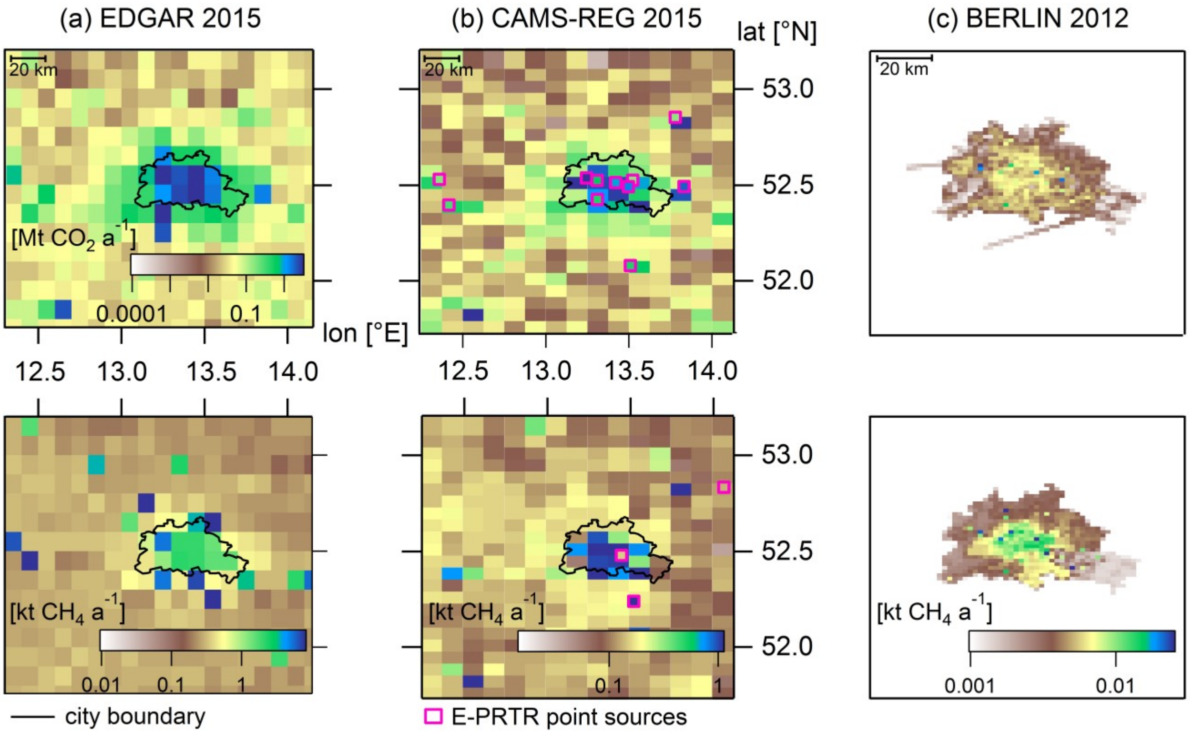

Figure 5.2: Emission maps of CO_2 (upper row; same colour scale for every panel) and CH_4 (lower row; different colour scales) from three inventories: (a) EDGAR v5.0 for 2015 with a resolution of 0.1° × 0.1°; (b) CAMS-REG for 2015 with a resolution of 0.0625° × 0.125°, superimposed are selected point sources from E-PRTR (2015, 2016) for simulation purpose; (c) BERLIN for 2012 with a resolution of 0.01° × 0.01°. The horizontal stripes in CO_2 are due to take-off and landing at the two major airports. Note that the BERLIN inventory is slightly enlarged (distance scale).

Total CO_2 emissions from Berlin range from 16.8 to 24.2 Mt a^{-1} between different inventories and thus agree within a factor of ~1.4. The CO_2 emissions (note the uniform colour scale) are rather confined to the inner city, since they are closely coupled to ff consumption related to energy production and transport (Helfter et al., 2011), and thus to areas with high population density and locations of power plants. This is also reflected in the emission sectors, as the majority of emissions (79 to 82 %) within the three inventories are related to fuel combustion for the generation of electricity and heat. However, the emission strength itself differs, while the inventories agree in the numbers for the road transport sector. According to EDGAR, the relative CO_2 contribution from the road traffic sector for Berlin (~10 %) is slightly lower than e.g. for greater Paris (~16 %) or London (~22 %). This is most likely explainable by the high dominance of point source emissions from power plants located within the city of Berlin. Roughly 94 % of CO_2 emissions from point sources reported to E-PRTR (2016) are released from power plants. In contrast, these emissions only account for zero and ~21 % for the inner and outer city of London, respectively, and for ~24 % for Paris. Strong CO_2 sources outside the city are located at different spots when comparing EDGAR and CAMS-REG.

With respect to CH_4, larger discrepancies are present between the inventories; both in the partitioning into different sectors and in the magnitude of emissions (factor ~8). Therefore, each CH_4 panel has a different colour scale. In EDGAR, strongest CH_4 sources are located outside the city and mainly consist of solid waste landfills and wastewater handling. In contrast, emissions reported in CAMS-REG are mainly due to fuel combustion for the generation of electricity and heat as well as fuel exploitation, with only little contribution of waste treatment and disposal. Hence, the spatial distribution of CH_4 emissions is similar to the CAMS-REG CO_2 emission distribution. Interestingly, BERLIN also reports almost no emissions from the waste sector, the main contribution of 2.3 kt CH_4 a^{-1} results from leakages during natural gas transport in pipelines and during storage in gasometers. According to the report for the Berliner Emissionskataster (AVISO GmbH and IE Leipzig, 2016), waste treatment in municipal sewage-treatment facilities occurs under aerobic conditions (where no CH_4 is produced) and composting facilities of organic waste (where CH_4 can be produced) are located outside of Berlin and are thus neglected in the inventory. In contrast, EDGAR uses for solid waste disposal and wastewater emissions a proxy mainly based on the distribution of urban and rural population (Janssens-Maenhout et al., 2012). In E-PRTR only three CH_4 point sources are listed, which do not always match with the emission hot spots in EDGAR and CAMS-REG. This highlights the importance of an experimental verification of GHG emissions around Berlin as performed for this thesis.

For Table 5.1 the emissions in EDGAR and CAMS-REG are estimated based on the percentage of the grid cell area being within the city boundary based on OpenStreetMap (2018), which uses an administrative boundary dividing Germany into 16 federal states, including Berlin. A sensitivity test, where only the grid cells in EDGAR (CAMS-REG) were taken, which contain at least 75 % of the city area, reveal that total emission estimates are lower, both for CH_4 with ~25 % (20 %) and for CO_2 with ~7 % (4 %). Nevertheless, the large discrepancies within the CH_4 inventories cannot be explained by this, as total CH_4 emissions still vary by a factor of ~6.

Table 5.1: CO_2 and CH_4 annual emission fluxes (integrated within the Berlin city boundary in the upper two panels; corrected according to the footprint analysis in the two lower panels) from the global EDGAR, European CAMS-REG and local BERLIN inventory. Fuel comb. is the abbreviation for “fuel combustion for the generation of electricity and heat”.

	EDGAR 2015	CAMS-REG 2015	BERLIN 2012	EDGAR 2015	CAMS-REG 2015	BERLIN 2012
Emission sector	**CO_2 [Mt a^{-1}][a]**			**CO_2 [%][a]**		
Total (ff + bf)	24.2 (22.5 + 1.7)	22.6 (15.4 + 7.1)	16.8	100	100	100
Fuel comb.	19 (17.5 + 1.5)[b]	17.9 (12.5 + 5.4)[c]	13.7[e]	79[b]	79[c]	82[e]
Road transport	2.4 (2.3 + 0.1)	2.5 (2.4 + 0.1)	2.7[f]	10	11	16[f]
Others	2.8 (2.7 + 0.1)	2.2 (0.5 + 1.6)	0.4	12	10	2
Emission sector	**CH_4 [kt a^{-1}]**			**CH_4 [%]**		
Total	25.7	15.4	3.4	100	100	100
Waste	20.3[d]	0.1	0.1	79[d]	1	3
Fuel comb.	2[b]	5.6[c]	0.8[e]	8[b]	36[c]	24[e]
Fuel exploitation	2.6	5.8	2.3	10	38	68
Others	0.8	3.9	0.2	3	25	5
Footprint corrected[g]	**CO_2 [Mt a^{-1}]** 41.9	30.6	n.a.	n.a.		
Footprint corrected[g]	**CH_4 [kt a^{-1}]** 94.3	21.9	n.a.	n.a.		

[a] The first column lists the emission fluxes for different emission sectors in Mt or kt per year [a^{-1}], the second column shows the relative share in percent. CO_2 is split into contributions from fossil fuel and biofuel when possible and indicated by parentheses (ff + bf).

[b-f] The EDGAR sector definitions follow the IPCC 1996 code, while CAMS-REG and BERLIN are sectored according to the SNAP (Selected Nomenclature for Air Pollution) categories. [b] Sum of sector energy for buildings, combustion for manufacturing, and power industry. [c] Sum of sector SNAP 1 (combustion in energy and transformation industries), SNAP 2 (non-industrial combustion plants) and SNAP 34 (emissions which cannot be clearly attributed to SNAP 3 (combustion in manufacturing industry) or SNAP 4 (production processes)). [d] Sum of sector solid waste incineration, solid waste landfills, and wastewater treatment. [e] Sum of SNAP 1, SNAP 2, SNAP 3, SNAP 4, SNAP 34, and extra category of heating. [f] Sum of minor roads and major roads. Emissions for minor roads were estimated based on NO_X emissions from the same inventory using the constant emission ratio for major roads (CO_2/NOx factor of 355.5 ± 45.4 kg CO_2 / kg NOx; see Kuhlmann et al., 2019a). Emissions for major roads were compiled from earlier inventories. Therefore, road transport emissions might slightly differ from Berlin's official numbers.

[g] The footprint corrected total emissions for CO_2 and CH_4 are given for the EDGAR and CAMS-REG inventory (for details see Fig. 5.8 and corresponding text).

5.1.2 Emission input for MECO(n) simulations

With the global/regional nested chemistry climate model MECO(n) (see Sect. 3.2) the transport of emitted tracers based on different emission inventories was simulated. During the campaign, simulated wind fields and GHG mole fractions from the city inventory BERLIN were available as forecast simulation and were used to for flight planning. Post-campaign model simulations including 7 individual source tracers were used for comparison with the airborne observations to better understand the source contribution to the detected GHG plumes.

Table 5.2: Overview of the different tracers simulated with MECO(n) and the corresponding emission sources. For a detailed description of the inventories see Sect. 5.1.1.

Tracer	Inventory input
c-CO_2 ("city")	BERLIN + E-PRTR
c-CH_4 ("city")	BERLIN (x4.5) + E-PRTR
w-CH_4 ("wastewater")	Status report of MLUL (2017) combined with EDGAR v4.3.2 wastewater emissions from 2012
l-CH_4 ("landfills")	CORRECTIV (2016) as input for LandGEM
t-CH_4 ("total")	BERLIN (x4.5) + E-PRTR+ w-CH_4 + l-CH_4
r-CO_2 ("regional")	BERLIN merged into CAMS-REG
r-CH_4 ("regional")	BERLIN (x4.5) merged into CAMS-REG

For the so-called "city" tracer (c-CO_2, c-CH_4; see Table 5.2) the high resolution and city-wide emission inventory BERLIN provided the input emissions. To account for surrounding sources, strong point emitters according to E-PRTR outside of Berlin were included. For CO_2, eight facilities with combined emissions of 5.7 Mt CO_2 in 2016 were added (which is roughly 1/4th to 1/3rd of total Berlin emissions), for CH_4 this applied to two sources: landfill Schoeneicher Plan (south of Berlin) with 1.37 kt CH_4 in 2016 and landfill Neuenhagen (NE of Berlin) with 0.13 kt CH_4 in 2015. These simulated "city" tracers serve as baseline for the later analysis.

As described in the previous section, inventorial CH_4 emissions show large discrepancies especially with respect to the waste sector. Therefore, additional information on locations of strong point sources, i.e. sewage-treatment plants and waste deposits was collected. Corresponding CH_4 emissions for the "wastewater" (w-CH_4) and "landfill" (l-CH_4) tracers were estimated to range between 1 and 7 kt CH_4 a^{-1} and between 0.02 and 16 kt CH_4 a^{-1}, respectively.

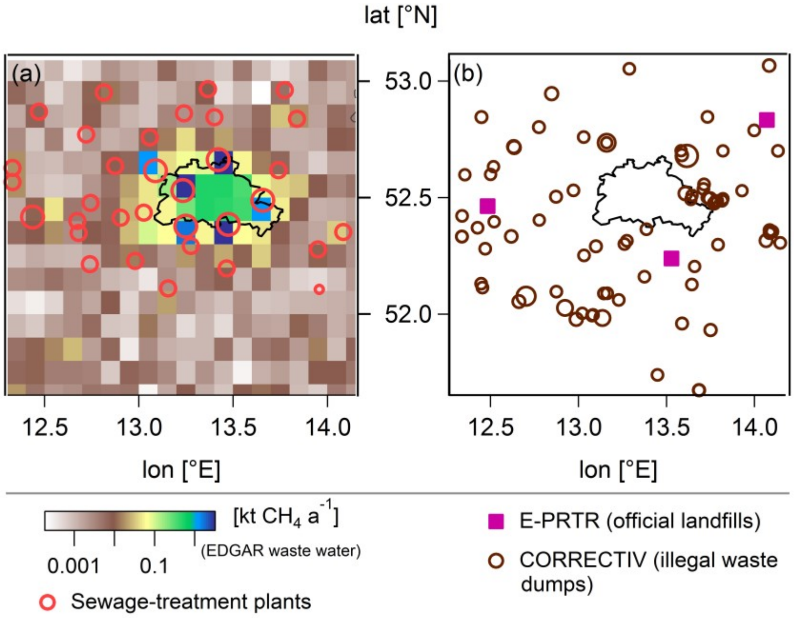

Figure 5.3: (a) Sewage-treatment plants (MLUL, 2017) are sized according to their population equivalent and superimposed on the EDGAR v5.0 wastewater CH_4 emission map. (b) Illegal waste deposits (CORRECTIV, 2016) are sized according to the amount of deposited waste (ranging from 0.06 to 416 kt of waste). Official landfills listed in E-PRTR (2015, 2016) are not sized.

Figure 5.3a shows sewage-treatment facilities superimposed on the EDGAR v5.0 wastewater CH_4 emission map from 2015. Information on sewage-treatment plants were taken from a status report of the Ministerium für Ländliche Entwicklung, Umwelt und Landwirtschaft (MLUL, 2017) and their exact position was determined with Google Earth. Since the report only covers the state of Brandenburg, one sewage-treatment plant within the Berlin city boundary was added (Ruhleben, Berliner Wasserbetriebe). Larger plants surrounding Berlin (they are sized according to their population equivalent) correlate very well with pixels of stronger EDGAR CH_4 emissions. Therefore their emission rates were transferred and the remaining smaller facilities were assigned with an arbitrarily chosen CH_4 rate of 1 kt a^{-1} to ensure a visible signal in the MECO(n) model output (note that although Fig. 5.3a shows the EDGAR v5.0 wastewater map of 2015, the values from 2012 (v4.3.2) were assigned to the facilities as the model run was not repeated after updating to the most recent inventory v5.0).

Landfills are another well-known CH_4 emission source, which are considered separately. In Fig. 5.3b official landfills (reported to E-PRTR) are mapped together with illegal waste dumps, which are based on information from the non-profit organization *CORRECTIV*. Their article discovered more than 100 illegal landfills in Brandenburg with at least three million tons of waste (CORRECTIV, 2016). However, the legal disposal of this waste would cost more than 320 million Euros. CH_4 emissions were calculated using the LANDfill Gas Emission Model (LandGEM, 2005, v3.02), provided by the United States Environmental Protection Agency (EPA). Input parameters are the amount of waste and the year of the first deposit as waste is continuously decomposing. If no information on the year was available, the most frequently reported year was used (i.e. year 2000). Furthermore, a constant decay rate ($k = 0.038$) and a degradable organic carbon content ($doc = 0.2028$) based on moderate climate were taken, and it was assumed that all waste material is from municipal solid waste landfills (EPA, 2010). Calculated emissions from both, sewage treatment and landfills, are not intended to represent true values, however, they serve as input for model sensitivity tests to study the importance of these sectors (see Sect. 5.3.4).

Last, to account not only for point sources outside of Berlin, but also the regional background, the BERLIN inventory was merged into the European CAMS-REG inventory (r-CO_2, r-CH_4). Since total CH_4 emissions for both inventories within Berlin differ by a factor of ~4.5 (see Table 5.1) it was necessary to scale the BERLIN CH_4 emissions with this factor to ensure that no artificial gradient in the simulated CH_4 mole fraction is introduced at the boundary between the two merged inventories. For CO_2 no scaling was applied, however, grid boxes at the outermost boundary of BERLIN with very low emissions were removed.

Simulations with the EDGAR emissions have not been performed as the inventory is a factor ~10 coarser than the MECO(n) model resolution (~1 km × 1 km). Hence, using such a coarse emission inventory with a much finer model resolution will not add useful information. Further, emissions related to the agriculture sector are not implemented explicitly as separate tracers. In EDGAR, CH_4 emissions from agriculture (enteric fermentation, manure management, agricultural waste burning and agricultural soils) account for less than 0.4 kt a^{-1}, hence only ~1.5 % of total CH_4 emissions within the Berlin city boundary.

5.2 The $[UC]^2$ mission overview in summer 2018

Under the framework of the $[UC]^2$ project, research flights were conducted in Berlin during summer 2018. The focus of this thesis is to analyse the urban GHG aircraft measurements, however, the overarching objective of $[UC]^2$ is to develop, apply and validate an urban climate model at high spatial resolution (<10 m) for three German cities: Hamburg, Stuttgart and Berlin (Scherer et al., 2019b). All airborne observational data are used for the validation subproject 3DO (3-Dimensional Observation of Atmospheric Processes in Cities; Scherer et al., 2019a).

The $[UC]^2$ mission was the second aircraft campaign from DLR-IPA deploying in situ instruments aboard the DLR Cessna Grand Caravan 208B. This single-engine aircraft is small and robust, and due to its relatively low speed (~50 m s^{-1}) the research instruments aboard (with a sampling rate of 0.5 Hz) are able to provide measurements at a fine spatial resolution (~100 m). Hence, the atmospheric composition, as well as gradients at the local scale can be well resolved. Besides the Picarro G1301-m instrument (see Chapter 4), the aircraft was equipped with a series of instruments to measure meteorological parameters and trace gas species: (1) a modified Aerodyne Quantum Cascade/Interband Cascade Laser (QCL/ICL) based spectrometer for CO_2, CH_4, ethane (C_2H_6), carbon monoxide (CO) and nitrous oxide (N_2O); for details see Kostinek et al. (2019); (2) a Cavity Attenuated Phase Shift (CAPS) Sensor for nitrogen dioxide (NO_2); (3) a 2B ozone (O_3) monitor; (4) a meteorological sensor package (METPOD), which includes a boom with a five-hole probe at its tip for measurements of meteorological data like temperature, pressure, humidity, wind direction and wind speed; for details see Mallaun et al. (2015); and (5) the AEROcontrol IGI system, which is a combination of differential GPS (Global Positioning System) and IRS (Inertial Reference System), for recording of aircraft position data.

Five research flights (~13 flight hours) were conducted with the DLR Cessna aircraft around Berlin between July 16th and 26th of 2018, see Fig. 5.4. The aircraft was stationed at the airfield Schoenhagen, located ~40 km southwest of Berlin. As discussed in Sect. 2.2.2 the flight strategy was optimised to study GHG fluxes using the mass balance approach. These typical mass balance flight patterns are roughly perpendicular to the prevailing wind direction, which was mainly from NW to NE. Flights were conducted between ~11:30 and ~15:00 UTC (+2 h for local time) to ensure a well-mixed boundary layer (BL). In order to characterise the BL during each flight, a vertical profile (upward spiral, typically between 0.3 and 3 km) was obtained at the Tempelhofer Feld (TF, south of the city centre). The horizontal extent of Berlin is approximately 35 to 45 km. In order to assure complete sampling of the urban outflow, the length of each stacked downwind transect (so-called "wall") was planned to cover more than 80 km at a typical downwind distance of roughly 30 to 40 km.

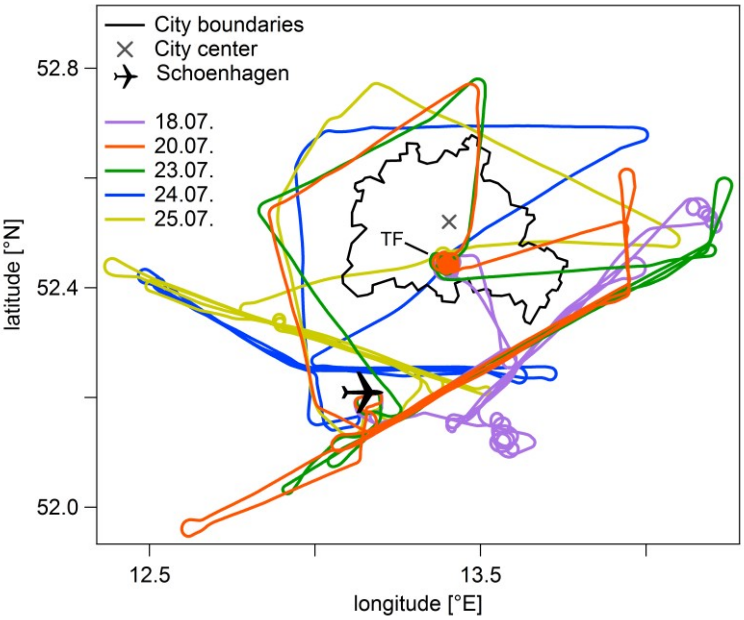

Figure 5.4: Flight routes of the DLR Cessna with take-off and landing from the airfield Schoenhagen during $[UC]^2$ in July 2018. At the Tempelhofer Feld (TF), located south of the city centre, an upward spiral was flown during each flight to characterise the boundary layer.

The flight planning mainly relied on the MECO(n) plume forecast of the GHG city tracers c-CO_2 and c-CH_4. With horizontal latitude-longitude projections, as well as vertical height profiles, the location of the urban pollution plume and the distance at which the plume is supposed to be vertically well mixed was determined. Furthermore, the meteogram for Berlin-Tempelhof provided by the German Weather Service (Deutscher WetterDienst, DWD) on the basis of their ICON (ICOsahedral Nonhydrostatic) forecast model was used, as well as animated forecasts based on ECMWF and GFS (Global Forecast System) from *windy.com* to verify the wind forecasts from MECO(n). Flight plans had to be submitted to Air Traffic Control (ATC) on the day before the flight and were approved (either as submitted or slightly modified) shortly before the flight. However, discrepancies between the previous day forecast and the actual wind conditions, together with the heavy air traffic situation in and around Berlin with its two major airports (Berlin-Tegel and Berlin-Schönefeld) generally hampered the realisation of the flight patterns designed for optimised sampling of the in- and outflow.

Table 5.3: Overview of five performed research flights with date (weekday), time of flight, average wind direction, average wind speed, BL depth and general weather situation. For the average wind speed and direction the average of the whole flight is considered, excluding winds above the BL when different. BL depth is estimated from meteorological measurements. [a)]BL has two layers.

Day of July 2018 (weekday)	Take-off and landing [UTC]	Avg. wind direction [deg]	Avg. wind speed [m s^{-1}]	BL depth [m]	Weather situation
18th (Wed.)	11:35-14:13	304 ± 14	8.5 ± 1.8	1079 ± 26 2648 ± 7[a)]	West of occlusion along border of Germany and Poland
20th (Fri.)	11:30-14:07	299 ± 27	4.8 ± 1.8	2737 ± 2	Ridge of high-pressure system, low level clouds
23rd (Mon.)	11:37-14:08	296 ± 16	5.6 ± 1.4	1419 ± 4	Clear sky
24th (Tues.)	12:12-14:59	25 ± 34	3.3 ± 1.3	2046 ± 1	Eastern edge of high-pressure system, low level clouds
25th (Wed.)	11:28-14:10	27 ± 28	3.3 ± 1.1	1969 ± 56	South-eastern edge of high-pressure system, low level clouds

Table 5.3 presents an overview of the performed research flights including date, flight time, average wind direction, average wind speed, BL depth, and the general weather situation. Time series for CO_2, CH_4 and flight altitude of each flight can be found in the Appendix (A.5), as well as altitude profiles of virtual potential temperature (θ_v), static temperature (TS), and relative humidity (RH) used to estimate the BL depth. The BL depths were determined considering the average of three different approaches (1) level of maximum gradient in θ_v, following Dai et al. (2014); (2) base level of an elevated TS inversion; and (3) level of minimum vertical gradient of RH, both following Seidel et al. (2010). BL depths were cross verified through the comparison with aerosol LIDAR measurements at Leipzig, Germany, performed within EARLINET (European Aerosol Research LIdar NETwork; Pappalardo et al., 2014; retrieved from *http://polly.tropos.de/?p=lidarzeit&Ort=1&Jahr=2018*; last access 04.10.2019). BL heights retrieved from the ECMWF forecast data, used for HYSPLIT calculations (see Sect. 3.3), were averaged within 50.85 °N to 50.75 °N and 12.45 °E to 14.2 °E and agree within ±250 m compared to the BL height deduced from the airborne measurements.

5.3 Mass balance flight on July 20th

In the following section the mass balance approach for a case study on July 20th is applied and discussed. During this flight strong CO_2 and CH_4 signals from urban emissions were clearly distinguishable from the atmospheric background variability and ideal meteorological conditions prevalent on that day allow for the use of the mass balance method. Using the flight on July 24th, the limitations of the mass balance approach are discussed in Sect. 5.4. The other three flights performed on 18th, 23rd and 25th of July were not suitable for the mass balance method due to the following reasons: Based on Table 5.3 and vertical meteorological profiles in the Appendix (A.5) it is apparent that the BL on July 18th and 25th was not clearly separated from the free troposphere and not well-mixed. In addition, the wind speed on July 18th was rather high with more than 8 m s^{-1} on average causing too little accumulation of emissions in the BL. On July 23rd meteorological conditions appeared to be favourable, however, the urban plume was most likely missed, mainly because of the large difference between forecasted and real wind direction (~40°) and the inflexibility to adapt the submitted flight pattern ad hoc due to heavy air traffic in and out of Berlin’s two major airports.

5.3.1 Flight pattern and airborne observations

On July 20th the research flight was conducted between ~11:30 and ~14:00 UTC, see Fig. 5.5. Forecasts indicated north-northwesterly winds and a BL height of ~2 km. However, during the flight, the wind came from the north-west with 4.8 m s^{-1} on average. The aircraft first headed towards the north (indicated by the black arrow) to perform the upwind leg roughly at the middle of the BL (~780 m). This upwind section is shaded grey on the altitude curve visible in Fig. 5.5b. A detailed vertical profile was obtained at the Tempelhofer Feld from ~350 m up to ~3.2 km (with an ascend rate of ~3 m s^{-1}), hereby detecting the lowest CH_4 mole fractions during the entire flight (note the splitted CH_4 axis). The in-flight derived BL height from the vertical profile was then used to adapt the heights of the following downwind transects to roughly 500 m, 1 km and 1.6 km. This so-called downwind “wall” is colour-coded in both panels according to the horizontal distance flown. Sampling of the urban plume started at point ‘A’ (marked with 0 km distance) towards the south-west as indicated with negative distances. Since in-flight observations of atmospheric GHG mole fractions did not reach background levels as observed at the starting point, the downwind transects were extended in-flight. Due to ATC restrictions this was only possible by flying strictly towards the north, as indicated with positive distances. Fig. 5.5a also includes HYSPLIT backward trajectories for the last 12 hours, which were started from the entire downwind “wall” at 13 UTC. Colour-coded is (for simplicity) only every 5th trajectory within the BL according to its relative time since its calculation start. They grey colours underneath depict, in addition, also trajectories being outside the BL. The trajectories reflect the prevalent wind direction and wind speed quite well (ECMWF forecast data and airborne wind measurements reveal Pearson correlation coefficients between 0.95 and 0.98; for details see Appendix A.6) and indicate a steady wind flow within the BL for at least 6 hours prior to our measurement.

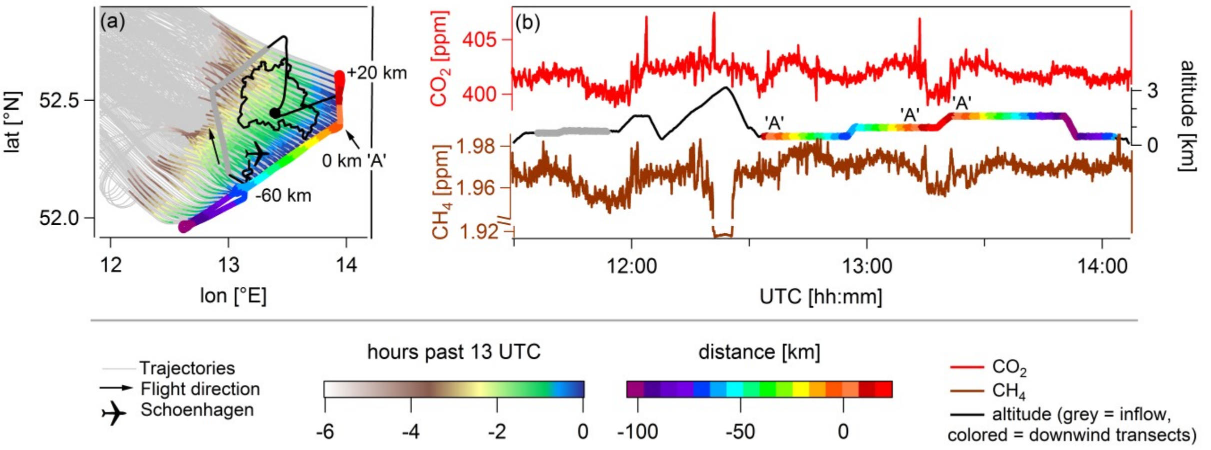

Figure 5.5: (a) Flight pattern of July 20th in black where the downwind "wall" is colour-coded according to the horizontal distance (0 km corresponds to the starting point 'A' at 52.41 °N and 13.95 °E). Backward trajectories (-12 h, in grey) are started from the downwind "wall" at 13 UTC, while every 5th trajectory within the BL is colour-coded according to its relative time since the calculation start. (b) Time series of CO_2, CH_4 and flight altitude. The grey sections of the altitude curve correspond to the inflow section of the flight; other colours same as in panel (a).

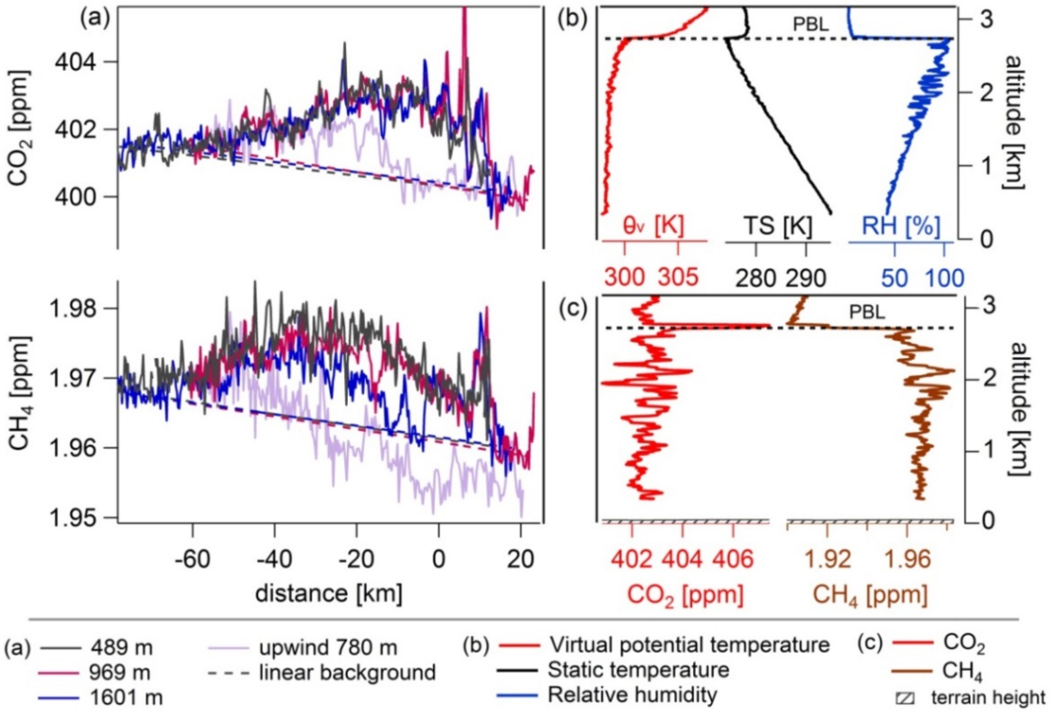

Figure 5.6: (a) Measured downwind CO_2 and CH_4 mole fractions (segment mean) at three different altitudes within the BL along the flown horizontal distance. The background based on the edges of the flight leg is shown with dashed lines, the background based on mole fractions measured upwind as light purple line (see Sect. 5.3.2 for details). (b) Vertical profile of virtual potential temperature (θ_v), static temperature (TS) and relative humidity (RH) at the Tempelhofer Feld. The derived BL depth is shown as black dashed line. (c) Vertical profile of CO_2 and CH_4 at the Tempelhofer Feld, the terrain height of ~43 to ~50 m reflects the west to east cross-section at the Tempelhofer Feld retrieved from Google Earth.

Figure 5.6a presents the measured CO_2 and CH_4 mole fractions along the horizontal distance at the three different altitudes of the "wall". The encountered CO_2 plume is detected approximately between -30 and 15 km, thus in the more northern part of the flight track, whereas the centre of the CH_4 plume extends more to the south-west (roughly between -50 and 15 km). A similar CO_2 distribution was observed at all altitudes with maximum enhancements of 4 ppm, indicating a generally well-mixed plume. Measured CH_4 mole fractions in the two lower flight levels are also coherent with enhancements of 21 ppb, but the highest flight level shows a different pattern with a dip in CH_4 between -20 and 0 km. Differences in the vertical distribution of CO_2 and CH_4 can be explained by a combination of three effects: a) differences in the spatial distribution of the emissions sources (see Sect. 5.1.1), b) differences in the emission height, and c) differences in the buoyancy of the gases at their release point. CO_2 is largely emitted via stacks and is released already at an elevated height above ground level, which may influence the distribution due to the altitude dependent wind speed and direction (Brunner et al., 2019). Furthermore, CO_2 emissions are closely coupled to fossil fuel combustion and thus to higher temperatures during the release, which enhance the buoyancy of the air parcels and the mixing in the vertical. In contrast, CH_4 emissions are usually not emitted during exothermic processes, therefore the vertical mixing might be less pronounced. In addition to these broad enhancements, some small-scale enhancements (~3 to 5 km wide peaks) are observed at ~7 km distance (in CO_2) and further north at ~11 km (in CH_4).

Figure 5.6b shows the vertical profile obtained at the Tempelhofer Feld (from roughly 12:00 to 12:30 UTC) of θ_v, TS and RH. The BL depth was determined from that profile to 2737 ± 2 m (dashed black line), where the uncertainty of 2 m reflects the average of the three different approaches used herein (see Sect. 5.2). The BL on July 20th was well-mixed and efficiently capped as seen in the strong gradients between the BL and the free troposphere.

5.3.2 Greenhouse gas flux results

The measurements on July 20th, presented in Fig. 5.6a, show that the urban CO_2 plume is well-mixed at the different sampling altitudes between ~500 m and ~1600 m, which is also well represented by the simulations with the MECO(n) model (see Fig. 5.9c). The vertical mixing of the CH_4 plume seems slightly less pronounced, as indicated by the measurements of the highest altitude transect. Based on the simulated vertical GHG distribution within the entire BL at the downwind transects (see Appendix A.7), it is further deduced that the CO_2 emissions are also well-mixed above and below the flight altitudes, thus throughout the BL, where emissions are efficiently trapped. Hence, the emission rate is estimated individually for each single transect, similar to the method described by e.g. (Karion et al., 2013a; Peischl et al., 2013). Thereby, actual wind (and temperature and pressure) measurements are considered at each GHG measurement point. The estimated mass flux is derived as the mean from the three single mass fluxes, which also account for the less homogeneous distribution of the CH_4 plume. As introduced in Sect. 2.2.2 and shown in Eq. (2.2), uncertainties in the mass flux are influenced by uncertainties in the choice of background mole fractions, wind speed, wind direction and varying BL depth. Table 5.4 lists the emission rate estimate and sources of uncertainties, which are discussed in the following.

Table 5.4: Estimated mass flux and uncertainties for CO_2 and CH_4 for July 20th.

	CO_2	**CH_4**
Mass flux	1.39 ± 0.76 t s^{-1}	5.20 ± 1.70 kg s^{-1}
Uncertainties		
Choice of background	± 52 %	± 21 %
Wind speed and direction	± 15 %	± 23 %
BL depth variation	± 9 %	± 10 %

Two approaches are used to obtain the atmospheric background mole fraction (see Fig. 5.6a). The first approach uses the linear interpolation of atmospheric mole fractions between the plume edges (indicated by the dashed lines). For this, the local plume was defined as area where the measured mole fractions exceeded the inward running mean (interval of ±30 s) plus one standard deviation (only for CO_2) for at least five consecutive measurement points. The atmospheric background then is calculated using the average of 60 measurement points outside the plume. One exception is the south-western end of the intermediate CH_4 transect (i.e. at negative distances), which is marked in purple. Due to missing observational data in that transect, a decrease in CH_4 mole fractions down to lower (and hence, atmospheric background) values could not been detected, as compared to the other two transects. In this case the mean CH_4 background determined from the other two transects was used. Each altitude transect thereby is treated separately to account for possible vertical atmospheric gradients, and both sides of each transect are considered to capture the horizontal gradients.

In a second approach to obtain the atmospheric background, the mole fractions measured during the upwind leg (indicated by the light purple line in Fig. 5.6a) were projected on the downwind “wall” using the calculated HYSPLIT trajectories. It is assumed that the mole fractions from the upwind leg are valid for the entire BL (i.e. for all three transects). Using this approach, quite good agreement between the CO_2 mole fractions measured on both edges of the downwind plume and in the upwind leg is obtained. However, the measured CO_2 mole fractions in the inflow leg are somewhat larger than the linearly interpolated background. For CH_4, the slope of the SW to NE gradient is steeper in the inflow leg compared to the slope in the downwind observations. The large impact of the choice of background mole fractions is reflected in the resulting flux calculations, which differ by nearly 50 % in the case of CO_2. Using the first approach, a stronger flux (2.12 t CO_2 s^{-1}) is obtained compared to the second approach (1.39 t CO_2 s^{-1}). For CH_4, the mean fluxes do not differ as much (~20 %). It is worth noting that the upwind leg was flown between ~11:35 and ~12:00 UTC, while the downwind “wall” was probed ~30 to ~110 min later. Consequently, with an average measured wind speed of 4.8 m s^{-1} and a distance of ~50 km between the up- and downwind transects, the air was not sampled in a Lagrangian manner. Such sampling involves first the measurement of an air mass at a specific starting location, and second the re-sampling of the same air mass after it has been transported to a new location.

These observations demonstrate the importance of separating the urban plume from enhancements caused by emissions from anthropogenic sources (or natural variability) upstream of the city, even in the case of a relatively isolated city as Berlin. Upwind of the flight track (to the east and west) two large nature parks are located (Naturpark Westhavelland, Biosphärenreservat Schorfheide-Chorin) with two municipalities in between (Neuruppin and Zehdenik) having a population density of only 50 to 100 inhabitants per km^2 (see Fig. 5.1). With respect to the emission maps in Fig. 5.2, their location is still included in the plots (at ~53 °N and 12.8 °E; ~53 °N and 13.3 °E, respectively), however, neither EDGAR nor CAMS-REG indicate any relevant sources of CO_2. For CH_4 (at least in EDGAR) two grid cells in the vicinity are coloured in green, indicating emissions from solid waste disposal.

Similar to Cambaliza et al. (2014), the influence of the uncertainty of the wind on the estimated flux is calculated by Δflux/Δu with Δflux being the change in the flux and Δu being the uncertainty in the perpendicular wind component. The measurement uncertainties in wind direction ($1\sigma = 2°$) and wind speed ($1\sigma = 0.3\ m\ s^{-1}$) translate into errors of ±15 % in the CO_2 flux and ±23 % in the CH_4 flux. Wind measurements during strong turns of the aircraft (i.e. more than 10° roll angle) were discarded for the analysis as deviations of up to 1 $m\ s^{-1}$ are possible (personal communication with C. Mallaun, 2019).

On July 20th the free troposphere was only penetrated once, but comparable conditions (i.e. pronounced inversions) were also prominent on July 18th (see Appendix A.5). On July 18th two vertical profiles were performed, separated by approximately two hours and only a difference of ~50 m (~2 %) in the BL depth was observed. If it is assumed that no significant BL variation (<2 %) occurred during the flight on July 20th, the errors are small in the estimated fluxes (<1 %). To test the sensitivity of the derived mass fluxes on the BL depth variability, the errors for larger variations are calculated as well. In the case the BL depth would change by 5 to 10 % (roughly 140 to 270 m), the errors in the estimated fluxes (<10 % for the CH_4 flux and <9 % for the CO_2 flux) are still smaller than the uncertainty arising from wind speed and wind direction (15 % for CO_2 and 23 % for CH_4, see Table 5.4).

Entrainment of free tropospheric air into the BL and subsequent mixing with BL air can be another possible source of error. It occurs when rising thermals and turbulent eddies in the BL overshoot the capping inversion, which are in turn replaced with air from above (Wallace and Hobbs, 2006). However, entrainment can be excluded in this case due to the strong pronounced inversions at the top of the BL as shown in Fig. 5.6b. In addition, due to the strong gradients in H_2O mole fractions (a drop of ~5 $g\ kg^{-1}$ in H_2O within 22 m) and an increase in potential temperature of ~3 K, it is not believed that actual air from aloft could have been entrained that much into the BL affecting the CH_4 and CO_2 mole fractions. Above the BL the wind vector is zero or slightly positive, thus pointing against entrainment from the free troposphere.

Considering all sources of uncertainties, the emission estimate results in 1.39 ± 0.76 t $CO_2\,s^{-1}$ and 5.20 ± 1.70 kg $CH_4\,s^{-1}$ (see Table 5.4). For this calculation the second approach to obtain the atmospheric background was chosen. Hence, important information of the inflow is considered, which obviously should not be neglected in the case of Berlin. However, the first approach (using the edges of the downwind track) is included as uncertainty estimate, since the use of the up- and downwind transects has the disadvantage, that the air masses were not sampled in a Lagrangian manner.

5.3.3 Discussion on emission fluxes

In order to be able to compare the flux estimate with the corresponding area of the three emission inventories EDGAR, CAMS-REG and BERLIN, first a footprint area with HYSPLIT is determined. The footprint reflects the percentage of the air mass within the BL at a specific location (of a defined latitude-longitude grid) between the upwind and the downwind track (as described in Sect. 3.3). To determine the horizontal edges, backward trajectories were released only for GHG enhancements greater than zero after subtracting the upwind mole fractions from the observed downwind mole fractions.

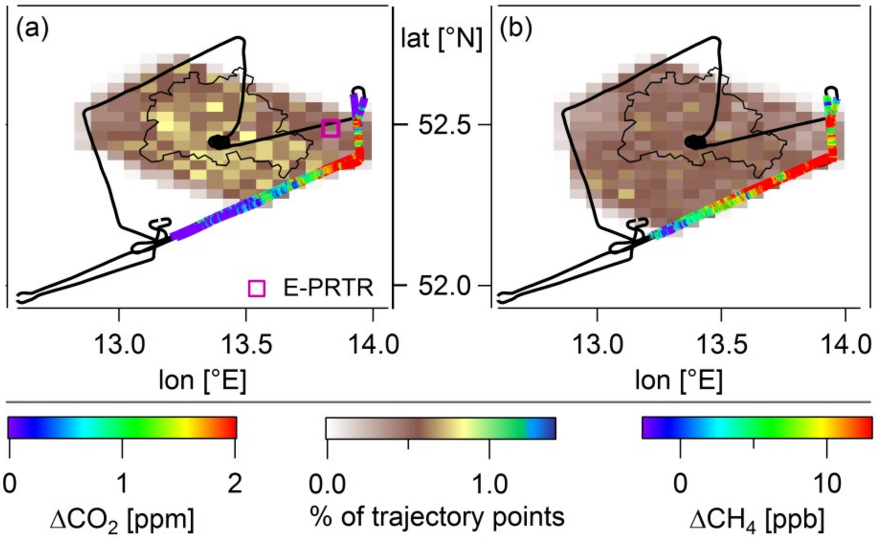

Figure 5.7: Footprint corresponding to a grid box of 0.03° × 0.065° for (a) the CO_2 and (b) CH_4 plume detected on July 20th. The purple marker in panel (a) indicates the location of three point sources from E-PRTR, which are located within a 1 km radius next to each other.

Figure 5.7 gives the flight route of July 20th, where the downwind "wall" is colour-coded according to the GHG enhancement, and the footprint analysis is shaded with respect to the observed CO_2 (panel a) and CH_4 (panel b) plume. The distribution of trajectory points in panel a is relatively homogeneous and indicates that the CO_2 plume covers the entire city. The sharp spikes in CO_2 (see Fig. 5.6a at roughly 7 km distance) are detected directly downwind of three CO_2 point sources listed in E-PRTR (2016): Fels-Werke GmbH, CEMEX Zement GmbH, and Vattenfall Europe New Energy Ecopower GmbH. They are located within a 1 km radius next to each other (marked in orange) and together report emissions of 1.9 Mt CO_2. In contrast, the footprint of the CH_4 plume indicates that sources in the south-west outside of Berlin contribute to the measured CH_4 enhancement.

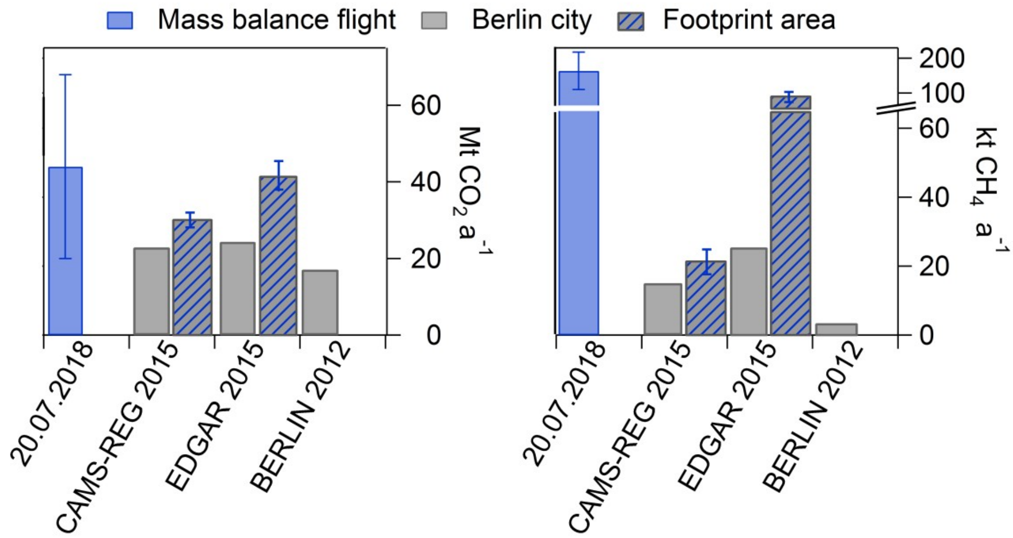

Figure 5.8: Estimated mass balance fluxes for CO_2 and CH_4 from the flight on July 20th in blue. Grey bars indicate inventorial fluxes within the Berlin city boundary. Striped bars represent the inventory fluxes enlarged by the area from the corresponding footprint analysis.

In a next step, the flux estimate is scaled to a yearly value (regardless of diurnal, weekly or seasonal cycles), the result is shown in Fig. 5.8 with blue bars. Grey bars denote emissions of CAMS-REG, EDGAR and BERLIN within the Berlin city boundary. The striped bars represent emissions from the footprint-corrected inventories of CAMS-REG and EDGAR, i.e. the emissions in the inventory grid cells covered by the footprint area are added up. Thus, 35 to 75 % larger emission rates are derived for CO_2 and 40 to 270 % larger emission rates for CH_4 if the sources located outside the definition of the city boundaries are considered. According to Stohl (1998), trajectories may deviate by 10 % of their travelled distance. Thus, the footprint area for this case study might be mislocated by up to ~7.5 km. The resulting deviation in the total inventorial emissions is considered by the error bars in Fig. 5.8.

CO_2 emissions

For the flight on July 20th, the annual CO_2 emission rate of ~44 ± 24 Mt a^{-1} is larger than the CAMS-REG and EDGAR footprint estimate, but agrees within error bars. Previous studies showed that urban CO_2 emissions based on EDGAR (especially related to the road transport sector) are likely overestimated, however, these studies only focused on American cities (Gately et al., 2013; McDonald et al., 2014; Gately and Hutyra, 2017). Gately et al. (2013) pointed out, that based on the road density proxy a downscaling of total US emissions leads to an overestimation of on-road emissions for areas with higher than average road densities (and vice versa). Also in the study by McDonald et al. (2014) vehicle emissions were overestimated by 40 to 80 % in Californian cities. No similar studies were found for European cities. While there is a strong seasonality of CO_2 fluxes due to domestic heating (with its emission maximum in winter), the contribution from road traffic (the second most important CO_2 sector for this study according to the inventories, see Table 5.1) is relatively constant throughout the year (Kuc et al., 2003; Gioli et al., 2012; and EDGAR monthly resolved emissions in 2010 as in Appendix A.8). As a consequence, inventorial CO_2 fluxes in summer (July) could be ~40 % lower than presented in Fig. 5.8. While the footprint corrected EDGAR estimate would still be in the (lower) range of the mass balance result, it would not overlap with the estimated CAMS-REG emission rate (inlcuding error bars). Thus, probing Berlin during different seasons would be very valuable.

Hase et al. (2015) reports on urban emissions apparent in XCO_2 signals from five ground-based Bruker EM27/SUN Fourier-Transform InfraRed (FTIR) spectrometers. Applying a simple dispersion model for three measurement days in June and July 2014 they retrieve a CO_2 source strength of 0.8 t s^{-1}. Compared to the estimate of Hase et al. (2015), the derived CO_2 emission flux of 1.39 ± 0.76 t s^{-1} is almost twice as large, but agrees well within the error estimate. The larger emission rate inferred is not surprising, as measurements were performed four years apart and CO_2 emissions have a very strong seasonal and diurnal cycle. In addition, due to the fixed location of FTIR spectrometers, emission rates might have been estimated from a different (possibly smaller) footprint area, which would result in lower emission rates.

At temperate latitudes the CO_2 uptake of plants usually predominates in spring and summer. A modelling study using synthetic CO_2 data by Mueller et al. (2018) showed for the Baltimore-Washington area that a substantial fraction of ~35 % of the CO_2 background variability is caused by biogenic sources and sinks in July. In contrast, Hardiman et al. (2017) simulates the biogenic carbon flux throughout Massachusetts, including the urban area Boston, but conclude that urban vegetation is probably not offsetting a significant fraction of anthropogenic emissions (only ~2 %). To account for the biospheric component of CO_2 (i.e. photosynthetic uptake and respiration), which needs to be investigated especially during summer months and in vegetated areas, the biogenic CO_2 flux is simulated with the Vegetation Photosynthesis and Respiration Model (VPRM, Mahadevan et al., 2008), which is coupled with WRF-GHG (Beck et al, 2013). The influence of the photosynthetic uptake and respiration on the assessment of the anthropogenic flux is estimated. According to the analysis, the maximum daytime photosynthetic uptake predicted over the footprint area is at most 12 % of the estimated anthropogenic flux. Due to that and the fact that the change of the predicted CO_2 biogenic signal over the small constrained area is low (well within the observed variability of the signal) an explicit correction for the biogenic influence is not needed. More information can be found in the Appendix A.9.

CH_4 emissions

In contrast to the observed location of the CO_2 plume, the CH_4 plume extended further to the southwest over the city limits. Also the XCH_4 signal of Hase et al. (2015) did not follow their XCO_2 pattern due to different sources, and a distinct background could not be observed. Compared to the footprint-corrected inventorial data, the annual CH_4 flux estimate of ~164 ± 54 kt a^{-1} is tremendously larger (factor ~7) than the CAMS-REG estimate, which has only little contribution of the waste sector. However, it agrees better with EDGAR, which considers larger emission amounts coupled to any form of waste treatment (for source partitioning see Table 5.1). According to Saunois et al. (2016), CH_4 produced in wastewater is dependent on the amount of organic content in the water itself. The inventories considered in their study give global emissions from wastewater in the range of 9 to 30 Tg in 2005 (3 to 9 % of global anthropogenic emissions). For the greater area of Berlin, EDGAR states that even 18

% of total emissions are related to wastewater handling and 48 % to solid waste deposition. In London, waste treatment and disposal is the primary source of CH_4 based on the National Atmospheric Emissions Inventory besides natural gas leakage (Pitt et al., 2019). As ethane (C_2H_6) is co-emitted with CH_4 in oil and gas operations, it can be used as a tracer for gas leakages. However, during the $[UC]^2$ research flights no significant variations in the QCLS C_2H_6 data were detected. When comparing total CH_4 emissions from Germany, CAMS-REG is only a factor of 0.4 lower than EDGAR (and both inventories agree for CO_2) as both inventories are scaled to fit to the reported country values. As a result, it is concluded that the waste sector (SNAP 9) in CAMS-REG is most likely underrepresented in the Berlin area either in terms of strength or in terms of spatial distribution, or a combination of both.

5.3.4 MECO(n) simulation results: underestimated and missing CH_4 sources

With the high-resolution numerical model MECO(n) of ~1 km × 1 km the CO_2 and CH_4 mole fractions are simulated based on different tracers for sources as described in Sect. 5.1.2. By comparing the model output to the airborne measurements, it is aimed to better understand the source sectors and regions contributing to the measured pollution plumes. Note that in the MECO(n) model simulations the potential temporal source strength variability (on daily, weekly or seasonal timescales) cannot be captured, as only annual averaged emissions from the prescribed inventories are available.

In a first step GHG mole fractions are simulated based on the local BERLIN inventory to separate the urban emissions (called c-CO_2 and c-CH_4 for “city”, see Table 5.2). Due to the model biases (as discussed below) the applied MECO(n) setup is only able to capture the spatial distributions of the GHG, but is limited in the representation of absolute values. In Fig. 5.9 different perspectives are presented. Panels (a) and (b) show the 2D distribution of simulated column-averaged dry air mole fraction at 13 UTC to illustrate the plume extent. Panel (c) depicts on the right axis the simulated GHG mole fractions (indicated in grey), which have been sampled on-line along the flight track (submodel S4D). Together with the measured GHG enhancements on the left axis, the GHG distribution along the horizontal distance of the flight track is shown. The measured enhancements refer to the upwind mole fractions being subtracted from the observed downwind mole fractions and are indicated in dark red. The average measured wind direction during the flight was 299 ± 27°. The MECO(n) results reflect the prevalent wind direction quite well with 305 ± 36°, therefore the location of the simulated c-CO_2 plume agrees well with the measured CO_2 plume. In addition, the shape of the simulated plume is consistent with observations and also the coherent c-CO_2 mole fractions at all heights. However, the maximum enhancements differ by a factor of ~2. This is either the result from underestimated prescribed emissions, coupled to any form of model biases or a combination of both. Large differences in simulated wind speed (+2.1 m s^{-1}) compared to observations reduce the simulated c-CO_2 enhancements. Furthermore, differences in the simulated BL depth (~600 m lower than observed) influence the GHG dilution within the BL and increase the enhancement, but also affect the plume width. Simulated emissions from the point sources east of Berlin (see Fig. 5.7a), which are reflected by the sharp CO_2 measurement spikes at ~7 km distance (see Fig. 5.6a), are clearly visible at ~52.5 °N and ~13.8 °E, as well as in the simulated c-CO_2 mole fraction along the flight track.

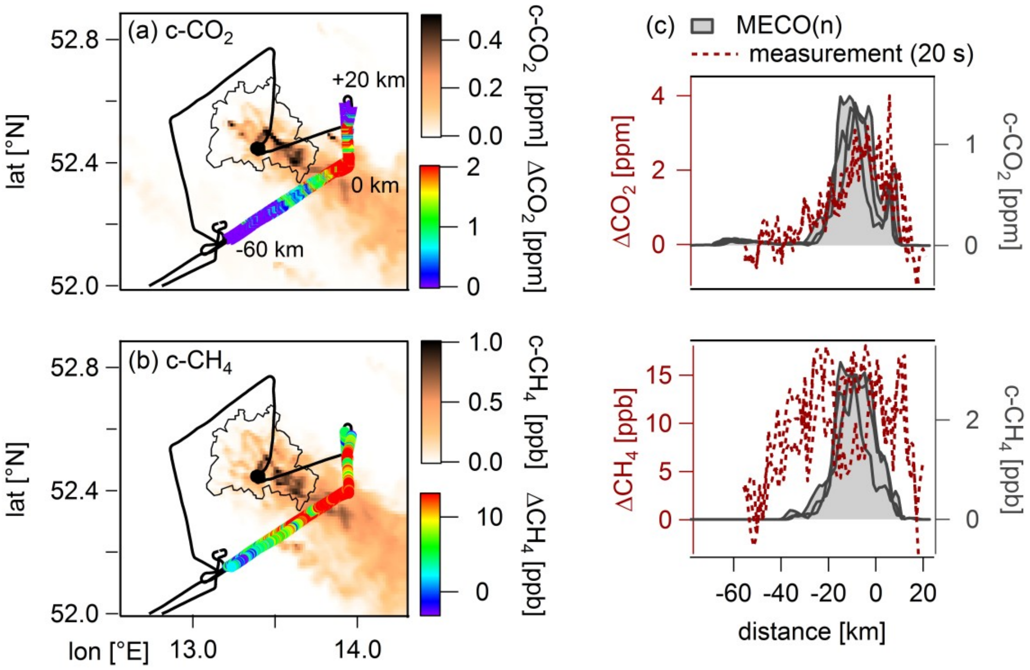

Figure 5.9: 2D distributions of simulated column-averaged dry air mole fractions of (a) the c-CO_2 and (b) the c-CH_4 tracer at 13 UTC of July 20th. The flight route is shown in black and the downwind "wall" is colour-coded according to the measured CO_2 and CH_4 enhancement. Panel (c) presents GHG mole fractions along the horizontal distance (simulated mole fractions in grey; GHG measurements, averaged on the model time resolution of 20 s, in dark red).

With respect to simulated c-CH_4 (grey) and measured CH_4 (dark red), it stands out that simulated c-CH_4 enhancements are far too low (factor of ~5), although the BERLIN inventory is already scaled with a factor of ~4.5 (see Table 5.2). In addition, the observed plume is significantly wider. This implies a huge underestimation of urban source strengths in the BERLIN inventory, or missing CH_4 emissions in the surroundings of Berlin. Thus, a number of different tracers (see Sect. 5.1.2) were implemented in order to investigate the origin of the unexpected missing CH_4 sources, which are required to reproduce the observed CH_4 pattern.

The outer parts of the plume could not be reproduced by the "regional" tracer r-CH_4 (coupled CAMS-REG inventory; not shown), therefore further studies were performed to examine the contribution from emissions of the waste sector to the detected CH_4 plume. Figure 5.10 depicts simulated CH_4 mole fractions from the tracers related to wastewater treatment plants (w-CH_4, panel a), landfills (l-CH_4, panel b) and to the combined tracer t-CH_4 (which is "city" plus "wastewater" plus "landfills", panel c). Largest wastewater facilities (they are sized according to their population equivalent) are located directly outside of the city; smaller facilities are found more frequently in the west and south-west and produce a rather homogenous CH_4 mole fraction distribution field despite their nature of point sources. Simulated CH_4 mole fractions from the landfill tracer indicate more point-like distributions of enhanced CH_4 either from waste-rich dumps (they are sized according to the amount of deposited waste) or from a spatial concentration of several dumps, e.g. seen in the north of Berlin. Figure 5.10c shows the mole fractions from the combined t-CH_4 tracer. As already stated in Sect. 5.1.2 it is not claimed that the emission rate estimate for wastewater and landfills are correct, however, the inhomogeneous CH_4 distribution, resulting from the t-CH_4 tracer, is consistent with the results of Hase et al. (2015) , who report a less uniform and more varying CH_4 background compared to CO_2. The mean mole fraction from the three altitude transects for each tracer (w-CH_4, l-CH_4, and t-CH_4) is shown in Fig. 5.10d along the horizontal distance of the flight route together with the measured CH_4 enhancement (mean of the lower two flight transects only). Although these model results do not directly reproduce the measured CH_4 plume shape, emissions from wastewater plants and landfills broaden and enhance the simulated city wide c-CH_4 plume (see Fig. 5.9c).

As stated in Sect. 5.1.2 agricultural emissions from enteric fermentation and manure management were not implemented explicitly in MECO(n) as their contribution to total CH_4 emissions in the greater Berlin area, according to EDGAR, only amounts to 14 %, compared to 72 % related to the waste sector (landfills, wastewater and solid waste incineration). Roughly 518 thousand head of cattle, the main ruminant animals, were held in 2018 in Brandenburg (*https://agrarbericht.brandenburg.de/abo/de/start/produktion/tierhaltung/).* A comparison of the given administrative districts of main husbandry and the estimated footprint area of potential CH_4 emissions only leads to an overlap of 5-10 % of all animals and was therefore regarded to have a minor impact. The results of the MECO(n) simulation, however, suggest that for a better understanding of the regional CH_4 budget, emission strengths from all these sources need to be experimentally verified by e.g. a ground based observation campaign in the greater region of Berlin.

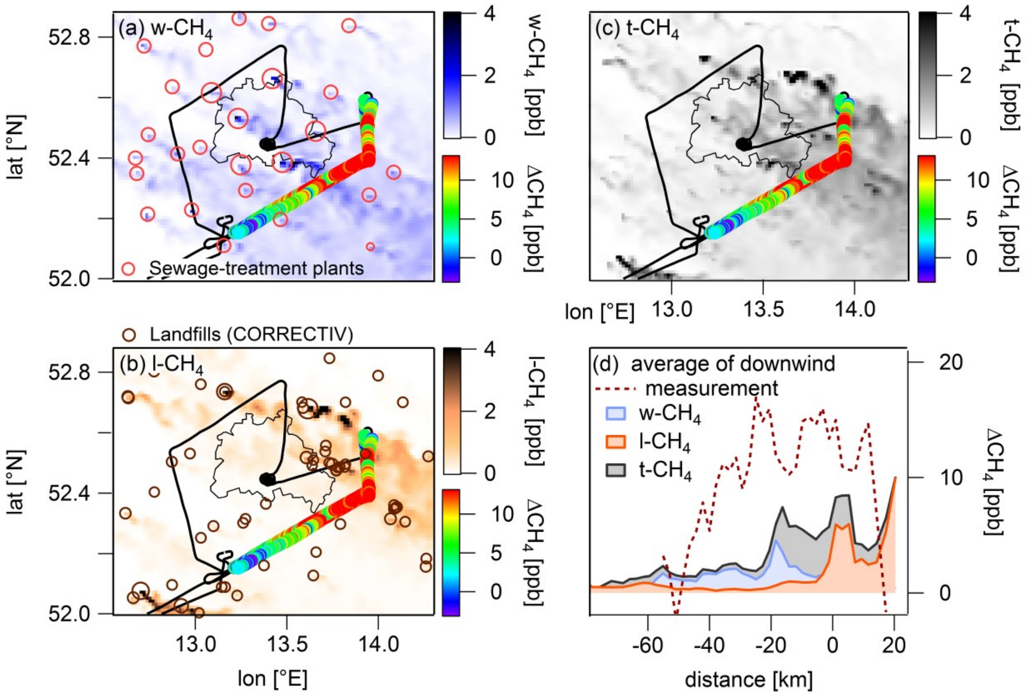

Figure 5.10: 2D distributions of simulated column-averaged dry air mole fractions of (a) the w-CH_4, (b) the l-CH_4, and (c) the t-CH_4 tracer at 13 UTC of July 20th. The flight route is shown in black and the downwind "wall" is colour-coded according to the measured CH_4 enhancement. Panel (d) presents the average GHG mole fractions along the flown horizontal distance. For the simulated mole fractions based on the three tracers (w-CH_4 in blue, l-CH_4 in orange and t-CH_4 in black) all three flight transects are considered. For the averaged measured CH_4 enhancement (dark red) only the lower two flight transects are taken.

5.3.5 GHG variability as observed from tall tower measurements

Within the Berlin area two tall tower measurement stations are located: Gartow, which is roughly 145 km NW of Berlin; and Lindenberg, which is roughly 65 km SE of Berlin. Both belong to the ICOS atmosphere station network (*https://www.icos-cp.eu/observations/atmosphere/stations*). For wind directions from the NW (as prevalent on July 20th) Gartow can be regarded as upwind location and Lindenberg as downwind location with respect to the city.

Hourly CH_4 and CO_2 measurements at both stations are analysed over the period of July 2018 (ICOS RI, 2019). First, GHG mole fractions at Lindenberg are checked for wind directions ranging from 290° to 320° (indicated by the dashed square in Fig. 5.11), i.e. where Berlin lies directly in its upwind. With respect to the two highest sampling heights (40 m and 98 m) there is no signature of higher GHG mole fractions discernible. Hence, Lindenberg is located too far away to track Berlin's urban GHG emissions reliably by tall tower measurements. Second, it is investigated to what extent the upwind (i.e. Gartow) and downwind (i.e. Lindenberg) measurements differ from each other for wind directions from the northeast (not shown). Again, no consistency is found, e.g. sometimes GHG mole fractions are higher at Gartow, sometimes higher at Lindenberg. Hence, to investigate the GHG emissions from the capital Berlin, airborne measurements have proven to be a useful tool.

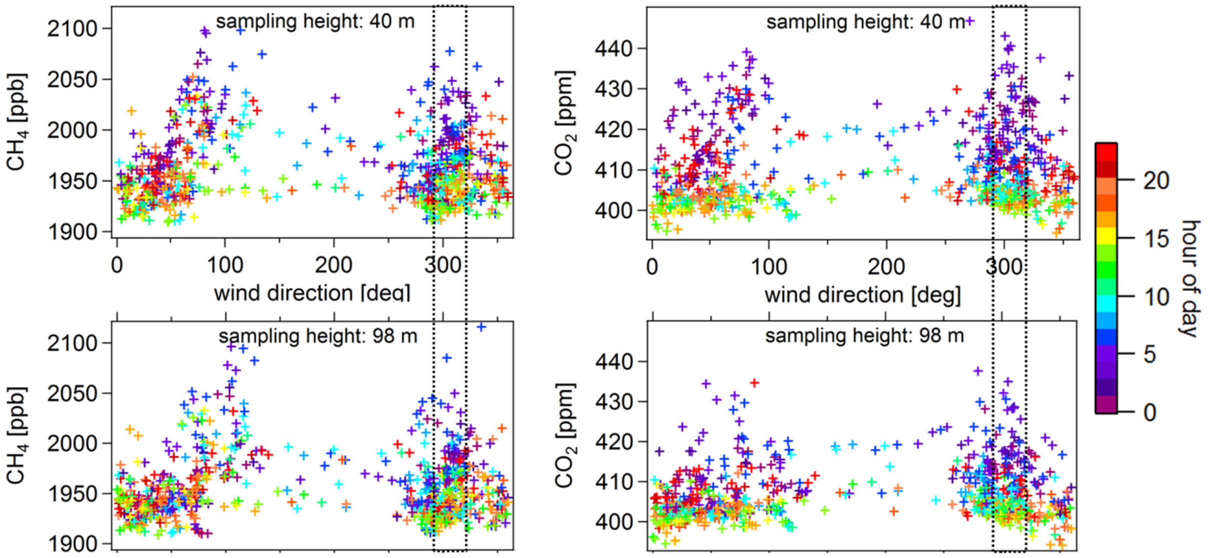

Figure 5.11: Correlation of CH_4 (left panels) and CO_2 (right panels) with wind direction at the tall tower site Lindenberg, downwind of Berlin, for two different sampling heights (40 m and 98 m). The time period between 01st and 31st of July 2018 is covered. Data are retrieved from the ICOS Data Portal (ICOS RI, 2019).

5.4 Greenhouse gas plumes as observed on July 24th

From the results of Sect. 5.3 two hypotheses can be formulated. First, the reported urban CO_2 emissions from Berlin are well constrained, since the simulated c-CO_2 enhancements are in the same order of magnitude as the measured CO_2 enhancements. Second, and in contrast, the reported urban CH_4 emissions are largely underestimated. Based on this single research flight on July 20th it was shown, that simulated c-CH_4 enhancements are dramatically smaller than the measured CH_4 enhancements. To analyse the robustness of this hypothesis in more detail, observations from an additional flight performed on July 24th are analysed and compared with the MECO(n) simulated GHG mole fractions.

5.4.1 Wind situation and HYSPLIT backward trajectories

The time series of the whole flight (~12:10 to ~15:00 UTC) can be found in Fig 5.12a. Due to problems at the beginning with the Picarro instrument, the measurement record starts with ~1 h delay. The flight pattern (see later Fig. 5.13) was constructed similar to the one on July 20th with an upwind transect at the middle of the BL (~796 m) and a vertical profile at the Tempelhofer Feld (~0.3 to ~3.2 km; ascend rate of ~3.1 m s^{-1}). The plume was sampled downwind of Berlin at three different altitudes (494, 827 and 1308 m), which is also indicated by the colour-coded flown horizontal distance in Fig. 5.12a. The sampling hereby started from 0 km distance towards the east (indicated with positive values). Instead of forecasted northern winds (E-W alignment of the flight transects), the wind was blowing from the NNE with 3.3 m s^{-1} on average. To aim for sampling background air, the transects were prolonged towards the NW (indicated with negative distances; determined by restrictions from ATC).

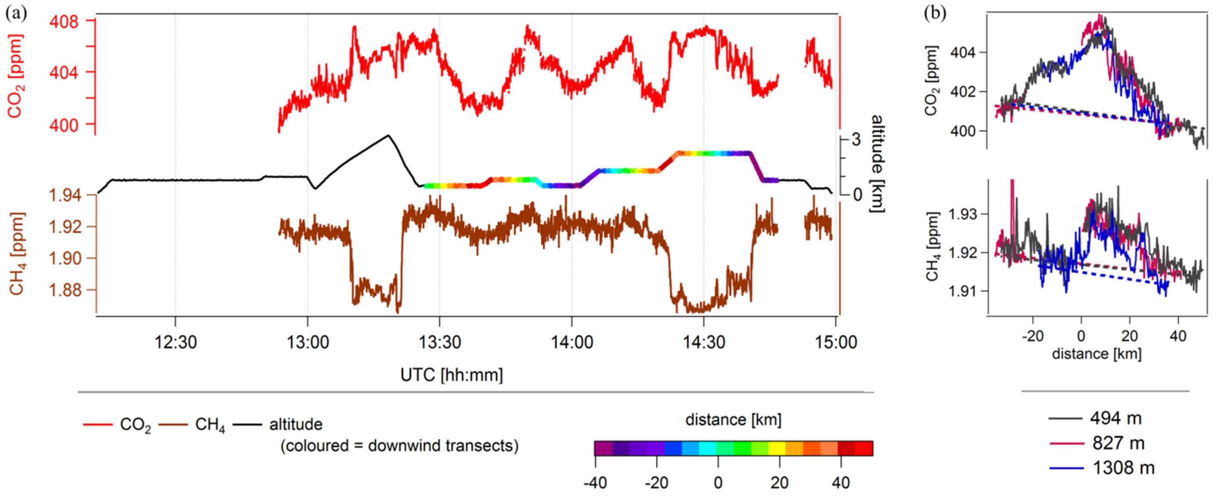

Figure 5.12: (a) Time series of measured CO_2 and CH_4 mole fractions on July 24th. The downwind "wall" is colour-coded according to the flown horizontal distance. (b) Measured GHG mole fractions (segment mean) at three different altitudes within the boundary layer along the flown horizontal distance. The background based on the edges of the flight leg is shown with dashed lines.

The measured CO_2 and CH_4 mole fractions at different altitudes are shown along the flown horizontal distance in Fig. 5.12b. Mole fractions were enhanced above the background by up to 5 ppm CO_2 and 18 ppb CH_4. As seen in the comparable CO_2 concentration at all heights, the BL is generally well-mixed, which is consistent with the meteorological vertical profile (see A.5). Measured CH_4 mole fractions are coherent in the two lower flight transects, however, show a different pattern at the highest altitude (similar to observations on July 20th) with a dip in CH_4 between ~20 and ~30 km. The encountered GHG plume on this day is broader for CO_2 than for CH_4 and can be divided into two parts: a positive correlation between the GHGs east of ~0 km distance ($R = +0.82$) and a slightly negative correlation to the northwest ($R = -0.20$). With respect to the atmospheric background, the dashed lines in panel (b) indicate the linear interpolated background mole fractions based on the edges of the flight track. They are in the eastern part lower than in the western part (~1.5 ppm for CO_2 and ~4 to 6 ppb for CH_4).

It is refrained from estimating GHG fluxes based on the mass balance approach for this second case study, because analyses indicate that due to very low wind speeds emissions accumulated above Berlin during the night and in the morning of July 24th. Steady winds are, however, essential for the mass balance approach. Calm winds during the night and in the morning were recorded by seven ground based measurement stations within and around Berlin (*http://wind.met.fu-berlin.de/wind/archiv/form.php*). The wind speed increased dependent on the location between 6 and 9 UTC. This rise of low level winds (<400 m) in the morning is in agreement with five ascents of a captive balloon system located at the Tempelhofer Feld. Measurements were performed by the DWD within the [UC]^2 project and the data were processed and provided by R. Becker, P. Stanislawsky and M. Koßmann. The average measured wind speed at 08:30 UTC was only 2.2 ± 0.7 m s^{-1}, but was strongly rising to 3.9 ± 0.7 m s^{-1} already at 9:39 UTC. Additional balloon ascents afterwards (at 10:28, 11:44 and 13:12 UTC) show similar and relatively consistent wind speeds (3.3 ± 0.9, 3.8 ± 0.7 and 4.3 ± 0.6 m s^{-1}, respectively). The downwind "wall" is approximately 30 to 40 km downwind of the city centre. With an averaged measured wind speed during the flight of 3.6 m s^{-1}, the air masses would have needed three hours to travel from the city centre towards the flight route. Thus it is uncertain whether the accumulation due to calm winds was already swiped away.

Figure 5.13 displays HYSPLIT backward trajectory calculations being started from the three downwind transects within the BL at 14:30 UTC. Colour-coded is hereby the height of the trajectory. All calculations reach 6 h backward in time. The accumulation of air masses in the western part of the plume is visible (as expressed by their plume age, i.e. the shortened length of the trajectories), being consistent with the observed change in GHG mole fractions. Based on the trajectories, it is obvious that assessing the uncertainty of the background by using upwind CO$_2$ and CH$_4$ measurement data is not applicable. It should be noted that the trajectories do not exhibit a consistent pattern at the different altitudes within the BL. This is however contradictory to the uniformly observed CO$_2$ mole fractions at all heights.

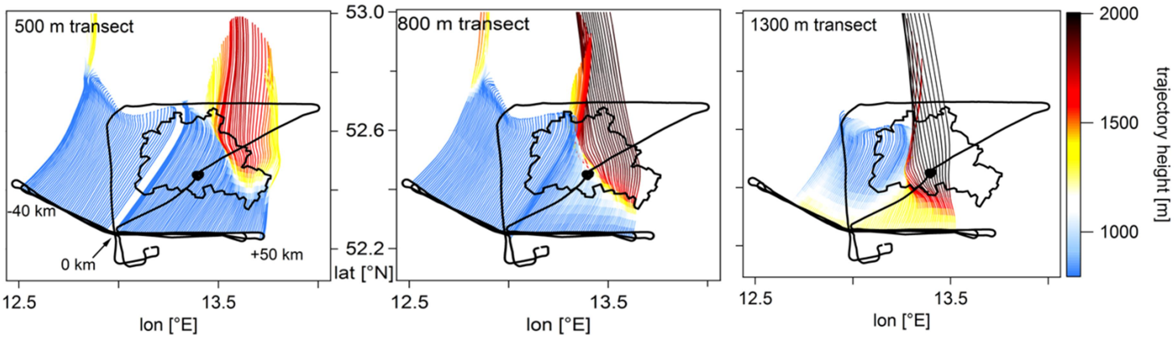

Figure 5.13: Backward trajectory calculations for July 24th. Trajectories were started at 14:30 UTC from the downwind flight track backwards in time for 6 hours. Colour-coded is the height of the trajectory according to its relative position.

5.4.2 MECO(n) simulation results

Despite that the flight on July 24th is not used for the mass balance calculation, it contains valuable information in combination with the MECO(n) simulation results. The flight track is depicted in Fig. 5.14a and b together with the simulated full atmospheric column-averaged dry air mole fractions from the c-CO_2 and c-CH_4 tracer at 14 UTC. The downwind "wall" is colour-coded according to the measured enhancement (here the linear background is subtracted from the observed downwind mole fractions). Figure 5.14a indicates that the simulated c-CO_2 plume only captures the eastern part of the detected plume, although the simulated wind direction is similar to the measured wind direction (+2°). The mole fractions along the flight track are depicted in panel (c) and confirm that the eastern part of the CO_2 plume is well captured by c-CO_2, however, the western part is missing. Neither in the EDGAR inventory, nor in E-PRTR any strong source of CO_2 is present west of Berlin (or within western Berlin), which could explain the observations. Also, in the simulated mole fraction from the r-CO_2 tracer this part of the plume could not be reproduced. The disagreement in the plume shape possibly might also arise from a transport and/or timing bias in the MECO(n) simulation. The time-series of the simulated GHG plume on the 24th of July (see Appendix A.10) shows, that the plume meanders from east to west, i.e. already at 16 UTC the plume is located more in the west. However, the simulated maximum c-CO_2 enhancement of ~2 ppm is 2 to 3 times lower than the measured enhancement of ~5 ppm. MECO(n) simulates a higher BL depth (~200 m) and overestimates the wind speed (+2.6 m s^{-1}), thus leading to simulated GHG mole fractions which are much more diluted within the BL. Although this dilution cannot be properly quantified, it can be deduced that the order of magnitude of simulated c-CO_2 mole fractions is in much better agreement with the measurements than it is the case for CH_4, similar to the results from the flight on July 20th. The lower panel of Fig. 5.14c indicates that the plume structure of c-CH_4 is well simulated, as well as the coherent mole fractions at all heights. The maximum simulated enhancement of only ~4 ppb is, however, heavily underestimated (factor 4 to 5).

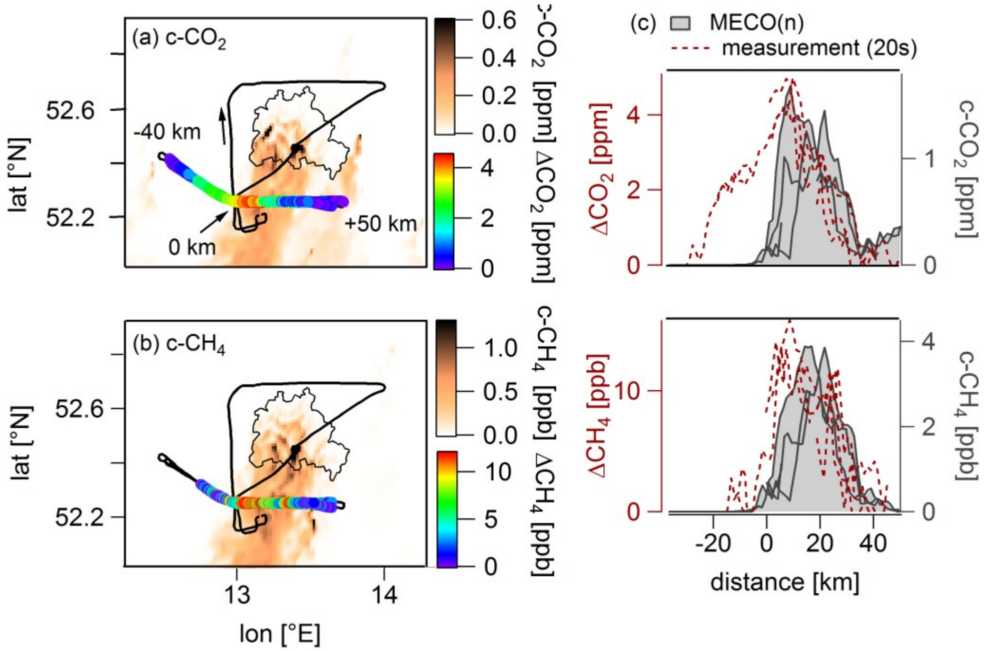

Figure 5.14: Measured and simulated GHG mole fractions on July 24th. Panel (a) and (b) show the 2D distributions at 14 UTC of the simulated column-averaged dry air mole fractions of the c-CO_2 and c-CH_4 tracer, respectively. The flight route is drawn in black and the downwind "wall" is colour-coded according to the measured CO_2 and CH_4 enhancement. Panel (c) presents GHG mole fractions along the horizontal distance with simulated mole fractions in grey and observed GHG mole fractions in dark red, which are averaged to the models resolution of 20 s.

5.4.3 Co-emissions of nitrogen dioxide

According to Reuter et al. (2019) nitrogen dioxide (NO_2) is, together with CO_2, released during the high-temperature combustion of fossil fuels. But compared to CO_2, NO_2 has a much shorter lifetime of only several hours and lower atmospheric background mole fractions. Hence, recently emitted NO_2 stands out from the ambient signal by several orders of magnitude in the vicinity of sources and can therefore be used as a tracer of recently emitted CO_2. The BERLIN inventory likewise consists of individual area, point and line sources of NOx (=NO_2 + NO), which were projected on a 0.01° × 0.01° longitude-latitude grid (~1 km resolution). Therefore, c-NOx emissions can be simulated with the MECO(n) model and predicted enhancements downwind of Berlin along the $[UC]^2$ research flight tracks are found to be very similar in their pattern to the simulated c-CO_2 enhancements ($R = 0.98$).

Within the scope of the $[UC]^2$ measurement campaign, the airborne research flights were coordinated with the daily overpass time of the Copernicus Sentinel-5 Precursor (S5P) satellite at ~11:30 UTC. The TROPOMI (TROPOspheric Monitoring Instrument) spectrometer on board provides vertical column densities of trace gases like tropospheric NO_2 and aerosols with a fine spatial resolution of 3.5 × 5.5 km^2 and is therefore able to resolve small scale structures, such as pollution plumes from e.g. power plants or cities (TROPOMI ATBD, 2019). The satellite-based NO_2 observations, provided by T. Erbertseder (DLR, Earth Observation Centre), are therefore also compared to the airborne observations.

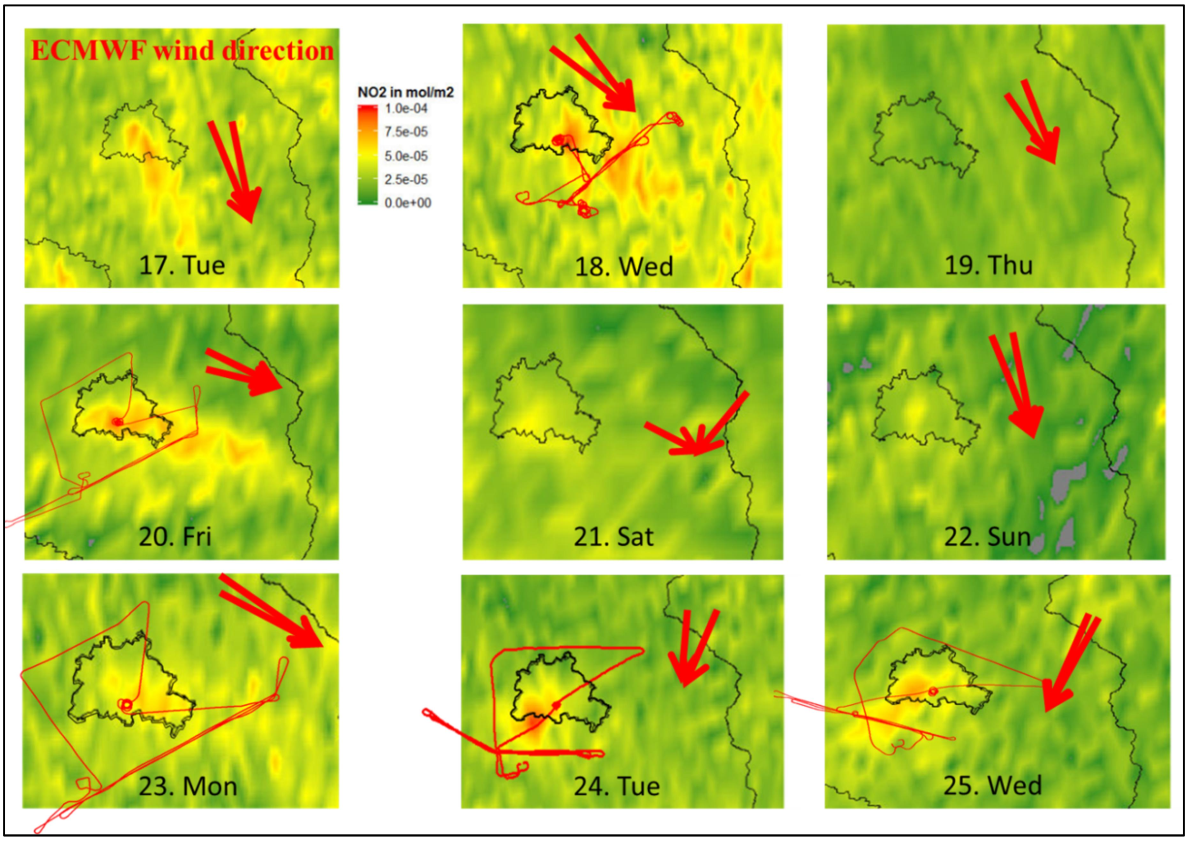

Figure 5.15: Tropospheric NO_2 observations at ~11:30 UTC from S5P for each day of the $[UC]^2$ campaign period, provided by T. Erbertseder (DLR, Earth Observation Centre). Superimposed are the research flight tracks and the range of ECMWF wind direction is indicated by red arrows.

The general spatial distribution of the enhanced tropospheric NO_2 column densities is in agreement with the ECMWF wind direction during the campaign period, see Fig. 5.15. On July 19th and 22nd the cloud cover probably hampered the detection of the urban plume, as well as the large wind variability on July 21st. With respect to July 24th, a prominent NO_2 signal is discernible in the southwest of Berlin, just outside the city boundary. The downwind flight transects are probed two to three hours after the satellite overpass, hence the direct comparison of the plume location and structure is hampered. However, since the location of the urban plume can be identified in the TROPOMI NO_2 data, a direct temporal collocation of the satellite-based and airborne measurements should be possible. Then, the extent of the satellite detected NO_2 plume can be taken to estimate the edges of the CO_2 plume as it is anticipated for the CO2M mission (Kuhlmann et al., 2019b).

5.5 Concluding remarks

This study contributes to the sparse knowledge of GHG emissions from European cities by studying the CO_2 and CH_4 plumes downwind of the German capital Berlin and estimating emission rates using a mass balance method. Emission inventories available for Berlin (EDGAR, CAMS-REG and BERLIN) differ by a factor of ~1.4 for CO_2 and by a factor of ~8 for CH_4.

In July 2018, in situ CO_2 and CH_4 measurements were performed aboard the DLR Cessna Grand Caravan in the outflow of Berlin to assess the urban GHG emissions from the city. The measurements showed that even with sensitive airborne in situ measurements it remains challenging to detect Berlins GHG emissions, which fits to the observations reported by Hase et al. (2015) who used ground-based FTIR spectrometer measurements, and by Kuhlmann et al. (2019a) who used synthetic CO_2 satellite observations. The detection and separation of the urban GHG plume, however, was possible during two research flights performed on July 20th and July 24th. GHG enhancements were observed at different heights of a well-mixed and efficiently capped boundary layer. Using the mass balance approach, a CO_2 flux of $1.39 \pm 0.76\,\mathrm{t\,s^{-1}}$ was obtained for the flight on July 20th, which is in the same order of magnitude as the numbers given in the presented inventories. Sampled air masses homogenously passed the city of Berlin prior to the measurement, where they were enriched with emissions. Simulated citywide CO_2 mole fractions agree well with the CO_2 measurements in location and shape, while a quantitative comparison of simulated and measured maximum enhancements is hampered due to deviations in the wind speed and BL depth.

For the same flight a CH_4 mass flux of $5.20 \pm 1.70\,\mathrm{kg\,s^{-1}}$ was calculated, which is almost two times larger than the highest reported value in the inventories (i.e. the footprint-corrected estimate from EDGAR). Simulated citywide CH_4 mole fractions were substantially lower than observed, indicating an underrepresentation of urban emissions in the local BERLIN inventory. The CH_4 plume (in contrast to the CO_2 plume) partly originated also from outside of the Berlin city boundary, hence, emissions from sources surrounding the city, which are missing in the investigated inventories, contribute to the observed CH_4 pattern. Such sources might include emissions from wastewater treatment plants and illegal landfills. However, for a clear attribution, a verification of these emissions is required by ground-based measurements and/or further airborne in situ observations.

Although Berlin can be considered as a relatively isolated city (especially for the densely populated region of Central Europe), the need for precisely determining the inflow GHG mole fractions and the natural variability of the background mole fraction is demonstrated in order to suitably apply the mass balance approach. One possibility to improve the estimation of the background is to sample the upwind and downwind transects in a Lagrangian manner, e.g. also using two aircraft simultaneously. To further improve knowledge on the regional CH_4 budget in the greater Berlin area, subsequent measurement campaigns are needed with a special focus on emission sources located outside the city boundaries. Furthermore, different seasons should be investigated to reflect the seasonal cycle of the emissions.

This study showed that bottom-up CO_2 and, in particular, CH_4 emission inventories are subject to large uncertainties at the city scale, even for major cities in highly developed countries like Germany, and that top-down emission estimates are an invaluable tool to verify emission estimates and to reveal missing sources in emission inventories.

6 Studying the tropospheric methane distribution of Europe and Asia on the mesoscale to synoptic scale

While Chapter 5 focused on the analysis of urban GHG emissions using local-scale measurements around Berlin, this chapter investigates the distribution of CH_4 and CO_2 on larger spatial scales - from hundreds to thousands of kilometres on two continents: Europe and Asia. The corresponding observational data were collected within two airborne field campaigns, namely EMeRGe-Europe and EMeRGe-Asia. The mission's acronym already reflects its overarching scientific mission goal: Effect of Megacities on the transport and transformation of pollutants on the Regional to Global scales. The specific research questions (see also Sect. 1.2) on the larger spatial scale analysis will be addressed:

RQ 5) Can signatures of urban and other emission sources be detected by airborne measurements in the regional scale distribution of CH_4 in Europe and Asia?

RQ 6) How do the regional CH_4 emission distributions in Europe and in Asia compare with each other and with previous observations?

This chapter starts with an introduction to anthropogenic CH_4 and CO_2 emission inventories for the European and Asian countries covered by the EMeRGe mission (Sect. 6.1). The implementation of various emission tracers in the MECO(n) model setup is described as well. An overview of both EMeRGe campaigns and a classification of flights are introduced in Sect. 6.2. Observations from Europe and Asia are presented in Sect. 6.3 and 6.4, respectively, including an analysis with focus on the above given research questions. In Sect. 6.5 the results with respect to previously published studies are discussed, similarities and differences in the vertical GHG distribution of both measurement regions are described and findings of the EMeRGe observations are summarised.

6.1 European and Asian greenhouse gas emissions

6.1.1 Comparison of reported anthropogenic emissions and their trend over time

Consistent emission inventories are crucial to identify and assess emission reduction policies (Crippa et al., 2019). This section introduces CO_2 and CH_4 emission trends since the beginning of the century from selected countries, which were in the focus of the EMeRGe campaigns. The emission trends are based on the bottom-up inventories listed below:

(a) Two different versions of the *global* gridded emission inventory EDGAR: v4.3.2 covers the decade until 2012 (Janssens-Maenhout et al., 2019) and v5.0 presents up-to-date emission distributions until 2018 for CO_2 and 2015 for CH_4 (Crippa et al., 2019); both have a resolution of $0.1° \times 0.1°$.

(b) Two *regional* inventories cover Europe and Asia, respectively: CAMS-REG v3.1 with a resolution of 0.05° × 0.1° (Granier et al., 2019) and REAS (Regional Emission Inventory in ASia) v2.1 with a resolution of 0.25° × 0.25° (Kurokawa et al., 2013).

(c) CO_2 emissions from the Global Carbon Atlas, a community platform providing carbon data based on various scientific institutions and scientist from all over the world (*http://www.globalcarbonatlas.org/en/content/project-overview*).

Regional and urban emissions for selected case studies are presented in the respective subsections of Sect. 6.3 and 6.4. The available CO_2 inventories for both continents are relatively consistent for specific countries as depicted in Fig. 6.1. For each individual European (and Asian) country the range of the reported emissions is between 0.1 and 11 % (0.1 and 30 %) of the mean value. The given values in the following refer to EDGAR v5.0 since it is the most recent one and provides information for both continents until 2018. Germany is the largest CO_2 emitter in Europe with ~750 Mt CO_2 in 2018. Its emissions are more than twice the emissions from the UK. Although the total population in Germany is only ~20 % larger than in the UK (UN, 2019), total energy consumption is roughly 40 % higher (Enerdata, 2019), and especially the share of using coal is more dominant (22 % vs. 5 % of total energy consumption), which might explain the overall higher CO_2 emissions. All countries, however, show a decreasing trend in emissions over time mostly because energy sources changed from coal and liquid ff to renewables (Crippa et al., 2019). The most significant emission reduction since 2000 occurred in the UK (-32 %); mainly due to reductions in the emission sectors “public electricity and heat production” and “manufacturing and industries” (see Appendix A.11). The smallest emission reduction is reported for the Benelux area (-10 %). The emission minimum apparent in all states in 2009 is associated with the Great Recession and the reduced economic activity. In 2018, CO_2 emissions per capita, are highest in the BeNeLux countries with 10 tons per person (p^{-1}) and year (a^{-1}) and lowest in France ($5\,t\,p^{-1}\,a^{-1}$).

In Asia (Fig. 6.1b), China and Hong Kong (HK) exceed all other countries by far, with almost 10 (and 15) times higher CO_2 emissions compared to Japan (and Germany). Han et al. (2020) evaluated nine global and regional ff CO_2 emission datasets of China. Despite large uncertainties and discrepancies in the emissions, a mean value for 2016 is given with 9.8 ± 0.6 Gt $CO_2\,a^{-1}$, which is ~10 % lower than the EDGAR v5.0 estimate of China (~10.9 Gt). While CO_2 emissions slightly decrease in Japan (-3 %), all other countries show an increasing trend (strongest in China and HK +205 %, weakest in Taiwan +44 %) due to their emerging economies and an increase in ff consumption (Crippa et al., 2019). The per capita emission is lowest in the Philippines ($1\,t\,p^{-1}\,a^{-1}$) and highest in Korea ($27\,t\,p^{-1}\,a^{-1}$), hence the variability between the countries is more pronounced than for Europe.

Country-specific CO_2 emissions and trends, as reported by the different inventories, were shown to be consistent among each other. As presented in Sect. 2.2.1 bottom-up inventories rely on activity and technology mix data. Total CO_2 emissions are mostly estimated based on national ff consumption data, which are well monitored. Further, the emissions themselves depend mostly on the total mass and carbon content of the fuel and less on the type of combustion (Janssens-Maenhout et al., 2019). Hence, CO_2 emissions from the EU15 countries in EDGAR v4.3.2 are estimated with a standard deviation (2σ) of only 5 % (Janssens-Maenhout et al., 2019). In contrast, it increases for CH_4 emissions to 32 %. CH_4 has much more diverse emission sources than CO_2, which require different emission factors, detailed information on, e.g. types of fermentation or the composition of organic matter, and various proxies in the inventories.

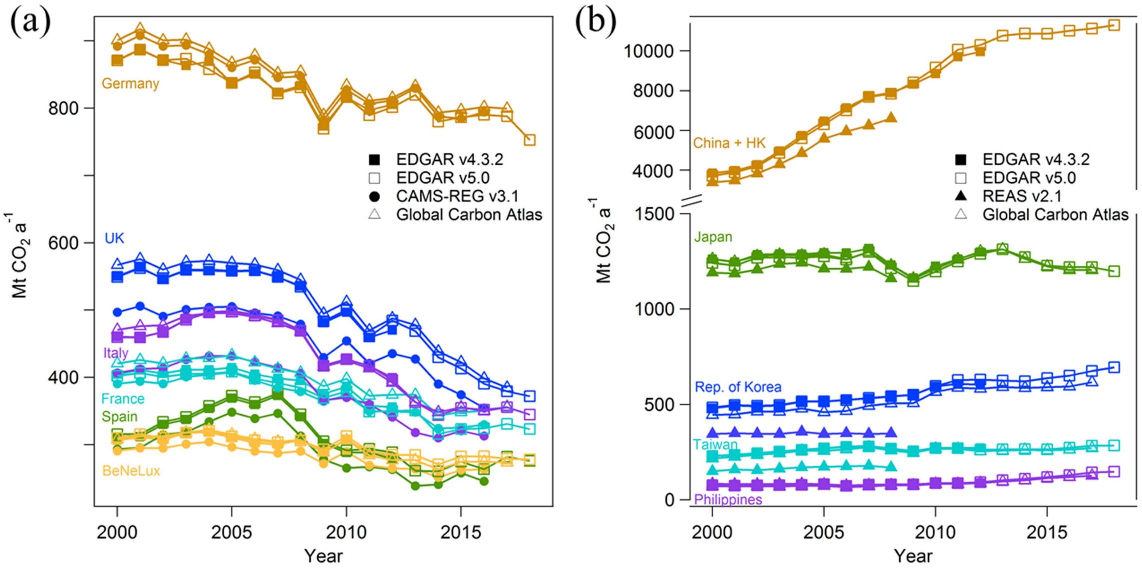

Figure 6.1: CO_2 emissions in Mt per year for selected countries in (a) Europe and (b) Asia between 2000 and 2018 (HK: Hong Kong). Note the split CO_2 axis in panel (b). EDGAR data are retrieved from *https://edgar.jrc.ec.europa.eu/overview.php?v=432_GHG* and *https://edgar.jrc.ec.europa.eu/overview.php?v=50_GHG*; CAMS-REG and REAS data from *https://eccad3.sedoo.fr/*; and Global Carbon Atlas data from *http://globalcarbonatlas.org/en/CO2-emissions*.

With respect to CH_4 (Fig. 6.2), the different inventories greatly differ among each other for some countries, not only in the absolute values but also in the trend curves. This is most evident for the UK and Germany. EDGAR v5.0 emissions in 2012 are not only ~1.6 (for the UK) and ~1.2 (for Germany) times higher than in v4.3.2, but they also show much more variability over time. The more recent version uses new spatial proxies to distribute emissions dependent on urban and rural population (Pesaresi et al., 2019), which might be introducing such large deviations. For the Benelux region, however, both EDGAR versions are consistent, and CAMS-REG is a factor of ~1.3 lower. These facts highlight the need for dedicated measurement campaigns, as analysed in this thesis, to improve knowledge on the behaviour of CH_4 emissions on both continents, Europe and Asia. As for EDGAR v5.0, the country that emits the highest amount of CH_4 in Europe in 2015 is the UK (panel a), with dominant emissions from “solid waste disposal on land” (see Appendix A.11). Except for Spain, where emissions are relatively constant (+3 %), all other countries show a decreasing trend between 2000 and 2015, with the largest emission reduction reported in the UK (-30 %) and lowest in France (-12 %). The emissions per person range from 27 kg p^{-1} a^{-1} in Italy, to 64 kg p^{-1} a^{-1} in the UK.

In Asia (Fig. 6.2b), China with HK is emitting the most CH_4 and is characterised by the strongest increase (+38 %), especially due to rising “fugitive emissions from solid fuels”. Although China’s government has been regulating CH_4 emissions from coal mining since

2010 by either utilizing or flaring the gas, a recent study using GOSAT observations suggests that the impact is low and that CH_4 emissions are still increasing (Miller et al., 2019). Emissions from Korea and Taiwan are relatively stable (±0.5 %), while they decline in Japan (-10 %). Emissions per person range from 16 $kg\,p^{-1}\,a^{-1}$ in Japan, to 55 $kg\,p^{-1}\,a^{-1}$ in Korea, hence are lower compared to the emissions per person in Europe.

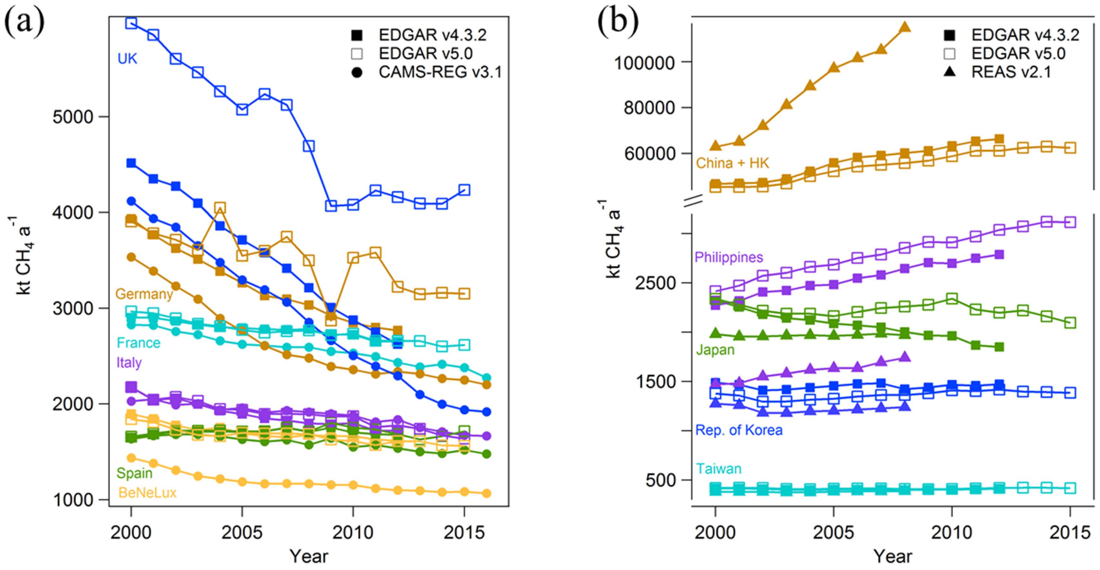

Figure 6.2: CH_4 emissions in kt per year for selected countries in (a) Europe and (b) Asia between 2000 and 2016 (only until 2015 for Asia); HK: Hong Kong. Note the split CH_4 axis in panel (b). Data sources same as in the caption of Fig. 6.1.

6.1.2 Emission input for MECO(n) simulations

For EMeRGe-Europe the chemistry climate model MECO(n) (see Sect. 3.2) simulates trace gas mole fractions based on three different input options as discussed below. They are run in two simulations but are subject to the same dynamics. In order to compare the output with the airborne observations, the tracers have been on-line sampled along the flight tracks.

The *first simulated CH_4 tracer* is initialised from gridded CH_4 emissions. Annual averaged CH_4 emissions from EDGAR v5.0 for the year 2015 are used with a resolution of 0.1° × 0.1°. The input for the *second simulated CH_4 tracer* is provided by the RCP8.5 (Representative Concentration Pathway) scenario. Such scenarios are used to evaluate the state of the climate based on different future perspectives, taking into account trends in, e.g., technology, energy, and land use patterns, as well as emissions of GHG and air pollutants (van Vuuren et al., 2011). The 8.5 scenario in the IPCC (Intergovernmental Panel on Climate Change) Fifth Assessment Report assumes a moderate technological change, but high energy demand and high GHG emission rates, leading to a radiative forcing that exceeds 8.5 $W\,m^{-2}$ in the year 2100 (Riahi et al., 2011). These emission scenarios do not provide gridded emissions, but zonal averaged mole fractions of CH_4. In MECO(n), CH_4 is relaxed toward these values at the ground level. For both simulated tracers basic gas-phase chemistry is considered according to the atmospheric chemistry module MECCA (Module Efficiently Calculating the Chemistry of the Atmosphere; Sander et al., 2005). Finally, *so-called auxiliary city tracers* are implemented in the model setup. These are chemically inert (exponential decay, mean lifetime of 25 days) and represent point sources with identical, but artificial, emissions in each of the 17 major European city centres (London, Paris, Brussels, Milan, Venice, Essen, Barcelona, Split, Madrid, Hamburg, Stuttgart, Berlin, Prague, Marseille, Rome, Munich and Naples). Their purpose is to easily identify emissions coming from the city centres.

6.2 Overview of the conducted EMeRGe missions in Europe and Asia

The EMeRGe missions were coordinated by the University of Bremen and aim to investigate the transport of emission plumes from Major Population Centres (MPCs) as well as the transformation of their chemical composition. EMeRGe hypothesises that the transport, dispersion and transformation of MPC emission plumes are influenced by the nature of the local emissions itself, by the prevalent meteorology and topography, as well as by photochemical oxidation processes (Burrows et al., 2016). Therefore, the campaign was, to a large extent, tailored on short-lived species downstream of the MPCs.

6.2.1 Scientific payload

The German research aircraft HALO was used to conduct the research flights. It is a modified Gulfstream G550 with an exceptional long range of up to 10 000 km (or more than 10 flight hours) and provides with its large payload capacity a unique measurement platform to observe many atmospheric species simultaneously (HALO, 2006).

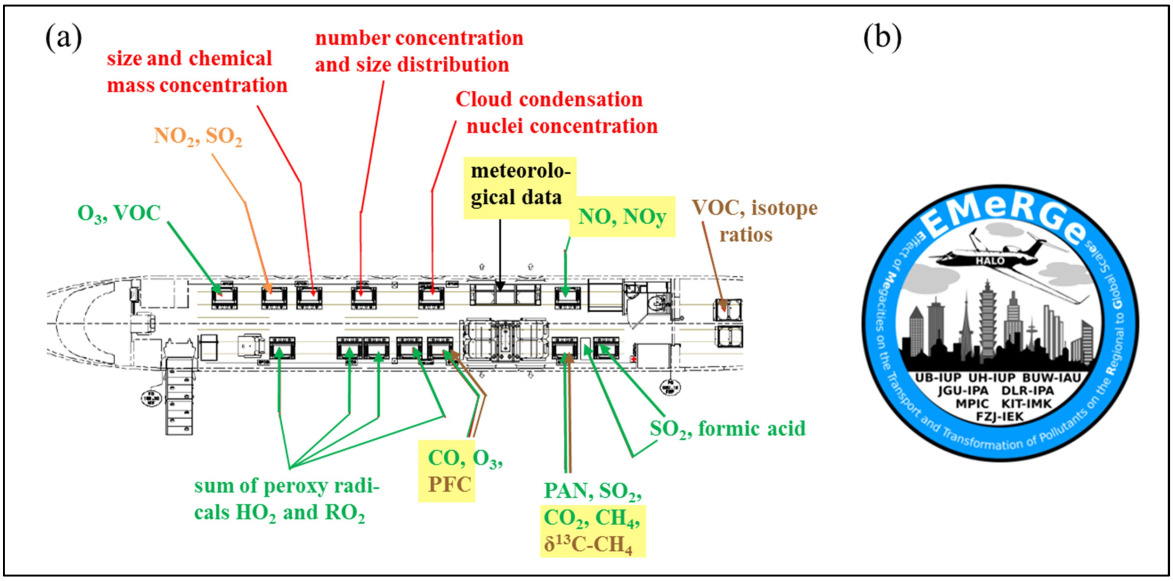

Figure 6.3: (a) HALO cabin layout with the measured species aboard the aircraft. For a detailed list of the corresponding instruments and the principal investigator, see Appendix A.12. (b) EMeRGe logo; both taken and adapted from University of Bremen (2020).

The cabin layout was similar for both EMeRGe missions and determines the location of the scientific instruments on board. The measured species are shown together with the campaign logo in Fig. 6.3. The scientific payload covers in situ instruments to observe gas phase species (green), aerosols (red) and meteorological data (black), as well as air samplers (brown) and a remote sensing instrument (orange). A detailed summary of corresponding measurement instruments, their acronyms and the responsible principal investigator are listed in the Appendix (A.12). The airborne CH_4 and CO_2 measurements, obtained with the DLR Picarro instrument, are marked in yellow. Further species, which are discussed in the context of the GHG measurements, are highlighted as well. The following species are subject to individual PhD theses of EMeRGe colleagues (all in preparation): VOC (E. Förster, KIT), slant column densities of NO_2 and SO_2 (K. Bigge, University of Heidelberg), aerosol size and chemical mass concentration (K. Kaiser, MPI), aerosol number concentration and size distribution (J. Wolf, DLR-IPA) as well as SO_2 and formic acid (L. Eirenschmalz, DLR-IPA).

6.2.2 Classification of flights

The flight tracks of both missions are depicted in Fig. 6.4. HALO mainly flew at low altitudes to capture the urban emission plume within the atmospheric boundary layer (BL) or in the lower troposphere. Downwind of the MPCs "shuttles" were flown, i.e. repeated flight transects at different stacked altitudes.

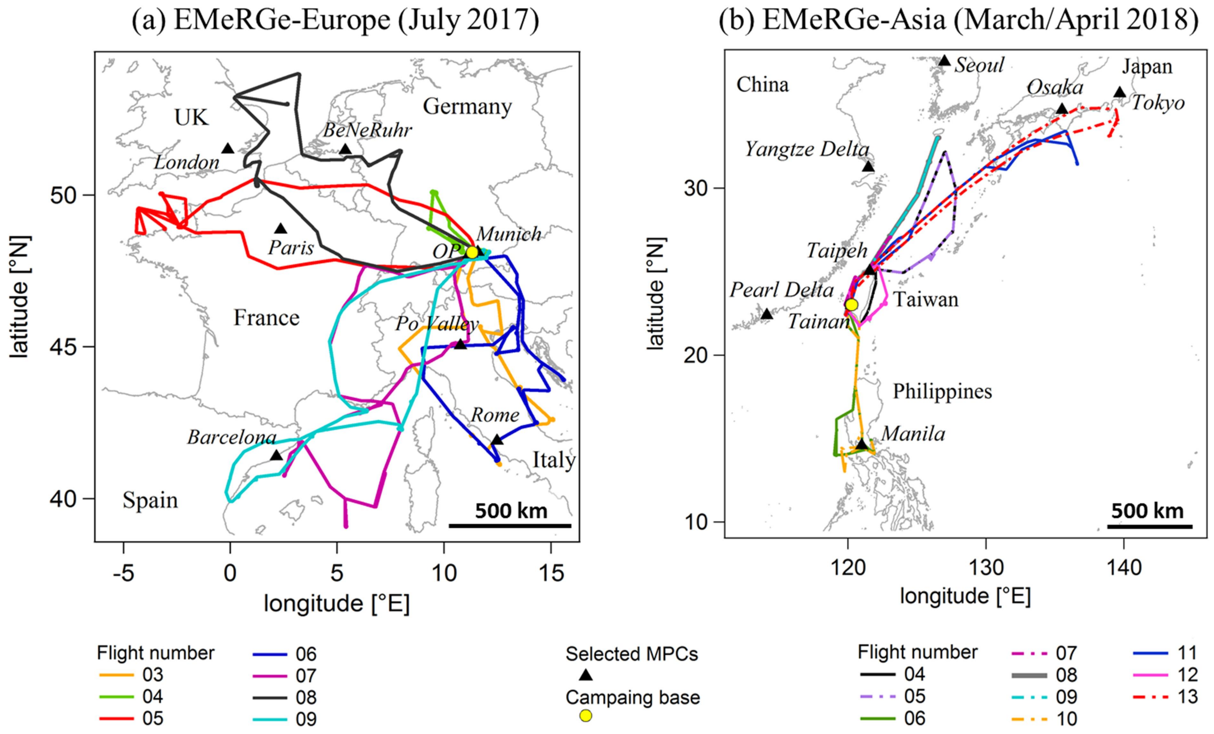

Figure 6.4: HALO flight routes of the (a) European and (b) Asian EMeRGe mission in July 2017 and March/April 2018, respectively. Yellow dots mark the aircraft base and black triangles the selected MPCs.

The European measurement campaign (Fig. 6.4a) took place in summer 2017 from July 11th to 28th from Oberpfaffenhofen (yellow dot near Munich) in Germany. Note that flights 01 and 02 were test flights, thus the research flights are numbered 03 to 09. For the seven performed research flights (~50 flight hours) Table 6.1 lists the target region, the approximate distance from the flight transect to the target region, the flight altitude, the time of sampling and the flight number. Pollution plumes were sampled at a variety of distances ranging from directly being in the target area (e.g. across the BeNeRuhr area, F08) to flying downwind at distances between 90 km (e.g. Barcelona, F07) to more than 400 km (e.g. London in the English Channel, F05). Flight altitudes were between 500 m and 5 km. Flight times extended from the morning until the late afternoon. A quasi-Lagrangian approach was performed e.g. downwind of Rome (towards the coast of Croatia, F06) and Barcelona (towards Sardinia, F07).

Table 6.1: Overview of selected EMeRGe-Europe flight transects according to their target region. The table further lists the rough distance to the source, flight altitude and time of downwind transects, as well as the flight number. The star (*) denotes the urban emissions discussed in Sect. 6.3.

Target region	**Distance to source [km]**	**Flight altitude [km]**	**Flight time [UTC]**	**Flight number**
London*	~150 - ~250	0.7 - 1.3	10:00-12:45	08
London	~220 - ~420	0.5 - 2.6	12:00-16:30	05
BeNeRuhr*	across the area	1.0 - 2.5	12:45-14:15	08
Po Valley	across the valley	1.0	15:15-15:30	03
Po Valley	along the valley, ~100 and ~160	0.8, shuttles (0.5, 1.6, 3.2 and reverse)	09:30-12:00	06
Barcelona*	~90 and ~300	two shuttles (1.6, 0.5)	12:45-13:30 and 14:00-14:45	07
Paris	~130	2.3	17:00-17:30	05
Paris	~100	2.2	08:45-09:15	08
Rome	~200	shuttle (4.9, 3.6, 1)	13:30-14:45	03
Rome	~200 and ~350	shuttles (3.2, 1.6, 0.5 and reverse)	14:15-16:15	06

The EMeRGe-Asia campaign was conducted in spring 2018 between March 10th and April 9th from Tainan (Taiwan, yellow dot in Fig. 6.4b). In total, 10 flights (~80 h) were performed to analyse the pollution plumes of MPCs in China (Beijing, Yangtze River Delta, Pearl River Delta), Japan (Osaka, Nagoya, Tokyo), Taiwan (Tainan), Republic of Korea (Seoul) and the Philippines (Manila). Because of restrictions to enter the Chinese airspace, flight patterns were mainly planned above the sea. Table 6.2 gives, similar to Table 6.1, an overview of the ten performed local research flights (transfer flights from Europe to Asia are marked with 01 to 03 and 14 to 16). The flight tracks in Asia, compared to Europe, cover a much larger area with respect to the flight distance itself and with respect to the distance to the source. While the European mission covers an hypothetical map of ~1500 km × 1500 km, the Asian mission extends to about ~2500 km × 2500 km. Except for Manila (F06) and sources along the western coast of Taiwan (all flights), the pollution plumes were sampled at distances greater than 500 km away from the source, mainly at flight altitudes between ~300 m and ~5 km.

Table 6.2: Overview of selected EMeRGe-Asia flight transects, similar to Table 6.1. The star (*) denotes the urban emissions discussed in Sect. 6.4.

Target region	Distance to source [km]	Flight altitude [km]	Flight time [UTC]	Flight number
Mainland China	>1000	5.1	06:50-07:20	04
China (HK region)	~1000	4.7	05:40-06:00	09
Yangtze River Delta	~500	0.3, 0.9, 0.1	04:20-06:00	08
Yangtze River Delta	~1000	0.9	01:20-02:00	14
Manila*	~100	1.3, 1.5, 1.7	02:30-03:50	06
Cambodia	>500	1.6 and 4.8	05:10-06:00	03
Korea	>500	3.1	01:40-02:10	09
Japan	~500 <500	2.0 1.9	01:40-01:50 04:10-04:40	11
Coast of Taiwan*	<50	0.5-4.6	00:00-10:00	all

The flight patterns of both campaigns were tailored to the needs of studying transport and chemical processes of short-lived species downstream of MPCs. Short-lived species are transformed in the atmosphere within seconds (e.g. OH; Heal et al., 1995), several hours or days (e.g. SO_2; Seinfeld and Pandis, 2016) due to chemical reactions and removal processes. GHG remain due to their long atmospheric lifetime of years to several decades and build up background mole fractions of substantial magnitude (see Sect. 2.1.2). Therefore, it is especially relevant for GHG to perform measurements upwind of a target region (see Berlin case study, Sect. 5.3.2). For the majority of flights, except Barcelona (F09), Rome (F03, 06) and Manila (F10), however, upwind sampling of the atmospheric composition was not possible due to ATC restrictions. The different lifetimes also determine how far downwind a pollution plume is sampled. Short-lived species, as long as they are enhanced above the negligible background by several orders of magnitude, are still detectable at large distances. GHG are also mixed with the background air, but the enhancement magnitude diminishes much faster and therefore measurements closer to the source are needed. EMeRGe focused on several target regions across whole Europe and SE Asia but specific MPCs were never sampled more than twice. In combination with HALO being a large aircraft, the flight routes were not flexible enough to react ad hoc on changes observed in the atmospheric mole fractions measured aboard the aircraft due to restrictions of the submitted flight plans from various ATCs. Hence, sufficient downwind sampling to capture the whole vertical and horizontal extent of the urban plumes was hampered in many cases.

Although this does not permit a quantitative analysis similar to the case study of Berlin (see Chapter 5), the comprehensive data set on the two continents allows studying the impact of urban GHG emissions on the regional to synoptic-scale GHG budget. In Sect. 6.3 the observations of EMeRGe-Europe are discussed in the context of identifying the urban plume from London and the BeNeRuhr area (F08) as well as from Barcelona (F07), both are marked with a star in Table 6.1. In addition, a distinct biomass burning plume is compared to the observed urban emission plumes, and isotope measurements of δ^{13}C reveal insight into possible CH_4 sources. Observations of EMeRGe-Asia are presented in Sect. 6.4. The urban plume from Manila (F06) as well as two other types of prominent pollution events encountered during the flights are discussed: Distinct GHG plumes with a horizontal extent of more than 200 km were observed in the free troposphere (F04, 05, 08, 09) and narrow GHG peaks with a horizontal extent of less than 50 km were frequently distinguishable at Taiwan's west coast at lower altitudes (observed during almost all research flights). In addition to the GHG measurements, simultaneous observations of CO (M. Lichtenstern), nitrogen oxide (NO) and the sum of all reactive nitrogen species (NO_y; H. Ziereis and P.Stock) are used together with results from the regional CO-tagging by HYSPLIT (H_CO; Sect. 3.3) and from MECO(n) (Sect. 3.2).

6.3 Observations during EMeRGe-Europe in summer 2017

The EMeRGe-Europe mission was conducted in July 2017. According to the report on the European State of the Climate 2017 (Copernicus, 2018), global average surface temperatures were 0.5 °C warmer than the climatological mean (1981 to 2010), ranking the year 2017 on 2nd place (after 2016) of the warmest years on record[6.1].

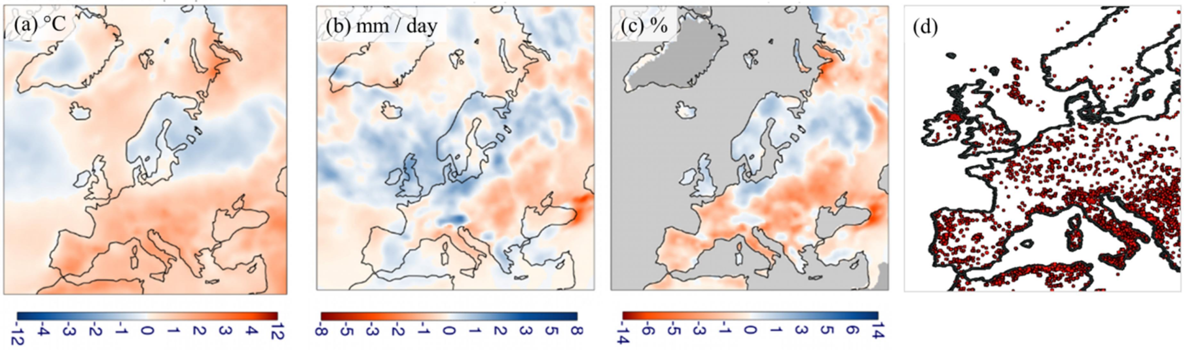

Figure 6.5: ERA-Interim (a) surface air temperature, (b) precipitation and (c) soil moisture anomalies of the uppermost 7 cm of soil for summer 2017 (June, July, August) relative to the seasonal average from 1981-2010 (Copernicus, 2018). Panel (d) shows wildfires during the campaign period (July 11th to 28th) as detected by VIIRS and MODIS (retrieved from NASA Worldview, *https://worldview.earthdata.nasa.gov/*).

European annual average temperatures were 0.8 °C higher than the climatological mean, and especially in southwestern Europe, the summer 2017 was exceptionally hot (+1.7 °C), as depicted in Fig. 6.5a. Averaged annual European precipitation (panel b) was close to the climatological mean (-0.2 mm/day), however, large spatial differences were present in summer with extensive precipitation in the Alps and northern Italy, where heavy rainfall events caused extensive flooding. Dry soils were apparent over most of Europe with large

---

[6.1] With today, i.e. the year 2020, 2016 is still the hottest year on record, while 2019 is on second place (*https://public.wmo.int/en/media/press-release/wmo-confirms-2019-second-hottest-year-record*).

negative soil moisture anomalies in summer (panel c). These dry conditions, together with high temperatures, led to significant wildfire activities, especially in Italy, southern France and on the Iberian Peninsula. The intense wildfires detected throughout the EMeRGe campaign phase by VIIRS (Visible Infrared Imaging Radiometer Suite) and MODIS (MODerate Resolution Imaging Spectroradiometer) are shown in panel (d).

6.3.1 Regional and vertical CH_4 distribution

The CH_4 observations obtained during all European research flights are presented in Fig. 6.6. Due to the fact that HALO was frequently repeating same flight routes at stacked altitudes, the observations in panel (a) are gridded into bins of 0.05° × 0.05° in latitude and longitude direction, and the maximum measured CH_4 mole fraction in each bin is displayed. Panel (b) shows the vertical profile of CH_4 percentiles (P10, P50 and P99) in 1 km vertical bins. The profiles represent individual flights (blue) and a mission mean (black).

Encountered CH_4 enhancements are most distinctive in the altitude range up to 2.5 km, which corresponds to the typical BL height above land (as discussed in Sect. 2.3). The highest CH_4 mole fractions of 2 to 2.4 ppm are encountered during two flights in the Po Valley and in its outflow above the Adriatic Sea. Downwind of London and across the BeNeRuhr region CH_4 is enhanced by up to 2 ppm. For all three cases, the individual P99 profiles show also the most pronounced structure at lower altitudes. The enhancement in P99 observed between 2 and 3 km is associated with a biomass burning (bb) plume detected at the French coast with max. mole fractions of 2 ppm. Enhanced CH_4 can also be observed near Munich and downwind of Rome and Barcelona, but with less magnitude (1.94 to 1.96 ppm). A slight latitudinal gradient in the upper troposphere seems to exist with enhanced CH_4 in the south of Europe.

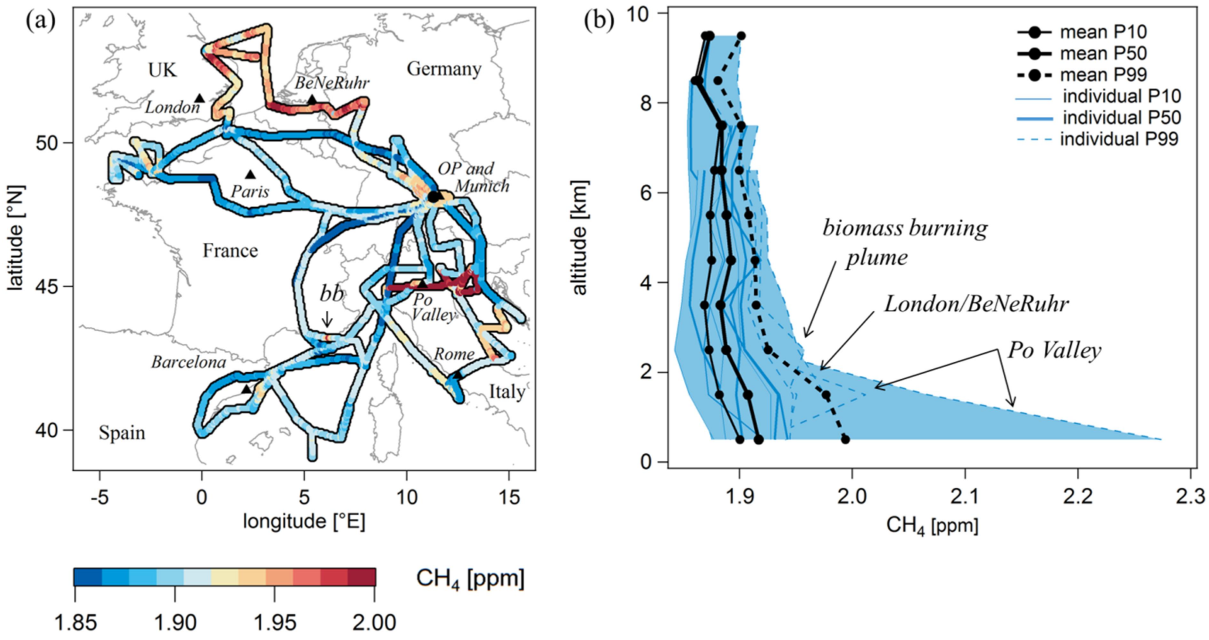

Figure 6.6: (a) Maximum measured CH_4 mole fractions in 0.05° × 0.05° bins. (b) Individual vertical flight profiles of CH_4 and the mission mean. P10, P50 and P99 represent the 10th, 50th and 99th percentile, respectively.

6.3.2 Urban case study I: London and the industrialised BeNeRuhr region

According to CH_4 emissions from EDGAR (see Fig. 6.7a), the urban emission hot spot London can be clearly distinguished from its surroundings, although high CH_4 emissions are also extending beyond the city boundary (indicated by the black line). Greater London (as indicated by the square) is dominated by CH_4 emissions from solid waste landfills (~80 %), followed by wastewater treatment (~7 %) and enteric fermentation (~6 %). Emissions in the BeNeRuhr region show several emission hot spots and a mix of different sources: enteric fermentation (~30 %), fuel exploitation (~26 %), solid waste landfills (~15 %), manure management (~14 %) and wastewater treatment (~ 9%). The North Sea is characterised by numerous offshore oil and gas exploitation facilities (OSPAR Convention, 2017; see panel b), which are recognised as important sources of CH_4 (Cain et al., 2017; Riddick et al., 2019). Strong point-source emitters on land (>0.1 kt CH_4 a^{-1}) are available from E-PRTR (2017) and sized according to their emissions from 0.1 to 68 kt CH_4 a^{-1}. While Belgium is almost absent of point sources, EDGAR depicts a clear maximum of CH_4 distributed over larger areas.

The flight track of HALO on July 26th (F08) is depicted in Fig. 6.7b. The aircraft passed London and performed four downwind legs at altitudes of roughly 0.7, 1.3, 0.7 and 0.7 km, respectively. The two intermediate legs are marked with S1 (for "Shuttle"). The weather situation was dominated by an Atlantic low pressure system with its warm front moving towards (July 25th) and across Great Britain (July 26th), hence south-southwestern winds were prevalent on that part of the flight track. HALO then turned towards the coast of Belgium and the Netherlands, crossed Belgium at ~1 km altitude and performed a second shuttle above the Ruhr area at altitudes of ~0.9, ~1.6 and ~2.5 km (marked with S2). The BeNeRuhr region was characterised by north-westerly winds of a cut-off low.

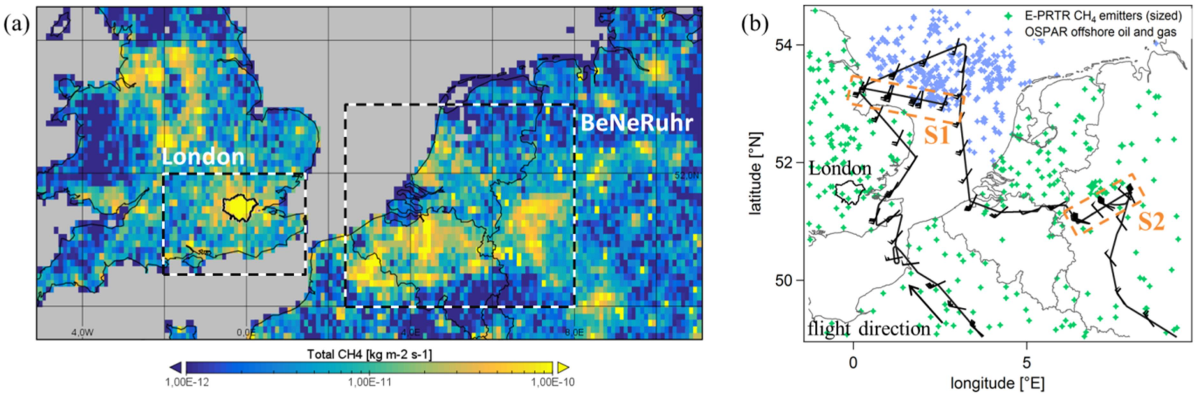

Figure 6.7: (a) Total CH_4 emissions for the year 2015 from EDGAR v5.0. Greater London and the BeNeRuhr area are marked by squares which also define the source regions specified for the HYSPLIT simulations. (b) HALO flight track marked with the location of performed shuttles (S1 and S2) and CH_4 emission point sources on land (E-PRTR, 2017) and from offshore oil and gas platforms (OSPAR Convention, 2017). Wind barbs indicate the measured wind direction and strength aboard HALO.

In Fig. 6.8a the flight track of HALO is colour-coded according to the measured CH_4 mole fractions, indicating elevated CH_4 downwind of London and across the BeNeRuhr area. Panel (b) shows the corresponding time series for a number of different measured species as well as simulated H_CO tracers. The London flight part is emphasised by an orange dashed square, the BeNeRuhr part by a blue dashed square. The start and end of each square along the flight track is indicated by thick orange and blue lines in panel (a). Discussed enhancements in CO_2 and CH_4 are marked with P1 to P4 (for "Plumes"). P1 corresponds to the southernmost flight leg of the e-shape, which is closest to London. The sharp decrease at ~10:40 UTC does most likely not represent the end of the plume, since the flight altitude was changed. P2 corresponds to the second (and lower altitude) leg of S1 as well as to the leg which is furthest away from London and thus the northernmost. According to the ERA-Interim reanalysis data HALO is flying at the upper edge of the BL during both London plumes. P3 starts with the crossing of the Belgian coast and HALO was flying entirely within the BL when crossing the BeNeRuhr region. P4 denotes the two lowest legs of shuttle S2 in the Ruhr area. Note that only one leg of each shuttle is visible in the latitude-longitude plot as the others lie underneath.

With respect to the short-lived nitrogen compounds NO and NO_y, there is a remarkable similarity in their pattern to the simulated H_CO enhancements from both, London and BeNeRuhr. CO_2 and CH_4, with a much longer atmospheric lifetime, follow the H_CO pattern in general as well, but they exhibit much more small scale variability than NO and NO_y, especially outside the predicted H_CO plumes. CO_2 is depleted in the BeNeRuhr region but shows three distinct and sharp enhancements (*i, j*). Measured CO mole fractions are higher in the BeNeRuhr region with a more pronounced structure than downwind of London.

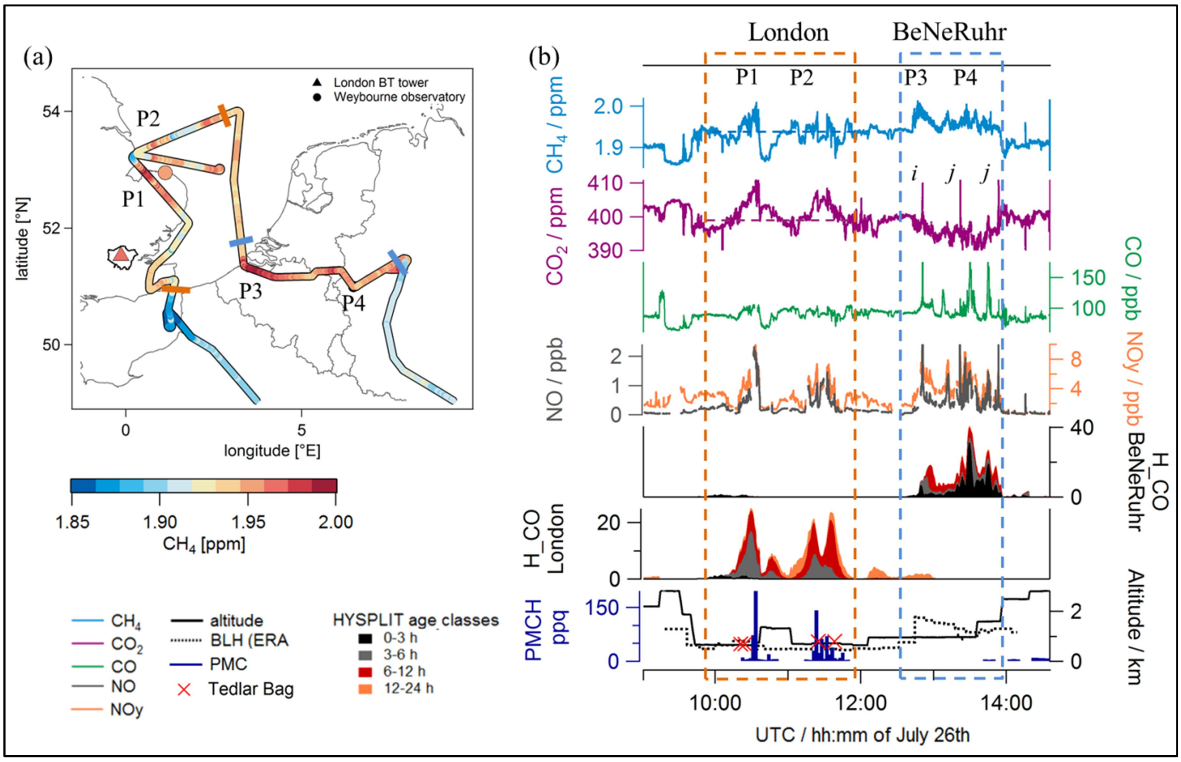

Figure 6.8: (a) HALO flight track colour-coded according to the measured CH_4 mole fractions. Same colour scale applies for measurements at two ground-based stations within London (triangle; Forster, 2013) and at the eastern UK coast (circle, for reference see text). (b) Time series of CH_4, CO_2, CO, NO, NO_y, HYSPLIT simulated CO enhancements (H_CO) from BeNeRuhr and London (for area definition see Fig. 6.7a), PMCH tracer (H. Schlager), flight altitude (solid line) and boundary layer height (dashed line), which is retrieved from ERA-Interim reanalysis data at 12 UTC of the same day. Red crosses denote the sampling location of the Tedlar Bags as analysed in Sect. 6.3.5. P1 to P4 denote plumes of enhanced GHG.

Identification of the London plume

It is analysed if the CH_4 and CO_2 plume downwind of London can be clearly identified, traced back to the city and quantified roughly 150 to 250 km downwind of the city. For the BeNeRuhr area, as HALO was flying directly above the target region, individual source signatures are discussed at the end of this section.

In the first London plume (P1), both GHG patterns behave similar to the predicted H_CO enhancements. From the correlation plot in Fig. 6.9 it is clear, that CH_4 and CO_2 correlate very well (Pr = 0.8, indicated in red). Hence, sufficiently downwind of London the urban emissions, which consist of different sources close to each other, are well-mixed and most likely responsible for the strong correlation. Within plume P2, only CO_2 seems to follow the H_CO pattern, and both GHG differ in their spatial distribution with no correlation (Pr = -0.1, indicated in orange). This indicates that air masses sampled in P1 and P2 are of different origin or influenced by different transport processes.

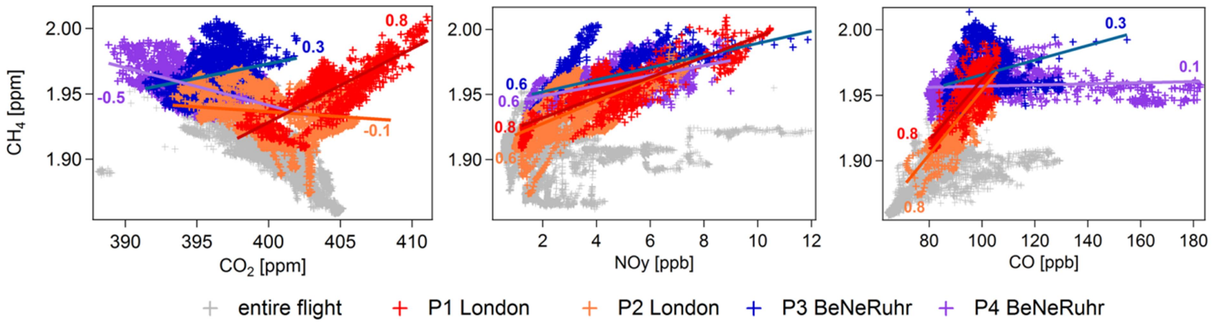

Figure 6.9: Correlations of CH_4 with CO_2, NO_y and CO for four selected GHG plumes (for plume distinction see Fig. 6.8). Values denote the Pearson correlation coefficient Pr.

To analyse the origin of the sampled air masses, the performed Lagrangian tracer experiment led by H. Schlager, DLR-IPA (similar as described in Ren et al., 2015), is of great support. A small amount of an inert PMCH tracer (perfluoromethyl-cyclohexane), which has an extremely low background mole fraction in the atmosphere, was released from central London prior to the research flight (7th floor of the Imperial College, 05:00 to 05:33 UTC). After several hours of transport with the prevailing wind, it was sampled aboard the aircraft, see bottom panel of Fig. 6.8b. The tracer was only released at a single point and therefore it does not represent the whole pollution plume of the city, which extends much more in the horizontal and vertical. However, the local London pollution is evident in both encountered plumes P1 and P2. Within central London a permanent GHG observation station is located at the top of the British Telecom (BT) tower, marked with a triangle in Fig. 6.8a. Three to six hours prior to the HALO fly-by, i.e. when the air masses probed with HALO passed London according to HYSPLIT backward trajectories, observed CH_4 mole fractions were in the range of 1.942 to 1.992 ppm (personal communication with C. Helfter, UK Centre for Ecology & Hydrology, 2018). Hence, they agree with the magnitude of measured airborne CH_4. Another permanent GHG observation station is the Weybourne Atmospheric Observatory located northeast of London (marked with a circle). At roughly the time when HALO flew by, the reported mean value of 1.958 ppm CH_4 (Forster, 2013) is also consistent with the airborne measured CH_4 mole fractions. Hence, a similar strong pollution source (most likely London) is evident in both encountered air masses in P1 and P2. The correlation of CH_4 with CO and NO_y is depicted in Fig. 6.9 in the same colours as for the correlation with CO_2 (red for the first and orange for the second London plume). Unlike CO_2, both tracer-tracer correlations are similar for P1 and P2. The correlation coefficients are similar high in both London plumes, i.e. CH_4/CO with Pr = 0.8 and CH_4/NO_y with Pr = 0.6 to 0.8.

Therefore, the different CO_2 and CH_4 signatures in P1 and P2 might be explainable by two interacting effects: differences in the emission height and differences in the buoyancy of the gases at their release point, which might be particularly noticeable at the upper edge of the BL (see BLH in Fig. 6.8b). While CO_2 emissions are closely coupled to ff consumption and thus to higher temperatures during their release, the buoyancy of the air parcels and the mixing in the vertical might be enhanced. In addition, 1/4th of CO_2 emissions in the greater London area are emitted via stacks from power plants (E-PRTR, 2017), hence emissions are released at a certain elevated height above ground level. In contrast, CH_4 emissions are usually not emitted during exothermic processes, therefore the vertical mixing might be less pronounced.

Quantification of the London CH_4 plume

Greenhouse gas emissions from London have been in the focus of several airborne (O'Shea et al., 2014; Ashworth et al., 2019; Pitt et al., 2019) and ground-based studies (Lowry et al., 2001; Helfter et al., 2011). The earliest study from Lowry et al. (2001) used isotope measurements between 1996 and 1998 to determine the source contributions to the CH_4 budget. Their fluxes are dominated by emissions from landfills and waste treatment and are larger than the National Atmospheric Emission Inventory (NAEI). O'Shea et al. (2014) and Pitt et al. (2019) both measured CH_4 and CO_2 enhancements downwind of London in 2012 and 2016, respectively, by aircraft. While O'Shea et al. (2014) reports a strongly positive correlation of CO_2 and CH_4 in the measured plume (with a plume age of ~4 to 5 h), their estimated fluxes are higher than the NAEI inventory by a factor of 2.3 for CO_2 and 3.4 for CH_4. In contrast, Pitt et al. (2019) developed a new modelling approach accounting for urban emissions which are not only confined to the urban area, but also located in the near vicinity of the city. Their estimated fluxes are also compared to the NAEI inventory, but were found to be lower for CO_2 (factor of 0.71) and roughly similar for CH_4 (factor of 1.03). Three flights around London in July 2017 allowed for the distinction between the London plume under west wind and significant local sources in the SE of England during quiescent south-westerlies (Ashworth et al., 2019). Estimated CH_4 fluxes from Greater London were twice (and 2.5 times) as high compared to O'Shea et al. (2014) (and Pitt et al., 2019) and for CO_2 within 10 % (and 30 %) respectively. In the following it is evaluated if a quantification of urban emissions is possible roughly 150 to 250 km downwind of the city.

As indicated in Sect. 6.2.2 the flight strategy does not allow for a quantitative analysis similar to the case study of Berlin. In the case of London, four flight transects were planned to cross the urban plume downwind in different distances as well as at different altitudes, but no upwind measurements were performed. It was tested, if observations from Mace Head could be used instead. This ground-based station is located at the west coast of Ireland and is often used to study the background composition of clean air masses from the North Atlantic Ocean during westerly winds (*http://www.macehead.org/*). A fraction of calculated HYSPLIT trajectories passed the station at altitudes below ~1.5 km roughly two days prior to the measurement (-48 to -52 h). The measured variability in CH_4 mole fractions at this remote location is already between 1.928 and 1.951 ppm (Prinn et al., 2018), hence, in the same order of magnitude as the airborne detected enhancements downwind of London and therefore not suitable for an upwind background determination. Although a rough downwind background, based on measurements outside of the pollution plume can be set visually for CH_4 and CO_2, as indicated by the horizontal dashed lines in Fig 6.8b, it is uncertain how far the plume P1 extents to the northwest as the flight altitude was changed before reaching background mole fractions. Hence, the extent of the plume is not detectable.

MECO(n) model comparison

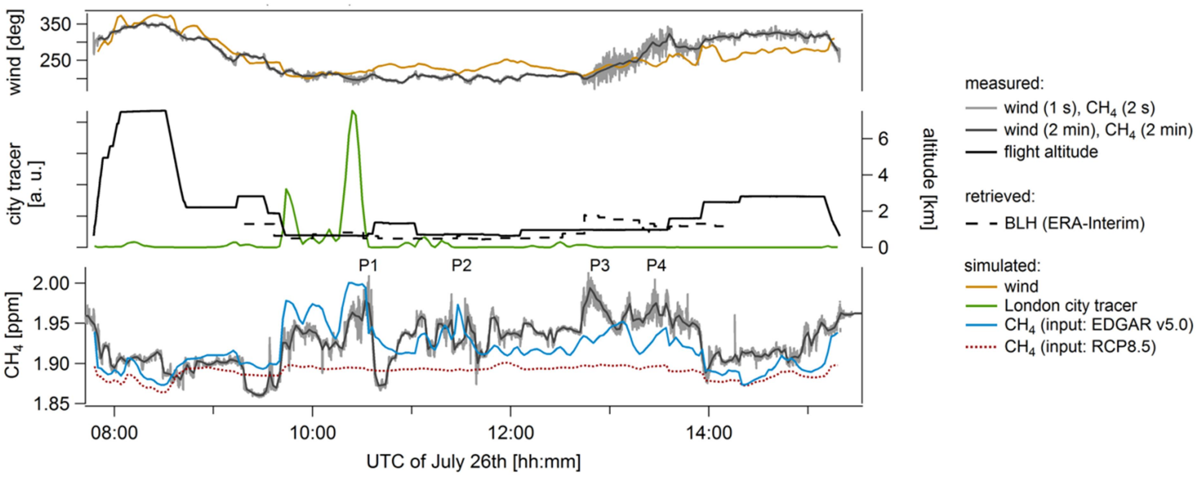

Figure 6.10: MECO(n) model simulation output of wind direction (orange, upper panel), artificial London city tracer (green) and CH_4 mole fractions from two different inventories, v5.0 (blue, lower panel) and RCP8.5 (red, lower panel). All model tracers are at 12 km spatial and 2 min temporal resolution. Measured wind and CH_4 data with a resolution of 1 s and 2 s respectively (light grey) were averaged on the model time resolution of 2 min (dark grey).

To improve the understanding of the urban plume the obtained airborne measurements are compared to the output of the MECO(n) simulation. The model accurately represents the prevalent wind situation, since the measured and simulated wind direction throughout the entire flight agree well (Pr = 0.8), see upper panel of Fig. 6.10. Except between ~10:30 and ~12:30 UTC MECO(n) depicts more south-westerly wind, and from ~13:20 UTC towards the end of the flight more westerly wind than observed. The larger noise in the wind measurements in P3 and P4 is due to flying within the turbulent BL. The simulated city tracer (middle panel), emitting from central London, shows a strong increase in P1. In addition, the simulated CH_4 mole fractions based on EDGAR (lower panel, depicted in blue) are matching the observation pattern accurately in P1, although they are biased to higher values (+25 ppb). Hence, the simulated transport seems to be valid in this case. In both plumes, P1 and in the peak to its left (i.e. earlier in time), the London city tracer, the simulated EDGAR-CH_4 and the measured CH_4 mole fractions are encountered above land. In P2, the London city tracer signal is hardly discernible and simulated EDGAR-CH_4 mole fractions are smaller than measured, but some parts of the structure are reproduced. Either MECO(n) is not able to represent the land-sea transport accurately, i.e. the emissions from the BL over London are not transported above the marine boundary layer of the North Sea. Or, the simulated London plume is misplaced in the horizontal and/or vertical. Both, or a combination, are possible since the MECO(n) model simulates in P2 more southwestern wind than observed aboard the aircraft.

In summary, London is a significant source of CH_4, which is clearly distinguishable in emission inventories like EDGAR. It was shown that the corresponding urban plumes can be identified in the CO_2 and CH_4 signal measured aboard the aircraft with the help of the regional CO-tagging from HYSPLIT as well as with complementary measurements of short-lived pollutants. For a proper quantification a following dedicated flight experiment should include the following suggestions:

- Airborne measurements are needed upwind of London to assess if air masses had already been polluted from source regions farther upwind.
- Downwind flight legs in the target area should be planned flexible enough to identify how broad the pollution plume is based on online observations aboard the aircraft.
- Downwind measurements, which are closer to London, allow for excluding surrounding sources, e.g. as introduced by the numerous CH_4 emitting facilities according to E-PRTR.
- To avoid unnecessary difficulties in both, the interpretation of observations and simulations, flight tracks should either be planned over land or over sea since the mixing and dispersion of urban pollution and GHG is strongly dependent on the structure of the boundary layer over land and the interaction of air masses above the marine BL.
- Simultaneous ethane measurements aboard the aircraft provide a useful tool to account and separate for offshore oil and gas emissions, e.g. as potentially induced by numerous offshore platforms in the North Sea. Recently, Riddick et al. (2019) measured the CH_4 leakage of eight individual platforms in the North Sea and determined a median loss of 0.23 %. This value is almost two times higher than reported in the local inventory.

For a quantitative analysis of the London GHG emissions, as detected during the EMeRGe flight, a more in depth inverse modelling approach with known locations of emission sources needs to be used, which is however not feasible in the timeframe of the thesis.

Source signatures in the BeNeRuhr area

With respect to the BeNeRuhr area, only CH_4 follows the H_CO pattern in P3 and P4, while CO_2 is clearly depleted and shows strong and sharp enhancements of up to 410 ppm (*i*) and 460 ppm (*j*), see Fig. 6.8b. These peaks can be attributed to emissions of nearby facilities. The first one (*i*) is detected near Antwerp/Bruges and lies downwind of an iron and steel manufactory (ArcelorMittal Belgium). According to E-PRTR (2017) it emits large amounts of CO_2 (~4000 kt) and CO (~90 kt), some NOx (~5 kt), but only little CH_4 (~0.8 kt), which is consistent with the airborne observations. The second and third peak (*j*) is detected at different flight altitudes but at the same measurement location near Wuppertal/Cologne. Northwest of the detected peak two RWE (Rheinisch-Westfälisches Elektrizitätswerk AG) power plants release large amounts of CO_2 (~55000 kt) and NOx (~35 kt) but only little CO (~10 kt) and no CH_4, which is also reflected in the measurements. Hence, CO_2 is clearly dominated by point source emissions. In contrast, the observed CH_4 pattern, which shows broader enhancements, most likely stems from a mix of different area sources as already indicated by the various source categories in EDGAR and the absence of Belgian point sources in E-PRTR. The different emission sources for CO_2 and CH_4 are supported by the non-existing correlation between the two gases in P3 (Pr=0.3) and P4 (Pr=-0.5), see Fig. 6.9.

In the MECO(n) simulation (Fig. 6.10), the EDGAR-CH_4 tracer captures some variability of the measured mole fractions in P3 and P4, however the magnitude especially in P3 is too small and the background is biased to lower values (-25 ppb). Hence, EDGAR emissions might be too low in that region or important CH_4 sources might be missing. The simulated RCP8.5-CH_4 mole fractions show in both regions, London and BeNeRuhr, no variation, indicating that the prescribed zonal mean CH_4 mole fractions at the surface are not representative for the UK and the BeNeRuhr area due to their diverse emission sources.

6.3.3 Urban case study II: Barcelona

The second urban case study focuses on Barcelona (Spain), which is a coastal city surrounded by mountains towards the continental side. It is located ~100 km south of the Pyrenees, a large mountain range reaching ~3500 m altitude. In terms of population, Barcelona has roughly 1/3rd less inhabitants than London (as for 2015; UN, 2018a). Total CH_4 emissions according to EDGAR (Fig. 6.11) are evenly distributed across northeastern Spain (indicated by the white square) with a maximum to the west of the Barcelona province. According to E-PRTR (2017) the CH_4 point sources are half and half related to the rearing of poultry or pigs and to landfills. CH_4 emissions from the city itself are higher than the surroundings, but not as prominent as in the case of London. The following source sectors, according to EDGAR, are responsible for CH_4 emissions in NE Spain: manure management (~38 %), enteric fermentation (~32 %), solid waste landfills (~13 %) and wastewater treatment (~6 %).

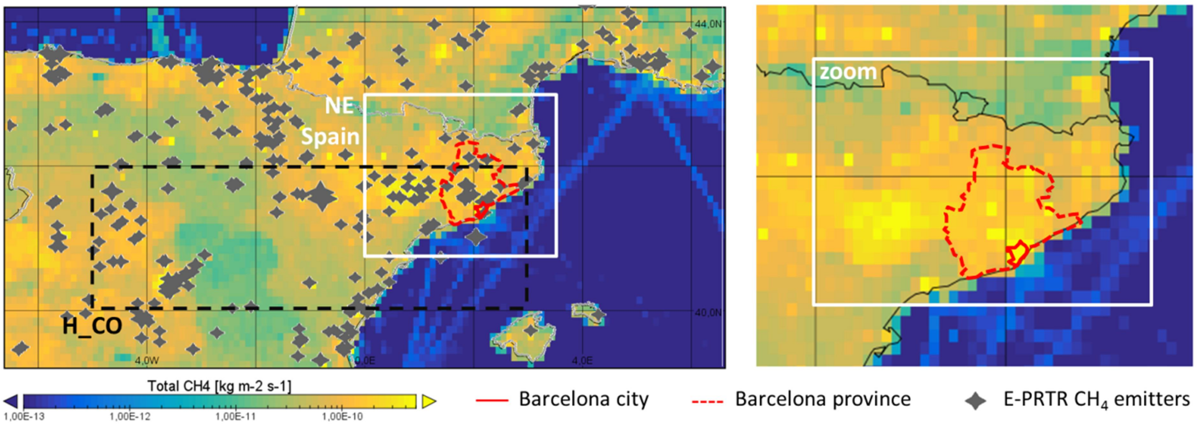

Figure 6.11: Total CH_4 emissions for the year 2015 from EDGAR v5.0. The NE area of Spain is marked with a white square. The source region specified by HYSPLIT (H_CO tracer) is indicated with a black square, covering the Madrid and Barcelona region. CH_4 emission point sources are from E-PRTR (2017).

The pollution plume ~90 km downwind of Barcelona was probed within F07 on July 24th, see Fig. 6.12. The figure is composed similar to Fig. 6.8 except H_CO denotes here contributions from Spain (i.e. Barcelona and Madrid region, for area definition see Fig. 6.11) and no PMCH tracer experiment was performed. HALO crossed the plume twice in the early afternoon at two different flight altitudes: at 1.6 km, which is nearer to the coast, and at 0.5 km, which is further away. P1 and P2 denote two plumes with detected CH_4 enhancements of ~1.94 ppm.

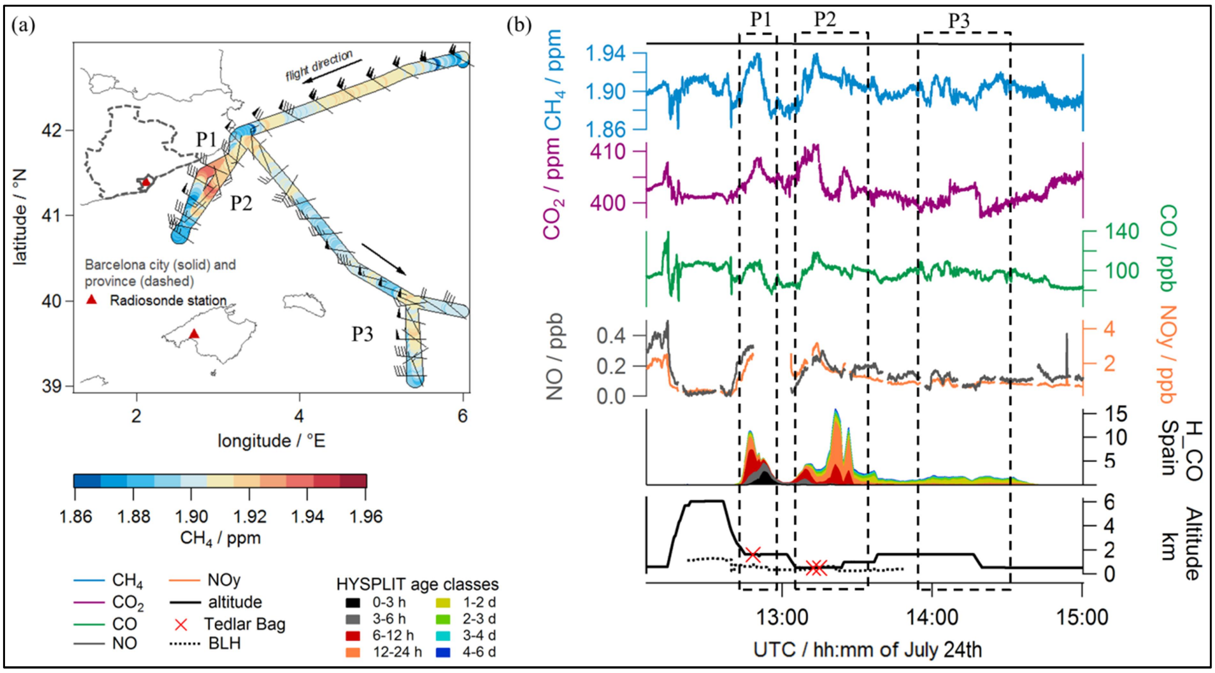

Figure 6.12: (a) HALO flight track colour-coded according to the measured CH_4 mole fractions. Red triangles denote two radiosonde stations (IGRA, 2017). The solid grey line indicates the city boundary of Barcelona; the dashed line corresponds to the greater province of Barcelona. (b) time series of CH_4, CO_2, CO, NO, NO_y, HYSPLIT modeled CO enhancement, flight altitude and boundary layer height, which is retrieved from ERA5 reanalysis data at 13 UTC. Red crosses denote sampling locations of Tedlar Bags as analysed in Sect. 6.3.5. P1 and P2 denote plumes of enhanced GHG; P3 the location of a quasi-Lagrangian transported air mass.

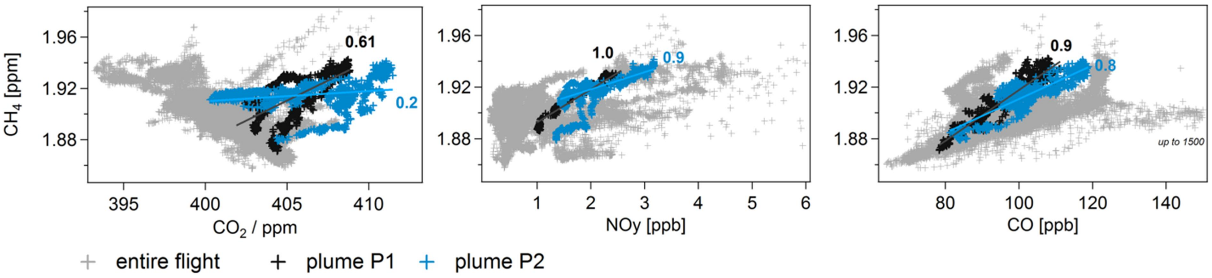

Figure 6.13: Correlations of CH_4 with CO_2, NO_y and CO for two selected GHG plumes (for plume distinction see Fig. 6.12).

Enhanced CH_4 is in both plumes (P1 and P2) strongly correlated with NO_y (Pr = 1 and 0.9) and CO (Pr = 0.9 and 0.8), see Fig. 6.13, however less with CO_2 (Pr = 0.6 and 0.2), especially due to the CO_2 double-peak structure in P2. The simulated H_CO enhancements in P1 agree with the observed trace gas patterns. The wind, as measured aboard the aircraft, was coming at this upper altitude leg from WNW with 8.7 m s^{-1} on average and HALO was flying above the marine BL according to ERA5 reanalysis data at 13 UTC of the same day. Since the

HYSPLIT simulation allows for a classification of the H_CO enhancements by their age (see Sect. 3.3), in P1 mostly fresh pollution is predicted (plume age of zero to -12 h) as indicated by the darker colours in Fig. 6.12b. In P2, H_CO differs from the airborne observations. A plume with older air masses is dominating in the second half, while the trace gases (except CO_2) show enhancements in the first half. At this lower altitude transect the wind speed was low (2.9 m s^{-1}) with directions from the SSW and SSE and HALO was just within the marine BL. It should be noted that HYSPLIT trajectories are subject to a ~10 % deviation of their travelled distance (Stohl, 1998), hence with the longer transport time (as indicated by the age), the predicted plume structure gets more uncertain.

Identification of the Barcelona plume

The different wind situations in both plumes P1 and P2 together with the varying HYSPLIT age classes, the non-agreement of H_CO with the observed trace gas pattern in P2, but the relatively consistent tracer-tracer correlations of CH_4 with CO and NO_y raise the question where the detected pollution plumes P1 and P2 come from.

The upper level WNW wind is consistent with two radiosonde soundings from Barcelona and Mallorca at 12 UTC (IGRA, 2017), marked with red triangles in Fig. 6.12a. The low level wind (<700 m) from the Barcelona sounding indicates ENE to ESE wind and W to NW wind from the Mallorca sounding. The 10 m wind (*wetter3.de*) confirms the calm winds in this region with no preferred direction. Hence, the different wind direction measured aboard the aircraft is not the result of an artefact or measurement failure. In order to verify the BLH from ERA5 reanalysis data, the standard deviation of the z-axis acceleration measured by the aircraft is a good indicator for turbulence, and thus representing most likely when the aircraft was within the BL. However, no significant difference between P1 and P2 is perceptible (±0.16 vs. ±0.21 m s^{-2}), as e.g. compared to penetrating the BL above sea later at ~15 UTC (±0.32 m s^{-2}). Hence, although P1 is measured above the Marine Boundary Layer (MBL), emissions are most likely coastal outflow from the Barcelona area. GHGs and air pollutants are emitted within the BL over land, which deepens throughout the day, and are advected horizontally across the shore towards the sea with the prevailing wind. This mechanism has been observed and simulated within many studies (e.g. Dacre et al., 2007; Peake et al., 2011). As HYSPLIT predicts very fresh pollution in P1, this scenario is likely. In addition, the ratio between NO and NO_y can be used as an indicator for the age of an air mass (Wang and Prinn, 2000). In P1 the ratio is higher (compared to P2), hence indicating fresher air masses where NO is not yet chemically converted to NO_y. Since P2 is also measured above the MBL (or at least near its top), but indicates a more aged plume, air masses encountered in P2 might be an emission mix of aged urban and fresh coastal pollution (as NO_y is still unusually high).

With respect to the atmospheric background, NO and NO_y nicely return to lower values outside the tagged plumes P1 and P2. The longer living species CH_4, CO_2 and CO exhibit much more variability between the flight altitudes, making it difficult to indicate a plume solely based on these measurements. Hence, observations of short-lived species are necessary to identify the urban plume at flight distances roughly 100 km away from the investigated source, which was already indicated by the measurements downwind of London (see Sect.

6.3.2). Further, short-lived species are useful to distinguish between younger and older GHG signatures. As stated in Sect. 6.2.2, also a quasi-Lagrangian sampling was aimed (see P3 in Fig. 6.12) by performing another shuttle at ~1.6 and ~0.5 km altitude to the west of the island Sardinia with the goal to capture the same air masses from Barcelona again. Although, neither the short lived nitrogen pollutants nor HYSPLIT indicate any influence from the Barcelona area, CH_4 and CO_2 are slightly enhanced, but not correlated. HYSPLIT backward trajectories indicate that air masses at the 0.5 km leg were lifted at the Atlantic coast by the Pyrenees and dropped at the Spanish/French coast of the Mediterranean Sea roughly six hours prior to our measurement. At the higher flight altitude (1.6 km leg) trajectories seem to originate from the BL of the Spanish central mainland. In the absence of enhancements from short-lived species the CO_2 and CH_4 enhancements might be caused by advection from more distant air masses or represent the natural variability of the GHG in the atmosphere.

MECO(n) model comparison

Similar to Fig 6.10 the observational data are compared to the MECO(n) results. The overall correlation of simulated and observed wind direction is poorer (Pr = 0.5) than for London. Especially with respect to P2 the wind directions differ by almost 180°, where the simulated wind ranges from NWW to N, while the actual wind came more from the south. Hence, the magnitude of the simulated Barcelona city tracer (dark red) in P2 is unlikely to reflect the real situation and is therefore neglected. However, the wind direction in P1 is well simulated and the transported Barcelona city tracer correlates with the measured CH_4 enhancement. A GHG signal from Barcelona might be distinguishable in the simulated EDGAR-CH_4 mole fractions, however the simulated enhancement of ~25 ppb is roughly half of the measured enhancement of ~50 ppb. In addition, the simulated CH_4 background is continuously too low.

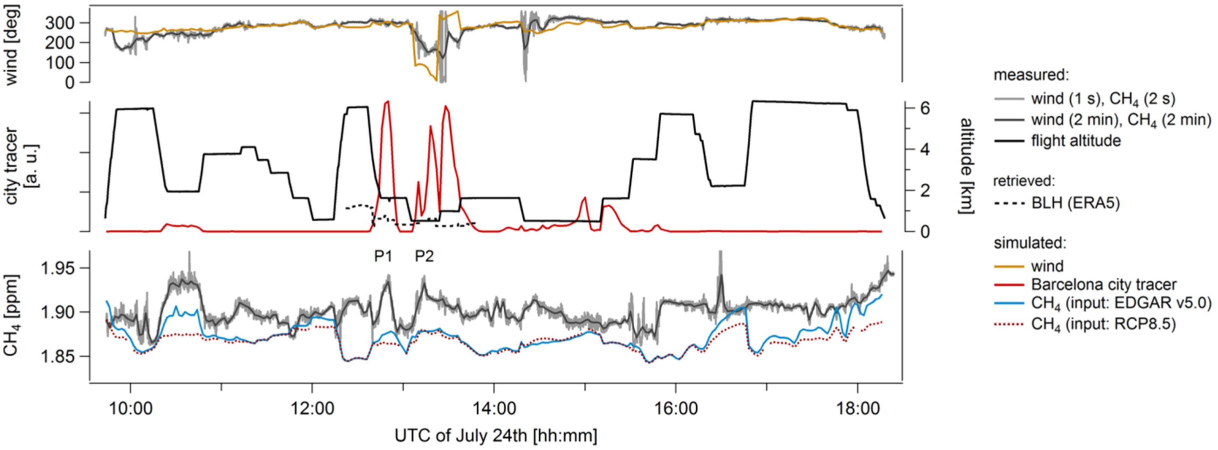

Figure 6.14: MECO(n) model simulation output of wind direction (orange, upper panel), artificial Barcelona city tracer (red) and CH_4 mole fractions from two different inventories, EDGAR v5.0 (blue, lower panel) and RCP8.5 (red, lower panel).

Interestingly, and in contradiction to the simulations from London, CH_4 mole fractions from both CH_4 tracers (EDGAR and RCP8.5) show almost the same values and consistent spatial patterns. Total CH_4 emissions from Spain are only half of UK emissions (see Fig. 6.2a) and apparently it does not matter if a gridded inventory like EDGAR or prescribed zonal mean mole fractions at the surface from the RCP8.5 scenario is chosen in this case. This observation points towards dominant area sources in the region of NE Spain.

In summary, downwind of Barcelona enhancements of GHG were identified at two different altitudes with less magnitude than in London although the measurements were performed closer to the source. The GHG plumes but might be a mix of urban pollution and other sources, potentially distributed over larger areas. Hence, a smaller defined H_CO region covering only the Barcelona region is necessary for the interpretation.

6.3.4 A biomass burning event

Europe experienced high summertime temperatures in 2017, especially in southwestern Europe with dry soil conditions, enhancing the activities of wildfires (see Fig. 6.5). On July 24th (F07) a biomass burning (bb) plume was probed by chance near Marseille as indicated in Fig. 6.15. A characteristic smell was noticed aboard the aircraft and the bb plume was clearly visible by looking out of the window. The European Forest Fire Information System reported a major fire in Bastidonne, depicted by the red marker in panel (a). According to an article of france bleu (2017) the fire started at ~9 UTC in the morning and roughly 800 ha were burning under strong winds of up to 90 km h^{-1}. The fire plume was detected ~65 km downwind aboard the aircraft at an altitude of ~2.2 km. Over a flight distance of approx. 40 km the measured species are clearly enhanced, see panel (b). Acetonitrile, which is a specific tracer for bb (Holzinger et al., 2005), also shows significant enhancements of up to ~3 ppb. Strong winds (~80 km h^{-1}) were also encountered aboard the aircraft.

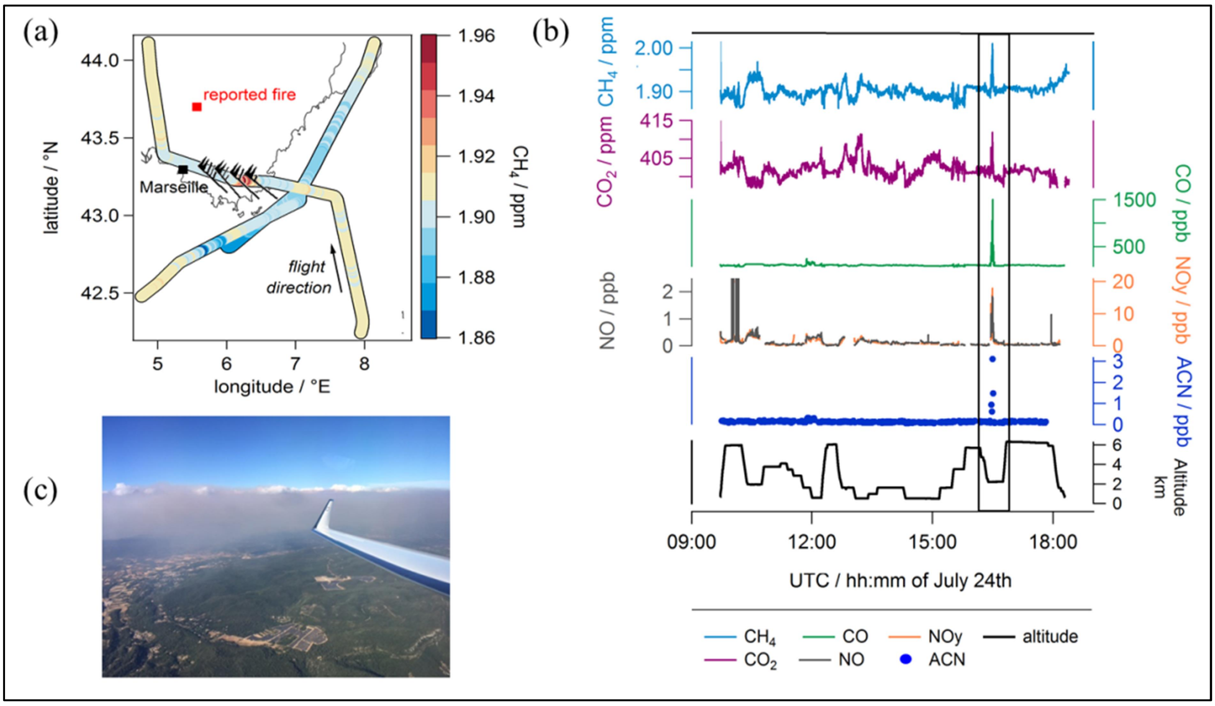

Figure 6.15: (a) HALO flight track of July 24th, 2017 colour-coded according to the measured CH_4 mole fractions. The Bastidonne fire is marked in red. (b) Time series of CH_4, CO_2, CO, NO, NO_y and Acetonitrile (E. Förster, KIT). The even larger enhancements in NO and NO_y roughly at 10 UTC are due to the formation of lightning NOx (=NO_2 + NO) above the Alps. (c) Photograph of the detected bb plume (courtesy of E. Förster).

With respect to CH_4, bb is responsible for only ~2 to ~3 % of total global anthropogenic CH_4 emissions (Saunois et al., 2019). Emissions from ff production and use (~30 % to ~42 %), as well as from agriculture and waste (~56 %) dominate the total budget. During the same flight, roughly at 13 UTC, the urban plume ~90 km downwind of Barcelona was investigated (see Sect. 6.3.3). A direct comparison of measurements reveals that the bb plume reaches higher maximum CH_4 mole fractions (2.01 vs. ~1.94 ppm) and enhancements (Δ115 vs. Δ50-70 ppb), but its extent is less than half of the urban plume width (~40 vs. ~100 km). At both locations, the wind direction was roughly perpendicular to the flight track. The integrated area of the bb plume is only ~1/3rd to 1/4th of the urban plume.

In summary, emissions from bb plumes do not contribute as much as urban areas to the total global CH_4 budget, but it was shown that regional GHG patterns can strongly be influenced by fresh bb emissions.

6.3.5 Carbon isotope measurements

As presented in Sect. 2.1.2 the isotopic signature can be used to distinguish CH_4 emission sources by their underlying emitting process into biogenic, thermogenic and pyrogenic CH_4. During the EMeRGe campaign 98 ambient air samples were taken aboard HALO using Tedlar® gas sampling bags (*www.dupont.com/brands/tedlar.html* and Appendix A.12). The samples were afterwards analysed with respect to their $\delta^{13}C(CH_4)$ value in the laboratory of the Royal Holloway University of London, with a technique similar as described in Fisher et al. (2006). The sampling strategy aboard was defined to capture ambient air in (urban) pollution plumes as well as in atmospheric background air for reference. Each bag needed ~20 s to be filled.

Total CH_4 mole fractions from the Tedlar bags were first compared to the simultaneous CH_4 measurements from the Picarro instrument, i.e. a ~20 s average of the continuous data was taken to account for their filling time. While 84 % of sampled bags agreed within ±15 ppb, the remaining 16 % were excluded from further analysis. In order to obtain the isotopic value of a source region, so-called Keeling plots are used (Pataki et al., 2003), where the $\delta^{13}C(CH_4)$ value is plotted against the inverse of the CH_4 mole fraction, see Fig. 6.16. The principle behind is, that the measured atmospheric mole fraction is the sum of the background signal and an additional signal produced by the source, which enhances the mole fraction above the background value. The intercept of an orthogonal distance regression line with the y-axis is then representing the isotopic signature of the source. In Fig. 6.16 data from Tedlar bags sampled in the Barcelona and London plume (sampling locations are marked with red crosses along the altitude curve of Fig. 6.12 and 6.8), across the Po Valley and in its outflow over the Adriatic Sea, as well as within the bb plume are used.

The source of the bb plume, i.e. the fire, was clearly identified (see Sect. 6.3.4) and the encountered plume has by far the least negative source value of ~-44 ‰. Hence, the signature of the air masses is consistent with literature observation trends, where pyrogenic CH_4 due to the combustion of organic matter is relatively enriched in ^{13}C. In terms of the absolute isotopic source value, Sherwood et al. (2017) compiled a global database of $\delta^{13}C(CH_4)$ values from fossil fuel (natural gas, coal gas, shale gas), microbial (rice paddies, ruminants, termites, waste, landfills, wetlands) and biomass burning sources (see also Fig. 2.4). The obtained value of ~-44 ‰ for the bb plume rather lies in the fossil fuel probability distribution. It has to be noted that the two bags were sampled in the bb burning plume towards the edges, hence, larger errors are possible as the peak isotopic values might be missed. Further, the results from Sherwood et al. (2017) need to be treated with caution. Although they included 10 706 samples from 190 studies, far more data on the origin from fossil fuels (82 %) were available than from microbial and biomass burning (together 18 %). Samples which were taken across the Po Valley and in its outflow above the Adriatic Sea show consistent isotopic source signatures (~-52 ‰). This is expected when air masses from the same source region are sampled. Barcelona (~-65 ‰) shows compared to London (~-57 ‰) a more negative isotopic signal, hence air masses are relatively enriched in $^{12}C(CH_4)$, indicating more dominant biogenic sources in the Barcelona plume. The observed isotopic values (-52 to -65 ‰) overlap with both, ff (especially coal) and microbial sources according to Sherwood et al. (2017).

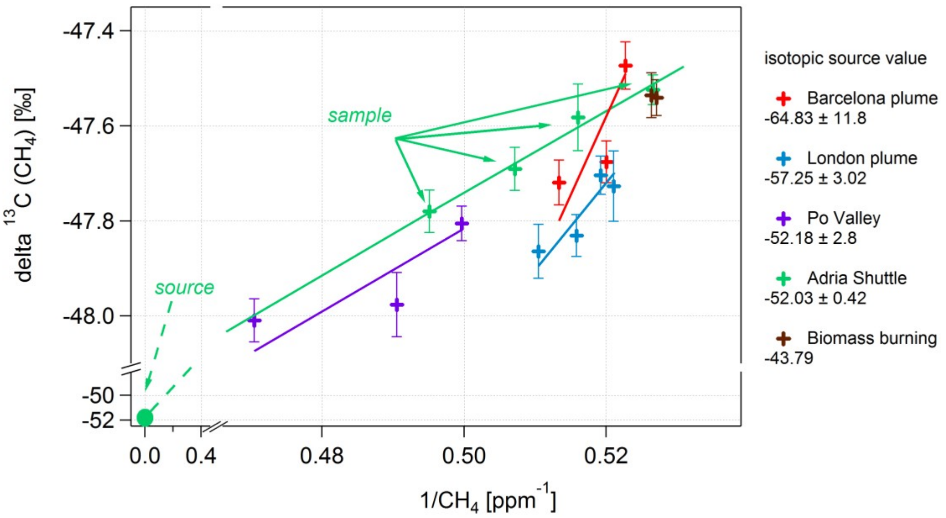

Figure 6.16: Keeling plot produced from the data obtained from flights to Barcelona, London, the Po Valley (across the valley and in its outflow on the Adriatic Sea) and within a biomass burning plume. The isotopic source signature is given by the y-intercept of an orthogonal distance regression line. Error bars denote the standard deviation of the measurements.

In summary, a significant trend was observed in the isotopic $\delta^{13}C(CH_4)$ values from specific source regions throughout Europe. For a more comprehensive analysis, it is suggested to deploy an in situ isotopic measurement instrument aboard the aircraft to continuously sample the atmosphere. Such instruments are, however, at the moment only used for ground-based measurements (e.g. Fisher et al., 2006; Rella et al., 2015). In the next section (6.4), observations from the EMeRGe-Asia campaign are presented.

6.4 Observations during EMeRGe-Asia in spring 2018

The typical outflow of continental Asian emissions occurs within the BL behind cold fronts (e.g. Carmichael et al., 1998) or within the free troposphere due to frontal lifting (e.g. Bey et al., 2001), convection and orographic forcing. In spring, strong cold fronts frequently pass northern China due to the existence of the Siberian High and the Aleutian Low over the

Pacific (Bey et al., 2001). In contrast, during early summer cold fronts are less frequent and the warmer air from the south initiates the development of deep convection. This outflow pattern was also confirmed by Liu et al. (2003), who combined aircraft CO measurements and a global 3D chemical tracer model. Figure 6.17 depicts the seasonal averaged horizontal flux of Asian anthropogenic CO at lower altitudes (1000 to 700 hPa column), clearly indicating the strong CO boundary layer outflow during winter (DJF) and spring (MAM). Biomass burning from SE Asia is not expected to mix with the BL outflow as it is rapidly transported to the upper troposphere by deep convection or by frontal lifting.

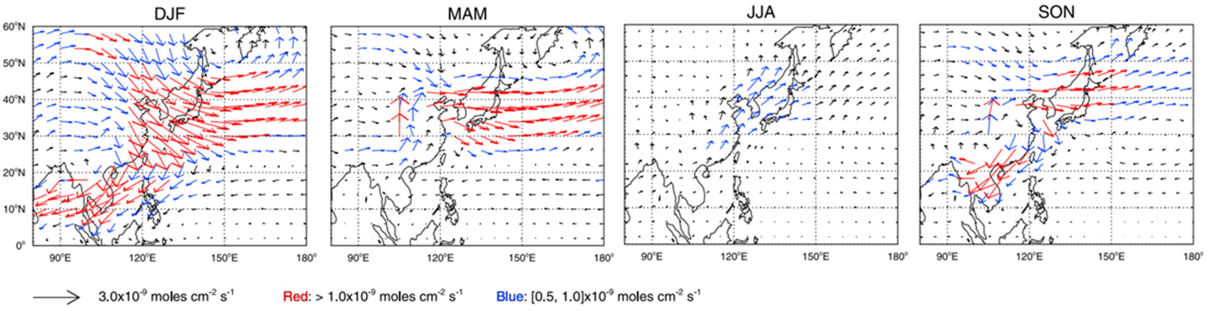

Figure 6.17: Average horizontal flux of Asian anthropogenic CO in the 1000 to 700 hPa column in 1996 (Liu et al., 2003).

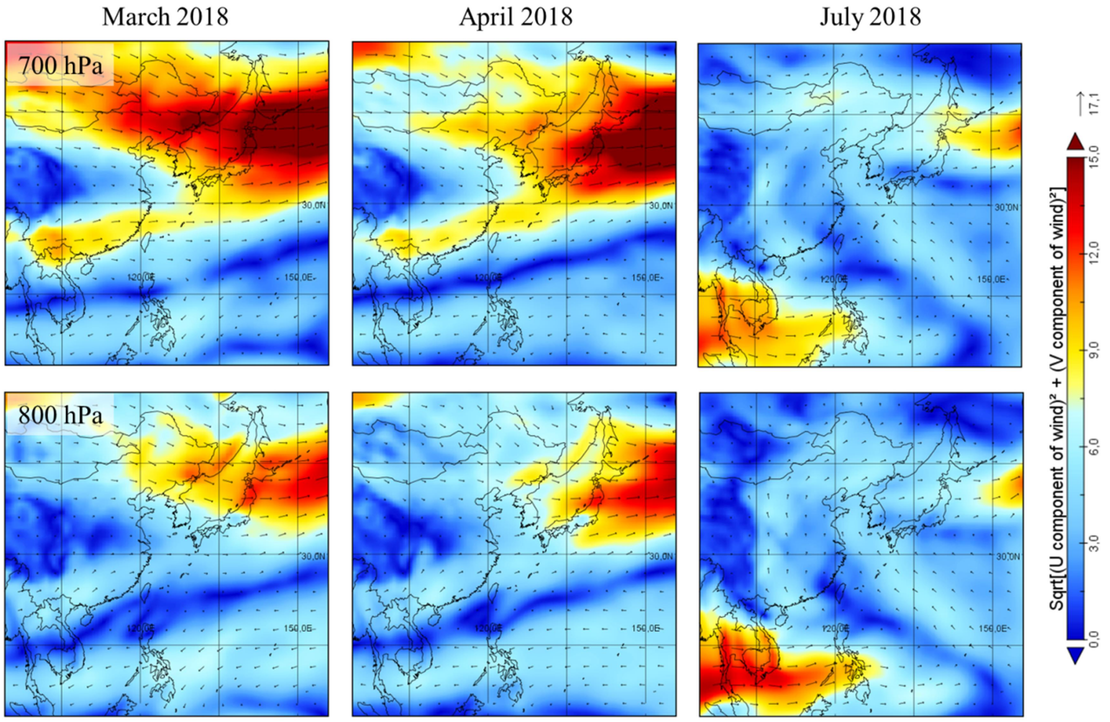

Figure 6.18: Monthly wind field mean of daily means for March, April and July 2018 as from ERA-Interim reanalysis data. Upper rows represent the 700 hPa pressure level and lower rows the 800 hPa level. Wind flow from the Chinese continent in March and April towards the Pacific is prevalent.

During EMeRGe-Asia flight restrictions in the Chinese airspace forced HALO to fly mainly above sea. Hence, in order to probe the Asian outflow, the mission was conducted in late spring from March 10th to April 9th, 2018. Monthly wind fields at 700 and 800 hPa from ERA-Interim reanalysis data are analysed for March, April and July 2018 (see Fig. 6.18). The associated flow of air masses from southern and northern China towards the Pacific dominates at 700 hPa in March and April. Winds are weaker at the 800 hPa level but show similar flow trends. In contrast, during July, the wind patterns reverse and air masses from the ocean hit the continent. The Chinese outflow occurs in the far north (>45°N).

6.4.1 Regional and vertical CH_4 distribution

Similar to the European observations (see Sect. 6.3.1), maximum measured CH_4 mole fractions obtained during the Asian mission are presented on a 0.05° × 0.05° latitude-longitude grid in Fig. 6.19a. Panel (b) shows vertical profiles of CH_4 percentiles (P10, P50 and P99) in 1 km vertical bins from individual flights (blue) and a mission mean (black).

Highest CH_4 mole fractions (up to 2.1 ppm) are detected off the entire Asian continent and at the western coast of Taiwan at low altitudes (<2 km). In contrast to the European profiles, single flight profiles do not stand out as e.g. observed in the London/BeNeRuhr area or the Po Valley, but a more uniform enhancement is prevalent. This is due to the different sampling strategy between EMeRGe-Europe and Asia. The longer transport distances in Asia until sampling allows the potential urban plumes to be mixed already with other pollution plumes and/or background air. Further CH_4 enhancements are detected west of Manila and south of Japan (both up to 1.99 ppm). The mission mean profile shows, similar to the European one, a flat profile in the upper troposphere between ~6 and ~10 km, however the individual P99 profiles suggest, that in some cases the Asian outflow extends up to ~9 km.

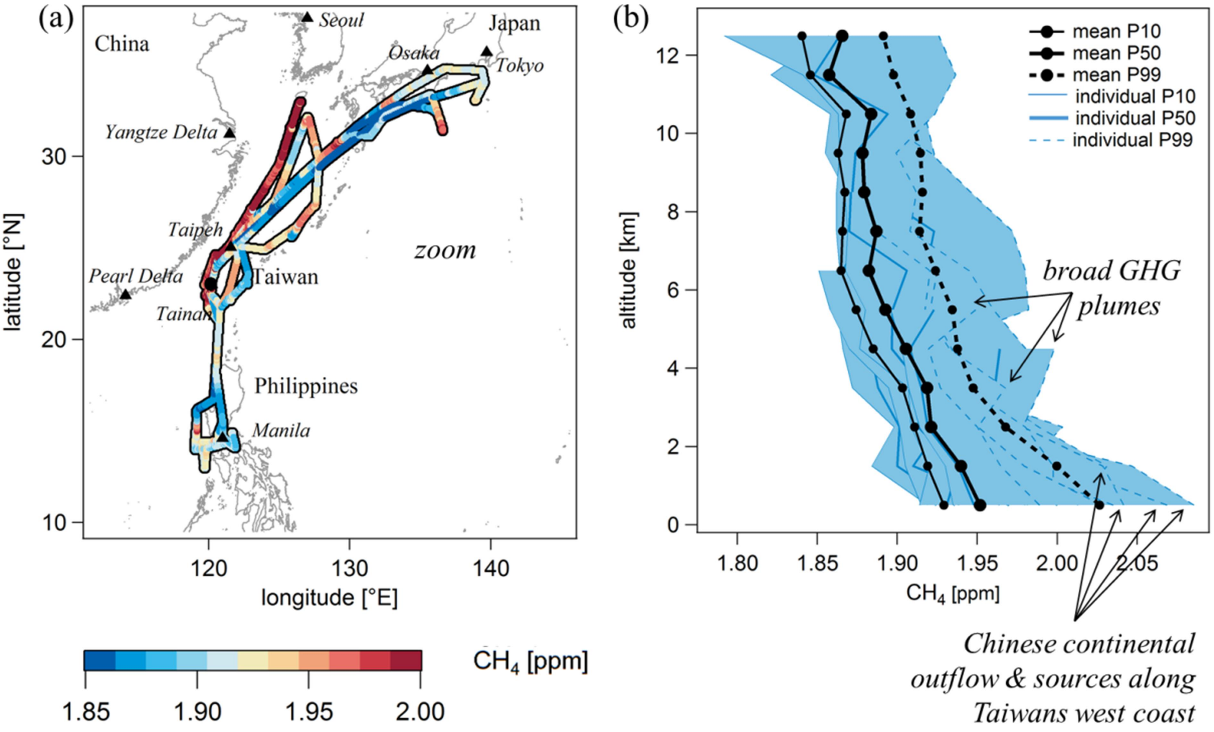

Figure 6.19: (a) Maximum measured CH_4 mole fractions in 0.05° × 0.05° bins. Panel (b) depicts individual vertical flight profiles of CH_4 and the mission mean. P10, P50 and P99 represent the 10^{th}, 50^{th} and 99^{th} percentile, respectively.

6.4.2 Urban case study: Manila

On March 20th (F06) HALO flew towards the south to perform up- and downwind measurements of Manila, the capital of the Philippines. With its ~13 million inhabitants it is the 18th biggest city in the world (as for 2015; UN, 2018a) and the most densely populated one. The area surrounding Manila has a unique topography and thus emission distribution and wind situation, as depicted in Fig. 6.20.

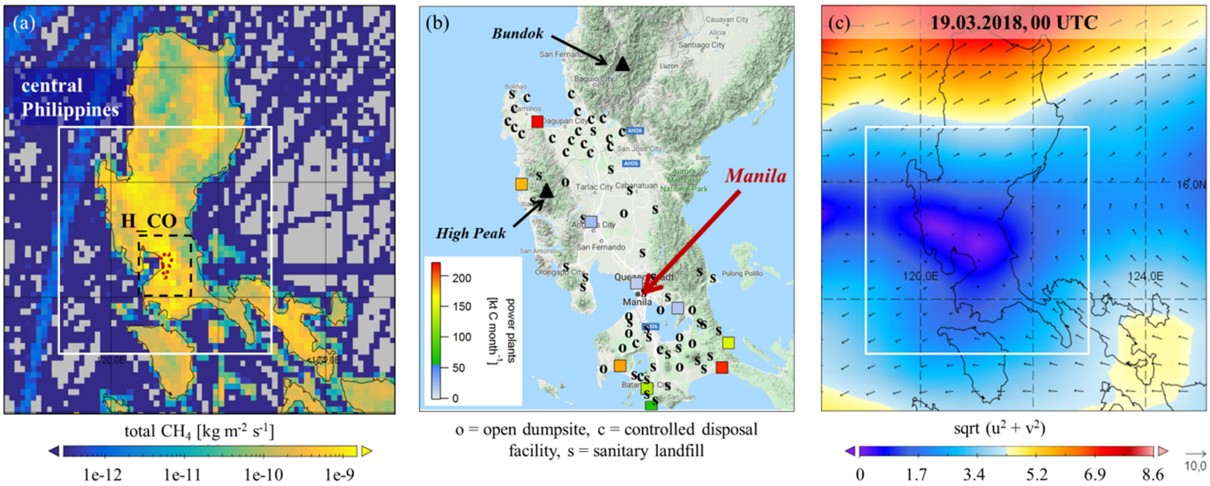

Figure 6.20: (a) Total CH_4 emissions for the year 2015 from EDGAR v5.0. Central Philippines are marked by a white square and the source region specified for the HYSPLIT runs is marked with a black square (H_CO tracer). The city boundary of Manila is indicated by the dotted black line. (b) Topography from Google Maps. Superimposed are locations of power plants, colour-coded according to their monthly carbon emissions in March 2018 (Oda and Maksyutov, 2015). Landfills are also highlighted (personal communication Environmental Management Bureau, Solid Waste Management Division, 2018). Note that this panel is slightly enlarged. (c) ERA-Interim reanalysis wind situation at 850 hPa on March 19th, 2018, 00 UTC.

The lowlands extend from Manila towards the north (panel b) and host the main traffic routes, the majority of the population and most of the industry. They are flanked by mountains to the east and west with summits up to 2000 m (High Peak) and 2800 m (Bundok). Hence, high emission rates of CH_4 concentrate around Manila and the lowlands, as apparent in the total CH_4 emission distribution from EDGAR v5.0 (panel a). The central Philippines (indicated by the white square) are dominated by CH_4 emissions related to the sector agricultural soils (~36 %), which includes emissions from rice cultivation, followed by wastewater treatment (~18 %), solid waste landfills (~15 %) and enteric fermentation (~12 %). Panel (b) includes locations of power plants which are colour-coded according to their monthly carbon emissions in March 2018 from the ODIAC (Open-Data Inventory for Anthropogenic Carbon dioxide) fossil fuel emission dataset (Oda and Maksyutov, 2015). Locations of landfills, which are a significant source of CH_4, are marked with “o” for open dumpsite, “c” for controlled disposal facility and “s” for sanitary landfill (personal communication Environmental Management Bureau, Solid Waste Management Division, 2018). An open dumpsite is an open site without a pollution control system, while a sanitary landfill has impermeable layers as protection. The landfill locations are only roughly specified since the only available information was the municipality. However, it is obvious that most landfills are located either in the north of the peninsula, like the highest CO_2 emitting power plant

(~380 kt C month^{-1}; Oda and Maksyutov, 2015) or south of Manila. Exemplarily, the ERA-Interim reanalysis wind situation at 850 hPa and 00 UTC is depicted in panel (c). Along the lowlands, very low wind speeds are present which may allow for the accumulation of emissions.

The flight track of HALO is depicted in Fig. 6.21a and is colour-coded according to the measured CH_4 mole fractions with elevated CH_4 in two areas west of Manila. The corresponding trace gas time series is shown in panel (b), where H_CO denotes the HYSPLIT simulated CO enhancements from Manila (for area definition see Fig. 6.20a). HALO headed towards the Philippines and first overflew the city of Manila at an altitude of ~2.6 km. The upwind transects east of the city followed at ~1.6 and ~2 km, roughly between 1 and 2 UTC. The three downwind transects were obtained at stacked flight altitudes of ~1.7, ~1.5 and ~1.3 km until ~4 UTC. The observed CH_4 enhancements, encountered at the three downwind transects, can be divided into two plumes, one in the north and one in the south. They are marked with P1 and P2, respectively.

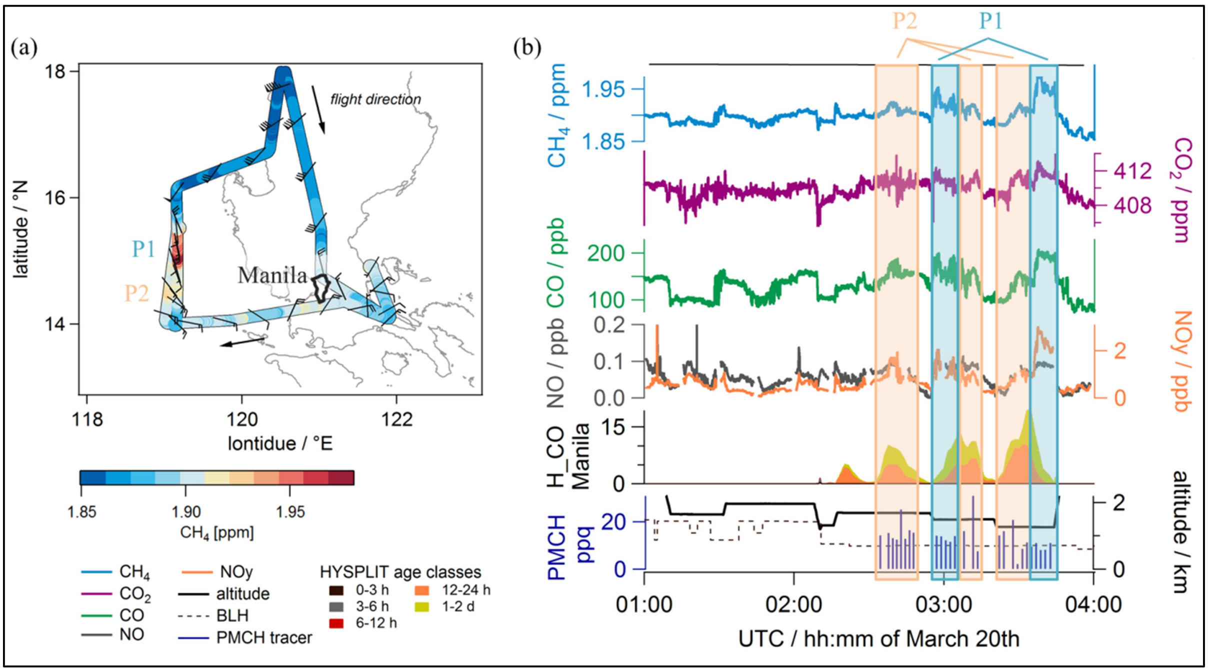

Figure 6.21: (a) HALO flight track colour-coded according to the measured CH_4 mole fractions. Arrows denote the flight direction. The bold black line denotes the spatial extent of Manila. (b) Time series of CH_4, CO_2, CO, NO, NO_y, HYSPLIT modelled CO enhancement, PMCH tracer (H. Schlager), flight altitude and boundary layer height retrieved from ERA-Interim reanalysis data at 3 UTC. The plumes P1 and P2 mark CH_4 enhancements at the downwind flight transects. The local time in Manila is UTC +8 h.

P1 marks a plume with strongly enhanced CH_4 mole fractions in the northern part of the downwind flight track, which was observed at two different altitudes. Maximum measured CH_4 reaches ~1.95 ppm (Δ of ~50 ppb) at the 1.5 km flight transect and ~1.99 ppm (Δ of ~90 ppb) at 1.3 km, hence mole fractions increase with decreasing flight altitude. The same feature is also present in CO and NO_y. In contrast, NO and CO_2 remain relatively stable. Fo CO_2 it is not surprising as the Philippines are the Asian country with lowest CO_2 emissions of only ~150 Mt CO_2 in 2018 (see Fig. 6.1b). The northern edge of P1 could not be determined as the flight altitude was changed before reaching background mole fractions. A second plume

(P2) is distinguishable in the southern part of the flight track with lower, but consistent CH_4 mole fractions of ~1.92 ppm at the three different altitude transects. Downwind of Manila the H_CO tracer is simulated at all three flight levels with highest mole fractions in the lowest flight leg. The P2 plume shape agrees better with the H_CO enhancements from Manila than P1. However, HYSPLIT has the disadvantage that it represents the topography of the Central Philippines with a maximum terrain height of only ~900 m, hence the simulated transport may not be accurate. A PMCH tracer (similar to the one described in Sect. 6.3.2) was released from 05:05 to 06:11 UTC the day before the flight in central Manila (rooftop of One Corporate Center) and was detected aboard the aircraft. Its average mole fractions decrease with height (15.5, 14.9 and 10.9 ppq, respectively) unlike CH_4, CO, NO_y and the H_CO tracer.

As shown in Fig. 6.20b and c, the area surrounding Manila is characterised by lowlands with a mountain range to its east and west. The topography also affects the wind situation of the lower troposphere, inducing a stagnation of the easterly winds along the valley. This unique setting leads to the assumption that P2 may only corresponds to air masses directly from Manila, while P1 can be a mixture of air masses from Manila and from sources in the northern valley, which in turn might have been accumulated the night before and transported through the valley towards the flight track. This is supported by highest PMCH mole fractions sampled within P2 and by the lower NO/NO_y ratio in P1 compared to P2. Hence, P2 might be of fresher air masses than P1, which in turn experienced chemical conversion during their way through the valley.

In summary, Manila and the surrounding area is particularly interesting for CH_4, while CO_2 showed no distinct behaviour. The complex topography however hampers a clear attribution of the origin of air masses without a small scale numerical model accurately representing the orography.

6.4.3 GHG outflow observed in the free troposphere

During EMeRGe-Asia a prominent pollution event, other than individual urban outflows, was observed persistently during four flights (F04, 05, 08 and 09). At an altitude of ~3 to ~5 km, well-defined and large-scale plumes with enhanced CH_4 and CO_2 mole fractions were distinguishable from the free tropospheric background. They extended over ~140 to ~300 km in the horizontal and have been observed at different times (~7, 5, 4 and 2 UTC, respectively). Two of the GHG plumes, detected during F04/F09, are discussed in detail (see Fig. 6.22). The time series of both flights is presented in panel (a) and (b), respectively. The GHG plumes, both with an extent over ~300 km, are marked with a black rectangle. The enhancements of roughly 40/30 ppb CH_4 and 5/4 ppm CO_2 show similar magnitudes as observed during flight transects in the BL. The gradients at the edges of the defined plumes during F04 are sharper than during F09.

Backward trajectories are started from the GHG plumes using HYSPLIT, see panel (c) and (d). They suggest that the plume in F04 could be the result of a Long-Range Transport (LRT) event from mainland China. Weather charts at 500 hPa of geopotential and vertical velocity on March 15th (*wetter3.de*) indicate uplift ahead of a cold front. Such LRT events of CO_2 were previously analysed by e.g. Kim et al. (2015b) using a combination of observations (ground-based, satellite) and simulation results. They attributed almost half of the elevated CO_2 mole fractions in eastern China, Korea and Japan to emissions from central and eastern China. Although CO_2 is well-mixed around the globe, it shows regional characteristics of human activities, similar to air pollutants like CO or SO_2, which have been used as tracers for LRT events at the intercontinental scale for a long time. Shirai et al. (2012) analysed CO_2 measurements aboard a commercial aircraft (CONTRAIL, Comprehensive Observation Network for TRace gases by AIrLiner) using vertical profile observations over Narita (Japan) together with transport model simulations. They concluded that the variability of free tropospheric CO_2 mole fractions, especially prominent and frequent in spring, is mainly caused by CO_2 advection from East Asia. HYSPLIT backward trajectories released from the GHG plume in F09 indicate that air masses stayed at low altitudes for ~100 h. This low level outflow is connected to occur behind a cold front passing Korea on March 24th (*wetter3.de*), hence trajectories also passed Korea and/or northern China prior to the measurement.

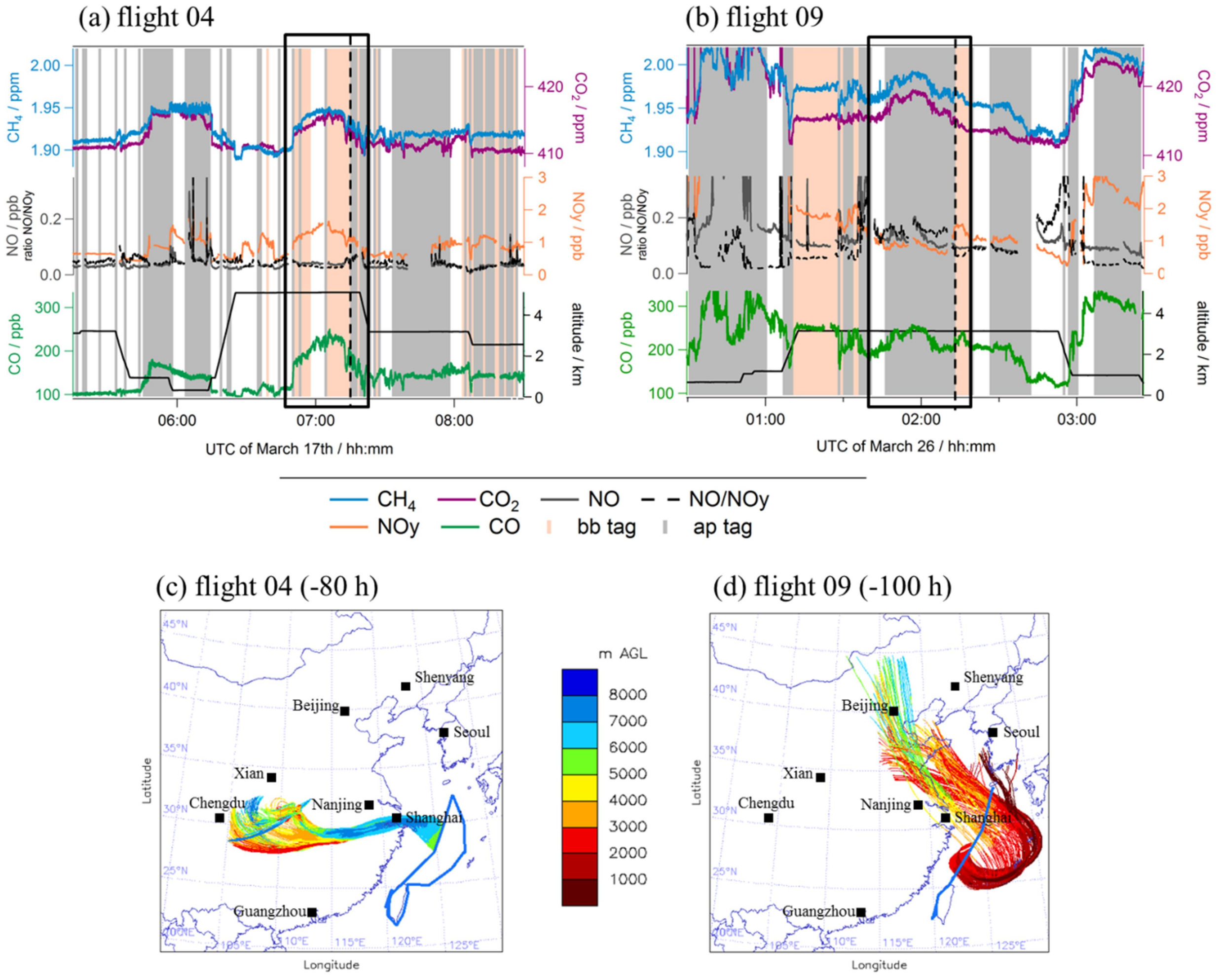

Figure 6.22: (a and b) HALO time series of CH_4, CO_2 NO, NO_y and CO during flight 04 (17.03.2018) and 09 (26.03.2018), respectively. The black squares indicate GHG plumes of large spatial extent. The black dashed line subdivides this plume into a biomass burning (bb) and anthropogenic pollution (ap) influenced part according to a tagging mechanism by E. Förster (KIT). (c and d) HYSPLIT backward trajectories started from both plume encounters for F04 (09) at 07 UTC (02 UTC) which reach 80 h (100 h) backward in time.

Collocated enhancements of CO_2 and CH_4 are also observed in CO, pointing towards air masses, which were possibly influenced by combustion processes. Based on Acetonitrile (ACN) and Benzene (BEN) observations taken aboard the aircraft, thresholds were identified above which an air mass can be tagged according to the influence of either biomass burning (bb; exceedance of ACN threshold) or anthropogenic pollution (ap; exceedance of BEN threshold without exceedance of ACN threshold) (E. Förster, PhD thesis under preparation). It should however be noted, that the bb tag can be overlaid by anthropogenic pollution as BEN can be a source of both, ap and bb. Hence, both GHG plumes during F04 and 09 can be subdivided into two minor plumes influenced by emissions from bb and ap, as indicated by the background colours in panel (a) and (b). This tagging is consistent with the observed changes in NO and NO_y mole fractions. While for the bb parts, NO_y is enhanced and NO is relatively low, the ap part shows enhanced NO but background NO_y mole fractions. Fire maps, based on VIIRS and MODIS from NASA Worldview indicate fires on March 14th and 15th in central China, collocated with the HYSPLIT trajectories originating from the surface for F04. At the corresponding times for F09, fires were occasionally detected along the western Korean coast, and more distinct further north of Korea.

The GHG plumes from F05 and 08 were analysed in the same way and their time series can be found in the Appendix (A.13). For F05, CO_2 and CH_4 enhancements (up to 3 ppm and 30 ppb respectively) are observed over a horizontal distance of roughly 250 km at ~5 km altitude. The tagging indicates solely an influence of bb. For F08 the plume (up to 20 ppb CH_4 and 3 ppm CO_2) extends over ~140 km and is characterised by ap. HYSPLIT trajectories indicate for both an origin from China, while for F05 also an influence of SE Asian emissions is possible, and for F08 from central Asia.

Tracer-tracer correlations

Tracer-tracer correlations of CH_4 against CO_2 and CO are analysed as depicted in Fig. 6.23. It is distinguished between the different flights (04, 05, 08 and 09), as well as between the bb and ap plumes of F04 and 09 (each labelled with P1 and P2).

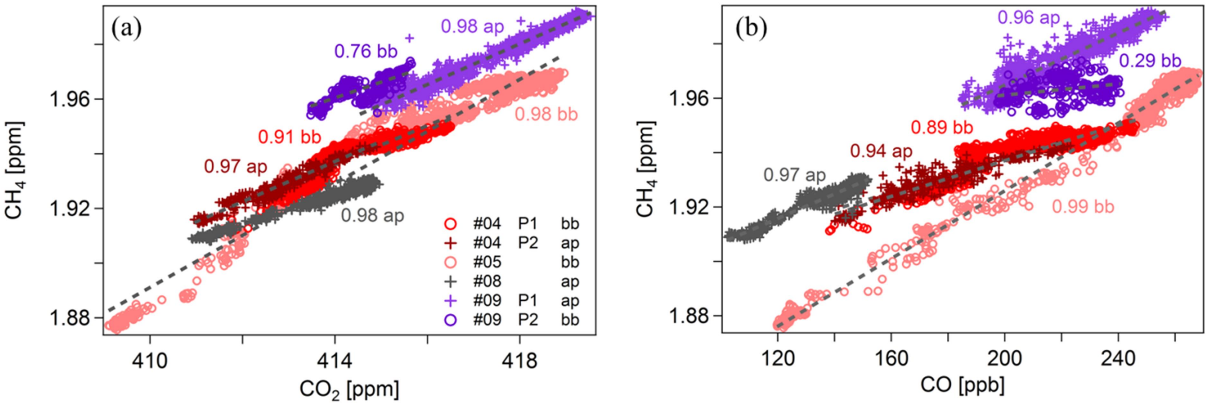

Figure 6.23: Correlations of CH_4 with (a) CO_2 and (b) CO in the six observed free tropospheric GHG plumes. For the separation into biomass burning (bb) and anthropogenic pollution (ap), a tagging mechanism by E. Förster was used (PhD thesis under preparation). The values denote correlation coefficients.

The correlation coefficient from CH_4 and CO_2 is close to one (0.91 to 0.98) for each of the six described plumes. In general, such correlations occur when either both gases share the same emission source or they are the result of mixing from various sources, which are collocated. Given the fact, that these correlations were observed far away from a potentially large area source, the latter is more likely. Further, during mixing of two homogenous reservoirs, i.e. the polluted BL air and the rather clean free tropospheric air, such a linear mixing line establishes only if the distribution and dilution of the plume with inert species is only influenced by dynamics (e.g. McKeen et al., 1996; Wang and Zeng, 2004). In the case of CO_2 and CH_4, the lifetime of the tracers is longer than the mixing time, hence maintaining the "footprint" of the source region for the four selected plumes. Since the atmospheric lifetime of CO (order of a few months) is also much longer than the considered timeframe of a few days, the same picture is valid for the correlation of CH_4 and CO, see panel (b). One exception stands out: the correlations of the bb dominated plume P2 in F09 is weak in both cases, but especially for CH_4/CO (0.29). Hence, indicating that this part of the plume might have experienced a different dynamical transport.

Enhancement ratios

Enhancement ratios between ΔCH_4 and ΔCO, as well as between ΔCO and ΔCO_2 are derived for the three tagged ap plumes (F04, 08 and 09) to gain more information on their source region. The enhancement ratios of the plumes are presented in Fig. 6.24 as triangles and are compared to observational studies as outlined below, grouped roughly according to the origin of the pollution plumes.

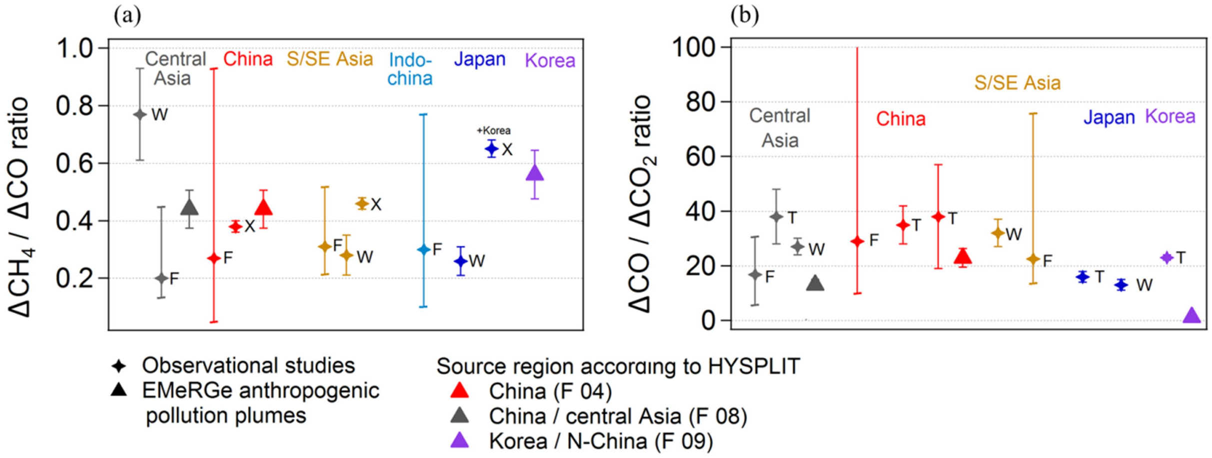

Figure 6.24: Enhancement ratios for (a) $\Delta CH_4/\Delta CO$ and for (b) $\Delta CO/\Delta CO_2$ for different pollution plumes. Triangles indicate the three GHG plumes, observed during EMeRGe, with an influence of anthropogenic pollution (ap) at middle altitudes (same colours as in Fig. 6.23). For the ratios, the area between the plume edges was defined using trapezoidal integration including an error of 10 %. Stars indicate ratios from published observational studies (W=Wada et al., 2011; X=Xiao et al., 2004; F=Fu et al., 2015, T=Takegawa et al., 2004).

With respect to $\Delta CH_4/\Delta CO$ similar enhancement ratios indicate that they can be used as an indicator for the chemical charcterisation of polluted air masses from specific source regions. Wada et al. (2011) (marked by "W") analysed Asian continental pollution being frequently transported in spring towards the ocean by cold frontal systems moving eastwards. The pollution, as defined of a ΔCO being enhanced by more than 2σ over more than 4 h, was measured by three ground-based stations in the western north Pacific for 10 years. The stations were influenced by other source regions as well: indicated in blue are local Japanese sources which contribute to the station measurements throughout the year. Indicated in yellowish are S/SE Asian emissions which are usually related to emissions of rice fields, but in spring the influence is minimal. And indicated in grey are emissions from central Asia, in this case from higher latitudes with less CO from pollution and more dominant CH_4 emissions from Siberia. Hence, the highest $\Delta CH_4/\Delta CO$ ratio is obtained. Xiao et al. (2004) (marked by "X") analysed airborne observations in the Asian outflow over the Pacific during the TRACE-P (TRAnsport and Chemical Evolution over the Pacific) campaign in spring 2001. Observations were clustered into Chinese outflow (indicated in red), tropical Asian outflow (indicated in yellowish) and Japanese/Korean outflow (indicated in blue). Fu et al. (2015) (marked by "F") analysed pollution events (as defined by elevations of at least 10 ppb CH_4 and 20 ppb CO) from three ground-based sites in NW and SW China between 2007 and 2010. They grouped the observations according to emission influences from mainland China (indicated in red), South Asia (indicated in yellowish), Indochina (indicated in light blue), and Central Asia (indicated in grey).

The $\Delta CH_4/\Delta CO$ ratio of the plumes observed during flight F04 (in red) and 08 (in grey), for which trajectories indicate an influence of Chinese and central Asian emissions, are consistent to each other (0.44) and with ratios from the previously discussed studies. The plume observed during F09, where trajectories pass Korea and northern China, is an outlier with a higher $\Delta CH_4/\Delta CO$ ratio than compared to the other two flight, alike the Japanese/Korean plume from Xiao et al. (2004). Kim et al. (2015a) reported from a decrease in average CO emissions in seven major South Korean cities by ~76 % between 1989 and 2013 due to technological improvements, emission mitigation strategies, and a shift from coal and oil to natural gas and nuclear power for energy production. This supports the observed pattern in this study, i.e. the Korean plume exhibits higher $\Delta CH_4/\Delta CO$ ratios than the plumes originating from the Chinese mainland.

Observed $\Delta CO/\Delta CO_2$ ratios are also available from Wada et al. (2011) and Fu et al. (2015) which exhibit similar ranges, except for emissions influenced from Japan which show slightly lower $\Delta CO/\Delta CO_2$ values. Takegawa et al. (2004) analysed CO/CO_2 ratios from the aircraft PEACE-A (Pacific Exploration of Asian Continental Emissions Phase A) campaign in January 2002. They state that $\Delta CO/\Delta CO_2$ enhancement ratios are related to the combustion efficiency. Based on emission inventories low ratios result from the combustion of well-processed gases and/or liquid fuels (e.g. prevalent in Japan and South Korea), while higher emission ratios are due to the combustion of poorly processed solid fuels (e.g. prevalent in China). Their airborne measurements (marked by "T") support the inventorial findings and thus can be used as a tracer to investigate the origin of anthropogenic pollution plumes. The obtained $\Delta CO/\Delta CO_2$ ratios for the ap plumes sampled during EMeRGe also agree with the published literature, i.e. for Central Asia and China the ratios are larger than for the plume with influence from Korean emissions.

In summary, it was shown that emissions from the Chinese mainland, being lofted ahead of a cold front or by convection, influence the GHG distribution of downwind regions, similar to findings from the study by Kim et al. (2015b) and Shirai et al. (2012). However, also CH_4 and CO can carry regional "footprint" characteristics after several days of transport, similar to CO_2, which was indicated by the strong tracer-tracer correlations and the consistent $\Delta CH_4/\Delta CO$ and $\Delta CO/\Delta CO_2$ enhancement ratios from EMeRGe compared to already published observational studies.

6.4.4 Local GHG emissions at Taiwan's west coast

In contrast to the large-scale GHG events (Sect. 6.4.3), distinct narrow peaks in CO_2 and CH_4 with horizontal extents of less than 50 km were observed at Taiwan's west coast at lower altitudes. Since HALO was stationed in Tainan during the mission phase, air masses along the western coast were sampled during almost every flight, allowing for a large dataset of observations. The respective flight tracks are indicated in orange in Fig. 6.25a. The CO_2 and CH_4 measurements are presented in panel (b), together with the flight altitude, and are strung together to obtain a comprehensive time series. The highest population density of Taiwan is concentrated to the west of the island, as indicated by the coloured map in panel (a).

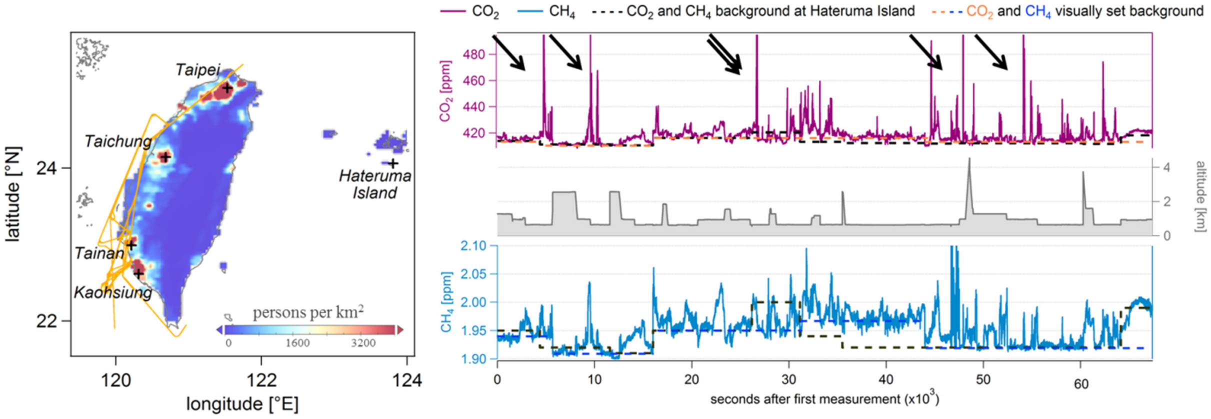

Figure 6.25: (a) HALO flight tracks at Taiwan's west coast. Colour-coded underneath is the population density (CIESIN, 2018), similar to Fig. 1.1. (b) Time series of CO_2, CH_4 and flight altitude along the selected flight tracks. Measurements are concatenated one after another. CO_2 axis is cut at 500 ppm, but peaks reach up to 780 ppm. In addition, ground-based CO_2 and CH_4 observations obtained at Hateruma Island (background station located east of Taiwan) are indicated as black dashed lines. CH_4 and CO_2 data are provided by Yasunori Tohjima and Hitoshi Mukai, respectively, from NIES (personal communication, 2018 and 2019, respectively). For comparison, a visually set GHG background for the respective flight tracks is indicated in colour (see the discussion in the text).

CO_2 emissions from power plants account for ~40 % of Taiwan's total CO_2 emissions (Oda and Maksyutov, 2011), and such point sources are also responsible for large uncertainties in gridded inventories (Oda and Maksyutov, 2011; Hogue et al., 2016). Power plants located in Taiwan are shown in Fig. 6.25a as triangles and are colour-coded according to their monthly carbon emissions in March 2018 (Oda and Maksyutov, 2015). The Taichung power plant is located at Taiwan's west coast and is the highest CO_2 emitting power plant in the world. Emissions are estimated with ~36 Mt CO_2 in 2009 according to CARMA v3.0 (CARbon Monitoring for Action). With respect to the emission strength, this power plant is comparable to CO_2 emissions from entire megacities like London (~ 32 Mt CO_2; Pitt et al., 2019).

During three flights (05, 08 and 12), six CO_2 peaks were detected with mole fractions larger than 500 ppm, reaching up to 780 ppm. They are indicated with black arrows in Fig. 6.25b and clearly stand out from the remaining measured CO_2 mole fractions. All six plumes were encountered downwind of the Taichung power plant, as indicated by the red markers in Fig 6.26a. The black wind barbs represent the wind direction measured aboard HALO while crossing the plume. The CO_2 peaks can further be clearly distinguished in the correlation plot in panel 6.26c (also marked in red). A CO_2 emission rate ranging from 17 to 53 Mt CO_2 a^{-1} was derived from the plumes of the Taichung power plant, using a simplified mass balance approach. Compared to the approach described in Sect. 2.2.2, only the average value for pressure, temperature, wind direction and wind speed was used, as well as the absolute CO_2 enhancement (max. minus background; described later). The wind direction had to be corrected due to not crossing the plume perpendicularly, thus, the width of the plume was roughly estimated to be one third of the flown aircraft distance. It is assumed, that the plume does not extend over more than 500 m in the vertical. The CARMA estimate of the Taichung power plant (~36 Mt CO_2) is within the calculated range of 17 to 53 Mt CO_2 a^{-1}. A lower emission rate is, however, also possible as CO_2 emissions of the power plant might have been reduced since 2009. An environmental report from 2015 states that already 1175 t CO_2 a^{-1} were reduced by introducing a photovoltaic system (Taiwan International Ports Corporation, 2015). Another newspaper article from 2017 revealed, that due to unhealthy levels of air pollution, coal consumption should be reduced by 24 %, which would also result in reduced CO_2 emissions (Taiwan News, 2017). However, the range and uncertainty of estimated CO_2 emission rates is large, and definitely too large to make a proper emission estimate. Small-scale model simulations are needed to gain information on the horizontal and vertical extent of the plume in order to narrow down the estimated range.

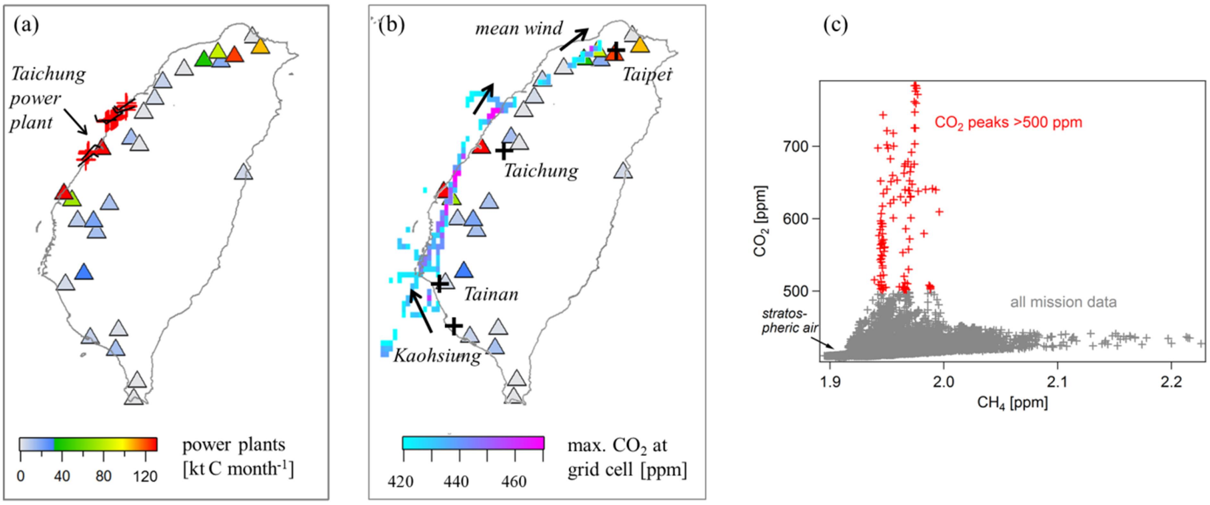

Figure 6.26: Panels (a) and (b) show Taiwan with its power plants (triangles), colour-coded according to their carbon emissions in kt per month, valid for March 2018 (Oda and Maksyutov, 2015). (a) Red markers are detected CO_2 plumes with mole fractions larger than 500 ppm. They are sampled downwind of the Taichung power plant as indicated by the measured wind direction aboard HALO (black barbs). (b) Maximum measured CO_2 (without the Taichung power plant plumes) as observed during all flights at the western coast of Taiwan in a latitude longitude grid of 0.05° × 0.032°. (c) Correlation of CO_2 and CH_4 of all research flights during EMeRGe-Asia. Red markers denote the Taichung power plant plumes.

In the next step, to allocate the remaining CO_2 peaks, an atmospheric background for each flight day was visually set (see orange dashed line in Fig. 6.25b). In case the wind blew from the east, the visually set background agrees well with the ground-based measurements at Hateruma Island (provided by Yasunori Tohjima and Hitoshi Mukai from the National Institute for Environmental Studies, NIES). The observational station is located on a small island east of Taiwan (see Fig. 6.25a) and is measuring clean pristine marine air under easterly winds. This individual background, as well as the Taichung power plant peaks, were removed from the data and the remaining measurements were gridded into bins of 0.05° × 0.032° and the maximum measured CO_2 mole fraction was derived in each bin, see Fig. 6.26b. Several hotspots (pink colours) can be distinguished, where the mean wind direction also indicates several power plants located upwind. The southernmost hot spot could be from the city Kaohsiung.

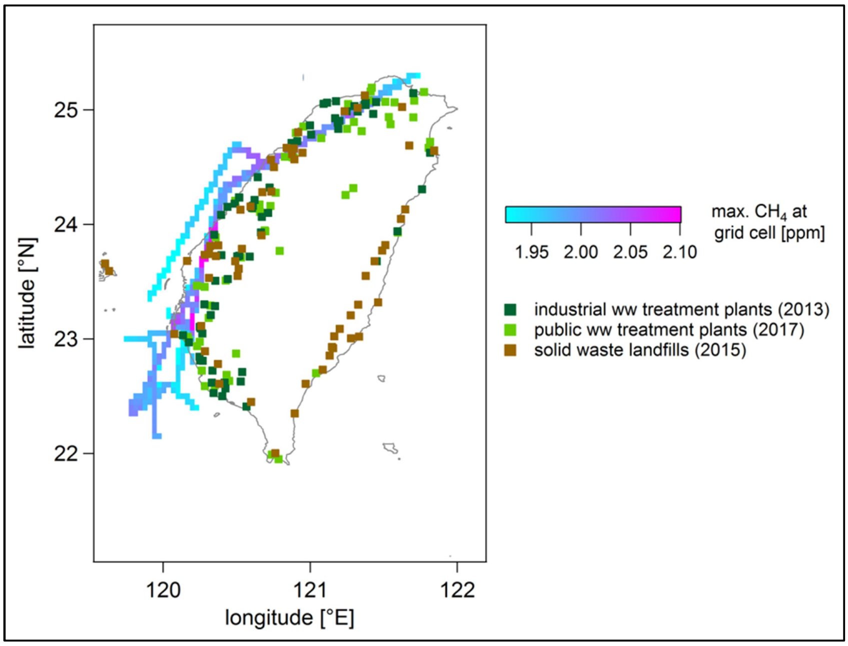

Figure 6.27: Maximum measured CH_4 during all flights at the western coast of Taiwan in a latitude longitude grid of 0.05° × 0.032°. Information on wastewater treatment plants (industrial and public) and landfills were provided from Chuan-Yao Lin (Academia Sinica, personal communication 2018).

With respect to CH_4, wastewater and solid waste disposal account for ~40 and ~20 % of total CH_4 emissions in Taiwan (EDGAR v5.0). Emissions from rice cultivation are estimated to contribute another ~15 %. However, according to Bartlett et al. (2003) the months March and April show, compared to the rest of the year, lowest emissions from rice paddies and natural wetlands. A modelling study of CH_4 emissions from rice paddies in Taiwan indicates that less than 10 % of CH_4 is emitted during the first crop season, which is usually from February to July, the remaining ~ 90 % are emitted in the second crop season from August to January (Liu and Wu, 2004). Hence, this source can be neglected for this study and it is assumed that encountered atmospheric CH_4 signals are dominated by emissions from urban and industrial sources. Industrial and public wastewater treatment plants, as well as solid waste landfills are shown in Fig. 6.27 (provided by Chuan-Yao Lin from Academia Sinica, personal communication 2018). They especially concentrate along the entire western coast and most probably contribute to the observed CH_4 distribution. Similar to CO_2, the background for CH_4

was removed, the data was gridded and the maximum measured CH_4 was estimated. Highest CH_4 mole fractions are detected at the south western coast. However, the enhancements extend much more in the horizontal and are thus broader compared to the point-like distribution of CO_2 maxima. This agrees well with the spread of landfills and sewage treatment plants along the west coast.

In summary, CO_2 measurements at the western coast of Taiwan were shown to be strongly influenced by local power plant emissions from Taichung. Observed CH_4 enhancements are also influenced by emission sources at the western coast, which are, however, spatially more dispersed.

6.5 Discussion

6.5.1 Comparison of spatial GHG distributions in Asia over time

Seventeen years before the EMeRGe-Asia mission took place, an airborne field campaign, called TRACE-P, was conducted by NASA, providing an opportunity to compare both measurement data sets. The flights were conducted between February and April of 2001 in the same region as the flight routes of EMeRGe. Both CO_2 (Vay et al., 2003) and CH_4 (Bartlett et al., 2003) mole fractions were measured aboard the aircraft.

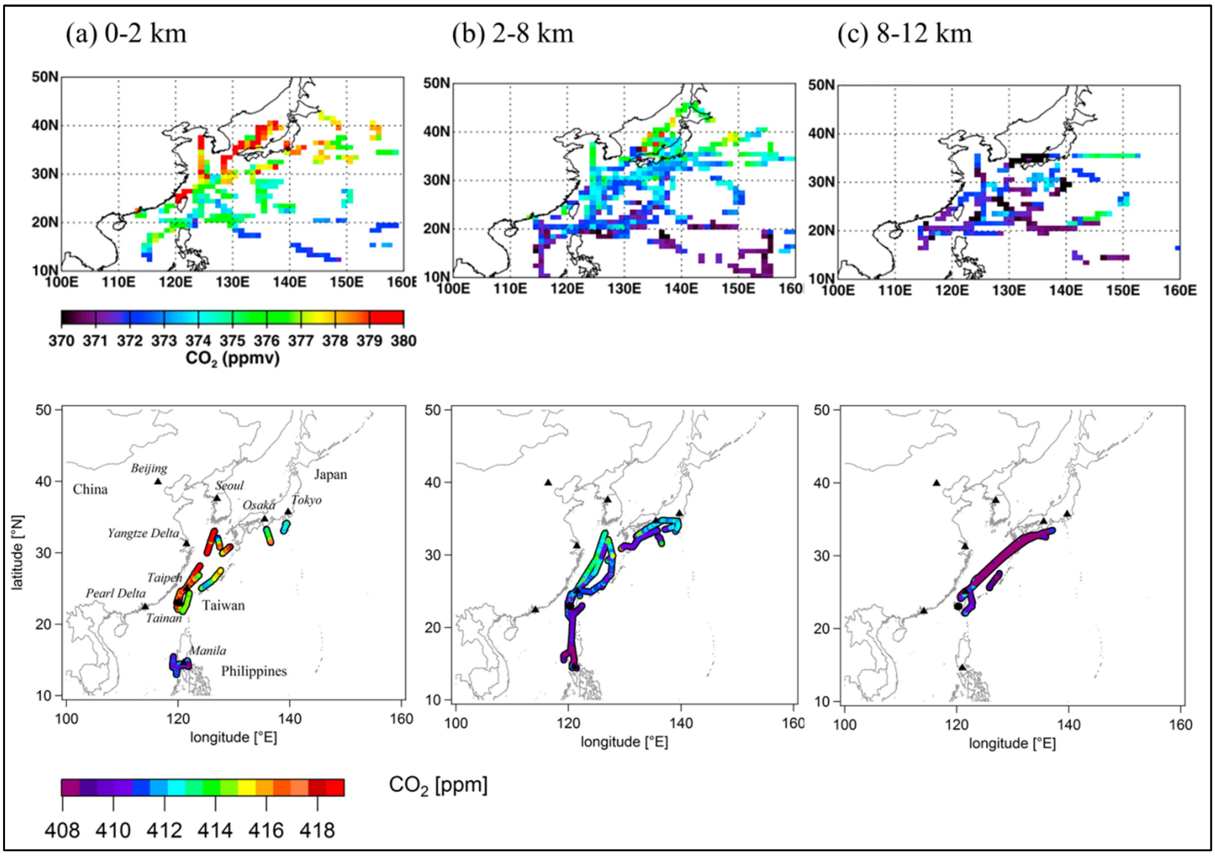

Figure 6.28: CO_2 observations in the Asian region for three different altitude regions: (a) 0 to 2 km, (b) 2 to 8 km, (c) 8 to 12 km. Upper row: average observations during TRACE-P in 2001 in a 1° latitude by 1° longitude grid (adapted from Vay et al.; 2003). Lower row: average observations during EMeRGe-Asia in 2018 in a 0.05° by 0.05° grid. Observations reach up to 12.5 km.

Figure 6.28 presents mean CO_2 observations for three different flight altitude regions from both campaigns, TRACE-P and EMeRGe-Asia. Although the average CO_2 mole fraction increased by nearly 40 ppm, the spatial patterns are highly similar. The highest CO_2 mole fractions are observed below 2 km and near the Chinese mainland, as well as close to western Taiwan. In panels (a) and (b), lower CO_2 is generally observed in the tropics (<20 °N) than in the extra-tropics. CO_2 decreases with altitude, but the continental outflow extends up to the middle troposphere. There is a clear latitudinal variability at lower altitudes that becomes less pronounced with increasing altitudes. Hence, the spatial distribution of emission sources, transported by the prevalent weather processes during spring, may not have changed much since 2001. During TRACE-P, lower values of CO_2 were observed with a mean of 374 ppm (367 to 416 ppm), compared to EMeRGe with a mean of 414 ppm (404 to 784 ppm). Globally, CO_2 values are increasing and have been recorded since the mid-70s at Mauna Loa (see Sect. 2.1.2). As both airborne missions were performed during spring (Feb-Apr 2001; March-April 2018), the seasonal cycle of CO_2 can be neglected. Considering only the accumulated growth rate of ~37 ppm CO_2 from 2001 until 2017, the difference between the campaigns' averages (~40 ppm) is explainable.

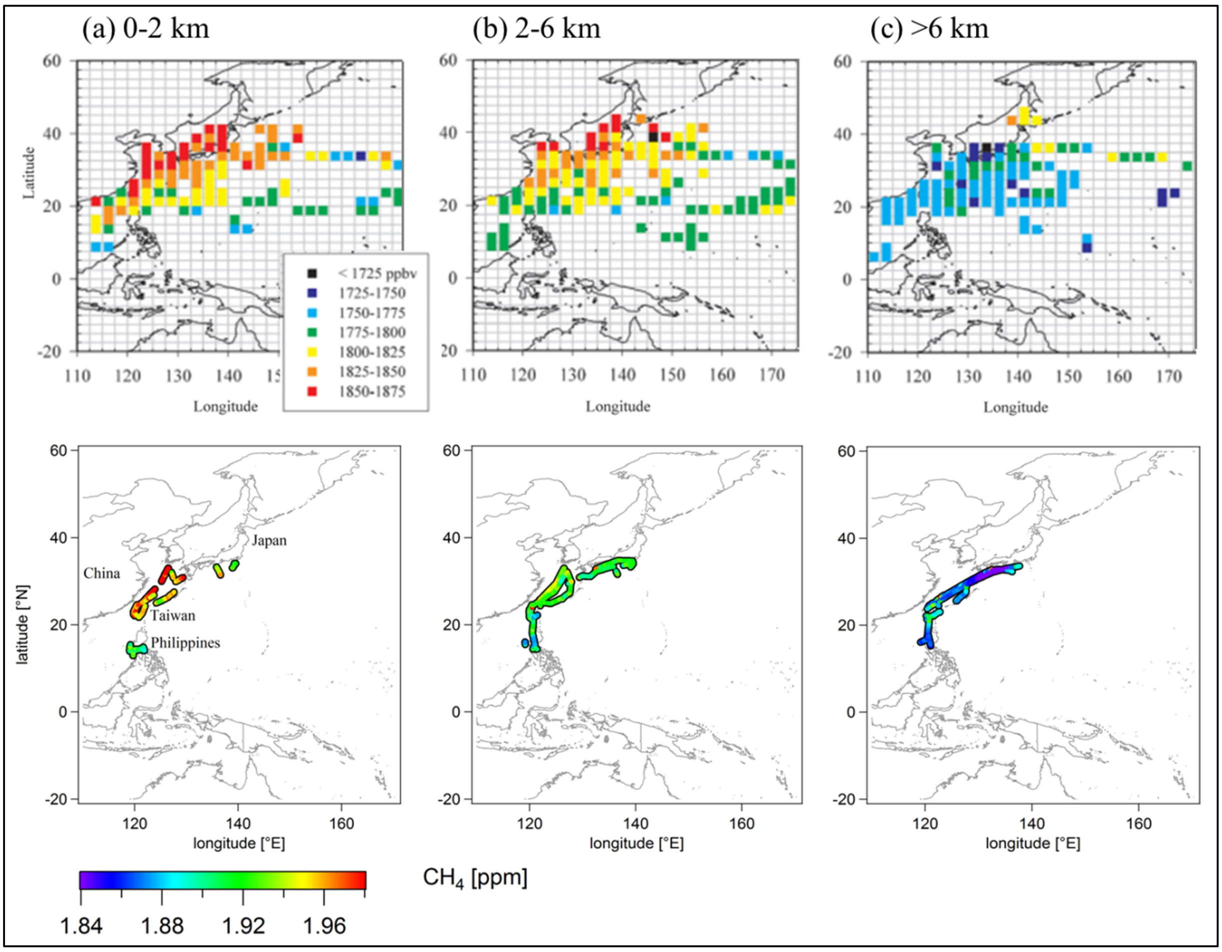

Figure 6.29: CH_4 observations in the Asian region for three different altitude regions (a) 0 to 2 km, (b) 2 to 6 km, (c) above 6 km. Upper row: average observations during TRACE-P in 2001 in a 2.5° latitude by 2.5° longitude grid (adapted from Bartlett et al., 2003). Lower row: average observations during EMeRGe in 2018 in a 0.05° by 0.05° grid. Observations reach up to 12.5 km.

Figure 6.29 presents mean CH_4 observations from both campaigns within the altitude ranges of 0-2 km, 2-6 km and above 6 km. Again, similarities in the general distribution are prevalent. The highest mole fractions are observed off the Chinese mainland at altitudes between 0 and 2 km. For the altitude bin of 2-6 km TRACE-P shows pronounced enhancements detected between the mainland and Japan, where EMeRGe did not perform any flights. Towards the tropics, CH_4 generally decreases in these altitude ranges. Above 6 km, CH_4 mole fractions are lower and the latitudinal gradient is less pronounced. The mole fractions in highly polluted air are roughly similar with a maximum of 2188 ppb measured during TRACE-P and 2226 ppb during EMeRGe. In terms of the mean CH_4 mole fraction, the value of TRACE-P is roughly 140 ppb smaller than during EMeRGE with 1790 ppb compared to 1927 ppb, respectively. The accumulated growth rate within the last seventeen years of ~81 ppb CH_4 is not sufficient to explain the difference.

6.5.2 Comparison of vertical GHG profiles from Europe and Asia

The mean vertical profiles of CO_2 and CH_4 from EMeRGe are shown in blue (Europe) and red (Asia) in Fig. 6.30. Solid lines represent the 50th percentile and dashed lines the 90th percentile. For comparison, mean vertical profiles observed from two aircraft campaigns, KORUS-AQ (KORean-United States Air Quality; *https://espo.nasa.gov/korus-aq*) and TRACE-P, are shown as grey triangles. KORUS-AQ, the more recent campaign, focused on air pollution in South Korea during May and June of 2016, performing measurement flights predominantly at its western coast, extending slightly above the Yellow Sea. The TRACE-P campaign, discussed above, analysed the Chinese continental outflow over the Pacific Ocean from February to April of 2001. A commercial and regularly flying passenger aircraft equipped with trace gas analysers to measure CO_2, known as the CONTRAIL project (*http://www.cger.nies.go.jp/contrail/index.html*), departs from Japanese airports. Flight tracks, available within the EMeRGe-Asia time period, cover mainly the South and East China Sea, extending into the Northern Pacific. Their profile is added as grey squares. At the surface, ground-based observations from NOAA Earth System Research Laboratories Global Monitoring Division (*https://www.esrl.noaa.gov/gmd/dv/site/index.php*) are considered for the respective data periods of each aircraft campaign. The average of nine European and nine Asian stations is taken (CO_2 data for one Asian station is only available until 2016).

With respect to CO_2, the increase in mole fractions from 2001 to 2018 is clearly visible. As previously discussed (Sect. 6.5.1), the accumulated growth rate of ~37 ppm CO_2 from 2001 until 2017 agrees with the difference of ~40 ppm between the TRACE-P campaign in 2001 and the EMeRGe-Asia campaign in 2018. While both airborne missions were performed during spring, the seasonal cycle of CO_2 was neglected, which must be considered when comparing different seasons. Hence, the profile of KORUS-AQ from 2016 shows higher CO_2 mole fractions compared to the EMeRGe-Europe campaign in July 2017. The EMeRGe measurements were performed in summer, where the seasonal cycle of CO_2 is at the decreasing slope, and the KORUS-AQ campaign was conducted in May, when the seasonal cycle peaks. The different shapes of the vertical CO_2 profiles can also be explained by the different seasons. During summer (EMeRGe-Europe), CO_2 is lower at the surface due to the uptake of vegetation, but is increasing with height, since the long lifetime of CO_2 allows the gas to be well-mixed around the globe. During spring (KORUS-AQ, EMeRGe-Asia), CO_2 is enhanced at the ground due to the anthropogenic release of CO_2 and absence of biogenic uptake, but decreases with higher altitudes.

The P50 CONTRAIL CO_2 data agree well with the P50 EMeRGe-Asia data from the same time period, even though the flight routes were slightly different, indicating that the EMeRGE mission sampled, despite chasing urban pollution plumes at the lowest altitudes (visible in the 1 km bin), a representative CO_2 distribution throughout the troposphere. The ground-based NOAA CO_2 data complement the airborne vertical profiles towards the ground. However, two exceptions can be named here: KORUS-AQ, where ground-based CO_2 is lower probably due to the aircraft sampling focusing on measuring air pollution in Korea, and EMeRGe-Europe, where ground-based CO_2 is slightly higher perhaps due to the marine and mountainous locations of seven of the NOAA stations.

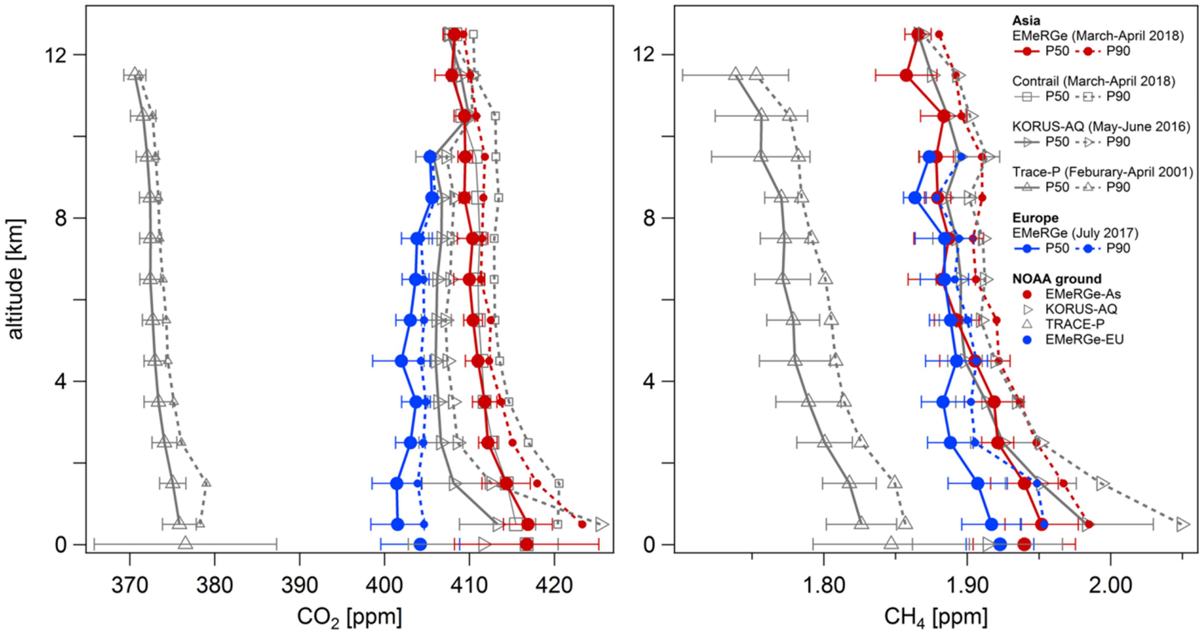

Figure 6.30: Vertical profiles of CO_2 and CH_4 observations (50th and 90th percentile) during EMeRGe-Europe and Asia. Additional vertical profiles are obtained from CONTRAIL data (made available within the EMeRGE community, only available for CO_2), KORUS-AQ (*https://www-air.larc.nasa.gov/cgi-bin/ArcView/korusaq*, last access 31.01.2019), TRACE-P (*https://www-air.larc.nasa.gov/pub/TRACEP/MERGES/DC8_LARC.ICT2010_FORMAT/10_SECOND/*, last access 08.01.2020) and NOAA ground based stations (*https://www.esrl.noaa.gov/gmd/dv/data/*; last access 5.12.2019).

As for CH_4 (see Fig. 6.30b), mole fractions between 2001 and 2018 also show an increasing trend. With respect to the differences between the two continents, Europe and Asia, global satellite observed distributions from SCIAMACHY and GOSAT both depict a clear hotspot of highest CH_4 values in East Asia (e.g. Frankenberg et al., 2006; Turner et al., 2015; Jacob et al., 2016; Maasakkers et al., 2019). The airborne observations from both EMeRGe campaigns show similar measured CH_4 enhancements, i.e. the difference between P90 and P50, at lower altitudes (<6 km). In contrast, the median background is higher (+26 ppb CH_4) in Asia compared to Europe. However, it is difficult to quantify if this difference in the performed airborne measurements is significant enough to agree with the global satellite observations. First, the seasonal cycle of CH_4 is pronounced, i.e. the global mean mole fraction in March

2018 is already 13 ppb higher than in July 2018 (as obtained from in situ Mauna Loa measurements, *https://esrl.noaa.gov/gmd/dv/iadv/graph.php?code=MLO&program=ccgg&type=ts*). Second, the global growth rate in 2018 is 8.29 ± 0.56 ppb (*https://www.esrl.noaa.gov/gmd/ccgg/trends_ch4/*). Hence, by simply adding these two values to the EMeRGe-European mean, the mean difference of 26 ppb would almost be compensated for and is reduced to 5 ppb. Further, the different distances to the sampled source locations between the aircraft measurements in Asia and Europe are not accounted for, hampering the direct comparison of CH_4 measurements on both continents. Mean CH_4 mole fractions obtained from the NOAA ground based stations are included in Fig. 6.30b as well. With respect to the corresponding EMeRGe campaign periods, the ground-based stations exhibit a mean difference of +17 ppb in Asia compared to Europe, which is lower than the difference (+26 ppb) discussed above. The Asian ground based observations show, compared to the lowest altitude bin of the Asian aircraft profile, much lower CH_4 mole fractions, although their standard deviations overlap.

6.5.3 Concluding remarks

The CH_4 observations from EMeRGe-Europe and Asia demonstrate that there is a significant variability of GHG mole fractions, especially at lower altitudes. This often coincided with entering the boundary layer over land (e.g. in the BeNeRuhr area and the Po Valley) or with pollution plumes having been frequently transported towards the sea (e.g. London, Barcelona, Manila). Although CH_4 is known as a well-mixed greenhouse gas, variations in its mole fractions were observed throughout the troposphere, especially the outflow of mainland China was lifted into higher altitudes by convection and cold fronts.

This thesis investigated if urban emissions can be identified and quantified in the regional European and Asian GHG distributions. It was shown that solely based on long-lived GHG, the identification of an urban plume gets more complex with increasing flight (and measurement) distance from the emission sources, since comparatively small GHG signals have to be distinguished from the variable and high atmospheric background mole fractions. With the help of various model tracers (CO tagging from HYSPLIT, city tracer from MECO(n), HYSPLIT backward trajectories) and complementary measurements of species with a much shorter atmospheric lifetime (CO, NO, NO_y) and hence lower atmospheric background, it was, however, possible to identify the urban (mixed) plumes of London, the BeNeRuhr area, Barcelona and Manila in the measured GHG signals. Maximum measured CH_4 mole fractions were in the range of 1.94 to 2.01 ppm, whereby the enhancement above a rough estimated background was between 50 and 80 ppb. The latter confirms the need for precise in situ measurements being able to detect only small GHG enhancements above a relatively large background concentration.

Although different (mixed) urban plumes were identified, a proper quantification of the urban GHG emission strength was hampered. Primarily the flight strategy used within the campaigns was not optimised to account for upwind sampling of the atmospheric species or for sufficient downwind sampling capturing the whole vertical and horizontal extent of the urban plumes. While the upwind sampling might be irrelevant for short-lived species, as long as no prominent sources are located upwind, it is especially relevant for GHG. Due to the long lifetimes of CH_4 and CO_2 they become well distributed in the atmosphere. The insufficient downwind sampling, important for all species, was primarily the consequence of restrictions from diverse air traffic controls in combination with HALO being a rather large aircraft. Hence, the flight routes were not flexible enough to react ad hoc to changes (or not) observed in the various atmospheric mole fractions measured aboard the aircraft. The quantification was also hampered due to the dense population in Europe, where many scattered, smaller cities and large industries surround MPCs. Similarly, the highest population density of China is centred along the entire eastern coast. Hence, the contribution of a single source to the measured GHG signals is hard to identify and to isolate the single urban hot spots, the flight distances from the source should have been decreased. For another airborne measurement campaign focusing on GHG, first, a smaller and more flexible aircraft is recommended, and second, the focus should be on the repeated probing of individual cities to get more confident results.

With respect to Europe, a few research flights were performed where no significantly enhanced GHG signals could be detected from urban areas. For example, Paris was overflown well above the boundary layer (>2 km during F05 and 08) and the flight distance to Rome (F03) and London (F05) was too large (~200 to ~400 km) to be able to distinguish urban emissions from the atmospheric background. By chance, a biomass burning plume near Marseille was probed with enhanced mole fractions of CH_4 up to 2.01 ppm. Its maximum enhancement was more than twice the enhancement of urban emissions probed within the same flight and thus fresh biomass burning plumes can strongly influence local GHG patterns. Such patterns involve a more distinct peak from a bb source compared to much broader peaks from megacities, resulting from many single sources spread over a rather large area. Further, with isotope measurements of $\delta^{13}C$ the general contribution of different emission sources to the total CH_4 budget was analysed.

As for Asia, two prominent features were encountered several times in the GHG measurements allowing their comparison to emissions from urban areas. First, distinct GHG plumes were detected within the free troposphere over distances covering several hundreds of kilometres, but with GHG enhancements comparable to sampled polluted air masses in the boundary layer. It was shown that these plumes were transported from the BL, mainly from mainland China, but during their transport, they were only subject to mixing and not to chemical conversion. Hence, anthropogenic signals from selected regions could be observed after several days of transport in the CO_2 and CH_4 mole fractions. Second, along the western coast of Taiwan strong and relatively narrow CO_2 and CH_4 enhancements could be attributed to emissions from point sources, such as power plants, as well as from more area-like sources, such as landfills and wastewater emissions, respectively.

Several projects in Europe and Asia already investigated emissions as well as transport and transformation processes from major population centres, which have recently been summarised in Zhu et al. (2013). Examples are IMPACT (Integrated Measurement Program for Aerosol and Oxidant Chemistry in Tokyo), PRIDE-PRD (Programme of Regional Integrated Experiments on Air Quality over Pearl River Delta of China), and CAREBeijing

(Campaigns of Air Quality REsearch in Beijing and Surrounding Region). However, their focus was on air quality and not on GHG. While during CITYZeEN (MegaCITY – Zoom for the ENvironment), a project to investigate the eastern Mediterranean, the Po Valley, the BeNeLux region and the Pearl River Delta, CO_2 and CH_4 were measured from SCIAMACHY, published papers mostly focus on satellite retrieval optimisations (e.g. Reuter et al., 2010; Heymann et al., 2012). MEGAPOLI (Megacities: Emissions, urban, regional and Global Atmospheric POLlution and climate effects, and Integrated tools for assessment and mitigation) focused on detailed measurements in Paris, including CO_2 but not CH_4 (Bréon et al., 2015; Ammoura et al., 2016). Hence, with the CH_4 and CO_2 observations from the EMeRGe campaigns in Europe and Asia, performed less than one year apart, an important contribution to the understanding of the variability of the GHG budget on two continents was given.

7 Summary and Conclusion

The two most important anthropogenic GHGs are carbon dioxide and methane, whose atmospheric concentrations are strongly affected by human activities. There is a good understanding of total GHG emissions at the global and national scale, but the knowledge of the smaller spatial and temporal CO_2 emission distribution (e.g. Bréon et al., 2015), as well as the individual contribution of single CH_4 source sectors to the total budget is limited (e.g. Kirschke et al., 2013; Saunois et al., 2017). However, an accurate knowledge of sources and sinks is necessary to monitor mitigation strategies aiming to limit future global warming. Since urban areas accommodate more than half of the world's population, they are recognised as significant GHG emitters (e.g. Kennedy et al., 2012; Zhu et al., 2013). So-called top-down estimates, as applied within this thesis, use atmospheric measurements to independently quantify urban GHG emissions. So far, airborne GHG studies mostly focus on cities in the United States (e.g. Mays et al., 2009; Cambaliza et al., 2015; Ren et al., 2018; Plant et al., 2019; Ryoo et al., 2019; Turnbull et al., 2019), but are limited for European urban centres (e.g. Gioli et al., 2014; O'Shea et al., 2014; Pitt et al., 2019) and are missing for cities in Asia.

Therefore, a CRDS analyser was characterised and deployed within three aircraft campaigns to measure CO_2 and CH_4 downstream of selected European and Asian urban agglomerations. The hypothesis of the present thesis (see Sect. 1.2) is that aircraft-borne in situ measurements are a useful tool for identifying urban CH_4 and CO_2 emissions and for quantifying their source strength. To evaluate this, local scale GHG plumes were studied downwind of Berlin during the $[UC]^2$ campaign. While emission sources for both gases are considered explicitly, sinks of CH_4 can be neglected for this thesis due to the short timescales of only a few hours, but the photosynthetic CO_2 uptake needs to be taken into account. The second part of the hypothesis claims that signatures of urban GHG emissions can also be detected in the regional GHG distribution. This is investigated by studying their impact on the meso- to synoptic scale CO_2 and CH_4 distribution using the data sets gained during both EMeRGe missions. The following research questions, defined to evaluate the hypothesis, have been successfully answered:

Investigations on the local scale – emissions from the city of Berlin in summer 2018

RQ 1) To what extent do annual GHG emissions from different bottom-up inventories agree for a major European capital like Berlin?

The comparison of three GHG emission inventories of different spatial resolution (~10 km to ~1 km), namely EDGAR, CAMS-REG and BERLIN, showed that estimated citywide CO_2 emissions agree among each other in their total value by a factor of ~1.4. They are further consistent in their primary source sector allocation, where ~80 % of total emissions stem from fuel combustion for the generation of electricity and heat. In contrast, CH_4 emissions within Berlin differ by a factor of up to 8 and show an inconsistency in the partitioning of the source sectors. While EDGAR mainly reports emissions related to the waste sector (79 %), CAMS-REG emissions are primarily due to fuel combustion and fuel exploitation (74 %), and BERLIN reports leakages as the strongest CH_4 source (68 %). This demonstrates that even for a major European city like Berlin the knowledge about the contribution of different CH_4

emission sources is limited, although very detailed emission data sets are available.

RQ 2) Can emission rates of GHG be estimated for the city of Berlin from airborne in situ instruments using a mass balance approach?

Airborne in situ instruments allow for fast and accurate measurements and are therefore well suited for a detailed characterisation of urban pollution plumes on spatial scales of few tens to hundreds of metres. Out of five research flights, strong CO_2 and CH_4 signals were clearly distinguishable from the variable background concentrations on July 20th, 2018, roughly 30 to 40 km downwind of the city centre. Moderate wind speed and steady wind direction led to a confinement of the urban emissions within a well-mixed and efficiently capped BL. Using the mass balance approach, a CO_2 emission rate of $1.39 \pm 0.76\,\mathrm{t\,s^{-1}}$ was obtained, where the largest uncertainty (52 %) results from the proper determination of the background mole fractions. For the derived CH_4 mass flux of $5.20 \pm 1.70\,\mathrm{kg\,s^{-1}}$ both, the determination of background mole fractions and uncertainties in wind direction and wind speed, contribute equally to the error (21 and 23 %, respectively). Hence, it is necessary to precisely determine the inflow GHG mole fractions and their ambient variability, even in the case of a relatively isolated city like Berlin. One possibility for an improvement would be to sample up- and downwind in a Lagrangian manner. The mass balance method could not be applied for the other flight days of the campaign due to meteorological (state of the BL, strength of the wind) and external (flight restrictions in the vicinity of major airports, changing wind forecasts) reasons. Hence, multiple attempts are needed to successfully quantify urban GHG emissions from cities.

RQ 3) How do top-down emission rates derived with the mass balance approach compare to bottom-up inventories?

Emission inventories usually report annual average values. To allow for a comparison, the measurement-based emission rates from July 20th were up-scaled to a yearly value. Moreover, in order to compare the same emission area, a footprint of the detected CO_2 and CH_4 plume was inferred using backward trajectory calculations. The derived annual CO_2 emission rate of $\sim 44 \pm 24\,\mathrm{Mt\,a^{-1}}$ is larger than the CAMS-REG ($+13\,\mathrm{Mt\,a^{-1}}$) and EDGAR ($+2\,\mathrm{Mt\,a^{-1}}$) footprint estimate but agrees with the error bars. A larger emission rate might be explained by the fact that observations were performed three years after the latest available year of the inventories. The photosynthetic uptake and release of CO_2 due to vegetation was estimated to be at most 12 % of the anthropogenic flux and is well within the observed variability. Due to the strong temporal variability of domestic heating and traffic, and hence to better reflect the seasonal emission changes, probing Berlin during different seasons would be valuable. With respect to CH_4, the annual emission rate of $\sim 164 \pm 54\,\mathrm{kt\,a^{-1}}$ is almost twice as large as the EDGAR footprint-corrected estimate and even a factor ~7 larger than CAMS-REG, which contains much fewer emissions from the waste sector compared to EDGAR.

RQ 4) Can simulations of regional models in combination with airborne measurements be used to identify GHG sources which are missing in the bottom-up inventories?

Since atmospheric measurements detect the sum of all sources and sinks in a well-mixed plume, numerical models (*here*: MECO(n)), using detailed bottom-up emission data divided by their emission type (*here*: the BERLIN inventory), are required to analyse the contribution of individual source sectors. Simulated and observed CO_2 mole fractions from July 20th agree well in location and shape, however, a quantitative comparison of maximum enhancements is hampered due to deviations in simulated wind speed and BL height. Simulated citywide CH_4 mole fractions are substantially lower than observed due to underrepresented urban emissions in the BERLIN inventory, as already indicated by the mass balance results. The simulated plume shape is narrower than observed because sources contributing to the measured CH_4 plume partly also originate from outside of the Berlin city boundary. The missing CH_4 sources were investigated by implementing additional tracers for waste emissions (wastewater treatment plants, unofficial waste deposits), which were not included in the original emission data set. Although the model results do not perfectly reproduce the shape of the measured CH_4 plume, the additional emissions clearly improve their agreement. Agricultural emissions are not explicitly considered since their contribution according to EDGAR is low for the Berlin area. However, the results of this study clearly show that emissions of all sources in the greater region of Berlin need to be better quantified by ground-based and/or aircraft measurements to fully understand the regional CH_4 budget of the Berlin area.

Investigations on the meso- to synoptic scale – emissions from European and Asian urban agglomerations in summer 2017 and spring 2018, respectively

RQ 5) Can signatures of urban and other emission sources be detected by airborne measurements in the regional scale distribution of CH_4 in Europe and Asia?

The EMeRGe measurements extended over an area of roughly 1500 × 1500 km (Europe) and 2500 × 2500 km (Asia), and therefore allow to investigate the impact of emissions from urban centres on the large-scale distribution of GHGs. CH_4 enhancements in Europe were mostly encountered in the BL, which is expected because emissions are usually surface-based and are diluted during the export into the free troposphere. The urban plumes of London and Barcelona could be identified in the regional CH_4 distribution, even they were sampled at larger downwind distances (~100 to 250 km), where emissions might have been diluted and/or mixed with pollution from surrounding sources. In order to assign these enhancements to their source region, supporting model simulations and complementary measurements of shorter-lived species with smaller background concentrations and thus better signal-to-background ratios are needed. In contrast to the urban emission plumes, a biomass burning event was observed near Marseille with comparable maximum CH_4 mole fractions. Its distinct peak strongly influences the local GHG distribution although the contribution of bb emissions to total global anthropogenic CH_4 is on the order of a few percent (Saunois et al., 2019).

During EMeRGe-Asia enhanced CH_4 mole fractions were detected off the entire Chinese coast at low altitudes, which can partly be traced back to the flight strategy. Flying into the Chinese air space was restricted, hence, potential plumes originating from urban agglomerations in China were probed far downwind (>500 km) over the sea and were already mixed with other pollution plumes and/or background air. In contrast to Europe, distinct and extensive CH_4 plumes were observed in the free troposphere with enhanced mole fractions of similar magnitude as sampled air masses in the polluted BL, indicating that the mid-tropospheric regional CH_4 budget in Asian springtime is heavily impacted by the outflow from China. Due to shorter sampling distances towards the Philippines (~100 km), the urban

GHG plume from Manila could be identified using model simulations and short-lived species as described above. At the western coast of Taiwan, the highest CH_4 mole fractions, encountered within narrow peaks, could be attributed to emissions from numerous point sources spread over larger areas such as landfills and wastewater treatment plants.

RQ 6) How do the regional CH_4 emission distributions in Europe and in Asia compare with each other and with previous observations?

The comprehensive data set allows for a comparison between summertime European and springtime Asian CH_4 observations. Based on altitude profiles, observed CH_4 enhancements appear to have a similar magnitude, but in Asia they emerge from a relatively higher atmospheric background concentration of roughly +26 ppb. Although global SCIAMACHY and GOSAT satellite observations depict a clear hotspot of highest CH_4 values in East Asia (e.g. Turner et al., 2015; Jacob et al., 2016; Maasakkers et al., 2019), it is difficult to evaluate if the difference in the performed airborne measurements is significant enough to validate this statement. A straightforward comparison between both continents is hampered due to the strong seasonal cycle of CH_4, its annual growth rate and the different sampling distances to the European and Asian sources. The observed CH_4 distribution in Asia was compared with measurements from a mission performed seventeen year earlier (TRACE-P by NASA), which also covered roughly the same regions during springtime. The spatial patterns, both in the horizontal and vertical, were found to be similar, although the mean mole fraction was ~140 ppb higher during EMeRGe. Here, the accumulated growth rate is, however, not sufficient to explain this increase. Further discrepancies might also result from different flight strategies since EMeRGE-Asia extended less far into the Pacific compared to TRACE-P.

To conclude, the hypothesis of the present thesis can be confirmed, although certain restrictions exist. Airborne measurements on the local scale are an important tool to identify urban GHG emissions downwind of a city as shown for the German capital Berlin. The sampling distance towards the city, the impact of suburban emissions, and the ideal state of the atmospheric BL and air flow hereby plays a crucial role if urban emissions can be detected or not. In addition, the dependency on air traffic control in a densely populated area hampering the ideal flight designs is critical. As was successfully demonstrated within this thesis, **the top-down approach can be used to quantify the urban source strength** and to evaluate bottom-up emission estimates. Even for major cities like Berlin, located in a highly developed country, inventories might lack information from specific sources or source sectors. On the meso- to synoptic scale, **the impact of individual urban GHG emissions on the regional GHG distribution in Europe and Asia can be detected**, as successfully shown for London, Barcelona and Manila, however, it is more complex and requires a more in-depth analysis. The identification of urban GHG signals depends on various boundary conditions tied to the source area, the airborne sampling strategy and on the analysis itself. The source strength must be high enough to emerge from the variable GHG background mole fractions. If the sampling distance between the selected area and the aircraft increases to more than ~100 km, complementary observations of short-lived species and state-of-the-art numerical models were shown to be of major importance to assign the GHG enhancements to the specific source areas.

8 Outlook

The extensive EMeRGe measurements constitute an important contribution to the limited knowledge of the GHG distribution on local to synoptic scales. A discussion of the gained data set and comparison with other publicly available measurements is foreseen to be published in the EMeRGe special issue (ACP/AMT). Significant CH_4 enhancements were detected downstream of several urban areas, including the Po Valley, the BeNeRuhr region, Barcelona, Munich, Manila, as well as coastal cities in Japan and China. To better characterise these urban emission hotspots, a detailed characterisation of them is highly desirable. The most promising approach to date is the performance of dedicated local flight experiments. For such mass balance approaches, improvements of the observational strategy, the modelling environment and the knowledge of the a-priori fluxes are needed:

- repeated airborne observations on several days to enhance the statistical significance and during different seasons to reduce interannual emission uncertainties;
- coordinated automobile-based measurements to improve the knowledge of the GHG distribution between the ground and the lowest performed flight track;
- stationary wind LIDAR instruments to monitor the evolution of lower tropospheric wind speed, wind direction and boundary layer height to increase confidence on these parameters used in the mass balance equation;
- better understanding of the bottom-up uncertainties in emission quantities, their spatial distribution and variability over time; and
- an improvement of the model infrastructure to simulate the impact of biogenic CO_2 fluxes.

The measurements described herein provide valuable insights on sources and areas of specific interest, and furthermore serve as a testbed for our process understanding and evaluation of existing methods. However, in order to independently measure the efficiency of emission reductions, as stated in the Paris Agreement, a long-term monitoring of anthropogenic GHG emissions is desired, and is most likely best performed with multiple complementary measurement approaches. Satellite-based observations therefore started to focus on the detection of CO_2 emissions from urban sources, e.g. within the Copernicus Anthropogenic CO_2 Monitoring (CO2M) mission, a proposed constellation concept using up to six satellites, or within CO2Image, an instrument concept aiming to localise CO_2 emissions from, but not limited to, relatively low-emitting power plants. Measuring CH_4 from space is more challenging, but future missions strive for a fine spatial resolution to detect individual point sources, e.g. by developing the GHGSat microsatellite fleet or a new generation of satellite imaging spectrometers based on AVIRIS-NG.

Overall, urban areas were shown to have a significant impact on the CH_4 and CO_2 budget, both on local and on larger spatial scales. Due to the increase in population and progressive urbanisation, cities will very likely continue to play a significant role as GHG emitters. Politics, economic policies and population should therefore be committed to reduce GHG emissions in order to fight climate change.

A Appendix

A.1 Publications

Klausner, T., Mertens, M., Huntrieser, H., Galkowski, M., Kuhlmann, G., Baumann, R., Fiehn, A., Jöckel, P., Pühl, M., and Roiger, A.: Urban greenhouse gas emissions from the Berlin area: A case study using airborne CO_2 and CH_4 in situ observations in summer 2018, *Elem. Sci. Anth.***2020a**, 8. DOI:10.1525/elementa.411.

Co-Author, sorted after publication date:

Fiehn, A., Kostinek, J., Eckl, M., Klausner, T., Gałkowski, M., Chen, J., Gerbig, C., Röckmann, T., Maazallahi, H., Schmidt, M., Korbeń, P., Nęcki, J., Jagoda, P., Wildmann, N., Mallaun, C., Bun, R., Nickl, A.-L., Jöckel, P., Fix, A., and Roiger, A.: Estimating CH_4, CO_2, and CO emissions from coal mining and industrial activities in the Upper Silesian Coal Basin using an aircraft-based mass balance approach, *Atmos. Chem. Phys. Discuss.* **2020**. https://doi.org/10.5194/acp-2020-282, in review.

Ohyama, H., Morino, I., Velazco, V.A., Klausner, T., Bagtasa, G., Kiel, M., Frey, M., Hori, A., Uchino, O., Matsunaga, T., Deutscher, N., DiGangi, J.P., Choi, Y., Diskin, G.S, Pusede, S.E., Fiehn, A., Roiger, A., Lichtenstern, M., Schlager, H., Wang, P.K., Cho, C.C.-K., Andrés-Hernández, M.D. and Burrows, J.P.: Validation of XCO_2 and XCH_4 retrieved from a portable Fourier transform spectrometer with those from in-situ profiles from aircraft borne instruments, *Atmos. Meas. Tech. Discuss.* **2020**. https://doi.org/10.5194/amt-2020-170, in review.

Nickl, A.-L., Mertens, M., Roiger, A., Fix, A., Amediek, A., Fiehn, A., Gerbig, C., Galkowski, M., Kerkweg, A., Klausner, T., Eckl, M. and Jöckel, P.: Hindcasting and forecasting of regional methane from coal mine emissions in the Upper Silesian Coal Basin using the online nested global regional chemistry-climate model MECO(n) (MESSy v2.53), *Geosci. Model Dev.* **2020**, 13, 1925-1943. DOI:10.5194/gmd-13-1925-2020.

Luther, A., Kleinschek, R., Scheidweiler, L., Defratyka, S., Stanisavljevic, M., Forstmaier, A., Dandocsi, A., Wolff, S., Dubravica, D., Wildmann, N., Kostinek, J., Jöckel, P., Nickl, A.-L., Klausner, T., Hase, F., Frey, M., Chen, J., Dietrich, F., Necki, J., Swolkien, J., Fix, A., Roiger, A. and Butz, A.: Quantifying CH_4 emissions from hard coal mines using mobile sun-viewing Fourier transform spectrometry, *Atmos. Meas. Tech.* **2019**, 12, 5217-5230. DOI:10.5194/amt-12-5217-2019.

Kostinek, J., Roiger, A., Davis, K. J., Sweeney, C., DiGangi, J. P., Choi, Y., Baier, B., Hase, F., Groß, J., Eckl, M., Klausner, T., and Butz, A.: Adaption and performance assessment of a quantum and interband cascade laser spectrometer for simultaneous airborne in situ observations of CH_4, C_2H_6, CO_2, CO and N_2O, *Atmos. Meas. Tech.* **2019**, 12, 1767-1783. DOI:10.5194/amt-12-1767-2019.

A.2 Meteorological definitions

The following definitions are taken from Wallace and Hobbs (2006).

Potential temperature θ, unit [K]: This parameter is used to compare temperatures of air masses at different heights of the atmosphere. It describes the temperature an air parcel would have if it is brought adiabatically to sea level (p_0 = 1000 hPa).

$$\theta = T\left(\frac{p_0}{p}\right)^{R/c_p}$$

With T and p being the temperature and pressure of the air parcel, R the gas constant for dry air [J K^{-1} kg^{-1}] and c_p [J K^{-1} kg^{-1}] the specific heat constant.

Specific humidity q, unit [kg kg^{-1}]: Relates the mass of water vapour m_v to the mass of humid air.

$$q = \frac{m_v}{m_v + m_d}$$

Relative humidity RH, unit [%]: Relates the actual mixing ratio w of the air to the saturation mixing ratio w_s.

$$RH = 100\frac{w}{w_s}$$

Geostrophic wind v_g: In the free atmosphere (i.e. absence of the frictional force), the geostrophic wind describes the balance between Coriolis force and pressure gradient force. In natural coordinates it is written as:

$$v_g = -\frac{1}{f}\frac{\partial \emptyset}{\partial n}$$

where f is the Coriolis parameter, $\emptyset$ the geopotential and n the direction normal to the isobars. The flow of v_g is parallel to the isobars and the low pressure is on the left.

A.3 Derivation of basic cavity ring-down spectroscopy equations

Eq. (2.4) can be obtained by subtracting the off-resonance loss (Eq. I) from the on-resonance loss (Eq. II).

Eq. I) loss in the empty cavity $\frac{tr}{\tau_2} = 2(1-R)$

Eq. II) loss in the cavity which contains an absorbing species $\frac{tr}{\tau_1} - 2\alpha L = 2(1-R)$

Eq. I) – Eq. II)

$$\frac{tr}{\tau_2} - \left(\frac{tr}{\tau_1} - 2\alpha L\right) = 0$$

$$\frac{tr}{\tau_2} = \frac{tr}{\tau_1} - 2\alpha L$$

$$\alpha = \frac{1}{2L}\left(\frac{tr}{\tau_1} - \frac{tr}{\tau_2}\right)$$

Using for the round trip time $tr = \frac{2L}{c}$ i.e. this is the time which is needed to complete one round trip; and L is the length of the cavity [m] and c the speed of light [m s^{-1}].

$$\alpha = \frac{1}{2L}\left(\frac{tr}{\tau_1} - \frac{tr}{\tau_2}\right)$$

$$\alpha = \frac{1}{c}\left(\frac{1}{\tau_1} - \frac{1}{\tau_2}\right)$$

This is equal to Eq. (2.4).

To derive Eq. I) and Eq. II) the following is considered:

Based on Lambert-Beers law, see Eq. (2.3), the intensity in an empty cavity decreases dependent on the number of reflections per round trip, the loss per reflection, and the number of round trips:

$$I_t = I_0 \exp\left(-\frac{\#\, of\ reflections}{round\ trip}\,\frac{loss}{reflection}\ \#round\ trips\right)$$

The number of reflections per round trip with two mirrors is 2; the loss per reflection is equal to the transmission *T* = *1-R* and the number of round trips from two way transit time of light is $n = \frac{tc}{2L}$.

$$I_t = I_0 \exp\left(-2\,(1-R)(\frac{tc}{2L})\right)$$

$$I_t = I_0 \exp\left(-(1-R)\,\left(\frac{tc}{L}\right)\right)$$

τ_2 is defined as the time when $I_t = I_0\, exp(-1)$. This is true when:

$$t = \tau_2 = \frac{tr}{2(1-R)}$$

This is equal to Eq. I).

Prove:

$$-(1-R)\left(\frac{tc}{L}\right)$$

$$-(1-R)\left(\frac{tr\ c}{2(1-R)L}\right)$$

$$-\left(\frac{tr\ c}{2\ L}\right)\ with\ tr=\frac{2L}{c}$$

$$-\left(\frac{2L\ c}{c\ 2L}\right)=\ -1$$

Based on Lambert-Beers law, see Eq. (2.3), the intensity in a cavity containing an absorbing species decreases dependent on the number of reflections per round trip, the loss per reflection, the number of round trips plus the absorption loss per round trip and the number of round trips:

$$I_t=\ I_0\exp\left(\begin{array}{c}-\dfrac{\#\ of\ reflections}{round\ trip}\ \dfrac{loss}{reflection}\ \#round\ trips+\\+\dfrac{absorption\ loss}{round\ trip}\ \#round\ trips\end{array}\right)$$

The absorption loss per round trip is $2\alpha L$.

$$I_t=\ I_0\exp\left(-(1-R)\left(\frac{tc}{L}\right)+2\alpha L\ \left(\frac{tc}{2L}\right)\right)$$

$$I_t=\ I_0\exp\left(-\ \left(\frac{tc}{L}\big((1-R)+(\alpha L)\big)\right)\right)$$

τ_1 is defined as the time when $I_t=I_0\ exp(-1)$. This is true when:

$$\tau_1=\frac{tr}{2((1-R)+\alpha L)}$$

This is equal to Eq. II).

Prove:

$$-\ \left(\frac{tc}{L}\big((1-R)+(\alpha L)\big)\right)$$

$$-\ \left(\frac{tr\ c}{2((1-R)+\alpha L)L}\big((1-R)+(\alpha L)\big)\right)$$

$$with\ tr=\frac{2L}{c}$$

$$-\left(\frac{2L\,c}{c\,2((1-R)+\alpha L)L}\left((1-R)+(\alpha L)\right)\right)$$

$$-\left(\frac{1}{(1-R)+\alpha L}\left((1-R)+(\alpha L)\right)\right)$$

$$-\left(\frac{(1-R)+\ \alpha L}{(1-R)+\alpha L}\right)=\ -1$$

A.4 Calibration set-up and time delay during EMeRGe-EU

Within EMeRGe-Europe the calibration gas flow was maintained due to overpressure, and not by using a MFC. According to a poster of Kitzis et al. (2017) the CO_2 mole fraction is dependent on the flow rate with which the instrument is calibrated, especially when the amount of gas in the calibration bottle, and thus the cylinder pressure, is reduced. Their work compared a low flow rate (0.3 L min^{-1}) with a high flow rate (5 L min^{-1}). CO_2 mole fractions from the lower flow were more stable (~0.1 ppm vs. ~0.3 ppm) over the pressure range and thus the lifetime of the bottle. Even this has only a minor impact on the overall uncertainty, for the following two campaigns (EMeRGe-Asia and $[UC]^2$) a MFC with a flow rate of 1 L min^{-1} was used instead of the overpressure flow. This also led to a reduction in the variability of the inlet pressure from ±10 hPa (overpressure flow) to ±1.5 hPa (MFC).

The calibration duration for EMeRGe-Europe was 15 min, however a laboratory test performed on January 9th, 2018 assessed to which amount the time can be reduced to save calibration gas but to still reach stable mole fractions of the supplied calibration gas. By reducing the amount of time from 15 to 10 min, the mean value of CO_2 and CH_4 were found to be the same. When supplying the gas for only 5 min, mean values for CO_2 started to differ by 0.04 ppm (and were found to be not relevant for CH_4).

The delay time was also experimentally determined. Closest to the inlet, the tubing was switched between outside hangar air ("low" CO_2) and HALO cabin air (rather high CO_2 values as many people were inside the aircraft). The delay time is then derived from the time between the switching and the first reasonable recorded signal. Out of eight measurements the average delay time is determined to be ~9 s.

A.5 Greenhouse gas time series and meteorological vertical profiles of the $[UC]^2$ research flights

Time series for CO_2, CH_4 and flight altitude of each of the five performed research flights during the $[UC]^2$ mission are presented in Fig. A.1. The GHG mole fractions from the Picarro analyser are corrected according to the delay time of the instrument (~15 s; see Sect. 4.2). Figure A.2 depicts the obtained vertical profile at the Tempelhofer Feld with respect to the meteorological variables of virtual potential temperature, static temperature and relative humidity to determine the boundary layer height.

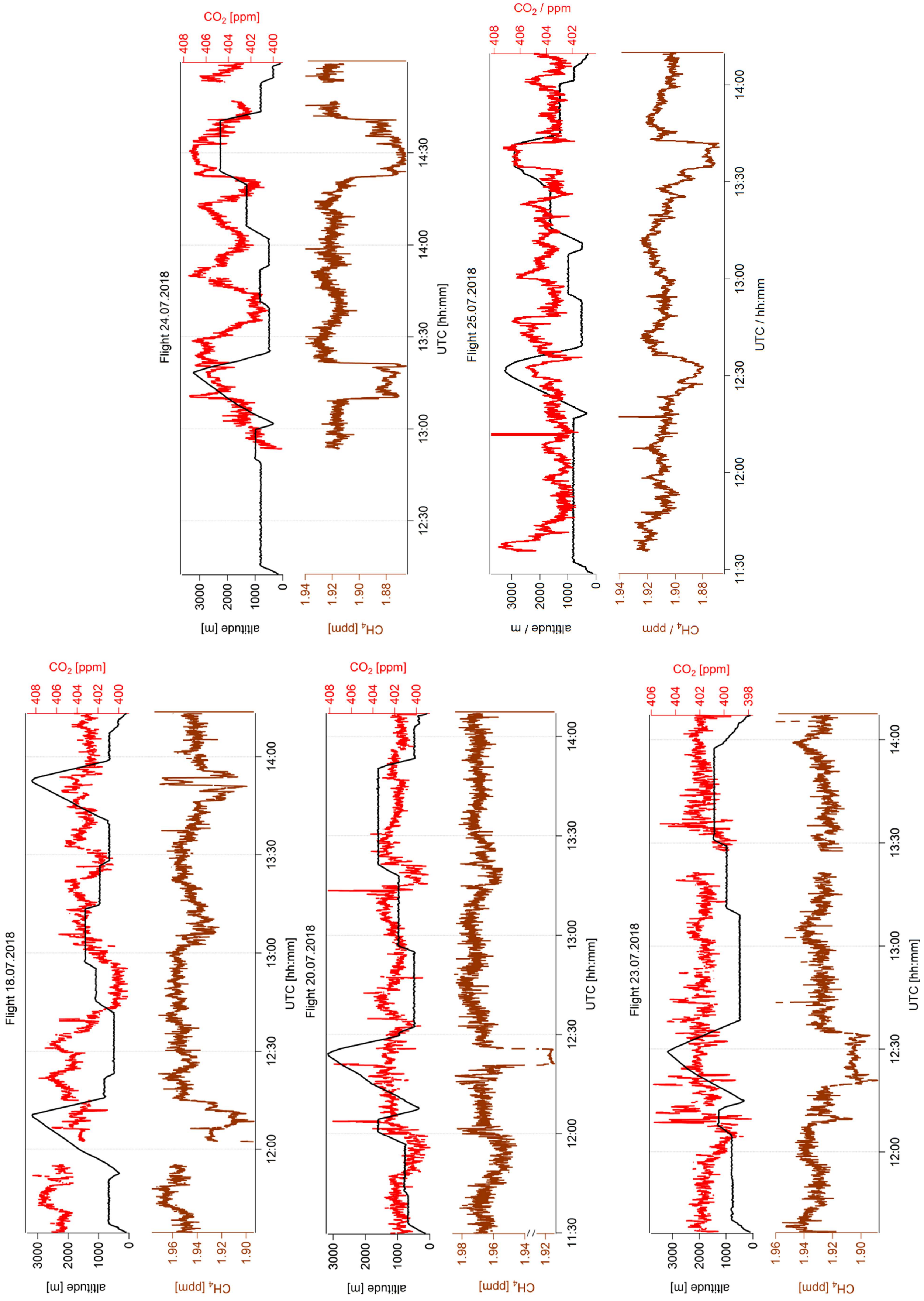

Figure A.1: Time series of CO_2, CH_4 and flight altitude for five research flights conducted during the $[UC]^2$ campaign in July 2018.

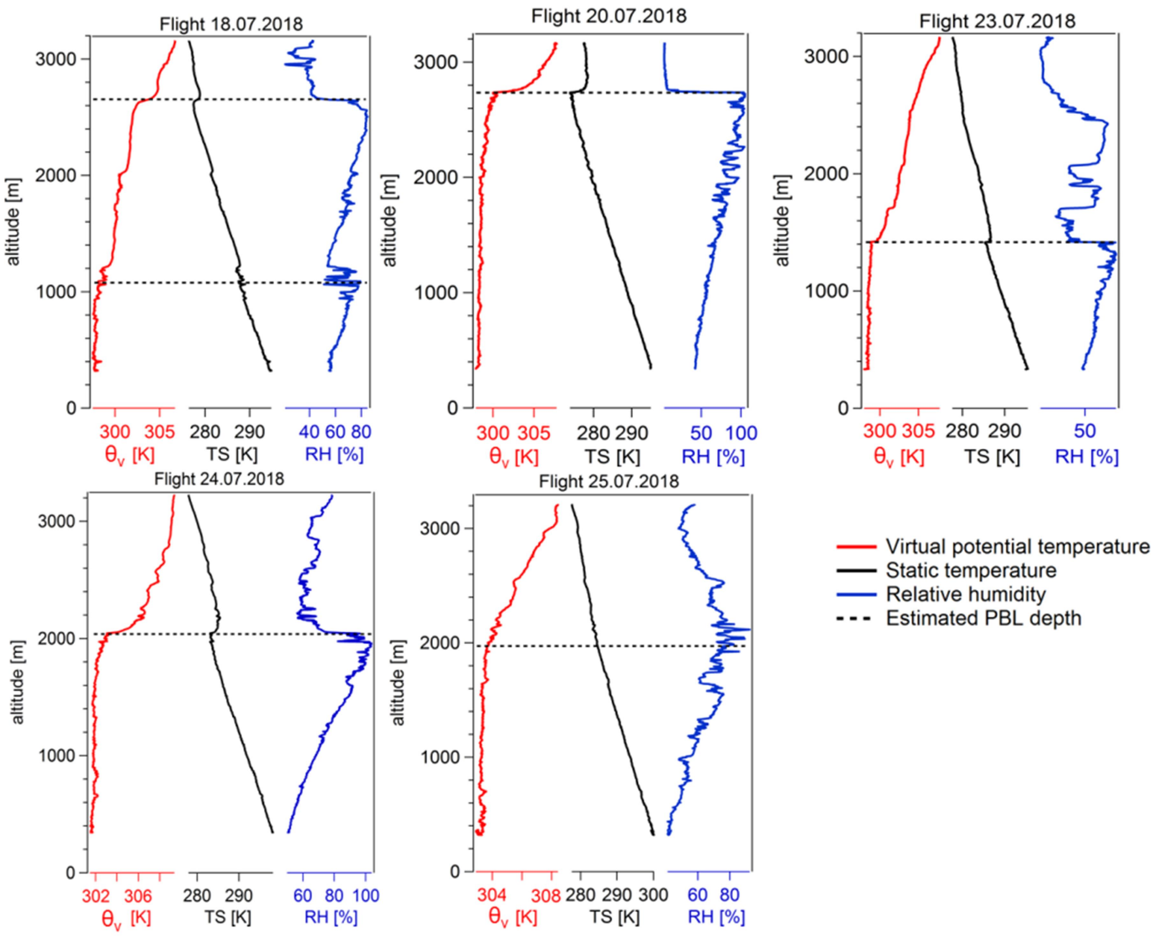

Figure A.2: Vertical profiles of the upward spiral at Tempelhofer Feld, Berlin. The BL depth (dashed black line) was determined from virtual potential temperature, static temperature and relative humidity, see Sect. 5.2.

A.6 Comparison of $[UC]^2$ wind data from airborne observations with HYSPLIT and MECO(n)

Comparison with HYSPLIT

The airborne wind measurements during the $[UC]^2$ campaign are compared to the ECMWF forecast data, which are used as input for HYSPLIT trajectory calculations (see Sect. 3.3). To capture the characteristics of the whole boundary layer three different pressure levels are considered: 750, 850 and 950 hPa.

Figure A.3 presents the time series of ECMWF wind direction (wa, upper panel) and ECMWF wind speed (ws, lower panel) within the whole campaign period from 16th of July at 8 UTC to 26th of July at 23 UTC. The three different pressure levels are expressed as solid lines. ECMWF data represent an area mean covering the flight tracks around Berlin (51.9° to 52.8°N, 12.3 to 14.3°E). Wind directions ranged from 270° to 100° with wind speeds from 1 to 15 $\mathrm{m\,s^{-1}}$. Wind measurements on the research flight days are indicated by crosses (FDLR is the aircraft call sign). Error bars are the deviation of the wind speed and wind direction as an average of the whole flight at pressure levels within ±5 hPa of the given pressure height was calculated. Figure A.4 shows the correlation between measured wind direction and wind speed on the flight days with ECMWF data. As the overall correlation (R = 0.95 to 0.98) is excellent, the ECWMF data are considered as reliable for further analysis. The wind direction markers in Fig. A.4 are sized according to the wind speed. Generally better agreement in wind direction was observed when wind speeds were higher.

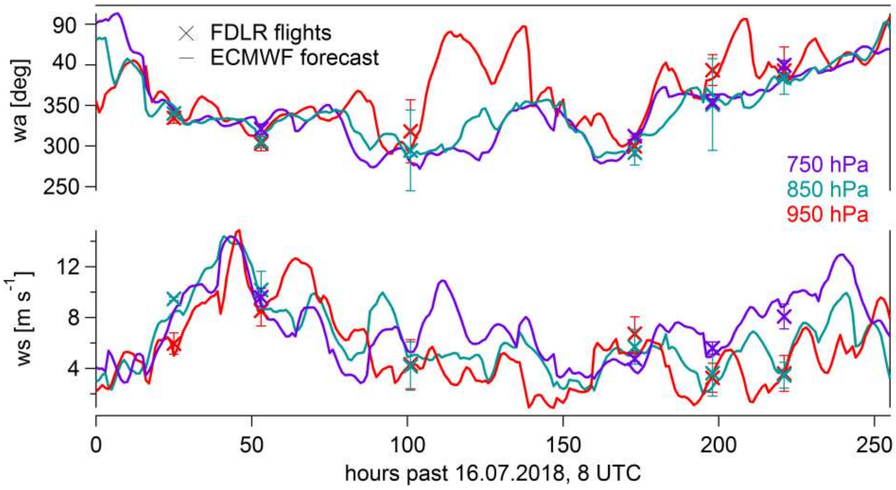

Figure A.3: (a) Time series of wind direction (upper panel) and wind speed (lower panel) during the campaign period (July 8th to 26th) from ECWMF forecast data (solid lines) and airborne measurement data (crosses) at three different pressure levels (purple, blue and red colour).

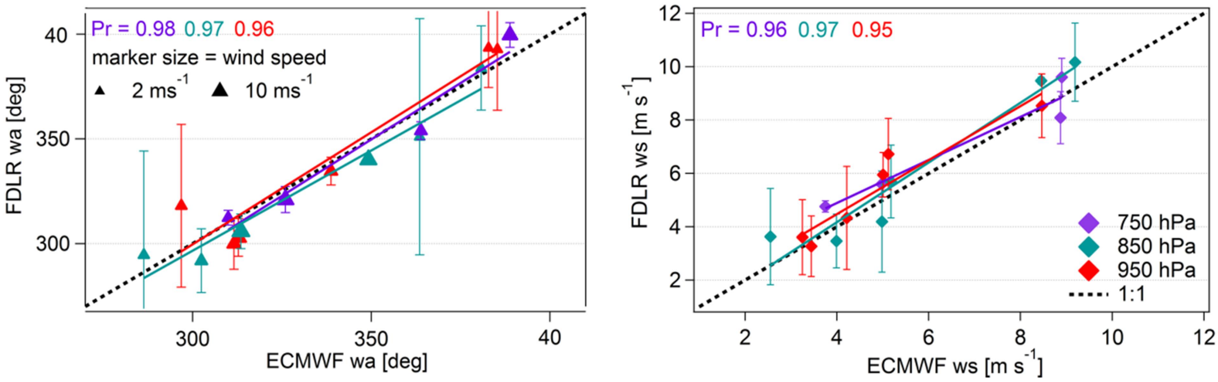

Figure A.4: Correlation of wind direction and wind speed between airborne measurement data (FDLR) and ECMWF forecast data at three different pressure levels. Correlation coefficients are abbreviated with Pr.

Comparison with MECO(n)

The wind situation as simulated by MECO(n) in the three different nesting instances (0.44°, 0.0625° and 0.01°; see Sect. 3.2) are shown as solid lines in Fig. A.5. The same time period as in Fig. A.3 is covered. The dashed vertical lines indicate 12 UTC for each day. Simulation data are analysed at 950 hPa (panel a), 850 hPa (panel b) and 750 hPa (panel c). Data represent an area average over Berlin (51.9° to 52.8°N, 12.3 to 14.3°E). Airborne wind measurements are shown as black markers. The arrows indicate the flights performed on July 20th and July 24th as presented in Chapter 5.

The three different instances simulate similar wind directions throughout the campaign period. With respect to the wind speed, the coarsest nest (depicted in green) deviates at the 750 and 850 hPa (~2.5 and ~1.5 km) level from the two finer nests (depicted in blue and red) especially towards the end of the campaign. For the analysed flights on July 20th and 24th the model at 0.01° resolution simulates the wind directions quite well as already indicated in the discussions in Sect. 5.3.4 and 5.4.2. Note that the 750 hPa level is already higher than accessed by the aircraft. For the flights on July 18th and 23rd the wind deviations are very large (~50 to ~60°). On July 18th a cold front passed Berlin which might not be well reproduced by the model and could explain the differences.

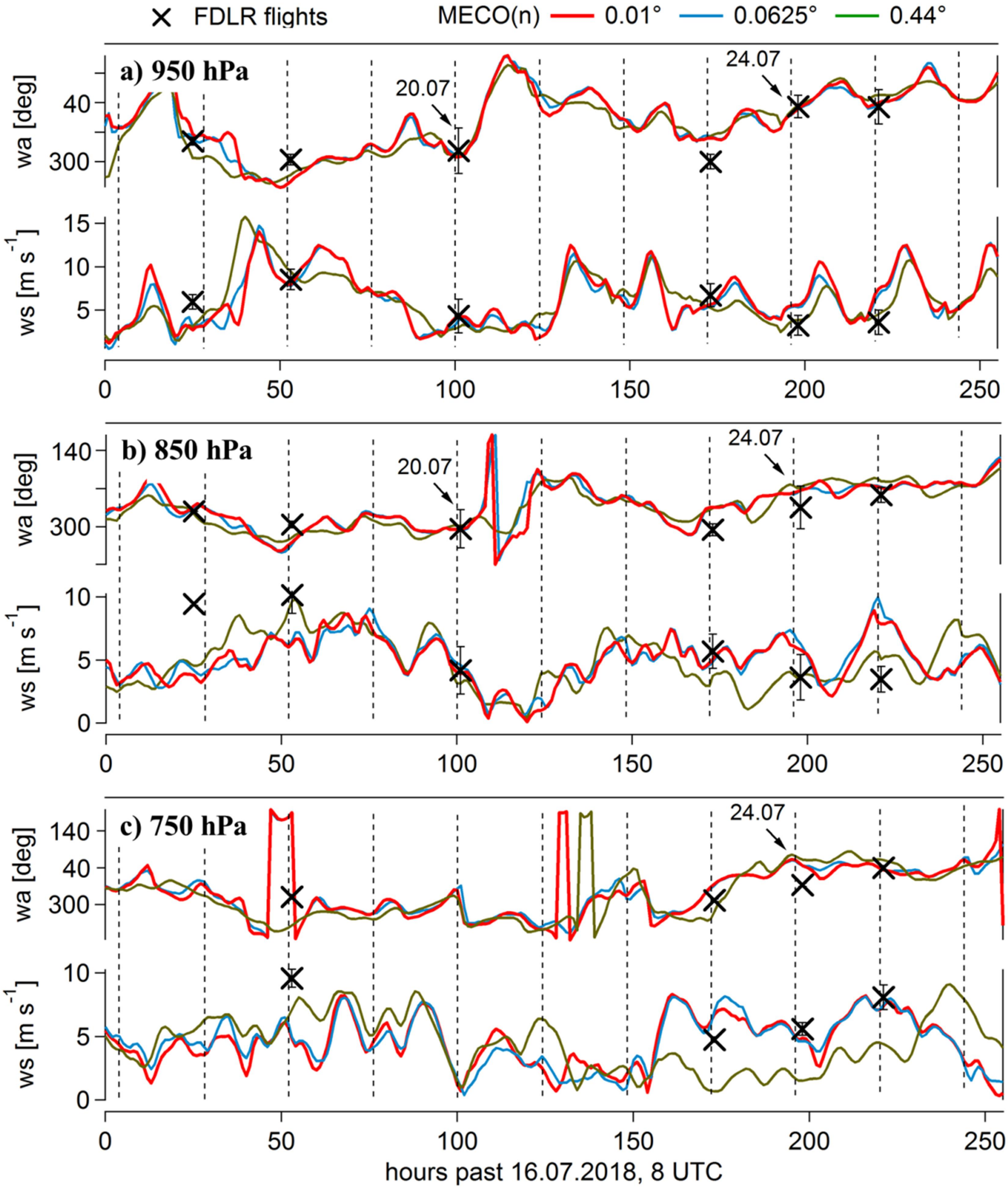

Figure A.5: (a) Time series of wind direction (upper panel) and wind speed (lower panel) during the campaign period (July 8th to 26th) from MECO(n) simulation results (solid lines) and airborne measurement data (black crosses) at three different pressure levels (a) 950 hPa, (b) 850 hPa and (c) 750 hPa.

A.7 Simulated vertical greenhouse gas distribution for the flight on July 20th, 2018

For the mass balance flight on July 20th, 2018 during the [UC]^2 mission the boundary layer extends from the surface up to ~2700 m, as indicated by meteorological measurements (see Fig. A.2). The part of the GHG plume between ~300 and ~1600 m was sampled by the aircraft; however the lowest ~300 m were not accessible due to flight restrictions over the city of Berlin. To still account for the distribution of GHG from the surface towards the top of the BL the vertical plume structure using the MECO(n) model is analysed. Figure A.6 shows for the third crossing of the Berlin plume at ~1600 m flight altitude the simulated c-CH_4 and c-CO_2 mole fractions in the vertical. Between the surface and the top of the BL the plume is not lofted nor depicts any vertical structures. Therefore the assumption of a well-mixed BL is valid.

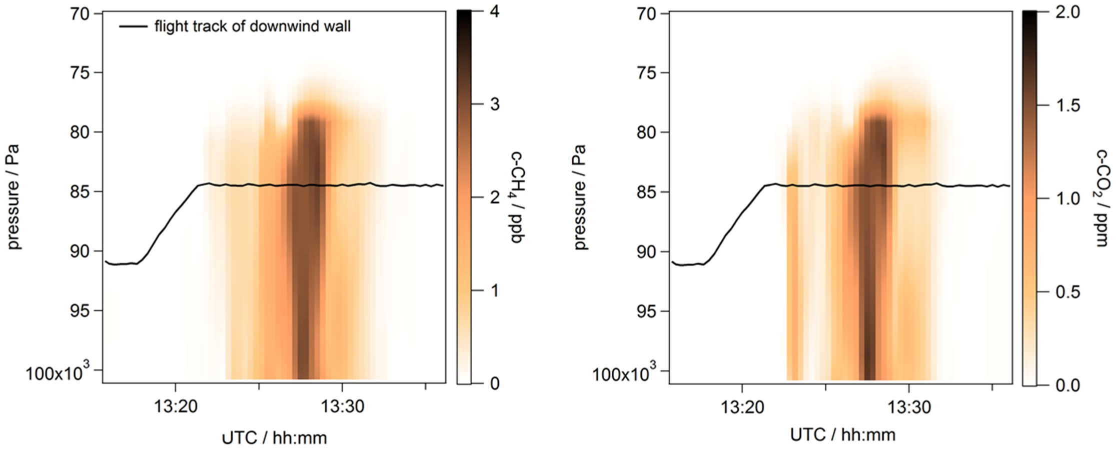

Figure A.6: Curtain of simulated c-CH_4 and c-CO_2. The third crossing of the Berlin plume at ~1600 m altitude is shown from ~13:20 to ~13:35 UTC.

A.8 Seasonality of greenhouse gas emissions in EDGAR

The seasonality of greenhouse gas emissions with respect to Berlin is investigated using monthly resolved emissions from EDGAR v4.3.2 for the year 2010, see Fig. A.7. Emissions were considered within the Berlin city boundary for January (blue bars) and July (red bars), representing wintertime and summertime emissions, as well as the monthly mean (grey bars). For definition of the merged source sectors “fuel combustion for the generation of electricity and heat” and “fuel exploitation” see Table 5.1. With respect to total fossil fuel CO_2, emissions are ~30 % higher in January than the monthly mean and ~40 % lower in July. The largest seasonality is present in the merged sector fuel combustion, with above monthly emissions in January and below monthly emissions in July. Emissions from road transport are constant throughout the year. The inventorial seasonal cycle is consistent with e.g. Gioli et al. (2012). Their long-term observations in Florence reveal a strong seasonality of CO_2 fluxes due to domestic heating with its maximum in winter, while contributions from road traffic are relatively constant throughout the year. Total CH_4 emissions also vary dependent on the season, however their seasonal cycle is less pronounced compared to CO_2, since total emissions are only ~10 % higher in January and ~15 % lower in July than the monthly mean. While CH_4 emissions from the waste sector and from fuel exploitation do not show any seasonality, emissions related to fuel combustion are slightly higher in January than in July.

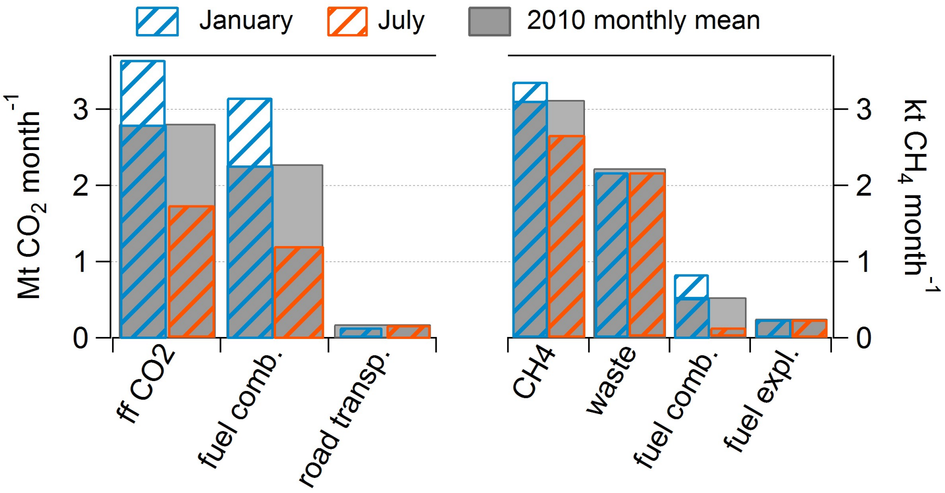

Figure A.7: Seasonality of EDGAR fossil fuel CO_2 and CH_4 emissions in 2010. Exemplarily for winter (and summer) the month January (and July) is considered. For sector definitions see Table 5.1. Data are retrieved from *https://edgar.jrc.ec.europa.eu/overview.php?v=432_GHG.*

A.9 Estimated biogenic carbon dioxide flux during $[UC]^2$

Especially during summer months and in vegetated areas the biospheric component of CO_2 (i.e. photosynthetic uptake and respiration) can alter the anthropogenic emission flux. For the mass balance flight on July 20th, 2018 the impact of the biosphere on the estimated CO_2 flux needs to be investigated. Therefore the biogenic CO_2 flux was simulated using VPRM (Mahadevan et al., 2008) coupled with WRF-GHG (Beck et al, 2013).

Figure A.8 shows the measured (solid lines) and simulated (dashed lines) CO_2 mole fractions downwind of Berlin on July 20th. The dashed lines represent the predicted result from WRF-GHG, simulating the biospheric CO_2 contribution using an online VPRM model driven by MODIS indices (Mahadevan et al., 2008). Here, signals predicted by the biosphere are analysed if only biogenic uptake was considered, i.e. assuming complete absence of anthropogenic sources. The mole fractions were derived from the simulation by replacing the upwind-simulated mole fractions of the WRF base reference by the actual upwind CO_2 measurements. Next, the simulated downwind mole fractions were corrected by that estimated bias. Therefore, the upwind measured and simulated CO_2 mole fractions are equal by definition and only depicted by the solid light purple line. Variation in the predicted dashed mole fractions corresponds to changes of biospheric-only CO_2 mole fractions at respective downwind measurement locations. At the edges of the flight track, which are assumed to represent the atmospheric background, the model matches the measured CO_2 pattern quite well, which leads to believe that the models' predictions are accurate.

As can be seen, the influence of the biosphere between upwind and downwind legs of the flight is predicted to be small and well within the variability of the measurements. On top of that, the change of the modeled signal inside the constrained area is variable with both altitude and distance (as defined on x-axis), reflecting the influence of vertical transport dynamics inside the BL superimposed on regional-scale variability of the predicted tracer fields. For the lowest leg the strongest uptake of CO_2 is estimated, however the surface-driven influence of biosphere gets less intense towards the higher flight altitudes. In turn, regional scale variability causes the relation between upwind and downwind simulations to be negative (distances between approx. 0 km to 20 km) or positive (-20 km to -10 km), depending on the horizontal location.

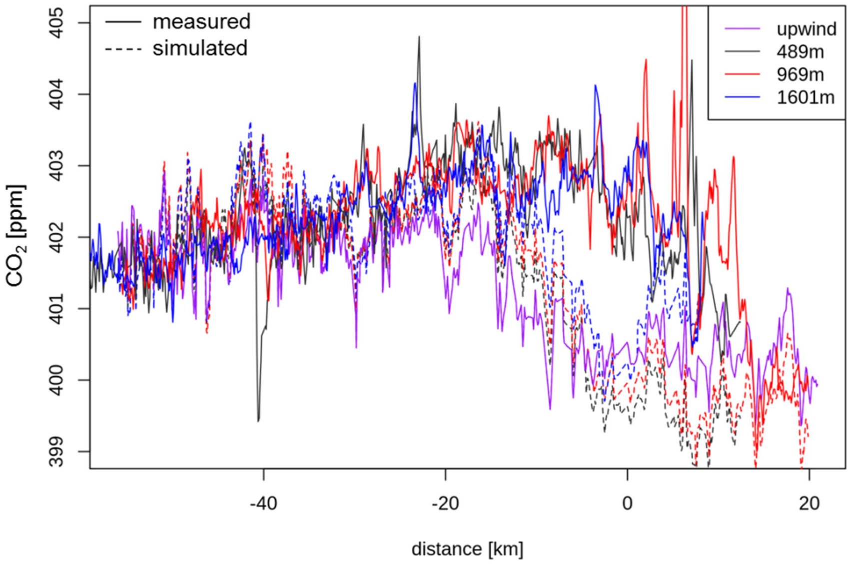

Figure A.8: Biogenic CO_2 mole fractions up- and downwind of Berlin on July 20th.

This variability in horizontal and vertical direction makes it difficult to accurately quantify the overall biogenic influence without adding an extra layer of complexity to the applied method. In fact, even if it were to be applied, the correction of the estimated anthropogenic flux would be very minor, as the difference in the mole fractions between the upwind leg and the simulated downwind legs within the city plume is usually not larger than 0.5 ppm. The estimated maximum enhancement from the city of ~4 ppm (which corresponds to an anthropogenic flux of 1.39 ± 0.76 t CO_2 s^{-1}) would be only slightly altered if a vertically-weighted mean of simulated mole fractions was used as background instead of upwind measurement. On top of that, the uncertainty of such estimation would be difficult to quantify without a detailed analysis of the modeled output.

It should also be noted that the estimates of the biogenic signals are potentially offset over the sections of the transects immediately downwind of the Berlin urban area. This is caused by misrepresentation of the urban biosphere in VPRM, as the driving MODIS indices cannot accurately discern the urban biosphere from other land use types within the city boundary due to insufficient spatial coverage. To properly account for the biogenic CO_2 signal, modifications to the VPRM system would be required, potentially in a manner similar to the one adopted by Hardimann et al. (2017).

Therefore, based on the available data, it is unnecessary to correct for the biogenic influence explicitly, and it is conservatively estimated that the anthropogenic emissions would not be enlarged by more than ~12 % if the biogenic uptake were to be considered. This number, corresponding to the total CO_2 biogenic flux in the constrained area, is conservative, and well within the overall uncertainty of calculated anthropogenic flux.

The modelling system used in this study was the same that was used for simulations performed in the scope of the CoMet 1.0 (Carbon Dioxide and Methane Mission). The setup consisted of a WRF-Chem v3.9.1.1. model (Skamarock et al, 2008) run with the GHG option enabled for a European-wide L60 10 km × 10 km domain with a nested L60 2 km × 2 km domain centred over Berlin. Meteorology was driven by the ERA5 product from Copernicus Climate Change Service (C3S, 2017). More details about the system setup can be found in Galkowski et al. (in prep).

A.10 Temporal evolution of the simulated c-CO_2 plume on July 24th

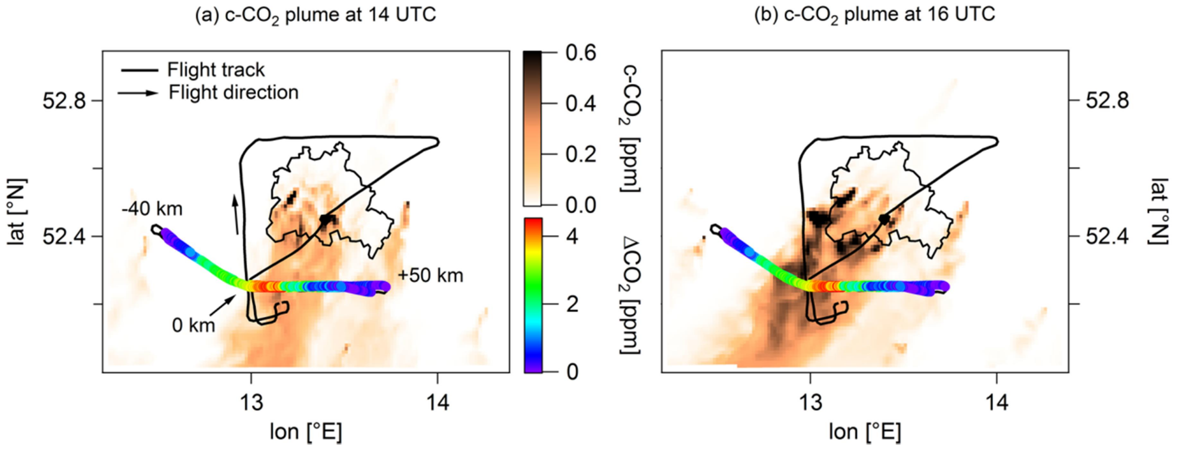

Figure A.9: Time-series of the simulated c-CO_2 plume on July 24th. Shown are snapshots at (a) 14 UTC, which is identical to Fig. 5.14a and (b) at 16 UTC to indicate, that the plume moves towards the west during the afternoon.

A.11 Source partitioning of EDGAR CO_2 and CH_4 emissions for European and Asian countries

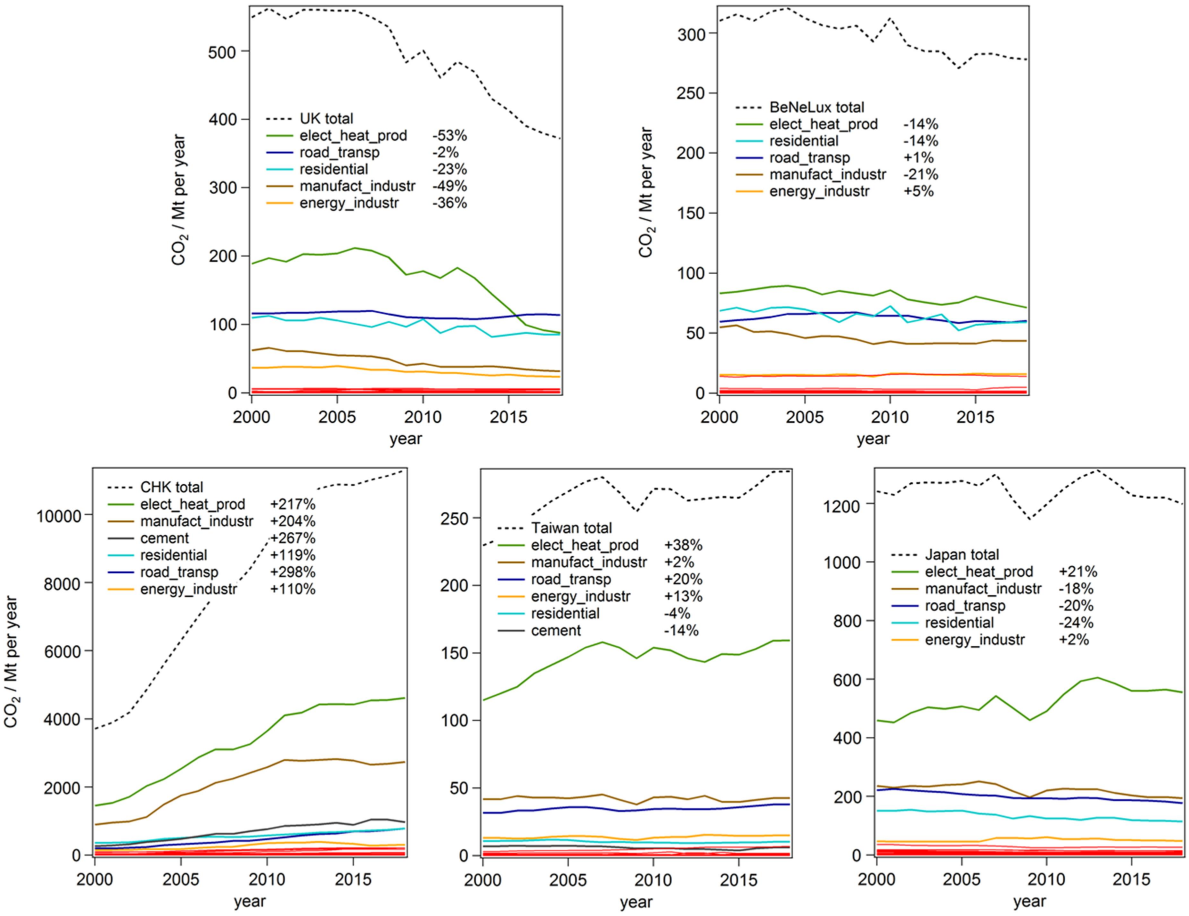

Figure A.10: Time series (2000-2018) of CO_2 emissions from selected countries (top panels: United Kingdom and Benelux; bottom panels: CHK which is China plus Hong Kong, Taiwan and Japan). Emissions are based on EDGAR v5.0 and differentiated by source sectors. Data are retrieved from *https://edgar.jrc.ec.europa.eu/overview.php?v=50_GHG*.

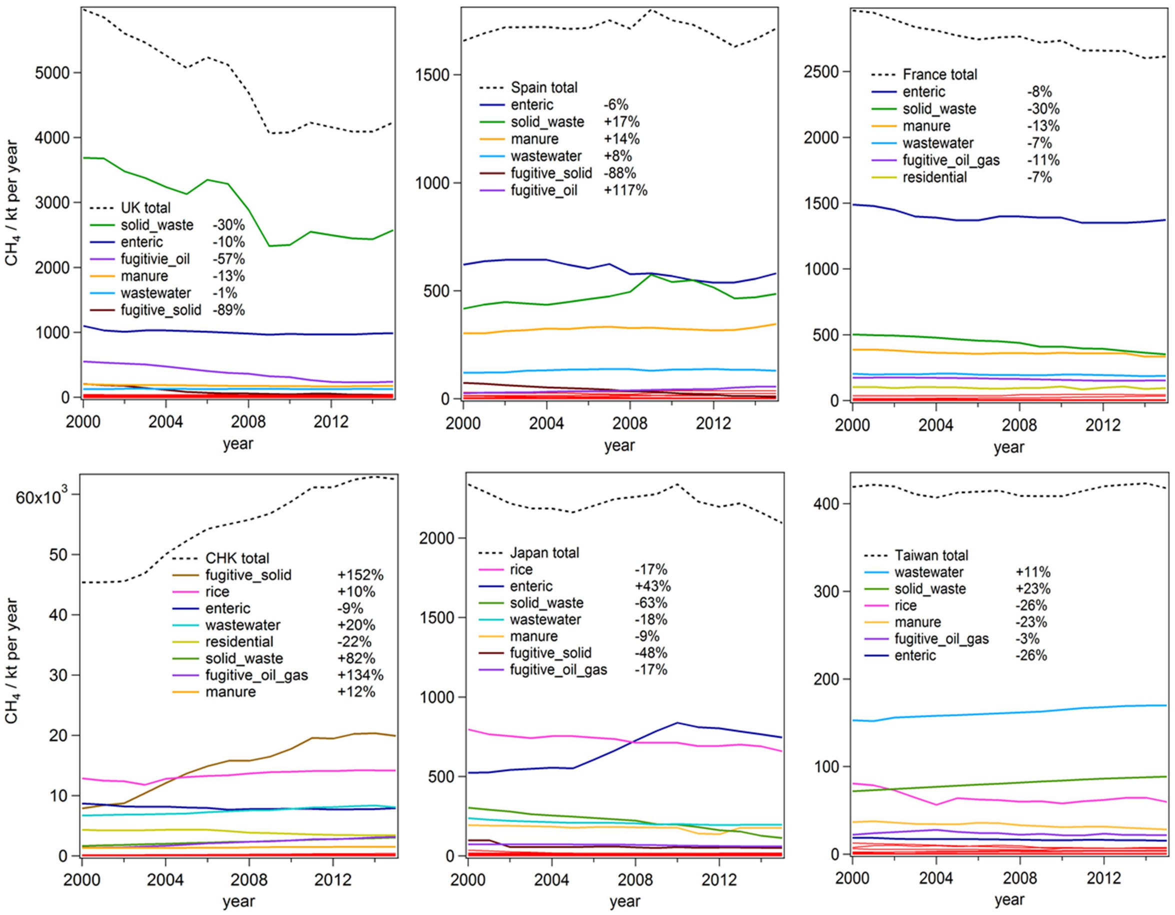

Figure A.11: Time series (2000-2015) of CH$_4$ emissions from selected countries (top panels: United Kingdom, Spain and France; bottom panels: CHK which is China plus Hong Kong, Japan and Taiwan). Emissions are based on EDGAR v5.0 and differentiated by source sectors. Data are retrieved from *https://edgar.jrc.ec.europa.eu/overview.php?v=50_GHG*.

A.12 Instrument payload of the EMeRGe aircraft campaigns

The cabin layout with the measured atmospheric species during both EMeRGe campaigns was already presented in Fig. 6.3a. The following Table A.1 lists them in more details, giving the name of the instruments (abbreviation and acronym), the measured atmospheric species and the responsible principle investigator.

Tedlar® gas sampling bags (*https://www.dupont.com/brands/tedlar.html*) were used to collect atmospheric samples of ambient air (see Sect. 6.3.5) and are briefly described in here. Such sampling bags are made of tedlar foil (PVF polyvinylfluorid) and are very robust and flexible. They assure minimum loss and conversion of the gas sample due to their impermeability for gases and due to the bags smooth surface the adsorption is extremely low. Further they can be used several times if they are correctly flushed with nitrogen. In order to collect Tedlar bags aboard HALO, a metal bellow vacuum pump (senior metal bellows MB-602) was integrated at the bottom of the same rack as the Picarro instrument and was used to permanently flush the inlet line of the individual sampling system. The majority of air was exhausted into the cabin through an overflow and by opening the Tedlar bag valve for roughly 20 s the bags were filled with ambient air. The subsequent laboratory analysis using a gas chromatography /

isotope-ratio mass spectrometry system was performed by R. Fisher at the Royal Holloway University of London. A description of the analytic system can be found in (Fisher et al., 2006).

Table A.1: List of scientific measurement instruments used aboard HALO during both EMeRGE campaigns. Their acronym, the measured species and the principal investigator are listed.

Instrument acronym	**Instrument**	**Measured species**	**Principal investigator**
FAIRO and PTR-MS	**F**ast **Airborne** **O**zone Measurements **P**roton **T**ransfer **R**eaction-**M**ass **S**pectrometer	O_3 volatile organic compounds (VOC)	Institute of Meteorology and Climate Research, Karlsruhe Institute of Technology
HAIDI	**H**eidelberg **A**irborne **I**maging **D**OAS **I**nstrument	2D trace gas slant column densities of NO_2 and SO_2	Institute for Environmental Physics, University of Heidelberg
C-ToF-AMS	**C**ompact **T**ime-**o**f-**F**light **A**erosol **M**ass **S**pectrometer	Aerosol composition (organics, sulfate, nitrate, ammonium, chloride)	Chemistry Department, Max Planck Institute for Chemistry, Mainz / University of Mainz
AMETYST	**A**erosol **ME**asuremen**T** **SYST**em	Fine aerosol number concentration, size distribution and volatility	DLR-IPA
HALO-CCN	**C**loud **C**ondensation **N**uclei Rack	Cloud condensation nuclei concentration, soot, microscopic properties	Chemistry Department, Max Planck Institute for Chemistry, Mainz
BAHAMAS	**BA**sic **HA**LO **M**easurement **A**nd **S**ensor **S**ystem	Basic aircraft position and meteorological data	DRL Flight Operations, Sensor and Data department

AENEAS	**MIRAH**	**CI-ITMS**	**PAN-GC**	**CATS**	**Tedlar Bags**	**AMTEX (with PERTRAS)**	**PeRCEAS**
Atmosph**E**ric **N**itrogen Oxides M**EAS**uring System	**M**easurement of Stable Carbon **I**sotope **R**atios in **A**tmospheric Trace Gases on **H**ALO	**C**hemical **I**onization **I**on **T**rap **M**ass **S**pectrometer	**P**eroxy**A**cetyl **N**itrate **G**as **C**hromatograph	Picarro GHG analyser, SO_2 fluorescence analyser	Tedlar Bag Sampling System	At**M**ospheric **T**race **EX**periment (**PER**flourocarbon on **TRA**cer **S**ystem)	**Pe**roxy **R**adical **C**hemical **E**nhancement and **A**bsorption **S**pectrometer
NO, NO_y	Whole air sampler (VOCs, carbon isotope ratios)	SO_2, formic acid	PAN	CO_2, CH_4, H_2O, SO_2	CH_4, $\delta^{13}C$	CO, O_3 (PFCs)	Sum of peroxy radicals HO_2 and RO_2
DLR-IPA	Institute of Atmospheric and Environmental Research, University of Wuppertal	DLR-IPA	DLR-IPA	DLR-IPA	DLR-IPA	DLR-IPA	Institute of Environmental Physics, University of Bremen

A.13 Additional broad GHG plumes as detected during EMeRGe-Asia

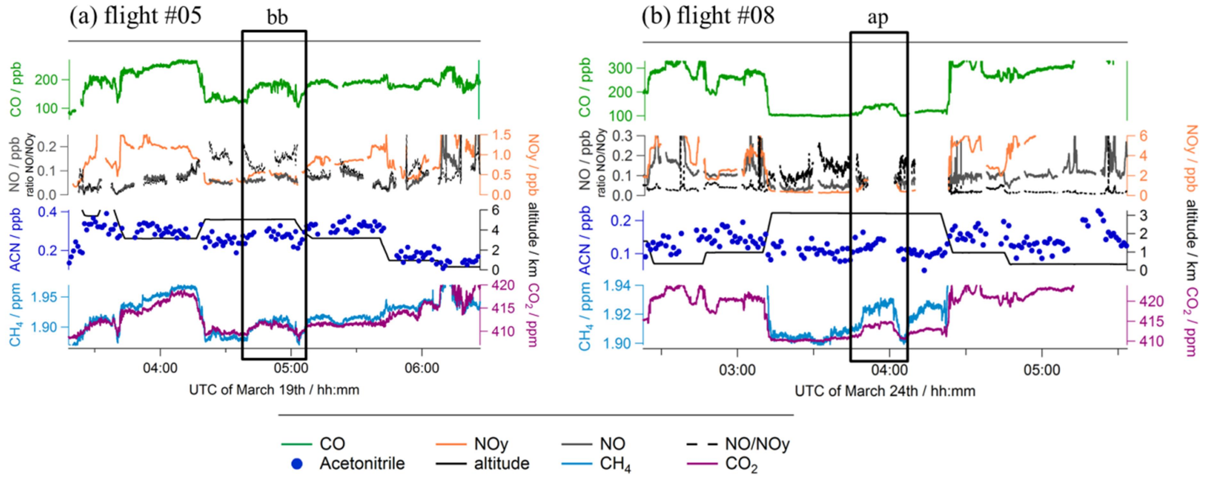

Figure A.12: (a and b) HALO time series of CO (M. Lichtenstern), NO and NO_y (H. Ziereis, P. Stock), Acetonitrile (E. Förster), CH_4 and CO_2 during flight #05 (19.03.2018) and #08 (24.03.2018), respectively. The black squares indicate GHG plumes of large spatial extent. The plumes are tagged with bb for biomass burning influence and ap for anthropogenic pollution according to a mechanism provided by E. Förster (KIT).

A.14 Carbon dioxide observations during EMeRGe

Similar to the presented CH_4 observations, CO_2 data from EMeRGe-Europe and Asia were gridded into bins of 0.05° × 0.05° in latitude and longitude direction, and the maximum measured CO_2 mole fraction in each bin was determined. The results are shown for Europe (Fig. A.13) and Asia (Fig A.14) for different altitude ranges.

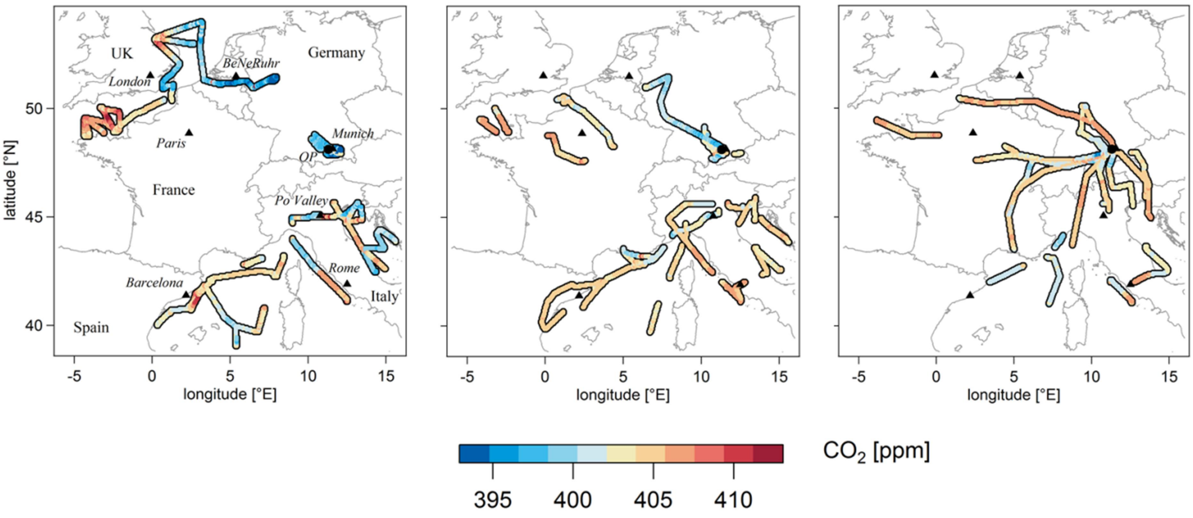

Figure A.13: Maximum measured CO_2 mole fractions from EMeRGe-Europe in 0.05° × 0.05° bins, grouped according to the flight altitude of 0 to 2 km, 2 to 4 km and 4 to 10 km.

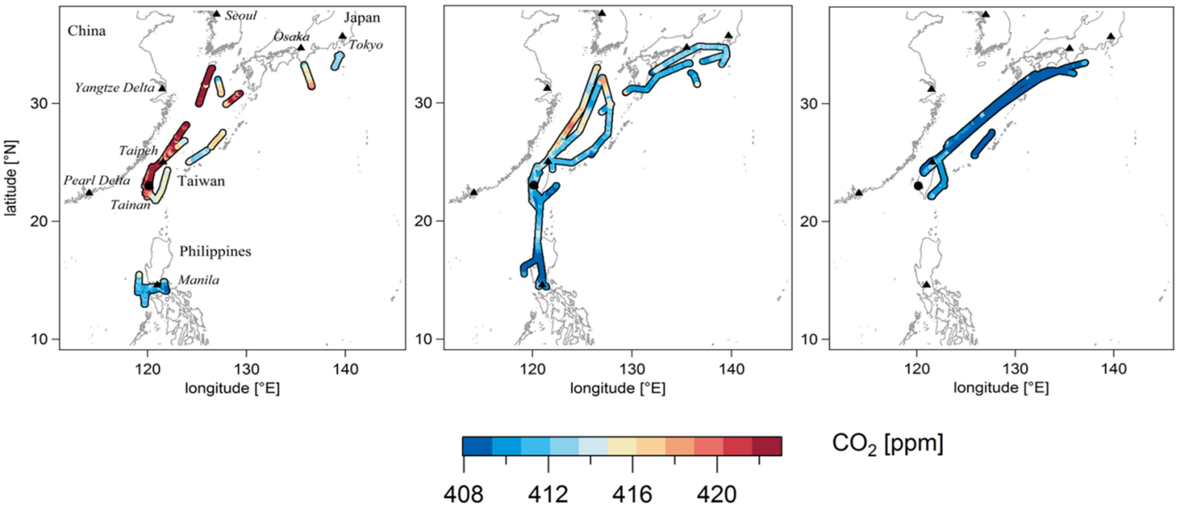

Figure A.14: Maximum measured CO_2 mole fractions from EMeRGe-Asia in 0.05° × 0.05° bins, grouped according to the flight altitude of 0 to 2 km, 2 to 8 km and larger than 8 km.

A.15 Data availability

Internally, all observational CO_2 and CH_4 data obtained within the EMeRGe and $[UC]^2$ mission are available on the HALO database (*https://halo-db.pa.op.dlr.de/*). With respect to the published manuscript (Klausner et al., 2020a), the following data accessibility statement was given: "Observational data (*https://doi.org/10.5281/zenodo.3706725*; Klausner et al, 2020b) and simulation results (*https://doi.org/10.5281/zenodo.3707990*; Mertens and Jöckel, 2020) are publicly available. The MECO(n) model system is part of the Modular Earth Submodel System (MESSy). MESSy is continuously further developed and applied by a consortium of institutions. The usage of MESSy and access to the source code is licenced to all affiliates of institutions which are members of the MESSy Consortium. Institutions can become a member of the MESSy Consortium by signing the MESSy Memorandum of Understanding. The COSMO model, as part of MECO(n), is licenced by the German Weather Service (DWD), or by the COSMO-CLM community. More information can be found on the MESSy Consortium Website (*http://www.messy-interface.org*). The code used for the present study has been based on MESSy version 2.54.0."

B List of abbreviations

Abbreviation	Description
German	
CH_4	Methan
CO_2	Kohlenstoffdioxid
THG	Treibhausgase
English	
AC	Alternating Current
ACN	Acetonitrile
ACP	Atmospheric Chemistry and Physics
AL	Air Liquide
AMT	Atmospheric Measurement Techniques
ATC	Air Traffic Control
AVIRIS-NG	Airborne Visible and Infrared Imaging Spectrometer Next Generation
BEN	Benzene
BeNeRuhr	Belgium, Netherlands, Ruhr area
bf	biofuel
BL	Boundary Layer
BLH	Boundary Layer Height
B-U	Bottom-up approach
C_2H_6	Ethane
CAMS	Copernicus Atmosphere Monitoring Service
CARMA	CARbon Monitoring for Action
CAPS	Cavity Attenuated Phase Shift
CEM	Controlled Evaporator Mixer
CH_3	Methyl radical

CH_4	Methane
CO	Carbon monoxide
CO_2	Carbon dioxide
CO2M	Copernicus Anthropogenic Carbon Dioxide Monitoring
CONTRAIL	Comprehensive Observation Network for TRace gases by AIrLiner
COSMO	COnsortium for Small-scale MOdeling
COSMO-CLM	COSMO model in CLimate Mode
CRDS	Cavity Ring-Down Spectrometry
CW	Continous Wave
DAS	Data Acquisition System
DC	Direct Current
DLR	Deutsches Zentrum für Luft- und Raumfahrt
DWD	Deutscher Wetterdienst
EARLINET	European Aerosol Research LIdar NETwork
EC	Environmental Chamber
ECHAM	European Centre for Medium Range Weather Forecasts Hamburg General Circulation Model
ECMWF	European Centre for Medium-range Weather Forecasts
EDGAR	Emission Database for Global Atmospheric Research
EMAC	ECHAM/MESSy Atmospheric Chemistry model
EMeRGe	Effect of Megacities on the transport and transformation of pollutants on the Regional to Global scales
EPA	Environmental Protection Agency
E-PRTR	European Pollutant and Transfer Register
EZ	Entrainment Zone
FAAM	Facility for Airborne Atmospheric Measurements
ff	fossil fuel
FT	Free Troposphere

FTIR	Fourier-Transform InfraRed spectrometer
GFS	Global Forecast System
GHG	Greenhouse Gas
GPS	Global Positioning System
GWP	Global Warming Potential
H_2O	Water vapour
HALO	High Altitude and LOng range
HK	Hong Kong
HYSPLIT	HYbrid Single-Particle Lagrangian Integrated Trajectory
ICON	ICOsahedral Nonhydrostatic forecast model
ICOS	Integrated Carbon Observation System
IPA	Institute of Atmospheric Physics
IPCC	Intergovernmental Panel on Climate Change
IR	Infrared
IRS	Inertial Reference System
KIT	Karlsruhe Institute of Technology
KORUS-AQ	KORean-United States Air Qualtiy
LandGEM	LANDfill Gas Emission Model
LIDAR	LIght Detection And Ranging
LRT	Long-Range Transport
MBL	Marine Boundary Layer
MECO(n)	MESSy-field ECHAM and COSMO models nested n times
MESSy	Modular Earth Submodel SYstem
METPOD	Meteorological sensor package
MF	Mole Fraction
MFC	Mass Flow Controller
ML	Mixed Layer

MODIS	MODerate Resolution Imaging Spectroradiometer
MPCs	Major Population Centres
N_2	Nitrogen
N_2O	Nitrous oxide
NASA	National Aeronautics and Space Administration
NIES	National Institute for Environmental Studies
NO	Nitrogen oxide
NO_2	Nitrogen dioxide
NOAA	National Oceanic and Atmospheric Administration
NO_y	Sum of all reactive nitrogen species
O_2	Oxygen
O_3	Ozone
OCO	Orbiting Carbon Observatory
OH	Hydroxyl radical
PFA	PerFluoroAlkoxy
PMCH	PerfluoroMethyl-CycloHexane
Pr	Pearson correlation coefficient
PTFE	PolyTetraFluoroEthylene
PVU	Power Vacuum Unit
QCLS	Quantum and interband Cascade Laser Spectrometer
Radar	Radio detection and ranging
RCP	Representative Concentration Pathway
REAS	Regional Emission Inventory in ASia
RF	Radiative Forcing
RWE	Rheinisch-Westfälisches Elektrizitätswerk
SCIAMACHY	SCanning Imaging Absorption spectroMeter for Atmospheric CHartographY

SL	Surface Layer
T-D	Top-Down approach
TF	Tempelhofer Feld
TRACE-P	TRAnsport and Chemical Evolution over the Pacific
TROPOMI	TROPOspheric Monitoring Instrument
$[UC]^2$	Urban Climate Under Change
UTC	Coordinated universal time
VIIRS	Visible Infrared Imaging Radiometer Suite
VPRM	Vegetation Photosynthesis and Respiration Model
ZA	Zero Air

C List of symbols

Symbol	Description
α	Absorption coefficient
a, b, c, d	Water vapour correction factors
$AL_{corrected}$	Corrected concentration of the Air Liquide standards
$AL_{measured}$	Measured concentration of the Air Liquide standards
c	Y-intercept of regression line
c_{avg}	Y-intercept of regression line (campaing average)
$(CH_4)_{dry}$	CH_4 mole fraction in dry air
$(CH_4)_{rep}$	Reported (raw) CH_4 mole fraction from the Picarro analyser
$(CO_2)_{dry}$	CO_2 mole fraction in dry air
$(CO_2)_{\mathrm{rep}}$	Reported (raw) CO_2 mole fraction from the Picarro analyser
c_p	Specific heat constant
$\delta^{13}C(CH_4)$	Delta 13-C notation
$drift_t$	Instrument drift with time
$drift_T$	Instrument drift with temperature
$(H_2O)_{rep}$	Reported (raw) water vapour value
I_0	Intensity of incident signal
I_t	Intensity of transmitted signal
$-k,k$	Horizontal boundaries of the plume
L	Path length
m	Regression slope
m_{avg}	Regression slope (campaing average)
m_d	Mass of dry air
MF_{final}	Final mole fraction
MF_{raw}	Raw mole fraction from the Picarro analyser
m_v	Mass of water vapour
N	Number density
N_{air}	Number density of air
p	Pressure
p_0	Pressure at sea level
$precision$	Measurement precision, equal to 1-sigma standard deviation

q	Specific humidity
R	Stable isotope ratio of $^{13}C/^{12}C$
R_{sample}	Ratio in the sample
$R_{standard}$	Ratio in the reference standard
$reprod._{primary}$	Reproducibility of the primary standard
$reprod._{secondary}$	Reproducibility of the secondary standard
RH	Relative Humidity
σ	Absorption cross section
τ	Ring-down time
θ	Potential temperature
t	Time
T	Temperature
tr	Round trip time
u	Horizontal wind
u_{total}	Total measurement uncertainty
$u_{water\ vapour}$	Uncertainty associated with the water vapour correction
V	Wind speed
v_g	Geostrophic wind
X_{dry}	GHG mole fraction in dry air
X_{wet}	GHG mole fraction in wet air
X_{rep}	Reported GHG mole fraction from the Picarro analyser
X_{bgr}	Background GHG mole fraction

D Bibliography

Alimonti, G., Cifarelli, L., and Wagner, F.: Our energy future starts from actual energy limits, *EPJ Web Conf.* **2018,** *189*, 3. DOI: 10.1051/epjconf/201818900003.

Allen, M.R., Dube, O.P., Solecki, W., Aragón-Durand, F., Cramer, W., Humphreys, S., Kainuma, M., Kala, J., Mahowald, N., Mulugetta, Y., Perez, R., Wairiu, M., and Zickfeld, K. **2018**: Framing and Context. In: Global Warming of 1.5°C. An IPCC Special Report on the impacts of global warming of 1.5°C above pre-industrial levels and related global greenhouse gas emission pathways, in the context of strengthening the global response to the threat of climate change, sustainable development, and efforts to eradicate poverty [Masson-Delmotte, V., P. Zhai, H.-O. Pörtner, D. Roberts, J. Skea, P.R. Shukla, A. Pirani, W. Moufouma-Okia, C. Péan, R. Pidcock, S. Connors, J.B.R. Matthews, Y. Chen, X. Zhou, M.I. Gomis, E. Lonnoy, T. Maycock, M. Tignor, and T. Waterfield (eds.)]. In Press.

Ammoura, L., Xueref-Remy, I., Vogel, F., Gros, V., Baudic, A., Bonsang, B., Delmotte, M., Té, Y., and Chevallier, F.: Exploiting stagnant conditions to derive robust emission ratio estimates for CO_2 , CO and volatile organic compounds in Paris, *Atmos. Chem. Phys.* **2016,** *16* (24), 15653–15664. DOI: 10.5194/acp-16-15653-2016.

Anderegg, W.R.L., Prall, J.W., Harold, J., and Schneider, S.H.: Expert credibility in climate change, *Proceedings of the National Academy of Sciences of the United States of America* **2010,** *107* (27), 12107–12109. DOI: 10.1073/pnas.1003187107.

Andrews, A.E., Kofler, J.D., Trudeau, M.E., Williams, J.C., Neff, D.H., Masarie, K.A., Chao, D.Y., Kitzis, D.R., Novelli, P.C., Zhao, C.L., Dlugokencky, E.J., Lang, P.M., Crotwell, M.J., Fischer, M.L., Parker, M.J., Lee, J.T., Baumann, D.D., Desai, A.R., Stanier, C.O., de Wekker, S.F.J., Wolfe, D.E., Munger, J.W., and Tans, P.P.: CO_2, CO, and CH_4 measurements from tall towers in the NOAA Earth System Research Laboratory's Global Greenhouse Gas Reference Network: Instrumentation, uncertainty analysis, and recommendations for future high-accuracy greenhouse gas monitoring efforts, *Atmos. Meas. Tech.* **2014,** *7* (2), 647–687. DOI: 10.5194/amt-7-647-2014.

Archer, D., Eby, M., Brovkin, V., Ridgwell, A., Cao, L., Mikolajewicz, U., Caldeira, K., Matsumoto, K., Munhoven, G., Montenegro, A., and Tokos, K.: Atmospheric Lifetime of Fossil Fuel Carbon Dioxide, *Annu. Rev. Earth Planet. Sci.* **2009,** *37* (1), 117–134. DOI: 10.1146/annurev.earth.031208.100206.

Ashrafi, K., Shafiepour-Motlagh, M., Aslemand, A., and Ghader, S.: Dust storm simulation over Iran using HYSPLIT, *Journal of environmental health science & engineering* **2014,** *12* (1), 9. DOI: 10.1186/2052-336X-12-9.

Ashworth, K., Bucci, S., Gallimore, P.J., Lee, J., Nelson, B.S., Sanchez Marroquin, A., Schimpf, M.B., Smith, P.D., Drysdale, W.S., Hopkins, J.R., Lee, J.D., Pitt, J.R., Di Carlo, P., Krejci, R., and McQuaid, J.B.: Megacity and local contributions to regional air pollution: An aircraft case study over London, *Atmos. Chem. Phys. Discuss.* **2019**. https://doi.org/10.5194/acp-2019-955, in review.

AVISO GmbH and IE Leipzig**, 2016**: Erstellung der Berliner Emissionskataster Industrie, Gebäudeheizung, sonstiger Verkehr, Kleingewerbe, sonstige Quellen, Baustellen – Schlussbericht Juni 2016. *Techn. rep.* https://www.berlin.de/senuvk/umwelt/luftqualitaet/de/emissionen/download/Endbericht_Emissionkataster_2015.pdf last access 30.09.2019.

Bartlett, K.B., Sachse, G.W., Slate, T., Harward, C., and Blake, D.R.: Large-scale distribution of CH_4 in the western North Pacific: Sources and transport from the Asian continent, *J. Geophys. Res.* **2003,** *108* (D20), 955. DOI: 10.1029/2002JD003076.

Beck, V., Gerbig, C., Koch, T., Bela, M.M., Longo, K.M., Freitas, S.R., Kaplan, J.O., Prigent, C., Bergamaschi, P., and Heimann, M.: WRF-Chem simulations in the Amazon region during wet and dry season transitions. Evaluation of methane models and wetland inundation maps, *Atmos. Chem. Phys.* **2013,** 13(16): 7961–7982. DOI: https://doi.org/10.5194/acp-13-7961-2013.

Berden, G., and Engeln, R.: Cavity Ring-Down Spectroscopy: Techniques and Applications*,* John Wiley & Sons, Ltd: Chichester, UK, **2009**. ISBN: 978-1-405-17688-0.

Bergamaschi, P., Karstens, U., Manning, A.J., Saunois, M., Tsuruta, A., Berchet, A., Vermeulen, A.T., Arnold, T., Janssens-Maenhout, G., Hammer, S., Levin, I., Schmidt, M., Ramonet, M., Lopez, M., Lavric, J., Aalto, T., Chen, H., Feist, D.G., Gerbig, C., Haszpra, L., Hermansen, O., Manca, G., Moncrieff, J., Meinhardt, F., Necki, J., Galkowski, M., O'Doherty, S., Paramonova, N., Scheeren, H. A., Steinbacher, M., and Dlugokencky, E.: Inverse modelling of European CH_4 emissions during 2006–2012 using different inverse models and reassessed atmospheric observations, *Atmos. Chem. Phys.* **2018,** *18* (2), 901–920. DOI: 10.5194/acp-18-901-2018.

Bey, I., Jacob, D.J., Logan, J.A., and Yantosca, R.M.: Asian chemical outflow to the Pacific in spring: Origins, pathways, and budgets, *J. Geophys. Res.* **2001,** *106* (D19), 23097–23113. DOI: 10.1029/2001JD000806.

Bousquet, P., Ringeval, B., Pison, I., Dlugokencky, E.J., Brunke, E.-G., Carouge, C., Chevallier, F., Fortems-Cheiney, A., Frankenberg, C., Haglustaine, D.A., Krummel, P.B., Langenfelds, R.L., Ramonet, M., Schmidt, M., Steele, L.P., Szopa, S., Yver, C., Viovy, N., and Ciais, P.: Source attribution of the changes in atmospheric methane for 2006–2008, *Atmos. Chem. Phys.* **2011**, 11 (8), 3689–3700. DOI: 10.5194/acp-11-3689-2011.

Brandt, A.R., Heath, G.A., Kort, E.A., O'Sullivan, F., Pétron, G., Jordaan, S.M., Tans, P., Wilcox, J., Gopstein, A.M., Arent, D., Wofsy, S., Brown, N.J., Bradley, R., Stucky, G.D., Eardley, D., and Harriss, R.: Methane leaks from North American natural gas systems, *Science (New York, N.Y.)* **2014,** *343* (6172), 733–735. DOI: 10.1126/science.1247045.

Bréon, F.M., Broquet, G., Puygrenier, V., Chevallier, F., Xueref-Remy, I., Ramonet, M., Dieudonné, E., Lopez, M., Schmidt, M., Perrussel, O., and Ciais, P.: An attempt at estimating Paris area CO_2 emissions from atmospheric concentration measurements, *Atmos. Chem. Phys.* **2015,** *15* (4), 1707–1724. DOI: 10.5194/acp-15-1707-2015.

Brunner, D., Kuhlmann, G., Marshall, J., Clément, V., Fuhrer, O., Broquet, G., Löscher, A., and Meijer, Y.: Accounting for the vertical distribution of emissions in atmospheric CO_2 simulations, *Atmos. Chem. Phys.* **2019,** *19* (7), 4541–4559. DOI: 10.5194/acp-19-4541-2019.

Burrows, J.P., Andrés, H.M.D., Koppmann, R., Pfeilsticker, K., Platt, U., Pozzer, A., Schlager, H., Schneider, J., Verkoussis, M., and Zahn, A.: White Paper EMeRGe: Effect of Megacities on the Transport and Transformation of Pollutants on the Regional to Global Scales, **2016**. Available on the internal campaing data website.

Busch, K.W., and Busch, M.A.: Cavity-ringdown spectroscopy. An ultratrace-absorption measurement technique, ACS symposium series 720, *American Chemical Society* **1999**. ISBN: 0-8412-3600-3.

Cain, M., Warwick, N.J., Fisher, R.E., Lowry, D., Lanoisellé, M., Nisbet, E.G., France, J., Pitt, J., O'Shea, S., Bower, K.N., Allen, G., Illingworth, S., Manning, A. J., Bauguitte, S., Pisso, I., and Pyle, J.A.: A cautionary tale: A study of a methane enhancement over the North Sea, *J. Geophys. Res.* **2017,** *122* (14), 7630–7645. DOI: 10.1002/2017JD026626.

Cambaliza, M.O.L., Shepson, P.B., Caulton, D.R., Stirm, B., Samarov, D., Gurney, K.R., Turnbull, J., Davis, K.J., Possolo, A., Karion, A., Sweeney, C., Moser, B., Hendricks, A., Lauvaux, T., Mays, K., Whetstone, J., Huang, J., Razlivanov, I., Miles, N.L., and Richardson, S.J.: Assessment of uncertainties of an aircraft-based mass balance approach for quantifying urban greenhouse gas emissions, *Atmos. Chem. Phys.* **2014,** *14* (17), 9029–9050. DOI: 10.5194/acp-14-9029-2014.

Cambaliza, M.O.L., Shepson, P.B., Bogner, J., Caulton, D.R., Stirm, B., Sweeney, C., Montzka, S.A., Gurney, K.R., Spokas, K., Salmon, O.E., Lavoie, T.N., Hendricks, A., Mays, K., Turnbull, J., Miller, B. R., Lauvaux, T., Davis, K., Karion, A., Moser, B., Miller, C., Obermeyer, C., Whetstone, J., Prasad, K., Miles, N., and Richardson, S.: Quantification and source apportionment of the methane emission flux from the city of Indianapolis, *Elem. Sci. Anth.* **2015,** *3*, 37. DOI: 10.12952/journal.elementa.000037.

Carmichael, G.R., Uno, I., Phadnis, M.J., Zhang, Y., and Sunwoo, Y.: Tropospheric ozone production and transport in the springtime in east Asia, *J. Geophys. Res.* **1998,** *103* (D9), 10649–10671. DOI: 10.1029/97JD03740.

Chen, H., Winderlich, J., Gerbig, C., Hoefer, A., Rella, C.W., Crosson, E.R., van Pelt, A.D., Steinbach, J., Kolle, O., Beck, V., Daube, B.C., Gottlieb, E.W., Chow, V.Y., Santoni, G.W., and Wofsy, S.C.: High-accuracy continuous airborne measurements of greenhouse gases (CO_2 and CH_4) using the cavity ring-down spectroscopy (CRDS) technique, *Atmos. Meas. Tech.* **2010,** *3* (2), 375–386. DOI: 10.5194/amt-3-375-2010.

CIESIN, **2018** Center for International Earth Science Information Network - CIESIN - Columbia University. 2018. Gridded Population of the World, Version 4 (GPWv4): Population Density, Revision 11. Palisades, NY: NASA Socioeconomic Data and Applications Center (SEDAC). https://doi.org/10.7927/H49C6VHW last access 02.09.2019.

Copernicus, **2018**: Report on the European State of the Climate 2017. https://climate.copernicus.eu/CopernicusESC last access 03.04.2020.

CORRECTIV, **2016**: Stories: Müllparadies Brandenburg. https://correctiv.org/artikel/2016/03/02/muellparadies-brandenburg last access 18.08.2019.

Cottle, P., Strawbridge, K., and McKendry, I.: Long-range transport of Siberian wildfire smoke to British Columbia: Lidar observations and air quality impacts, *Atmospheric Environment* **2014,** *90*, 71–77. DOI: 10.1016/j.atmosenv.2014.03.005.

Crawford, A.M., Stunder, B.J.B., Ngan, F., and Pavolonis, M.J.: Initializing HYSPLIT with satellite observations of volcanic ash: A case study of the 2008 Kasatochi eruption, *J. Geophys. Res.* **2016,** *121* (18), 10,786-10,803. DOI: 10.1002/2016JD024779.

Crippa, M., Oreggioni, G., Guizzardi, D., Muntean, M., Schaaf, E., Lo Vullo, E., Solazzo, E., Monforti-Ferrario, F., Olivier, J.G.J., and Vignati, E.: Fossil CO_2 and GHG emissions of all world countries. 2019 report, EUR 29849, *Publications Office of the European Union: Luxembourg*, **2019**.

Crosson, E.R.: A cavity ring-down analyzer for measuring atmospheric levels of methane, carbon dioxide, and water vapor, *Appl. Phys. B.* **2008,** *92* (3), 403–408. DOI: 10.1007/s00340-008-3135-y.

Dacre, H.F., Gray, S.L., and Belcher, S.E: A case study of boundary layer ventilation by convection and coastal processes, *J. Geophys. Res.* **2007,** *112* (D17), D18304. DOI: 10.1029/2006JD007984.

Dai, C., Wang, Q., Kalogiros, J.A., Lenschow, D.H., Gao, Z., and Zhou, M.: Determining Boundary-Layer Height from Aircraft Measurements, *Boundary-Layer Meteorol* **2014,** *152* (3), 277–302. DOI: 10.1007/s10546-014-9929-z.

Dlugokencky, E.J.: Conversion of NOAA atmospheric dry air CH_4 mole fractions to a gravimetrically prepared standard scale, *J. Geophys. Res.* **2005,** *110* (D18), 273. DOI: 10.1029/2005JD006035.

Dlugokencky, E.J., Nisbet, E.G., Fisher, R., and Lowry, D.: Global atmospheric methane: Budget, changes and dangers, *Philosophical transactions. Series A, Mathematical, physical, and engineering sciences* **2011,** *369* (1943), 2058–2072. DOI: 10.1098/rsta.2010.0341.

Draxler R., and Hess G.D.: Description of the HYSPLIT_4 modeling system for trajectories, dispersion, and deposition, *Australian meteorological magazine* **1998**, 47(4), 295-308. https://www.researchgate.net/publication/235961417.

Enerdata, **2019**: Global Energy Statistical Yearbook 2019. https://yearbook.enerdata.net/total-energy/world-consumption-statistics.html last acces 06.04.2020.

EPA**, 2010**: Greenhouse gas emissions estimation methodologies for biogenic emissions from selected source categories: solid waste disposal, wastewater treatment, ethanol fermentation. https://www3.epa.gov/ttnchie1/efpac/ghg/GHG_Biogenic_Report_draft_Dec1410.pdf last access 05.06.2020.

E-PRTR The European Pollutant Release and Transfer Register, data version v18 *https://prtr.eea.europa.eu/#/home,* reporting for the year **2015, 2016** and **2017**.

Escudero, M., Stein, A.F., Draxler, R.R., Querol, X., Alastuey, A., Castillo, S., and Avila, A.: Source apportionment for African dust outbreaks over the Western Mediterranean using the HYSPLIT model, *Atmospheric Research* **2011,** *99* (3-4), 518–527. DOI: 10.1016/j.atmosres.2010.12.002.

Etheridge, D.M., Steele, L.P., Langenfelds, R.L., Francey, R.J., Barnola, J.-M., and Morgan, V.I.: Natural and anthropogenic changes in atmospheric CO_2 over the last 1000 years from air in Antarctic ice and firn, *J. Geophys. Res.* **1996,** *101* (D2), 4115–4128. DOI: 10.1029/95JD03410.

Etheridge, D.M., Steele, L.P., Francey, R.J., and Langenfelds, R.L.: Atmospheric methane between 1000 A.D. and present: Evidence of anthropogenic emissions and climatic variability, *J. Geophys. Res.* **1998,** *103* (D13), 15979–15993. DOI: 10.1029/98JD00923.

Fisher, R., Lowry, D., Wilkin, O., Sriskantharajah, S., and Nisbet, E.G.: High-precision, automated stable isotope analysis of atmospheric methane and carbon dioxide using continuous-flow isotope-ratio mass spectrometry, *Rapid communications in mass spectrometry : RCM* **2006,** *20* (2), 200–208. DOI: 10.1002/rcm.2300.

Forster, G.: Weybourne Atmospheric Observatory: Longterm methane measurements. NCAS British Atmospheric Data Centre, **2013**. https://catalogue.ceda.ac.uk/uuid/e9c9e975601f4ba4ac1756a 3c112a8d1 last access 13.02.2018.

france bleu, **2017**: Incendie dans le Luberon : 800 hectares détruits, une centaine d'habitations évacuées. https://www.francebleu.fr/infos/climat-environnement/urgent-un-feu-de-foret-dans-un-massif-la-bastidonne-1500891833 last access 31.03.2020.

Frankenberg, C., Meirink, J.F., Bergamaschi, P., Goede, A.P.H., Heimann, M., Körner, S., Platt, U., van Weele, M., and Wagner, T.: Satellite chartography of atmospheric methane from SCIAMACHY on board ENVISAT: Analysis of the years 2003 and 2004, *J. Geophys. Res.* **2006,** *111* (D7), 31101. DOI: 10.1029/2005JD006235.

Fu, X.W., Zhang, H., Lin, C.-J., Feng, X.B., Zhou, L.X., and Fang, S.X.: Correlation slopes of GEM/CO, GEM/CO_2 , and GEM/CH_4 and estimated mercury emissions in China, South Asia, the Indochinese Peninsula, and Central Asia derived from observations in northwestern and southwestern China, *Atmos. Chem. Phys.* **2015,** *15* (2), 1013–1028. DOI: 10.5194/acp-15-1013-2015.

Gately, C.K., and Hutyra, L.R.: Large Uncertainties in Urban-Scale Carbon Emissions, *J. Geophys. Res.* **2017,** *122* (20), 11,242-11,260. DOI: 10.1002/2017JD027359.

Gately, C.K., Hutyra, L.R., Wing, I.S., and Brondfield, M.N.: A bottom up approach to on-road CO_2 emissions estimates: Improved spatial accuracy and applications for regional planning, *Environmental science & technology* **2013,** *47* (5), 2423–2430. DOI: 10.1021/es304238v.

Gioli, B., Toscano, P., Lugato, E., Matese, A., Miglietta, F., Zaldei, A., and Vaccari, F.P.: Methane and carbon dioxide fluxes and source partitioning in urban areas: The case study of Florence, Italy, *Environmental pollution (Barking, Essex : 1987)* **2012,** *164*, 125–131. DOI: 10.1016/j.envpol.2012.01.019.

Gioli, B., Carfora, M.F., Magliulo, V., Metallo, M.C., Poli, A.A., Toscano, P., and Miglietta, F.: Aircraft mass budgeting to measure CO_2 emissions of Rome, Italy, *Environmental monitoring and assessment* **2014,** *186* (4), 2053–2066. DOI: 10.1007/s10661-013-3517-4.

Granier, C., Darras, S., Denier van der Gon, H., Doubalova, J., Elguindi, N., Galle, B., Gauss, M., Guevara, M., Jalkanen, J.-P., Kuenen, J., Liousse, C., Quack, B., Simpson, D., and Sindelarova, K.: The Copernicus Atmosphere Monitoring Service global and regional emissions (April 2019 version), Copernicus Atmosphere Monitoring Service (CAMS) report, **2019**. DOI:10.24380/d0bn-kx16.

Günzler, H., and Gremlich, H.-U.: IR-Spektroskopie. Eine Einführung, *Wiley-VCH Verlag GmbH & Co. KGaA*, Weinheim, **2003**. ISBN: 3-527-30801-6.

HALO, **2006**: High Altitude and Long Range Research Aircraft. http://www.halo.dlr.de/about/about.html last access 03.04.2020.

Han, P., Zeng, N., Oda, T., Lin, X., Crippa, M., Guan, D., Janssens-Maenhout, G., Ma, X., Liu, Z., Shan, Y., Tao, S., Wang, H., Wang, R., Wu, L., Yun, X., Zhang, Q., Zhao, F., and Zheng, B.: Evaluating China's fossil-fuel CO_2 emissions from a comprehensive dataset of nine inventories, *Atmos. Chem. Phys. Discuss.* **2020**. https://doi.org/10.5194/acp-2019-643, in review.

Hardiman, B.S., Wang, J.A., Hutyra, L.R., Gately, C.K., Getson, J.M., and Friedl, M.A.: Accounting for urban biogenic fluxes in regional carbon budgets, *The Science of the total environment* **2017,** *592*, 366–372. DOI: 10.1016/j.scitotenv.2017.03.028.

Hase, F., Frey, M., Blumenstock, T., Groß, J., Kiel, M., Kohlhepp, R., Mengistu Tsidu, G., Schäfer, K., Sha, M.K., and Orphal, J.: Application of portable FTIR spectrometers for detecting greenhouse gas emissions of the major city Berlin, *Atmos. Meas. Tech.* **2015,** *8* (7), 3059–3068. DOI: 10.5194/amt-8-3059-2015.

Hausmann, P., Sussmann, R., and Smale, D.: Contribution of oil and natural gas production to renewed increase in atmospheric methane (2007–2014): Top–down estimate from ethane and methane column observations, *Atmos. Chem. Phys.* **2016,** *16* (5), 3227–3244. DOI: 10.5194/acp-16-3227-2016.

Heal, M.R., Heard, D.E., Pilling, M.J., and Whitaker, B.J.: On the Development and Validation of FAGE for Local Measurement of Tropospheric OH and HO_2, *J. Atmos. Sci.* **1995,** *52* (19), 3428–3441. DOI: 10.1175/1520-0469(1995)052<3428:OTDAVO>2.0.CO,2.

Heimburger, A.M.F., Harvey, R.M., Shepson, P.B., Stirm, B.H., Gore, C., Turnbull, J., Cambaliza, M.O.L., Salmon, O.E., Kerlo, A.-E.M., Lavoie, T.N., Davis, K.J., Lauvaux, T., Karion, A., Sweeney, C., Brewer, W.A., Hardesty, R. M., and Gurney, K.R.: Assessing the optimized precision of the aircraft mass balance method for measurement of urban greenhouse gas emission rates through averaging, *Elem. Sci. Anth.* **2017,** *5* (0), 26. DOI: 10.1525/elementa.134.

Helfter, C., Famulari, D., Phillips, G.J., Barlow, J.F., Wood, C.R., Grimmond, C.S.B., and Nemitz, E.: Controls of carbon dioxide concentrations and fluxes above central London, *Atmos. Chem. Phys.* **2011,** *11* (5), 1913–1928. DOI: 10.5194/acp-11-1913-2011.

Helfter, C., Tremper, A.H., Halios, C.H., Kotthaus, S., Bjorkegren, A., Grimmond, C.S.B., Barlow, J.F., and Nemitz, E.: Spatial and temporal variability of urban fluxes of methane, carbon monoxide and carbon dioxide above London, UK, *Atmos. Chem. Phys.* **2016,** *16* (16), 10543–10557. DOI: 10.5194/acp-16-10543-2016.

Heymann, J., Bovensmann, H., Buchwitz, M., Burrows, J.P., Deutscher, N.M., Notholt, J., Rettinger, M., Reuter, M., Schneising, O., Sussmann, R., and Warneke, T.: SCIAMACHY WFM-DOAS XCO_2: reduction of scattering related errors, *Atmos. Meas. Tech.* **2012**, 5, 2375-2390. DOI:10.5194/amt-5-2375-2012.

HITRAN*online*, 2020. https://hitran.org/docs/iso-meta/ last access 27.05.2020.

Hofmann, C., Kerkweg, A., Wernli, H., and Jöckel, P.: The 1-way on-line coupled atmospheric chemistry model system MECO(n) – Part 3: Meteorological evaluation of the on-line coupled system, *Geosci. Model Dev.* **2012,** *5* (1), 129–147. DOI: 10.5194/gmd-5-129-2012.

Hogue, S., Marland, E., Andres, R. J., Marland, G., and Woodard, D.: Uncertainty in gridded CO_2 emissions estimates, *Earth's Future* **2016,** *4* (5), 225–239. DOI: 10.1002/2015EF000343.

Holzinger, R., Williams, J., Salisbury, G., Klüpfel, T., Reus, M. de, Traub, M., Crutzen, P. J., and Lelieveld, J.: Oxygenated compounds in aged biomass burning plumes over the Eastern Mediterranean: Evidence for strong secondary production of methanol and acetone, *Atmos. Chem. Phys.* **2005,** *5* (1), 39–46. DOI: 10.5194/acp-5-39-2005.

Hopkins, F.M., Kort, E.A., Bush, S.E., Ehleringer, J.R., Lai, C.-T., Blake, D.R., and Randerson, J.T.: Spatial patterns and source attribution of urban methane in the Los Angeles Basin, *J. Geophys. Res.* **2016,** *121* (5), 2490–2507. DOI: 10.1002/2015JD024429.

Huq, S., Kovats, S., Reid, H., and Satterthwaite, D.: Editorial: Reducing risks to cities from disasters and climate change, *Environment and Urbanization* **2016,** *19* (1), 3–15. DOI: 10.1177/0956247807078058.

ICOS RI, **2019**: ICOS ATC NRT CH_4, CO_2 and Meteo growing time series, Lindenberg (40.0, 98.0 m), 2018-06-01–2019-06-04, https://hdl.handle.net/11676/KUAe-h1L-yNR1iGXPn927YU0, https://hdl.handle.net/11676/l23pTk3v8_nZNwz5evSLSuwA, https://hdl.handle.net/11676/nj7O75BKQseHQ6p-gpP-niW2, https://hdl.handle.net/11676/inftlfslCvYWryg2V5qmwllf, https://hdl.handle.net/11676/VO0go83bM2MKpY2e5N3AoeJC, https://hdl.handle.net/11676/Rl6syy9MOQF-oz-SEKAc5-1Y.

IGRA, **2017**: Integrated Global Radiosonde Archive, station #SPM00008190 and #SPM00008302, version 2 data. https://www.ncdc.noaa.gov/data-access/weather-balloon/integrated-global-radiosonde-archive last access 05.09.2019.

IPCC; 2018: Summary for Policymakers. In: Global Warming of 1.5°C. An IPCC Special Report on the impacts of global warming of 1.5°C above pre-industrial levels and related global greenhouse gas emission pathways, in the context of strengthening the global response to the threat of climate change, sustainable development, and efforts to eradicate poverty [Masson-Delmotte, V., P. Zhai, H.-O. Pörtner, D. Roberts, J. Skea, P.R. Shukla, A. Pirani, W. Moufouma-Okia, C. Péan, R. Pidcock, S. Connors, J.B.R. Matthews, Y. Chen, X. Zhou, M.I. Gomis, E. Lonnoy, T. Maycock, M. Tignor, and T. Waterfield (eds.)]. *World Meteorological Organization, Geneva, Switzerland, 32 pp.*

Jacob, D.: Introduction to Atmospheric Chemistry, *Princeton University Press* **1999**. ISBN: 0-691-00185-5.

Jacob, D.J., Turner, A.J., Maasakkers, J.D., Sheng, J., Sun, K., Liu, X., Chance, K., Aben, I., McKeever, J., and Frankenberg, C.: Satellite observations of atmospheric methane and their value for quantifying methane emissions, *Atmos. Chem. Phys.* **2016,** *16* (22), 14371–14396. DOI: 10.5194/acp-16-14371-2016.

Janssens-Maenhout, G., Pagliari, V., Guizzardi, D., and Muntean, M.: Global emission inventories in the Emission Database for Global Atmospheric Research (EDGAR). Manual (I) - gridding: EDGAR emissions distribution on global gridmaps, EUR, Scientific and technical research series 25785, *Publications Office: Luxembourg*, **2012**.

Janssens-Maenhout, G., Crippa, M., Guizzardi, D., Muntean, M., Schaaf, E., Dentener, F., Bergamaschi, P., Pagliari, V., Olivier, J.G.J., Peters, J.A.H.W., van Aardenne, J.A., Monni, S., Doering, U., Petrescu, A.M.R., Solazzo, E., and Oreggioni, G.D.: EDGAR v4.3.2 Global Atlas of the three major greenhouse gas emissions for the period 1970–2012, *Earth Syst. Sci. Data* **2019,** *11* (3), 959–1002. DOI: 10.5194/essd-11-959-2019.

Jöckel, P., Kerkweg, A., Pozzer, A., Sander, R., Tost, H., Riede, H., Baumgaertner, A., Gromov, S., and Kern, B.: Development cycle 2 of the Modular Earth Submodel System (MESSy2), *Geosci. Model Dev.* **2010,** *3* (2), 717–752. DOI: 10.5194/gmd-3-717-2010.

Kadygrov, N., Broquet, G., Chevallier, F., Rivier, L., Gerbig, C., and Ciais, P.: On the potential of the ICOS atmospheric CO_2 measurement network for estimating the biogenic CO_2 budget of Europe, *Atmos. Chem. Phys.* **2015,** *15* (22), 12765–12787. DOI: 10.5194/acp-15-12765-2015.

Karion, A., Sweeney, C., Pétron, G., Frost, G., Michael Hardesty, R., Kofler, J., Miller, B.R., Newberger, T., Wolter, S., Banta, R., Brewer, A., Dlugokencky, E., Lang, P., Montzka, S.A., Schnell, R., Tans, P., Trainer, M., Zamora, R., and Conley, S.: Methane emissions estimate from airborne measurements over a western United States natural gas field, *Geophys. Res. Lett.* **2013a,** *40* (16), 4393–4397. DOI: 10.1002/grl.50811.

Karion, A., Sweeney, C., Wolter, S., Newberger, T., Chen, H., Andrews, A., Kofler, J., Neff, D., and Tans, P.: Long-term greenhouse gas measurements from aircraft, *Atmos. Meas. Tech.* **2013b,** *6* (3), 511–526. DOI: 10.5194/amt-6-511-2013.

Karion, A., Sweeney, C., Kort, E.A., Shepson, P.B., Brewer, A., Cambaliza, M., Conley, S.A., Davis, K., Deng, A., Hardesty, M., Herndon, S.C., Lauvaux, T., Lavoie, T., Lyon, D., Newberger, T., Pétron, G., Rella, C., Smith, M., Wolter, S., Yacovitch, T.I., and Tans, P.: Aircraft-Based Estimate of Total Methane Emissions from the Barnett Shale Region, *Environmental science & technology* **2015,** *49* (13), 8124–8131. DOI: 10.1021/acs.est.5b00217.

Kennedy, C., Demoullin, S., and Mohareb, E.: Cities reducing their greenhouse gas emissions, *Energy Policy* **2012,** *49*, 774–777. DOI: 10.1016/j.enpol.2012.07.030.

Kerkweg, A., and Jöckel, P.: The 1-way on-line coupled atmospheric chemistry model system MECO(n) – Part 1: Description of the limited-area atmospheric chemistry model COSMO/MESSy, *Geosci. Model Dev.* **2012a,** *5* (1), 87–110. DOI: 10.5194/gmd-5-87-2012.

Kerkweg, A., and Jöckel, P.: The 1-way on-line coupled atmospheric chemistry model system MECO(n) – Part 2: On-line coupling with the Multi-Model-Driver (MMD), *Geosci. Model Dev.* **2012b,** *5* (1), 111–128. DOI: 10.5194/gmd-5-111-2012.

Kim, K.-H., Sul, K.-H., Szulejko, J.E., Chambers, S.D., Feng, X., and Lee, M.-H.: Progress in the reduction of carbon monoxide levels in major urban areas in Korea, *Environmental pollution* **2015a,** *207*, 420–428. DOI: 10.1016/j.envpol.2015.09.008.

Kim, S.-Y., Lee, S.-D., Lee, J.-B., Kim, D.-R., Han, J.-S., Choi, K.-H., and Song, C.-K.: Analysis of Long-Range Transport of Carbon Dioxide and Its High Concentration Events over East Asian Region Using GOSAT Data and GEOS-Chem Modeling, *Advances in Meteorology* **2015b,** (1), 1–13. DOI: 10.1155/2015/680264.

Kirschke, S., Bousquet, P., Ciais, P., Saunois, M., Canadell, J.G., Dlugokencky, E.J., Bergamaschi, P., Bergmann, D., Blake, D.R., Bruhwiler, L., Cameron-Smith, P., Castaldi, S., Chevallier, F., Feng, L., Fraser, A., Heimann, M., Hodson, E.L., Houweling, S., Josse, B., Fraser, P.J., Krummel, P.B., Lamarque, J.-F., Langenfelds, R.L., Le Quéré, C., Naik, V., O'Doherty, S., Palmer, P.I., Pison, I., Plummer, D., Poulter, B., Prinn, R.G., Rigby, M., Ringeval, B., Santini, M., Schmidt, M., Shindell, D. T., Simpson, I.J., Spahni, R., Steele, L.P., Strode, S.A., Sudo, K., Szopa, S., van der Werf, G.R., Voulgarakis, A., van Weele, M., Weiss, R.F., Williams, J.E., and Zeng, G.: Three decades of global methane sources and sinks, *Nature Geosci* **2013,** *6* (10), 813–823. DOI: 10.1038/NGEO1955.

Kitzis, D., Schibig, M.F., and Mefford, T.: Stability and Material Testing Results of Aluminium Cylinders and Regulator Comparisons, Poster **2017**.

Klausner, T., Mertens, M., Huntrieser, H., Galkowski, M., Kuhlmann, G., Baumann, R., Fiehn, A., Jöckel, P., Pühl, M., and Roiger, A.: Urban greenhouse gas emissions from the Berlin area: A case study using airborne CO_2 and CH_4 in situ observations in summer 2018, *Elem. Sci. Anth.* **2020a,** *8. DOI:* 10.1525/elementa.411.

Klausner, T., Roiger, A., Fiehn, A., Giez, A., Dreiling, V., Zöger, M., and Mallaun, C.: Aircraft measurement data obtained within the framework of the 3DO measurement campaign in summer 2018 over Berlin, *zenodo* **2020b**. DOI: https://doi.org/10.5281/zenodo.3706725.

Kostinek, J., Roiger, A., Davis, K. J., Sweeney, C., DiGangi, J. P., Choi, Y., Baier, B., Hase, F., Groß, J., Eckl, M., Klausner, T., and Butz, A.: Adaptation and performance assessment of a quantum and interband cascade laser spectrometer for simultaneous airborne in situ observation of CH_4 , C_2H_6 , CO_2 , CO and N_2O, *Atmos. Meas. Tech.* **2019,** *12* (3), 1767–1783. DOI: 10.5194/amt-12-1767-2019.

Krautwurst, S., Gerilowski, K., Jonsson, H.H., Thompson, D.R., Kolyer, R.W., Iraci, L.T., Thorpe, A.K., Horstjann, M., Eastwood, M., Leifer, I., Vigil, S.A., Krings, T., Borchardt, J., Buchwitz, M., Fladeland, M.M., Burrows, J.P., and Bovensmann, H.: Methane emissions from a Californian landfill, determined from airborne remote sensing and in situ measurements, *Atmos. Meas. Tech.* **2017,** *10* (9), 3429–3452. DOI: 10.5194/amt-10-3429-2017.

Krings, T., Neininger, B., Gerilowski, K., Krautwurst, S., Buchwitz, M., Burrows, J.P., Lindemann, C., Ruhtz, T., Schüttemeyer, D., and Bovensmann, H.: Airborne remote sensing and in situ measurements of atmospheric CO_2 to quantify point source emissions, *Atmos. Meas. Tech.* **2018,** *11* (2), 721–739. DOI: 10.5194/amt-11-721-2018.

Kuc, T., Rozanski, K., Zimnoch, M., Necki, J.M., and Korus, A.: Anthropogenic emissions of CO_2 and CH_4 in an urban environment, *Applied Energy* **2003,** *75* (3-4), 193–203. DOI: 10.1016/S0306-2619(03)00032-1.

Kuenen, J.J.P., Visschedijk, A.J.H., Jozwicka, M., and van der Denier Gon, H.A.C.: TNO-MACC_II emission inventory, a multi-year (2003-2009) consistent high-resolution European emission inventory for air quality modelling, *Atmos. Chem. Phys.* **2014,** *14* (20), 10963–10976. DOI: 10.5194/acp-14-10963-2014.

Kuhlmann, G., Clément, V., Marshall, J., Fuhrer, O., Broquet, G., Schnadt-Poberaj, C., Löscher, A., Meijer, Y., and Brunner, D**.:** SMARTCARB – Use of Satellite Measurements of Auxiliary Reactive Trace Gases for Fossil Fuel Carbon Dioxide Emission Estimation,Final report of ESA study contract n°4000119599/16/NL/FF/mg, Tech. rep. Dübendorf, Switzerland: Empa, Swiss Federal Laboratories for Materials Science and Technology **2019a**. Available at: https://www.empa.ch /documents/56101/617885/FR_Smartcarb_final_Jan2019.pdf last access 04.11.2019.

Kuhlmann, G., Broquet, G., Marshall, J., Clément, V., Löscher, A., Meijer, Y., and Brunner, D.: Detectability of CO_2 emission plumes of cities and power plants with the Copernicus Anthropogenic CO_2 Monitoring (CO2M) mission, *Atmos. Meas. Tech.* **2019b,** *12* (12), 6695–6719. DOI: 10.5194/amt-12-6695-2019.

Kurokawa, J., Ohara, T., Morikawa, T., Hanayama, S., Janssens-Maenhout, G., Fukui, T., Kawashima, K., and Akimoto, H.: Emissions of air pollutants and greenhouse gases over Asian regions during 2000–2008: Regional Emission inventory in ASia (REAS) version 2, *Atmos. Chem. Phys.* **2013,** *13* (21), 11019–11058. DOI: 10.5194/acp-13-11019-2013.

LandGEM, **2005**: Landfill Gas Emission Model, Version 3.02 (XLS). https://www.epa.gov/catc/ clean-air-technology-center-products#software last access 18.08.2019.

Lavoie, T.N., Shepson, P.B., Cambaliza, M.O.L., Stirm, B.H., Karion, A., Sweeney, C., Yacovitch, T.I., Herndon, S.C., Lan, X., and Lyon, D.: Aircraft-Based Measurements of Point Source Methane Emissions in the Barnett Shale Basin, *Environmental science & technology* **2015,** *49* (13), 7904–7913. DOI: 10.1021/acs.est.5b00410.

LCCP London Climate Change Partnership: A climate change impacts in London evaluation study, Final report November **2002**. https://ukcip.ouce.ox.ac.uk/wp-content/PDFs/London_tech.pdf, last access 04.06.2020.

Le Quéré, C., Andrew, R.M., Friedlingstein, P., Sitch, S., Hauck, J., Pongratz, J., Pickers, P.A., Korsbakken, J.I., Peters, G.P., Canadell, J.G., Arneth, A., Arora, V.K., Barbero, L., Bastos, A., Bopp, L., Chevallier, F., Chini, L.P., Ciais, P., Doney, S.C., Gkritzalis, T., Goll, D.S., Harris, I., Haverd, V., Hoffman, F.M., Hoppema, M., Houghton, R.A., Hurtt, G., Ilyina, T., Jain, A.K., Johannessen, T., Jones, C.D., Kato, E., Keeling, R.F., Goldewijk, K.K., Landschützer, P., Lefèvre, N., Lienert, S., Liu, Z., Lombardozzi, D., Metzl, N., Munro, D.R., Nabel, J.E.M.S., Nakaoka, S.-i., Neill, C., Olsen, A., Ono, T., Patra, P., Peregon, A., Peters, W., Peylin, P., Pfeil, B., Pierrot, D., Poulter, B., Rehder, G., Resplandy, L., Robertson, E., Rocher, M., Rödenbeck, C., Schuster, U., Schwinger, J., Séférian, R., Skjelvan, I., Steinhoff, T., Sutton, A., Tans, P.P., Tian, H., Tilbrook, B., Tubiello, F.N., van der Laan-Luijkx, I.T., van der Werf, G.R., Viovy, N., Walker, A.P., Wiltshire, A.J., Wright, R., Zaehle, S., and Zheng, B.: Global Carbon Budget 2018, *Earth Syst. Sci. Data* **2018,** *10* (4), 2141–2194. DOI: 10.5194/essd-10-2141-2018.

Leng, C., Duan, J., Xu, C., Zhang, H., Wang, Y., Wang, Y., Li, X., Kong, L., Tao, J., Zhang, R., Cheng, T., Zha, S., and Yu, X.: Insights into a historic severe haze event in Shanghai: Synoptic situation, boundary layer and pollutants, *Atmos. Chem. Phys.* **2016,** *16* (14), 9221–9234. DOI: 10.5194/acp-16-9221-2016.

Leung, D.Y.C., and Lee, Y.T.: Greenhouse gas emissions in Hong Kong, *Atmospheric Environment* **2000,** *34* (26), 4487–4498. DOI: 10.1016/S1352-2310(00)00115-1.

Lian, J., Bréon, F.-M., Broquet, G., Zaccheo, T.S., Dobler, J., Ramonet, M., Staufer, J., Santaren, D., Xueref-Remy, I., and Ciais, P.: Analysis of temporal and spatial variability of atmospheric CO_2 concentration within Paris from the GreenLITE TM laser imaging experiment, *Atmos. Chem. Phys. Discuss.* **2019**. https://doi.org/10.5194/acp-2019-547, in review.

LI-COR Application Note #129: The importance of water vapor measurements and corrections. https://www.licor.com/documents/igs56gijkc4ftks30pci last access 23.10.2019.

Li, L., Chen, C.H., Huang, C., Chen, Z., Wang, H.L., and Huang, H.Y.: Preliminary measurement of the carbon dioxide emission in Shanghai, *Shanghai Academy of Environmental Science* **2008**.

Liu, C.-W., and Wu, C.-Y.: Evaluation of methane emissions from Taiwanese paddies, *The Science of the total environment* **2004,** *333* (1-3), 195–207. DOI: 10.1016/j.scitotenv.2004.05.013.

Liu, H., Jacob, Daniel, J, Bey, I., Yantosca, Robert, M, Duncan, Bryan, N, Sachse, and Glen, W.: Transport pathways for Asian pollution outflow over the Pacific: Interannual and seasonal variations, *J. Geophys. Res.* **2003,** *108* (D20), 6871. DOI: 10.1029/2002JD003102.

Liu, Q., Wang, Y.S., Wang, M.X., Li, J., and Liu, G.R.: Trends of greenhouse gases in recent 10 years in Beijing, *Chinese Journal of Atmospheric Sciences* **2005**, 29(2): 267-271, (in Chinese http://en.cnki.com.cn/Article_en/CJFDTOTAL-DQXK200502010.htm).

Liu, Z., He, C., Zhou, Y., and Wu, J.: How much of the world's land has been urbanized, really?: A hierarchical framework for avoiding confusion, *Landscape Ecol* **2014,** *29* (5), 763–771. DOI: 10.1007/s10980-014-0034-y.

Lowry, D., Holmes, C.W., Rata, N.D., O'Brien, P., and Nisbet, E.G.: London methane emissions: Use of diurnal changes in concentration and $\delta^{13}C$ to identify urban sources and verify inventories, *J. Geophys. Res.* **2001,** *106* (D7), 7427–7448. DOI: 10.1029/2000JD900601.

Maasakkers, J.D., Jacob, D.J., Sulprizio, M.P., Scarpelli, T.R., Nesser, H., Sheng, J.-X., Zhang, Y., Hersher, M., Bloom, A.A., Bowman, K.W., Worden, J.R., Janssens-Maenhout, G., and Parker, R.J.: Global distribution of methane emissions, emission trends, and OH concentrations and trends inferred from an inversion of GOSAT satellite data for 2010–2015, *Atmos. Chem. Phys.* **2019,** *19* (11), 7859–7881. DOI: 10.5194/acp-19-7859-2019.

Mahadevan, P., Wofsy, S.C., Matross, D.M., Xiao, X., Dunn, A.L., Lin, J.C., Gerbig, C., Munger, J.W., Chow, V.Y., and Gottlieb, E.W.: A satellite-based biosphere parameterization for net ecosystem CO_2 exchange: Vegetation Photosynthesis and Respiration Model (VPRM), *Global Biogeochem. Cycles* **2008,** *22* (2), n/a-n/a. DOI: 10.1029/2006GB002735.

Mallaun, C., Giez, A., and Baumann, R: Calibration of 3-D wind measurements on a single-engine research aircraft, *Atmos. Meas. Tech.* **2015,** *8* (8), 3177–3196. DOI: 10.5194/amt-8-3177-2015.

Marcotullio, P.J., Sarzynski, A., Albrecht, J., Schulz, N., and Garcia, J.: The geography of global urban greenhouse gas emissions: An exploratory analysis, *Climatic Change* **2013,** *121* (4), 621–634. DOI: 10.1007/s10584-013-0977-z.

Mays, K.L., Shepson, P.B., Stirm, B.H., Karion, A., Sweeney, C., and Gurney, K.R.: Aircraft-based measurements of the carbon footprint of Indianapolis, *Environmental science & technology* **2009,** *43* (20), 7816–7823. DOI: 10.1021/es901326b.

McDonald, B.C., McBride, Z.C., Martin, E.W., and Harley, R.A.: High-resolution mapping of motor vehicle carbon dioxide emissions, *J. Geophys. Res.* **2014,** *119* (9), 5283–5298. DOI: 10.1002/2013JD021219.

McGranahan, G., Balk, D., and Anderson, B.: The rising tide: Assessing the risks of climate change and human settlements in low elevation coastal zones, *Environment and Urbanization* **2016,** *19* (1), 17–37. DOI: 10.1177/0956247807076960.

McKeen, S.A., Liu, S.C., Hsie, E.Y., Lin, X., Bradshaw, J.D., Smyth, S., Gregory, G.L., and Blake, D.R.: Hydrocarbon ratios during PEM-WEST A: A model perspective, *J. Geophys. Res.* **1996**, 101(D1). DOI: https://doi.org/10.1029/95JD02733.

Mertens, M., and Jöckel, P.: Data from MECO(n) model simulations on “Urban greenhouse gas emissions from the Berlin area: A case study using airborne CO_2 and CH_4 in situ observations in summer 2018”, *zenodo* **2020**. DOI: https://doi.org/10.5281/zenodo.3707990.

Mertens, M., Kerkweg, A., Jöckel, P., Tost, H., and Hofmann, C.: The 1-way on-line coupled model system MECO(n) – Part 4: Chemical evaluation (based on MESSy v2.52), *Geosci. Model Dev.* **2016,** *9* (10), 3545–3567. DOI: 10.5194/gmd-9-3545-2016.

Mertens, M., Fiehn, A., Kerkweg, A., Klausner, T., Pühl, M., Roiger, A., and Jöckel, P: MECO(n) based CO_2 and CH_4 forecast system for aircraft measurement campaign in Stuttgart and Berlin, Poster ICCARUS **2019**, DWD Zentrale Offenbach.

Miller, S.M.,and Michalak, A.M.: The impact of improved satellite retrievals on estimates of biospheric carbon balance, *Atmos. Chem. Phys.* **2020,** *20* (1), 323–331. DOI: 10.5194/acp-20-323-2020.

Miller, S.M., Michalak, A.M., Detmers, R.G., Hasekamp, O.P., Bruhwiler, L.M.P., and Schwietzke, S.: China's coal mine methane regulations have not curbed growing emissions, *Nature communications* **2019,** *10* (1), 303. DOI: 10.1038/s41467-018-07891-7.

MLUL, **2017**: Ministerium für Ländliche Entwicklung, Umwelt und Landwirtschaft, Kommunale Abwasserbeseitigung im Land Brandenburg. https://mluk.brandenburg.de/sixcms/media.php/land_bb_test_02.a.189.de/Lagebericht-Abwasserbeseitigung2017.pdf last access 05.06.2020.

Mueller, K., Yadav, V., Lopez-Coto, I., Karion, A., Gourdji, S., Martin, C., and Whetstone, J.: Siting Background Towers to Characterize Incoming Air for Urban Greenhouse Gas Estimation: A Case Study in the Washington, DC/Baltimore Area, *J. Geophys. Res.* **2018,** *123* (5), 2910–2926. DOI: 10.1002/2017JD027364.

Myhre, G., Shindell, D., Bréon, F.-M., Collins, W., Fuglestvedt, J., Huang, J., Koch, D., Lamarque, J.-F., Lee, D., Mendoza, B., Nakajima, T., Robock, A., Stephens, G., Takemura T., and Zhang, H.: Anthropogenic and Natural Radiative Forcing. In: Climate Change 2013: The Physical Science Basis. Contribution of Working Group I to the Fifth Assessment Report of the Intergovernmental

Panel on Climate Change [Stocker, T.F., D. Qin, G.-K. Plattner, M. Tignor, S.K. Allen, J. Boschung, A. Nauels, Y. Xia, V. Bex and P.M. Midgley (eds.)]. *Cambridge University Press*, Cambridge, United Kingdom and New York, NY, USA, **2013**.

Nara, H., Tanimoto, H., Tohjima, Y., Mukai, H., Nojiri, Y., Katsumata, K., and Rella, C.W.: Effect of air composition (N_2 , O_2 , Ar, and H_2O) on CO_2 and CH_4 measurement by wavelength-scanned cavity ring-down spectroscopy: Calibration and measurement strategy, *Atmos. Meas. Tech.* **2012,** *5* (11), 2689–2701. DOI: 10.5194/amt-5-2689-2012.

Ngan, F., Stein, A., Finn, D., and Eckman, R.: Dispersion simulations using HYSPLIT for the Sagebrush Tracer Experiment, *Atmospheric Environment* **2018,** *186*, 18–31. DOI: 10.1016/j.atmosenv.2018.05.012.

Nisbet, E., and Weiss, R.: Atmospheric science. Top-down versus bottom-up, *Science* **2010,** *328* (5983), 1241–1243. DOI: 10.1126/science.1189936.

Nisbet, E.G., Dlugokencky, E.J., Manning, M.R., Lowry, D., Fisher, R.E., France, J.L., Michel, S.E., Miller, J.B., White, J.W.C., Vaughn, B., Bousquet, P., Pyle, J.A., Warwick, N.J., Cain, M., Brownlow, R., Zazzeri, G., Lanoisellé, M., Manning, A. C., Gloor, E., Worthy, D.E.J., Brunke, E.-G., Labuschagne, C., Wolff, E.W., and Ganesan, A.L.: Rising atmospheric methane: 2007-2014 growth and isotopic shift, *Global Biogeochem. Cycles* **2016,** *30* (9), 1356–1370. DOI: 10.1002/2016GB005406.

Nisbet, E.G., Manning, M.R., Dlugokencky, E.J., Fisher, R.E., Lowry, D., Michel, S.E., Myhre, C.L., Platt, S.M., Allen, G., Bousquet, P., Brownlow, R., Cain, M., France, J.L., Hermansen, O., Hossaini, R., Jones, A.E., Levin, I., Manning, A.C., Myhre, G., Pyle,J. A., Vaughn, B.H., Warwick, N.J., and White, J.W.C.: Very Strong Atmospheric Methane Growth in the 4 Years 2014–2017: Implications for the Paris Agreement, *Global Biogeochem. Cycles* **2019,** *33* (3), 318–342. DOI: 10.1029/2018GB006009.

Oda, T., and Maksyutov, S.: A very high-resolution (1 km×1 km) global fossil fuel CO_2 emission inventory derived using a point source database and satellite observations of nighttime lights, *Atmos. Chem. Phys.* **2011,** *11* (2), 543–556. DOI: 10.5194/acp-11-543-2011.

Oda, T., and Maksyutov, S. **2015**: ODIAC Fossil Fuel CO_2 Emissions Dataset (Version name ODIAC2019), Center for Global Environmental Research, National Institute for Environmental Studies, DOI:10.17595/20170411.001. (Reference date: 2020/03/23).

OpenStreetMap, **2018**: Extent of the region Berlin. http://download.geofabrik.de/europe/germany /berlin.html last access 02.10.2019.

Oreskes, N.: The scientific consensus on climate change, *Science* **2004,** *306* (5702), 1686. DOI: 10.1126/science.1103618.

O'Shea, S.J., Allen, G., Fleming, Z.L., Bauguitte, S.J.-B., Percival, C.J., Gallagher, M.W., Lee, J., Helfter, C., and Nemitz, E.: Area fluxes of carbon dioxide, methane, and carbon monoxide derived from airborne measurements around Greater London: A case study during summer 2012, *J. Geophys. Res.* **2014,** *119* (8), 4940–4952. DOI: 10.1002/2013JD021269.

OSPAR Convention, **2017**: Inventory of offshore installations, version 2017_01. https://odims.ospar.org/odims_data_files/ last access 31.03.2020.

Paldus, B.A., and Zare, R.N.: Absorption Spectroscopies: From Early Beginnings to Cavity-Ringdown Spectroscopy. In Busch, K.W., and Busch, M. A.: Cavity-Ringdown Spectroscopy, ACS symposium series 720, *American Chemical Society* **1999**, pp 49–70. DOI: 10.1021/bk-1999-0720.ch005.

Palmer, P.I., O'Doherty, S., Allen, G., Bower, K., Bösch, H., Chipperfield, M.P., Connors, S., Dhomse, S., Feng, L., Finch, D.P., Gallagher, M.W., Gloor, E., Gonzi, S., Harris, N.R.P., Helfter, C., Humpage, N., Kerridge, B., Knappett, D., Jones, R.L., Le Breton, M., Lunt, M. F., Manning, A.J., Matthiesen, S., Muller, J.B.A., Mullinger, N., Nemitz, E., Shea, S., Parker, R.J., Percival, C.J., Pitt, J., Riddick, S.N., Rigby, M., Sembhi, H., Siddans, R., Skelton, R. L., Smith, P., Sonderfeld, H., Stanley, K., Stavert, A. R., Wenger, A., White, E., Wilson, C., and Young, D.: A measurement-based verification framework for UK greenhouse gas emissions: An overview of the Greenhouse gAs Uk and Global Emissions (GAUGE) project, *Atmos. Chem. Phys.* **2018,** *18* (16), 11753–11777. DOI: 10.5194/acp-18-11753-2018.

Pappalardo, G., Amodeo, A., Apituley, A., Comeron, A., Freudenthaler, V., Linné, H., Ansmann, A., Bösenberg, J., D'Amico,G., Mattis, I., Mona, L., Wandinger, U., Amiridis, V., Alados-Arboledas, L., Nicolae, D., and Wiegner, M.: EARLINET: towards an advanced sustainable European aerosol lidar network, *Atmos Meas Tech* **2014***,* **7**: 2389–2409. DOI: 10.5194/amt-7-2389-2014.

Pataki, D.E., Ehleringer, J.R., Flanagan, L.B., Yakir, D., Bowling, D.R., Still, C.J., Buchmann, N., Kaplan, J. O., and Berry, J.A.: The application and interpretation of Keeling plots in terrestrial carbon cycle research, *Global Biogeochem. Cycles* **2003,** *17* (1), 21. DOI: 10.1029/2001GB001850.

Peake, D., Dacre, H., and Methven, J.: Coastal influences on pollution transport, *WIT Transactions on Ecology aand the Environment* **2011**, Vol 147. DOI: 10.2495/AIR110081.

Peischl, J., Ryerson, T.B., Holloway, J.S., Trainer, M., Andrews, A.E., Atlas, E.L., Blake, D.R., Daube, B.C., Dlugokencky, E.J., Fischer, M.L., Goldstein, A.H., Guha, A., Karl, T., Kofler, J., Kosciuch, E., Misztal, P.K., Perring, A.E., Pollack, I.B., Santoni, G.W., Schwarz, J.P., Spackman, J.R., Wofsy, S.C., and Parrish, D.D.: Airborne observations of methane emissions from rice cultivation in the Sacramento Valley of California, *J. Geophys. Res.* **2012,** *117* (D24). DOI: 10.1029/2012JD017994.

Peischl, J., Ryerson, T.B., Brioude, J., Aikin, K.C., Andrews, A.E., Atlas, E., Blake, D., Daube, B.C., de Gouw, J.A., Dlugokencky, E., Frost, G.J., Gentner, D.R., Gilman, J.B., Goldstein, A.H., Harley, R.A., Holloway, J.S., Kofler, J., Kuster, W.C., Lang, P.M., Novelli, P.C., Santoni, G.W., Trainer, M., Wofsy, S.C., and Parrish, D.D.: Quantifying sources of methane using light alkanes in the Los Angeles basin, California, *J. Geophys. Res.* **2013,** *118* (10), 4974–4990. DOI: 10.1002/jgrd.50413.

Peischl, J., Ryerson, T.B., Aikin, K.C., de Gouw, J.A., Gilman, J.B., Holloway, J.S., Lerner, B.M., Nadkarni, R., Neuman, J.A., Nowak, J.B., Trainer, M., Warneke, C., and Parrish, D.D.: Quantifying atmospheric methane emissions from the Haynesville, Fayetteville, and northeastern Marcellus shale gas production regions, *J. Geophys. Res.* **2015,** *120* (5), 2119–2139. DOI: 10.1002/2014JD022697.

Pesaresi, M., Florczyk, A., Schiavina, M., Melchiorri, M., and Maffenini, L.: GHS-SMOD R2019A - GHS settlement layers, updated and refined REGIO model 2014 in application to GHS-BUILT R2018A and GHS-POP R2019A, multitemporal (1975-1990-2000-2015). European Commission, Joint Research Centre (JRC) **2019** [Dataset] doi:10.2905/42E8BE89-54FF-464E-BE7B-BF9E64DA5218 PID: http://data.europa.eu/89h/42e8be89-54ff-464e-be7b-bf9e64da5218.

Phillips, N.G., Ackley, R., Crosson, E.R., Down, A., Hutyra, L.R., Brondfield, M., Karr, J.D., Zhao, K., and Jackson, R.B.: Mapping urban pipeline leaks: Methane leaks across Boston, *Environmental pollution* **2013,** *173*, 1–4. DOI: 10.1016/j.envpol.2012.11.003.

Picarro, **2009**: Picarro G1301-m CO2/CH4/H2O Flight Analyzer. https://www.picarro.com/assets/docs/CO2_CH4_flightanalyzer_datasheet.pdf last access 01.10.2019.

Pillai, D., Buchwitz, M., Gerbig, C., Koch, T., Reuter, M., Bovensmann, H., Marshall, J., and Burrows, J.P.: Tracking city CO_2 emissions from space using a high-resolution inverse modelling approach: A case study for Berlin, Germany, *Atmos. Chem. Phys.* **2016,** *16* (15), 9591–9610. DOI: 10.5194/acp-16-9591-2016.

Pitt, J.R., Allen, G., Bauguitte, S.J.-B., Gallagher, M.W., Lee, J.D., Drysdale, W., Nelson, B., Manning, A.J., and Palmer, P.I.: Assessing London CO_2, CH_4 and CO emissions using aircraft measurements and dispersion modelling, *Atmos. Chem. Phys.* **2019,** *19* (13), 8931–8945. DOI: 10.5194/acp-19-8931-2019.

Plant, G., Kort, E.A., Floerchinger, C., Gvakharia, A., Vimont, I., and Sweeney, C.: Large fugitive methane emissions from urban centers along the US East Coast, *Geophys. Res. Lett.* **2019**. DOI: 10.1029/2019GL082635.

Prather, M.J., Holmes, C.D., and Hsu, J.: Reactive greenhouse gas scenarios: Systematic exploration of uncertainties and the role of atmospheric chemistry, *Geophys. Res. Lett.* **2012,** *39* (9). DOI: 10.1029/2012GL051440.

Prinn, R., Weiss R, Arduini J, Arnold T, DeWitt H, Fraser P, Ganesan A, Gasore J, Harth C, Hermansen O, Kim J, Krummel P, Li S, Loh Z, Lunder C, Maione M, Manning A, Miller B, Mitrevski B, Muhle J, O'Doherty S, Park S, Reimann S, Rigby M, Saito T, Salameh P, Schmidt R, Simmonds P, Steele L, Vollmer M, Wang H J, Yao B, Yokouchi Y, Young D, and Zhou L.: History of chemically and radiatively important atmospheric gases from the Advanced Global Atmospheric Gases Experiment (AGAGE). *Carbon Dioxide Information Analysis Center (CDIAC), Oak Ridge National Laboratory (ORNL), Oak Ridge, TN (United States)*, **2018**.

Quay, P., Stutsman, J., Wilbur, D., Snover, A., Dlugokencky, E., and Brown, T.: The isotopic composition of atmospheric methane, *Global Biogeochem. Cycles* **1999,** *13* (2), 445–461. DOI: 10.1029/1998GB900006.

Rella,C.: Accurate Greenhouse Gas Measurements in Humid Gas Streams Using the Picarro G1301 Carbon Dioxide / Methane / Water Vapor Gas Analyzer, Qhite Paper, Picarro, Inc., Sunnyvale, California **2010**. https://www.picarro.com/support/library/documents/accurate_greenhouse_gas_measurements_in_humid_gas_streams_using_the_g1301, last access 04.06.2020.

Rella, C.W., Hoffnagle, J., He, Y., and Tajima, S.: Local- and regional-scale measurements of CH_4 , $\delta^{13}CH_4$, and C_2H_6 in the Uintah Basin using a mobile stable isotope analyzer, *Atmos. Meas. Tech.* **2015,** *8* (10), 4539–4559. DOI: 10.5194/amt-8-4539-2015.

Ren, X., Salmon, O.E., Hansford, J.R., Ahn, D., Hall, D., Benish, S.E., Stratton, P.R., He, H., Sahu, S., Grimes, C., Heimburger, A.M.F., Martin, C.R., Cohen, M.D., Stunder, B., Salawitch, R.J., Ehrman, S.H., Shepson, P.B., and Dickerson, R.R.: Methane Emissions From the Baltimore-Washington Area Based on Airborne Observations: Comparison to Emissions Inventories, *J. Geophys. Res. Atmos.* **2018,** *123* (16), 8869–8882. DOI: 10.1029/2018JD028851.

Ren, Y., Baumann, R., and Schlager, H.: An airborne perfluorocarbon tracer system and its first application for a Lagrangian experiment, *Atmos. Meas. Tech.* **2015,** *8* (1), 69–80. DOI: 10.5194/amt-8-69-2015.

Reuter, M., Buchwitz, M., Schneising, O., Heymann, J., Bovensmann, H., and Burrows, J.P.: A method for improved SCIAMACHY CO_2 retrieval in the presence of optically thin clouds, *Atmos. Meas. Tech.* **2010,** *3* (1), 209–232. DOI: 10.5194/amt-3-209-2010.

Reuter, M., Buchwitz, M., Schneising, O., Krautwurst, S., O'Dell, C.W., Richter, A., Bovensmann, H., and Burrows, J.P.: Towards monitoring localized CO_2 emissions from space: Co-located regional CO_2 and NO_2 enhancements observed by the OCO-2 and S5P satellites, *Atmos. Chem. Phys.* **2019,** *19* (14), 9371–9383. DOI: 10.5194/acp-19-9371-2019.

Riahi, K., Rao, S., Krey, V., Cho, C., Chirkov, V., Fischer, G., Kindermann, G., Nakicenovic, N., and Rafaj, P.: RCP 8.5—A scenario of comparatively high greenhouse gas emissions, *Climatic Change* **2011,** *109* (1-2), 33–57. DOI: 10.1007/s10584-011-0149-y.

Riddick, S.N., Mauzerall, D.L., Celia, M., Harris, N.R.P., Allen, G., Pitt, J., Staunton-Sykes, J., Forster, G.L., Kang, M., Lowry, D., Nisbet, E.G., and Manning, A.J.: Methane emissions from oil and gas platforms in the North Sea, *Atmos. Chem. Phys.* **2019,** *19* (15), 9787–9796. DOI: 10.5194/acp-19-9787-2019.

Rigby, M., Prinn, R.G., Fraser, P.J., Simmonds, P.G., Langenfelds, R.L., Huang, J., Cunnold, D.M., Steele, L.P., Krummel, P.B., Weiss, R.F., O'Doherty, S., Salameh, P.K., Wang, H.J., Harth, C.M., Mühle, J., and Porter, L.W.: Renewed growth of atmospheric methane, *Geophys. Res. Lett.* **2008,** *35* (22), 2635. DOI: 10.1029/2008GL036037.

Rockel, B., Will, A., and Hense, A.: The Regional Climate Model COSMO-CLM (CCLM), *metz* **2008,** *17* (4), 347–348. DOI: 10.1127/0941-2948/2008/0309.

Ryoo, J.-M., Iraci, L.T., Tanaka, T., Marrero, J.E., Yates, E.L., Fung, I., Michalak, A.M., Tadić, J., Gore, W., Bui, T.P., Dean-Day, J.M., and Chang, C.S.: Quantification of CO_2 and CH_4 emissions over Sacramento, California, based on divergence theorem using aircraft measurements, *Atmos. Meas. Tech.* **2019,** *12* (5), 2949–2966. DOI: 10.5194/amt-12-2949-2019.

Sander, R., Kerkweg, A., Jöckel, P., and Lelieveld, J.: Technical note: The new comprehensive atmospheric chemistry module MECCA, *Atmos. Chem. Phys.* **2005,** *5* (2), 445–450. DOI: 10.5194/acp-5-445-2005.

Saunois, M., Bousquet, P., Poulter, B., Peregon, A., Ciais, P., Canadell, J.G., Dlugokencky, E.J., Etiope, G., Bastviken, D., Houweling, S., Janssens-Maenhout, G., Tubiello, F.N., Castaldi, S., Jackson, R.B., Alexe, M., Arora, V.K., Beerling, D.J., Bergamaschi, P., Blake, D.R., Brailsford, G., Brovkin, V., Bruhwiler, L., Crevoisier, C., Crill, P., Covey, K., Curry, C., Frankenberg, C., Gedney, N., Höglund-Isaksson, L., Ishizawa, M., Ito, A., Joos, F., Kim, H.-S., Kleinen, T., Krummel, P., Lamarque, J.-F., Langenfelds, R., Locatelli, R., Machida, T., Maksyutov, S., McDonald, K.C., Marshall, J., Melton, J. R., Morino, I., Naik, V., O'Doherty, S., Parmentier, F.-J.W., Patra, P.K., Peng, C., Peng, S., Peters, G.P., Pison, I., Prigent, C., Prinn, R., Ramonet, M., Riley, W.J., Saito, M., Santini, M., Schroeder, R., Simpson, I.J., Spahni, R., Steele, P., Takizawa, A., Thornton, B.F., Tian, H., Tohjima, Y., Viovy, N., Voulgarakis, A., van Weele, M., van der Werf, G.R., Weiss, R., Wiedinmyer, C., Wilton, D.J., Wiltshire, A., Worthy, D., Wunch, D., Xu, X., Yoshida, Y., Zhang, B., Zhang, Z., and Zhu, Q.: The global methane budget 2000–2012, *Earth Syst. Sci. Data* **2016,** *8* (2), 697–751. DOI: 10.5194/essd-8-697-2016.

Saunois, M., Bousquet, P., Poulter, B., Peregon, A., Ciais, P., Canadell, J.G., Dlugokencky, E.J., Etiope, G., Bastviken, D., Houweling, S., Janssens-Maenhout, G., Tubiello, F.N., Castaldi, S., Jackson, R.B., Alexe, M., Arora, V.K., Beerling, D.J., Bergamaschi, P., Blake, D.R., Brailsford, G., Bruhwiler, L., Crevoisier, C., Crill, P., Covey, K., Frankenberg, C., Gedney, N., Höglund-Isaksson, L., Ishizawa, M., Ito, A., Joos, F., Kim, H.-S., Kleinen, T., Krummel, P., Lamarque, J.-F., Langenfelds, R., Locatelli, R., Machida, T., Maksyutov, S., Melton, J.R., Morino, I., Naik, V., O'Doherty, S., Parmentier, F.-J. W., Patra, P.K., Peng, C., Peng, S., Peters, G.P., Pison, I., Prinn, R., Ramonet, M., Riley, W.J., Saito, M., Santini, M., Schroeder, R., Simpson, I.J., Spahni, R., Takizawa, A., Thornton, B.F., Tian, H., Tohjima, Y., Viovy, N., Voulgarakis, A., Weiss, R., Wilton, D.J., Wiltshire, A., Worthy, D., Wunch, D., Xu, X., Yoshida, Y., Zhang, B., Zhang, Z., and Zhu, Q.: Variability and quasi-decadal changes in the methane budget over the period 2000–2012, *Atmos. Chem. Phys.* **2017,** *17* (18), 11135–11161. DOI: 10.5194/acp-17-11135-2017.

Saunois, M., Stavert, A.R., Poulter, B., Bousquet, P., Canadell, J. G., Jackson, R.B., Raymond, P.A., Dlugokencky, E.J., Houweling, S., Patra, P.K., Ciais, P., Arora, V.K., Bastviken, D., Bergamaschi, P., Blake, D.R., Brailsford, G., Bruhwiler, L., Carlson, K.M., Carrol, M., Castaldi, S., Chandra, N., Crevoisier, C., Crill, P. M., Covey, K., Curry, C. L., Etiope, G., Frankenberg, C., Gedney, N., Hegglin, M.I., Höglund-Isaksson, L., Hugelius, G., Ishizawa, M., Ito, A., Janssens-Maenhout, G., Jensen, K.M., Joos, F., Kleinen, T., Krummel, P.B., Langenfelds, R.L., Laruelle, G.G., Liu, L., Machida, T., Maksyutov, S., McDonald, K.C., McNorton, J., Miller, P.A., Melton, J.R., Morino, I., Müller, J., Murgia-Flores, F., Naik, V., Niwa, Y., Noce, S., O'Doherty, S., Parker, R.J., Peng, C., Peng, S., Peters, G.P., Prigent, C., Prinn, R., Ramonet, M., Regnier, P., Riley, W. J., Rosentreter, J.A., Segers, A., Simpson, I.J., Shi, H., Smith, S.J., Steele, L.P., Thornton, B.F., Tian, H., Tohjima, Y., Tubiello, F.N., Tsuruta, A., Viovy, N., Voulgarakis, A., Weber, T.S., van Weele, M., van der Werf, G.R., Weiss, R.F., Worthy, D., Wunch, D., Yin, Y., Yoshida, Y., Zhang, W., Zhang, Z., Zhao, Y., Zheng, B., Zhu, Q., Zhu, Q., and Zhuang, Q.: The Global Methane Budget 2000-2017, *Earth Syst. Sci. Data Discuss.* **2019**. https://doi.org/10.5194/essd-2019-128, in review.

Schaefer, H., Mikaloff Fletcher, S.E., Veidt, C., Lassey, K.R., Brailsford, G.W., Bromley, T.M., Dlugokencky, E.J., Michel, S.E., Miller, J.B., Levin, I., Lowe, D.C., Martin, R.J., Vaughn, B.H., and White, J.W.C.: A 21st-century shift from fossil-fuel to biogenic methane emissions indicated by $^{13}CH_4$, *Science* **2016,** *352* (6281), 80–84. DOI: 10.1126/science.aad2705.

Scherer, D., Ament, F., Emeis, S., Fehrenbach, U., Leitl, B., Scherber, K., Schneider, C., and Vogt, U.: Three-Dimensional Observation of Atmospheric Processes in Cities, *metz* **2019a,** *28* (2), 121–138. DOI: 10.1127/metz/2019/0911.

Scherer, D., Antretter, F., Bender, S., Cortekar, J., Emeis, S., Fehrenbach, U., Gross, G., Halbig, G., Hasse, J., Maronga, B., Raasch, S., and Scherber, K.: Urban Climate Under Change $[UC]^2$ – A National Research Programme for Developing a Building-Resolving Atmospheric Model for Entire City Regions, *metz* **2019b,** *28* (2), 95–104. DOI: 10.1127/metz/2019/0913.

Schneising, O., Burrows, J.P., Dickerson, R.R., Buchwitz, M., Reuter, M., and Bovensmann, H.: Remote sensing of fugitive methane emissions from oil and gas production in North American tight geologic formations, *Earth's Future* **2014,** *2* (10), 548–558. DOI: 10.1002/2014EF000265.

Schumann, U.: EMeRGe4 Comparison Report, June **2019**, Measurement and model data for HALO-FAAM comparison from EMeRGe flight 4, Version 3, available on the internal campaing data website.

Schwietzke, S., Sherwood, O.A., Bruhwiler, L.M.P., Miller, J.B., Etiope, G., Dlugokencky, E.J., Michel, S.E., Arling, V.A., Vaughn, B.H., White, J.W.C., and Tans, P.P.: Upward revision of global fossil fuel methane emissions based on isotope database, *Nature* **2016,** *538* (7623), 88–91. DOI: 10.1038/nature19797.

Seidel, D.J., Ao, C.O., and Li, K.: Estimating climatological planetary boundary layer heights from radiosonde observations: Comparison of methods and uncertainty analysis, *J. Geophys. Res.* **2010,** *115* (D16), 123. DOI: 10.1029/2009JD013680.

Seinfeld, J.H., and Pandis, S.N.: Atmospheric Chemistry and Physics. From Air Pollution to Climate Change, 3rd ed., *Wiley* **2016**. ISBN: 978-1118947401.

Seto, K.C., Dhakal, S., Bigio, A., Blanco, H., Delgado, G.C., Dewar, D., Huang, L., Inaba, A., Kansal, A., Lwasa, S., McMahon, J.E., Müller, D.B., Murakami, J., Nagendra, H., and Ramaswami, A.: Human Settlements, Infrastructure and Spatial Planning. In: Climate Change 2014: Mitigation of Climate Change. Contribution of Working Group III to the Fifth Assessment Report of the Intergovernmental Panel on Climate Change [Edenhofer, O., R. Pichs-Madruga, Y. Sokona, E. Farahani, S. Kadner, K. Seyboth, A. Adler, I. Baum, S. Brunner, P. Eickemeier, B. Kriemann, J. Savolainen, S. Schlömer, C. von Stechow, T. Zwickel and J.C. Minx (eds.)]. Cambridge University Press, Cambridge, United Kingdom and New York, NY, USA, **2014**.

Sherwood, O.A., Schwietzke, S., Arling, V.A., and Etiope, G.: Global Inventory of Gas Geochemistry Data from Fossil Fuel, Microbial and Burning Sources, version 2017, *Earth Syst. Sci. Data* **2017,** *9* (2), 639–656. DOI: 10.5194/essd-9-639-2017.

Shirai, T., Machida, T., Matsueda, H., Sawa, Y., Niwa, Y., Maksyutov, S., and Higuchi, K.: Relative contribution of transport/surface flux to the seasonal vertical synoptic CO_2 variability in the troposphere over Narita, *Tellus B: Chemical and Physical Meteorology* **2012,** *64* (1), 19138. DOI: 10.3402/tellusb.v64i0.19138.

Skamarock, W.C., Klemp, J.B., Dudhia, J., Gill, D.O., Barker, D.M., Duda, M.G., Huang, X.-Y., Wang, W., and Powers, J.G.: A Description of the Advanced Research WRF Version 3. NCAR Tech. Note NCAR/TN-475+STR, **2008**, 113 pp. DOI: 10.5065/D68S4MVH.

Statistisches Bundesamt, **2018**: Städte nach Fläche, Bevölkerung und Bevölkerungsdichte am 31.12.2018. www.destatis.de/DE/Themen/Laender-Regionen/Regionales/Gemeindeverzeichnis/Administrativ/05-staedte.html last access 25.09.2019.

Stohl, A**.:** Computation, accuracy and applications of trajectories – A review and bibliography, *Atmospheric Environment* **1998***,* 32(6): 947–966. DOI: https://doi.org/10.1016/S1352-2310(97)00457-3.

Stein, A.F., Draxler, R.R., Rolph, G.D., Stunder, B.J.B., Cohen, M.D., and Ngan, F.: NOAA's HYSPLIT Atmospheric Transport and Dispersion Modeling System, *Bull. Amer. Meteor. Soc.* **2015,** *96* (12), 2059–2077. DOI: 10.1175/BAMS-D-14-00110.1.

Streets, D.G., Zhang, Q., Wang, L., He, K., Hao, J., Wu, Y., Tang, Y., and Carmichael, G.R.: Revisiting China's CO emissions after the Transport and Chemical Evolution over the Pacific (TRACE-P) mission: Synthesis of inventories, atmospheric modeling, and observations, *J. Geophys. Res.* **2006,** *111* (D14), D15S03. DOI: 10.1029/2006JD007118.

Strukturatlas Land Brandenburg, **2017**: plot retrieved from an interactive tool on http://strukturatlas.brandenburg.de/ last access 22.01.2020.

Taiwan International Ports Corporation, **2015**: Port of Taichung, Environmental Report. https://www.twport.com.tw/Upload/A/RelFile/CustomPage/2920/52308caf-8783-4271-a23d-d580bce34b6a.pdf last access 31.03.2020.

Taiwan News, **2017**: Taiwan's Taichung Power Plant must reduce coal consumption by 24 percent in 2018. https://www.taiwannews.com.tw/en/news/3309637 last access 31.03.2020.

Takegawa, N., Kondo, Y., Koike, M., Chen, G., Machida, T., Watai, T., Blake, D.R., Streets, D.G., Woo, J.-H., Carmichael, G.R., Kita, K., Miyazaki, Y., Shirai, T., Liley, J. B., and Ogawa, T.: Removal of NOx and NOy in Asian outflow plumes: Aircraft measurements over the western Pacific in January 2002, *J. Geophys. Res.* **2004,** *109* (D23), 12,793. DOI: 10.1029/2004JD004866.

Tohjima, Y., Kubo, M., Minejima, C., Mukai, H., Tanimoto, H., Ganshin, A., Maksyutov, S., Katsumata, K., Machida, T., and Kita, K.: Temporal changes in the emissions of CH_4 and CO from China estimated from CH_4/CO_2 and CO/CO_2 correlations observed at Hateruma Island, *Atmos. Chem. Phys.* **2014,** *14* (3), 1663–1677. DOI: 10.5194/acp-14-1663-2014.

TROPOMI ATBD, **2019**: TROPOMI Algorithm Theoretical Basis Document. http://www.tropomi.eu/sites/default/files/files/publicS5P-KNMI-L2-0005-RP-ATBD_NO2_data_products-20190206_v140.pdf last access 27.04.2020.

Turnbull, J.C., Karion, A., Fischer, M.L., Faloona, I., Guilderson, T., Lehman, S.J., Miller, B.R., Miller, J.B., Montzka, S., Sherwood, T., Saripalli, S., Sweeney, C., and Tans, P.P.: Assessment of fossil fuel carbon dioxide and other anthropogenic trace gas emissions from airborne measurements over Sacramento, California in spring 2009, *Atmos. Chem. Phys.* **2011,** *11* (2), 705–721. DOI: 10.5194/acp-11-705-2011.

Turnbull, J.C., Karion, A., Davis, K.J., Lauvaux, T., Miles, N.L., Richardson, S.J., Sweeney, C., McKain, K., Lehman, S.J., Gurney, K.R., Patarasuk, R., Liang, J., Shepson, P.B., Heimburger, A., Harvey, R., and Whetstone, J.: Synthesis of Urban CO_2 Emission Estimates from Multiple Methods from the Indianapolis Flux Project (INFLUX), *Environmental science & technology* **2019,** *53* (1), 287–295. DOI: 10.1021/acs.est.8b05552.

Turner, A.J., Jacob, D.J., Wecht, K.J., Maasakkers, J.D., Lundgren, E., Andrews, A.E., Biraud, S.C., Boesch, H., Bowman, K.W., Deutscher, N.M., Dubey, M.K., Griffith, D.W.T., Hase, F., Kuze, A., Notholt, J., Ohyama, H., Parker, R., Payne, V. H., Sussmann, R., Sweeney, C., Velazco, V.A., Warneke, T., Wennberg, P.O., and Wunch, D.: Estimating global and North American methane emissions with high spatial resolution using GOSAT satellite data, *Atmos. Chem. Phys.* **2015,** *15* (12), 7049–7069. DOI: 10.5194/acp-15-7049-2015.

Turner, A. J., Jacob, D. J., Benmergui, J., Wofsy, S. C., Maasakkers, J. D., Butz, A., Hasekamp, O., Biraud, S. C. A large increase in U.S. methane emissions over the past decade inferred from satellite data and surface observations. *Geophys. Res. Lett.* **2016,** *43* (5), 2218–2224. DOI: 10.1002/2016GL067987.

UN, United Nations, Department of Economic and Social Affairs, Population Division, World Urbanization Prospects: The 2018 Revision, Population of Urban Agglomerations with 300000 Inhabitants or more, **2018a**. https://population.un.org/wup/Download/ last access 28.04.2020.

UN, United Nations, Department of Economic and Social Affairs, Population Division, World Urbanization Prospects: The 2018 Revision, Custom data acquired via website, **2018b.** https://population.un.org/wup/DataQuery/ last access 06.05.2020.

UN, United Nations, World Population Prospects **2019**, Total population (both sexes combined) by region, subregion and country. https://population.un.org/wpp/Download/Standard/Population/ last access 16.04.2020.

UNFCCC, **2015**: Paris Agreement, FCCC/CP/2015/L.9/Rev.1. https://unfccc.int/resource/docs/2015/cop21/eng/l09r01.pdf last access 25.09.2019.

University of Bremen, 2020: http://www.iup.uni-bremen.de/emerge/home/home.html last access 03.04.2020.

van Vuuren, D.P., Edmonds, J., Kainuma, M., Riahi, K., Thomson, A., Hibbard, K., Hurtt, G.C., Kram, T., Krey, V., Lamarque, J.-F., Masui, T., Meinshausen, M., Nakicenovic, N., Smith, S.J., and Rose, S.K.: The representative concentration pathways: An overview, *Climatic Change* **2011,** *109* (1-2), 5–31. DOI: 10.1007/s10584-011-0148-z.

Vay, S.A., Whoo J.-H, Anderson, B.E., Thornhill, K.L., Blake D.R., Westberg, D.J., Kiley, C.M., Avery, M.A., Sachse, G.W., Streets, D.G., Tsutsumi, Y., and Nolf, S. R.: Influence of regional-scale anthropogenic emissions on CO_2 distributions over the western North Pacific, *J. Geophys. Res.* **2003,** *108* (D20), 213. DOI: 10.1029/2002JD003094.

Verheggen, B., Strengers, B., Cook, J., van Dorland, R., Vringer, K., Peters, J., Visser, H., and Meyer, L.: Scientists' views about attribution of global warming, *Environmental science & technology* **2014,** *48* (16), 8963–8971. DOI: 10.1021/es501998e.

Verhulst, K.R., Karion, A., Kim, J., Salameh, P.K., Keeling, R.F., Newman, S., Miller, J., Sloop, C., Pongetti, T., Rao, P., Wong, C., Hopkins, F.M., Yadav, V., Weiss, R.F., Duren, R.M., and Miller, C.E.: Carbon dioxide and methane measurements from the Los Angeles Megacity Carbon Project - Part 1: Calibration, urban enhancements, and uncertainty estimates, *Atmos. Chem. Phys.* **2017,** *17.* DOI: 10.5194/acp-17-8313-2017.

Voosen, P.: Scientists flag new causes for surge in methane levels, *Science* **2016,** *354* (6319), 1513. DOI: 10.1126/science.354.6319.1513.

Wada, A., Matsueda, H., Sawa, Y., Tsuboi, K., and Okubo, S.: Seasonal variation of enhancement ratios of trace gases observed over 10 years in the western North Pacific, *Atmospheric Environment* **2011,** *45* (12), 2129–2137. DOI: 10.1016/j.atmosenv.2011.01.043.

Wallace, J. M., and Hobbs, P.V.: *Atmospheric Science. An introductory survey*, Second edition, *International Geophysics* **2006**, volume 92, Academic Press Elsevier. ISBN: 0-12-732951-X.

Wang, C., and Prinn, R.G.: On the roles of deep convective clouds in tropospheric chemistry, *J. Geophys. Res.* **2000,** *105* (D17), 22269–22297. DOI: 10.1029/2000JD900263.

Wang, Y., Stein, A.F., Draxler, R.R., de La Rosa, J.D., and Zhang, X.: Global sand and dust storms in 2008: Observation and HYSPLIT model verification, *Atmospheric Environment* **2011,** *45* (35), 6368–6381. DOI: 10.1016/j.atmosenv.2011.08.035.

Wang, Y., and Zeng, T.: On tracer correlations in the troposphere: The case of ethane and propane, *J. Geophys. Res.* **2004**, 109 (D24306). DOI: 10.1029/2004JD005023.

Wilkins, E.T.: Air Pollution and the London Fog of December, 1952, *Journal of the Royal Sanitary Institute* **1954,** *74* (1), 1–21. DOI: 10.1177/146642405407400101.

WMO, **2016**: 18th WMO/IAEA Meeting on Carbon Dioxide, other greenhouse gases and related measurement techniques (GGMT-2015), GAW Report No. 229. https://library.wmo.int/doc_num.php?explnum_id=3074 last access 04.06.2020.

WMO, **2020**: WMO Statement on the State of the Global Climate in 2019. https://library.wmo.int/doc_num.php?explnum_id=10211 last access 27.03.2020.

Wunch, D., Wennberg, P.O., Toon, G.C., Keppel-Aleks, G., and Yavin, Y.G.: Emissions of greenhouse gases from a North American megacity, *Geophys. Res. Lett.* **2009,** *36* (15). DOI: 10.1029/2009GL039825.

Xiao, Y.: Constraints on Asian and European sources of methane from CH_4-C_2H_6-CO correlations in Asian outflow, *J. Geophys. Res.* **2004,** *109* (D15), 955. DOI: 10.1029/2003JD004475.

Zhao, C.L., and Tans, P.P.: Estimating uncertainty of the WMO mole fraction scale for carbon dioxide in air, *J. Geophys. Res.* **2006,** *111* (D8), 81. DOI: 10.1029/2005JD006003.

Zheng, G.J., Duan, F.K., Su, H., Ma, Y.L., Cheng, Y., Zheng, B., Zhang, Q., Huang, T., Kimoto, T., Chang, D., Pöschl, U., Cheng, Y.F., and He, K.B.: Exploring the severe winter haze in Beijing: The impact of synoptic weather, regional transport and heterogeneous reactions, *Atmos. Chem. Phys.* **2015,** *15* (6), 2969–2983. DOI: 10.5194/acp-15-2969-2015.

Zhu, T., Melamed, M.L., Parrish, D., Gauss, M., Gallardo Klenner, L., Lawrence, M., Konare, A., and Liousse, C.: WMO/IGAC Impacts of Megacities on Air Pollution and Climate, GAW Report No. 205, **2013**. ISBN: 978-0-9882867-0-2.

Zimnoch, M., Necki, J., Chmura, L., Jasek, A., Jelen, D., Galkowski, M., Kuc, T., Gorczyca, Z., Bartyzel, J., and Rozanski, K.: Quantification of carbon dioxide and methane emissions in urban areas: Source apportionment based on atmospheric observations, *Mitig Adapt Strateg Glob Change* **2019,** *24* (6), 1051–1071. DOI: 10.1007/s11027-018-9821-0.

Danksagung

Hiermit möchte ich mich bei meinen Kollegen, Freunden und meiner Familie bedanken, die mich während der Promotion und meiner Tätigkeit am DLR-IPA begleitet und unterstützt haben.

Insbesondere bedanke ich mich bei meinem Doktorvater Markus Rapp für die Möglichkeit am IPA promovieren zu können und für sein Interesse an der Messung und Auswertung von Treibhausgasen und somit der Grundlage meiner Arbeit. Vielen Dank an ihn und auch an Hans Schlager, welche mir die Teilnahme an spannenden Messkampagnen, interessanten Konferenzen und aufschlussreichen Workshops im In- und Ausland ermöglicht haben.

Ein sehr großer Dank geht an Anke Roiger, nicht nur für die hervorragende wissenschaftliche Betreuung und die Möglichkeit immer eine Ansprechpartnerin zu haben, sondern auch für die angenehme Zusammenarbeit, die Arbeitspausen und vor allem ihre persönliche Motivation mich und meine Arbeit voranzubringen. Ebenso danke ich Heidi Huntrieser, welche immer ein offenes Ohr für mich hatte und sich mit viel Zeit und Hingabe jeglicher Diskussion gewidmet hat.

Vielen Dank an Monika Scheibe für die Einarbeitung in das Messinstrument und die Abläufe in der Datenauswertung. Mein Dank gilt hierbei auch Paul Stock und Julian Kostinek für ihre Hilfe bei allen möglichen technischen und experimentellen Anliegen.

Weiterhin danke ich auch der Nachwuchsgruppe „Treibhausgase“ sowie allen Kollegen am IPA der Abteilung Atmosphärische Spurenstoffe und Wolkenphysik für die angenehme, motivierende, aber auch freundschaftliche Arbeitsatmosphäre. Insbesondere möchte ich mich noch bei Mariano Mertens bedanken für seine Ausdauer und Bereitschaft meine Wünsche in diversen Modellläufen umzusetzen und die Ergebnisse mit mir zu diskutieren. Ein besonderer Dank gilt vor allem meinen Korrekturlesern, welche mir auch noch kurzfristig und tatkräftig am Ende beiseite gestanden haben! Zu guter Letzt auch ein herzliches Dankeschön an das EMeRGe und 3DO Team. Ohne diese tolle Kampagnenzeit hätte die Arbeit nur halb so viel Spaß gemacht.

Schließlich möchte ich mich auch bei meinen Eltern Maria & Reinhard und meiner Schwester Kristina bedanken, die mich in den letzten Jahren nicht nur unterstützt, sondern auch immer neugierig und interessiert an meinem Forschungsthema und meinem Arbeitsalltag waren. Alex, deine Geduld, deine aufmunternden Worte und dein Rückhalt sind unbezahlbar.